MAX-PLANCK-INSTITUT FÜR KOLLOID- UND GRENZFLÄCHENFORSCHUNG

NANOSTRUKTURIERTE MATERIALIEN DURCH NEUE TEMPLATSYSTEME UND NUTZUNG MESOPORÖSER SILIKATE ALS NANO-REAKTOREN

DISSERTATION

ZUR ERLANGUNG DES AKADEMISCHEN GRADES

DOKTOR DER NATURWISSENSCHAFTEN

IN DER WISSENSCHAFTSDISZIPLIN PHYSIKALISCHE CHEMIE

EINGEREICHT AN DER MATHEMATISCH-NATURWISSENSCHAFTLICHEN

FAKULTÄT DER UNIVERSITÄT POTSDAM

VON MATTHIJS GROENEWOLT

POTSDAM IM DEZEMBER 2004

1 Einleitung

Poröse Stoffe zeichnen sich durch eine hohe Oberfläche und einen erheblichen Anteil an Hohlräumen aus, was sie für verschiedenste Anwendungen in der Chemie interessant macht. So spielt die hohe innere Oberfläche poröser Materialien vornehmlich eine Rolle bei Chromatographie und Katalyse[1], während die Nutzung der vorhandenen Hohlräume die Möglichkeit bietet den Einfluss restriktiver Geometrien auf das Verhalten von Materie und chemischen Reaktionen zu untersuchen.[2,3]

Zusätzlich hat sich gezeigt, dass eine spezielle Synthese poröser Materialien, der „Nanocasting"–Prozess, als analytisches Werkzeug für die Charakterisierung lyotroper Phasen verwendet werden kann.[4,5,6]

Die vorliegende Arbeit gliedert sich grob in zwei Abschnitte, die sich mit Herstellung und Charakterisierung poröser Materialien unter Berücksichtigung der Bedeutung des „Nanocastings" für die Analytik, sowie ihrer Verwendung als „Nano"-Reaktor befassen.

Der erste Teil befasst sich mit der Darstellung und Analyse poröser Materialien.

Zunächst wird die Synthese neuartiger, hierarchischer Silikate mit Mesoporen, Poren mit einem Durchmesser zwischen 2- und 50 nm, beschrieben. Während bei monomodalen porösen Silikaten jetzt praktisch jede Porengröße zugänglich ist[7], gilt dies nicht für bimodale Systeme. Diese Materialien sind von Interesse, da die hierarchische Porenarchitektur eine Abstimmung von Transport und Trennung in chromatographischen Verfahren erlaubt.

Darauffolgend wird das Phasenverhalten eines neuen Templats für mesoporöse Systeme untersucht und dessen Eignung für die Synthese dünner, kristalliner Übergangsmetalloxidfilme demonstriert, da diese besondere Anforderungen hinsichtlich der „Robustheit" an die lyotropen Phasen erfordern.

Schließlich wird die quantitative Beschreibung zweier flüssigkristalliner Modellsysteme durch Anwendung des Nanocastings demonstriert.

Im zweiten Teil werden mesostrukturierte Silikate als Reaktionsmatritzen für die Synthese von Nanoteilchen benutzt.

Die Modell-Synthese von hochtemperaturresistenten Polyimid-Nanopartikeln, welche auf anderem Weg chemisch nicht zugänglich sind und deren nanometergroße Dimensionen produktionstechnisch von Interesse sind, wird beschrieben.

Des Weiteren wird die Darstellung neuartiger graphitischer Carbonitridverbindungen, deren Anwendungsspektrum vom Speichermedium über katalytisches Trägermaterial bis hin zum Kohlenstoffvorläufer reicht, als makroskopisches Referenzexperiment vorgestellt.

Die Verwendung mesoporöser Silikate bei dieser Reaktionsführung erlaubt schließlich die Synthese von graphitischen Carbonitrid–Nanopartikeln verschiedener Größenordnungen, und die Untersuchung des restriktiven Einflusses der Poren auf die Reaktion.

2 Mesoporöse Silikate: Neue Strukturen und Neue Template und deren Charakterisierung durch Nanocasting

Bei den meisten Verfahren zur Herstellung mesoporöser Materialien werden die Hohlräume von Templaten gebildet, die anschließend durch Extraktion oder thermische Behandlung entfernt werden. Jedoch sind die Unterschiede in den Syntheseansätzen fundamental.

Im Gegensatz zu MCM[8] oder SBA[9] Materialien, die in einem synergistischen Verfahren in verdünnten Lösungen niedermolekularer Tenside hergestellt werden, wird beim „True Liquid Crystal Templating“ (TLCT) oder „Nanocasting“ eine konzentrierte, lyotrope Phase, meist bestehend aus amphiphilen Blockcopolymeren, durch einen Sol-Gel-Prozess in einer anorganischen Matrix „eingefroren“.

Anders als bei synergistisch hergestellten Materialien, die keinerlei Rückschlüsse auf die ursprüngliche Anordnung der Template in der Lösung zulassen, ist nach der thermischen Entfernung des Templats beim Nanocasting das mesoporöse Produkt eine exakte Kopie der in Lösung vorliegenden lyotropen Phase. Röntgenuntersuchungen haben hierbei gezeigt, dass bei diesem Prozess alle relevanten Details der lyotropen Phase erfasst werden. Somit eignet sich dieses Verfahren, neben der Herstellung mesoporöser Materialien, ebenfalls zur einfachen und wenig aufwendigen Charakterisierung lyotroper Phasen.[4,5,6]

2.1 Hierarchische Mesoporöse Silikatstrukturen und deren Charakterisierung

Wie einleitend bereits erwähnt, ist mittlerweile der gesamte Mesobereich bei der Herstellung poröser Silikate abgedeckt. So können sämtliche Porengrößen und –architekturen zwischen 2 und 30 nm Porendurchmesser durch supramolekulare Aggregate von einfachen Tensiden oder Blockcopolymeren hergestellt werden. Verschiedene Techniken, wie das Mischen von Blockcopolymeren oder Quellen von Tensidmizellen, erlauben dabei eine exakte Porengrößeneinstellung und reduzieren die Anzahl der benötigten Template. Porengrößen zwischen 30 und 50 nm sind letztendlich durch Polymerlatices verschiedener Größen zugänglich.

Von besonderem materialwissenschaftlichem Interesse ist jedoch immer noch die Konstruktion von hierarchischen, bi- oder multimodalen Porenarchitekturen.

Hierdurch können selektive Trennverfahren realisiert werden, bei denen die größeren Poren den Transport bewerkstelligen und Diffusionslimitierungen verringern, was zu höherem Durchsatz führt, während die kleineren Poren für die Trennung zuständig sind.

Prinzipiell ist die Synthese solcher hierarchischer Systeme durch die Verwendung von Porogenen unterschiedlicher Größe möglich, die keine Mischaggregate miteinander bilden.

So ist eine bimodale Porenverteilung durch eine Mischung von Poylmerlatices mit Blockcopolymeren einfach zu realisieren[10,11], beschränkt die untere Grenze für den Durchmesser der „Transportporen“ jedoch auf etwa 30 nm.

Der hier gewählte Ansatz besteht darin, Blockcopolymere unterschiedlicher Blocklängen zu verwenden, die aufgrund ihrer chemischen Natur keine Mischmizellen miteinander bilden. Für die Bildung der kleinen Poren wurde ein Perfluoralkyl-*block*-poly(ethylenoxid) Oligomer bzw. Tensid, hier als F-PEO abgekürzt, gewählt. Die größeren Poren sollten von Blockcopolymeren deren Phasenverhalten bereits bekannt war, gebildet werden: Poly(styrol)-*block*-poly(ethylenoxid) kurz PS-PEO, welches Poren mit einem Durchmesser von 9 nm bildet, und Poly(ethylen-*co*-butylen)-*block*-Poly(ethylenoxid) kurz PB-PEO, welches zu 13 nm großen Poren führt.

Diese Arbeiten sowie experimentelle Details sind in Artikel Nr. 1 der Publikationsliste (*Mixed Micellar Phases of Nonmiscible Surfactants: Mesoporous Silica with Bimodal Pore Size Distribution via the Nanocasting Process*) zusammengefasst und sollen hier nur kurz rekapituliert werden.

Zunächst wurde das Phasenverhalten von F-PEO untersucht. Bedingt durch die äußerst starke Mikrophasenseparation des Fluor- und Ethylenoxidblocks zeigte sich ein großer flüssigkristalliner Bereich von 30-50 Gew. % Oligomer relativ zum eingesetzten Silikat. Die Porogene zeigten bereits bei der Analyse mittels Polarisationsmikroskopie ausgedehnte, µm-große, hexagonale Domänen, die auf der Nanometerskala als hexagonale Anordung der Poren im calcinierten Material mit dem Transmissionselektronenmikroskop (TEM) beobachtet werden konnten (Abb.1). Die untersuchten Oligomere bildeten dabei Poren von 3 nm Durchmesser entsprechend der Größe ihrer mizellaren Aggregate in der lyotropen Phase. Mittels Stickstoffsorption wurde die Zugänglichkeit der Poren untereinander und eine enge Porengrössenverteilung gezeigt. Dies unterstreicht die Eignung dieser Oligomere als Porenbildner für mesoporöse Materialien.

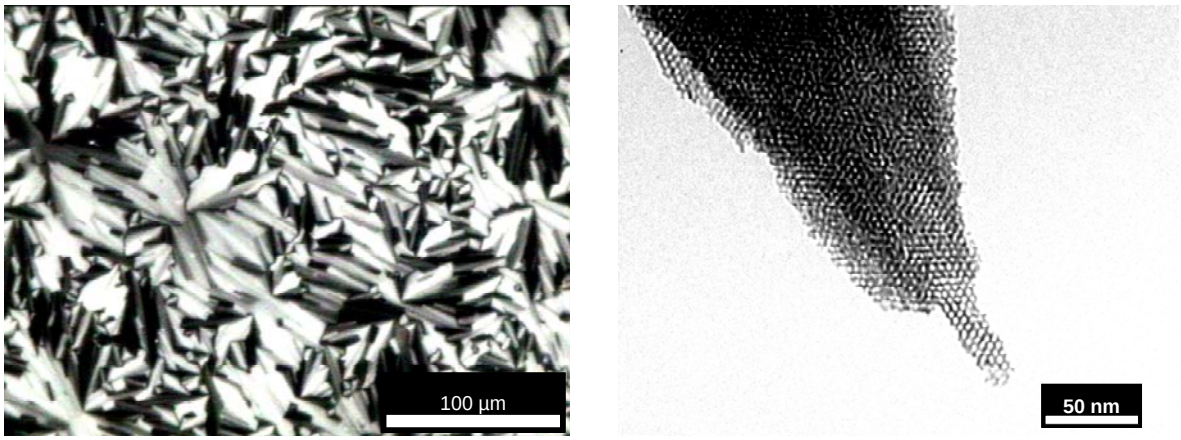

Abb.1: Links: Polarisationmikroskopische Aufnahme des lyotropen Flüssigkristalls in der Reaktionsmischung

Rechts: TEM Aufnahme derselben Probe vom kalzinierten Material

Bei der Bildung von gemischten lyotropen Phasen des F-PEO/PS-PEO und des F-PEO/PB-PEO Systems zeigte sich wie erwartet[12,13,14], eine vollständige Unmischbarkeit der verwendeten Polymere mit den flurorierten Oligomeren auf mizellarer Ebene.

Die relative Zusammensetzung sowohl des F-PEO/ PS-PEO- als auch des F-PEO/ PB-PEO-Systems wurde variiert, um festzustellen, ob es zu mesoskopischen Entmischungen kommt. Im Gegensatz zum gewünschten, auf makroskopischer Skala homogenen Material liegen hierbei die lyotropen Phasen der einzelnen Porogene getrennt nebeneinander vor.

Für das F-PEO/PS-PEO- System zeigte sich, dass bis zu einer Templatzusammensetzung von rund 35/65 Gew. % eine vollständige mizellare Mischbarkeit vorliegt, während höherere Anteile an F-PEO zunehmend in mesoskopischer Entmischung resultiert.

Abb.2 zeigt die TEM Aufnahme einer solchen mesoskopisch entmischten Probe.

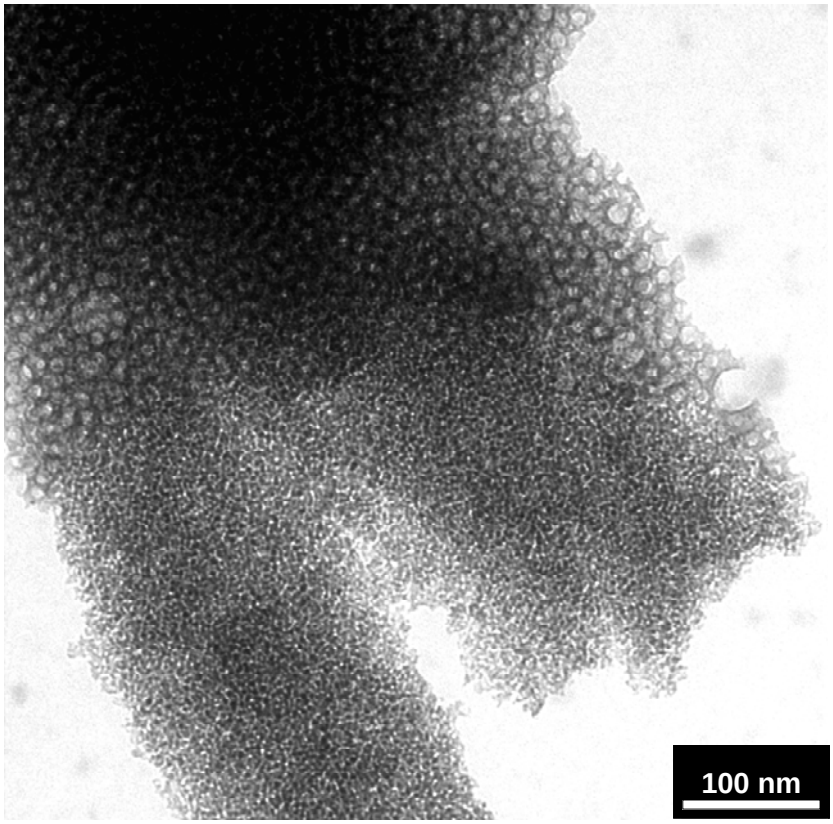

Abb.2: Mesoskopische Entmischung, bei der zwei lyotrope Phasen nebeneinander koexistieren (F-PEO/PS-PEO = 70/30 Gew. %)

Für das F-PEO/PB-PEO- System wurde mizellare Mischbarkeit für jede relative Zusammensetzung gefunden, die in einem homogenen Material mit bimodaler Porengrössenverteilung des calcinierten Silikats resultiert. Abb.3 zeigt zwei Aufnahmen mit unterschiedlicher relativer Zusammensetzung der beiden Porogene.

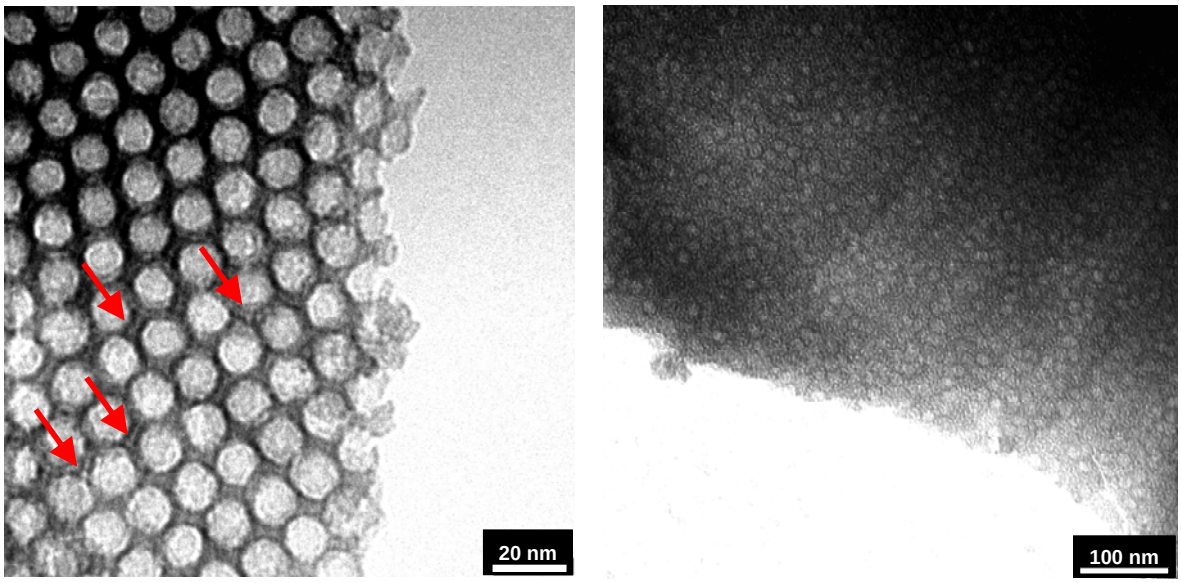

Abb.3: Links: (F-PEO/PB-PEO = 17/83 Gew. %) Stark vergrößerte Aufnahme mit geringem Gehalt an F-PEO. Die kleinen Poren sind schwierig zu erkennen. Experimentelle Fakten (s.Text) weisen aber darauf hin, dass die kleinen Poren in den Wänden der großen Poren lokalisiert sind, was sich durch eine „Stegstruktur“ (Pfeile) bemerkbar macht.

Rechts: (F-PEO/PB-PEO = 80/20 Gew. %) Bimodale Verteilung der Poren bei der die großen PB-PEO-Poren in einer Matrix der F-PEO-Poren eingebettet sind

Zwar sind in der Nahaufnahme des Materials mit geringem F-PEO Gehalt die kleinen Poren nicht eindeutig zu erkennen, jedoch war das Material nach dem Kalzinieren homogen schwarz, was dafür spricht, dass die F-PEO Mizellen zwischen den größeren PB-PEO Mizellen eingeschlossen werden. Da die Poren wegen ihrer räumlichen Trennung nicht durch Perkolation miteinander verbunden sind, verkohlt das Material lediglich, verbleibt jedoch innerhalb der Matrix. Sorptionsexperimente zeigten, dass das gesamte Porensystem unzugänglich war, was zusätzlich darauf hinweist, dass die kleineren Mizellen die perkolative Verbindung der großen Poren untereinander verhindern, die sonst über den Ethylenoxidblock gewährleistet wird.

Zusätzlich fällt in Abb.3 der Verlust der mizellaren Fernordnung der PB-PEO Aggregate mit zunehmendem Gehalt an F-PEO auf, welcher sich auch in SAXS-Experimenten (Abb.4) verfolgen lässt.

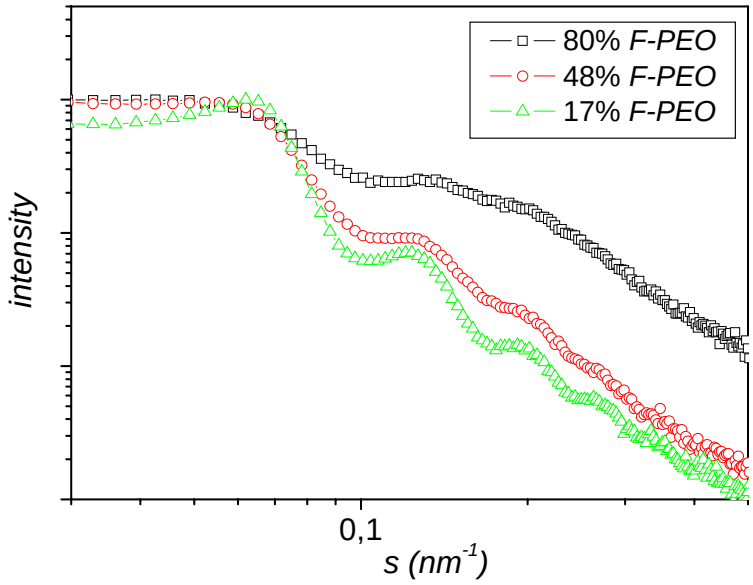

Abb.4: SAXS- Kurven für Silikate mit bimodaler Porenverteilung unterschiedlicher relativer Zusammensetzung. Während bei mittleren Anteilen F-PEO die Ordnung der großen Mesoporen erhalten bleibt, verschwindet diese mit zunehmendem Anteil an F-PEO. Bei hohen F-PEO Gehalten ist bereits eine breite Schulter bei höheren Streuvektoren zu sehen, die von den kleinen Poren stammt.

Das reine PB-PEO System neigt zu FCC- artigen, hochgeordneten Packungen der Mizellen. Sowohl in der TEM-Aufnahme von Abb.4 als auch in der SAXS- Streukurve ist die hohe Ordnung für die Probe mit einem relativen Anteil an F-PEO von 17 Gew. % deutlich zu sehen. Erhöht man diesen Anteil, verschwindet die Ordnung der PB-PEO Mizellen bis bei einem Gehalt von 80 Gew. % F-PEO eine breite Schulter bei größeren Streuvektoren in der SAXS- Kurve auftaucht, die von den kleinen Poren herrührt.

Bei einer ausreichend hohen relativen Konzentration des F-PEO ist die bimodale Verteilung zudem gut in den Stickstoff-Sorptionsisothermen sichtbar (Abb.5). Die beiden Stufen der

Kapillarkondensation der jeweiligen Porengrößen bei relativen Drücken von ca. 0,2 bzw. 0,8 sind in den Isothermen deutlich zu erkennen und spiegeln sich in der bimodalen Verteilung der Mesoporen wider. Des Weiteren zeigt sich der relative Anteil beider Porogene in den Sorptionsdaten und der zughörigen DFT-Analyse für die Porengrössenverteilung. Mit steigendem relativem Anteil des F-PEO wird die Kapillarkondensation bei $p/p_0 \sim 0,2$ ausgeprägter, da ein größerer Anteil an Mesoporen mit ~3 nm Durchmesser vorliegt. Gleichzeitig wird, sichtbar an der kleineren Hystereseschleife, die von den 13 nm Poren adsorbierte Stickstoffmenge kleiner, da weniger Poren dieser Größe zur Adsorption bereit stehen.

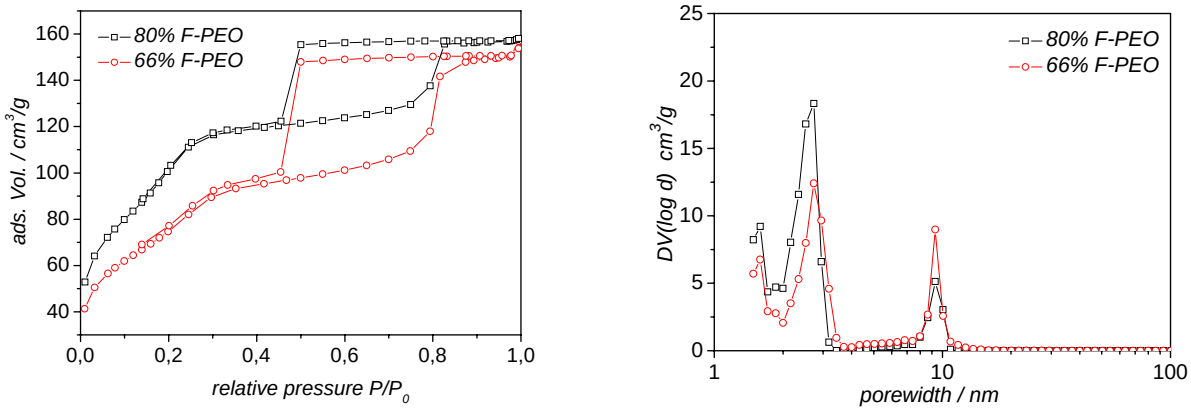

Abb.5: links: Sorptionsdaten für zwei Silikate mit unterschiedlicher relativer Templatzusammensetzung F-PEO/PB-PEO. Mit steigendem F-PEO Anteil wird die Kapillarkondensation bei kleinen relativen Drücken ausgeprägter, während die Hysterese, die von den Poren des PB-PEO herrührt, kleiner wird. Rechts: Zugehörige Porenverteilung aus der DFT -Berechnung der Sorptionsdaten. Je höher der relative Anteil von F-PEO ist, desto mehr Stickstoff wird von den kleinen Poren adsorbiert.

Bei einer Zusammensetzung von F-PEO/ PB-PEO = 66/34 Gew. % (die wegen der höheren Dichte des Fluor-Oligomers in etwa einer äquimizellaren Zusammensetzung entspricht) konnte zusätzlich eine interessante Metastabilität festgestellt werden, ähnlich einem

klassischen binären Phasendiagramm von Polymeren mit Mischungslücke in der symmetrischen Zusammensetzung.

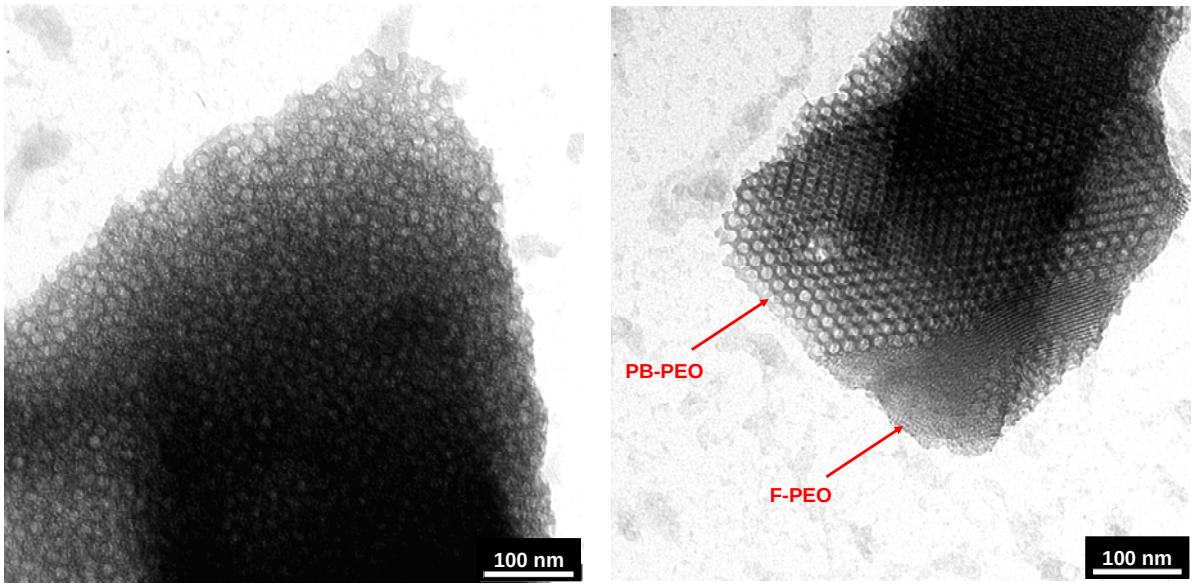

Abb. 6: Zwei Stellen der gleichen Probe mit einer Zusammensetzung von F-PEO/ PB-PEO = 66/34 Gew. %
Links: bimodale Verteilung und vollständige Mischbarkeit beider Mizellen. Rechts: Entmischung und Auskristallisieren in zwei nebeneinander vorliegende Flüssigkristalle.

Abb.6 zeigt zwei elektronenmikroskopische Aufnahmen derselben Probe. Während einmal eine homogene Verteilung der Mizellen beobachtet wird, ist in der anderen Aufnahme die Koexistenz zweier hochgeordneter, flüssigkristalliner Phasen zu sehen. Analog zu klassischen Polymergemischen, deren Phasen nur ungeordnet vollständig mischbar sind, kann es zu einem Auskristallisieren der reinen Verbindungen in Mikrodomänen kommen.
Zusammenfassend kann gesagt werden, dass besonders das F-PEO/PB-PEO System für die Synthese bimodaler Porensysteme geeignet ist.

2.2 Neue Robuste Templatphasen: Beschreibung und Anwendung

Neben der Entwicklung hierarchischer Strukturen spielt bei der Suche nach neuen Templaten besonders die Stabilität gegenüber externen Einflüssen bei der Synthese eine Rolle.

Während Faktoren wie z.B. Luftfeuchtigkeit bei der silikatischen Monolithsynthese eine untergeordnete Rolle spielen, ist dies bei der Synthese von dünnen Filmen nach dem „Evaporation Induced Self Assembly“ (EISA)- Verfahren durch das erhöhte Oberflächen/Volumen Verhältnis im zu synthetisierenden Material nicht mehr der Fall.[15,16,17]

Die Bildung und Stabilität selbstorganisierter Strukturen hängt maßgeblich von der Mikrophasenseparation der verschiedenen Blöcke ab, die wiederum vom hydrophoben Kontrast abhängt. Somit ist maximaler hydrophober Kontrast zwischen den Blöcken gewünscht, um die stabile Bildung lyotroper Phasen auch in anspruchsvolleren Lösungsmitteln als Wasser und sonstigen, normalerweise die Ausbildung lyotroper Strukturen störenden, externen Einflüssen zu gewährleisten.

Da sich in der silikatischen Sol-Gel Chemie, insbesondere dem Nanocasting-Ansatz und vielen anderen Sol-Gel Prozessen, die Grenzflächenkompatibilisierung des Polymers mit der verwendeten Reaktionsmischung über einen Poly(Ethylenoxid)-Block (PEO) als hydrophiler Komponente bewährt hat[18,19,20], sollte der hydrophobe Block, der den Kern in den mizellaren Aggregaten bildet, chemisch möglichst verschieden dazu sein.

Naheliegend ist hier die Verwendung ultrahydrophober Blöcke, z.B. perfluorierter Alkanblöcke, wie bereits weiter oben beschrieben. Ein Nachteil dieser Polymerklasse ist jedoch das Verbrennen zu toxischen Verbindungen bei der thermischen Entfernung des Templats. Ein Polymer, das Ultrahydrophobizität aufweist und relativ „untoxisch“ verbrennt ist Polyisobutylen (PIB).[21]

In Verbindung mit einem PEO-Block sollte dieses Polymer beide Vorteile, „Robustheit“ gegenüber externen Einflüssen und Eignung für die wässerige oder alkoholische Sol-Gel Chemie in sich vereinen.

Im Folgenden sind die Ergebnisse zur Untersuchung dieses neuen Templats zusammengefasst, die in Artikel Nr. 2 (*Polyisobutylene-block-poly(ethylene oxide) for robust*

Templating of Highly-Ordered Mesoporous Materials) der Publikationsliste ausführlich beschrieben werden.

Abb.7 zeigt TEM-Aufnahmen von Silikatabdrücken der lyotropen Phase des PIB-PEO Polymers in verschiedenen Konzentrationen.

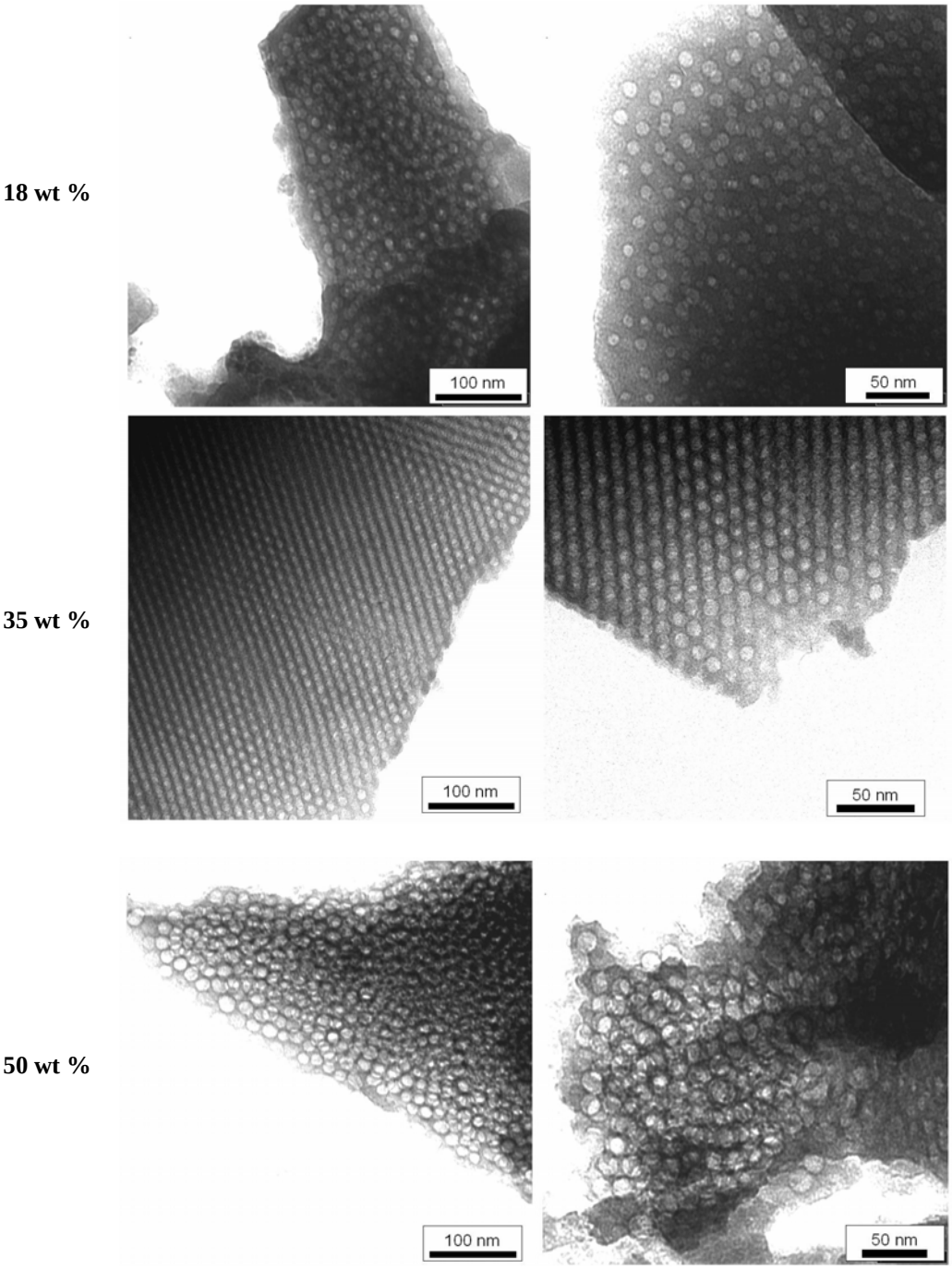

Abb 7: TEM Aufnahmen der Silikatabdrücke wässriger Lösungen unterschiedlicher PIB-PEO Konzentration. Zu sehen ist der Gang von einer isotropen, mizellaren Lösung über einen hochgeordneten Flüssigkristall hin zu einer glasartigen Phase vor dem Übergang in die lamellare Phase.

Wie erwartet wird zunächst eine mizellare L-Phase beobachtet, die mit steigender Konzentration über die energetisch günstigste Anordnung monodisperser Teilchen, der dichtesten Packung, in einem glasartigen Zustand deformierter Aggregate mündet. Besonders der Bereich um 35 Gew. % Templat, bezogen auf das Silikat scheint für die Synthese mesoporöser Systeme interessant, da er im Vergleich zu früheren Untersuchungen mit dem PB-PEO-Blockcopolymer noch geordneter ist und ausschließlich flüssigkristalline Monodomänen aufweist. Die Absenz einer Textur in der Polarisationsmikroskopie zeigt zudem, dass es sich hierbei um eine kubische Phase handelt. Die TEM Aufnahmen und die SAXS-Streudaten (Abb.8) sprechen ebenso für eine FCC-artige Anordnung der Micellen, wie sie auch schon für das PB-PEO-Templat gefunden wurde. Die SAXS-Analyse dieser Probe weist ebenfalls auf eine kubische FCC-Packung hin, wie man an der Modulation des zweiten Maximums in der Streukurve erkennt.

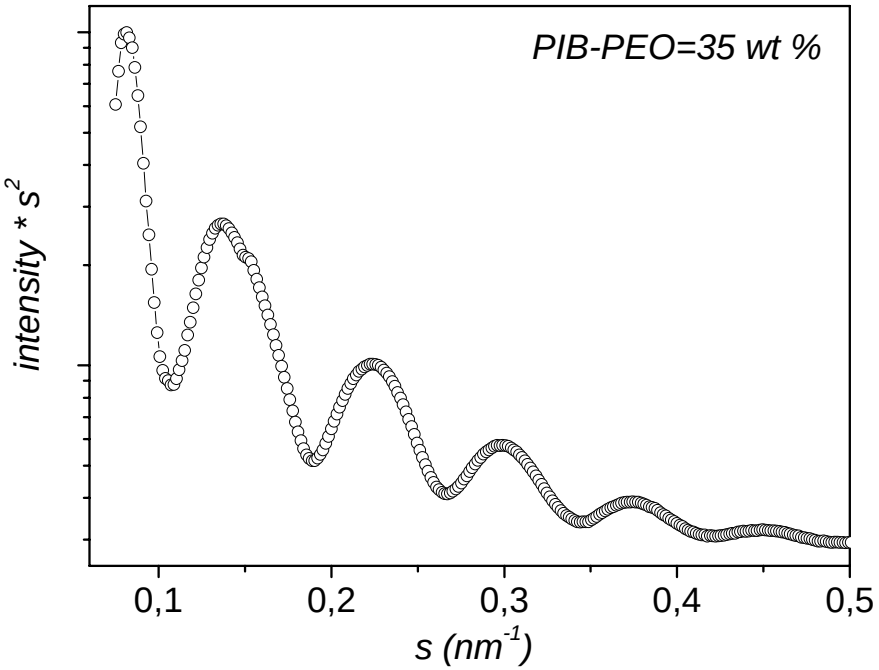

Abb.8: SAXS-Kurve für eine Templatkonzentration von 35 Gew. % relativ zum eingesetzten Silikat. Die hohe Ordnung ist an der Anzahl der Maxima zu erkennen, außerdem weist das 2. Maximum eine Modulation auf, die für eine FCC-artige Packung der Poren spricht.

In der Aufnahme mit 50 Gew. % Templat bezogen auf das Silikat, erkennt man das Vorliegen ellipsoider Objekte, die eine Tendenz zum Wechsel in den lamellaren Bereich andeuten. Generell zeigen die Aufnahmen, dass sich das Templat für die Herstellung mesoporöser Silikate eignet, zumal in keinem Konzentrationsbereich makroskopische Phasenentmischung festgestellt wurde. Der ultrahydrophobe Kern der mizellaren Aggregate verlangsamt die Austauschraten der Mizellen untereinander jedoch drastisch, sodass eine besonders sorgfältige Gleichgewichtseinstellung in verdünnten alkoholischen Lösungen vor der Templatierung benötigt wird. Abb.9 zeigt die Templatierung einer nicht equilibrierten, verdünnten (1 Gew. %), wässrigen Phase, bei der makroskopisch keine Phasenseparation zu erkennen war.

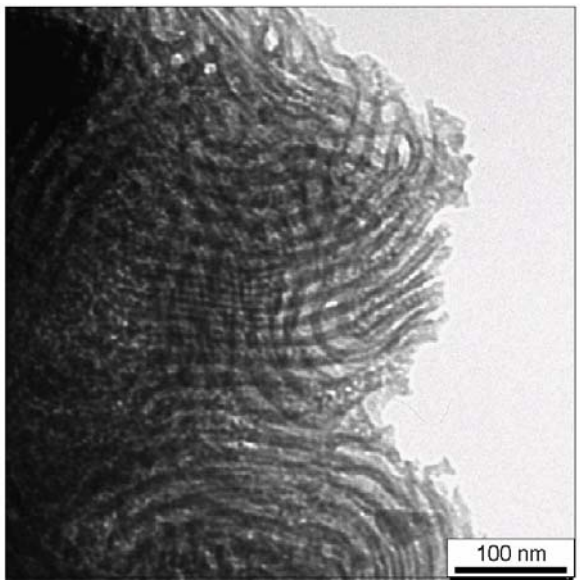

Abb.9: Aufnahme einer nicht equilibrierten 1 Gew. % Lösung des PIB-PEO Polymers

Solche mesostrukturierten, multilamellaren und vesikularen Phasen mit einer Periodizität von 15-20 nm wurden in Nachbarschaft zu unstrukturierten und unporösen Silikatteilchen im TEM gefunden, was für eine mesoskopische Entmischung in der Lösung auf einer Skala von einigen 100 nm spricht, die kinetisch durch die langsamen intermizellaren Austauschraten „eingefroren“ ist.

Die Robustheit des Templats wurde anschließend in Zusammenarbeit mit Dipl.-Chem. T. Brezesinski in Filmsynthesen von mesostrukturiertem, kristallinem TiO_2 (Anatas) durch den

EISA-Prozess demonstriert. Abb.10 zeigt die SEM-Aufnahme eines solchen kristallinen Films.

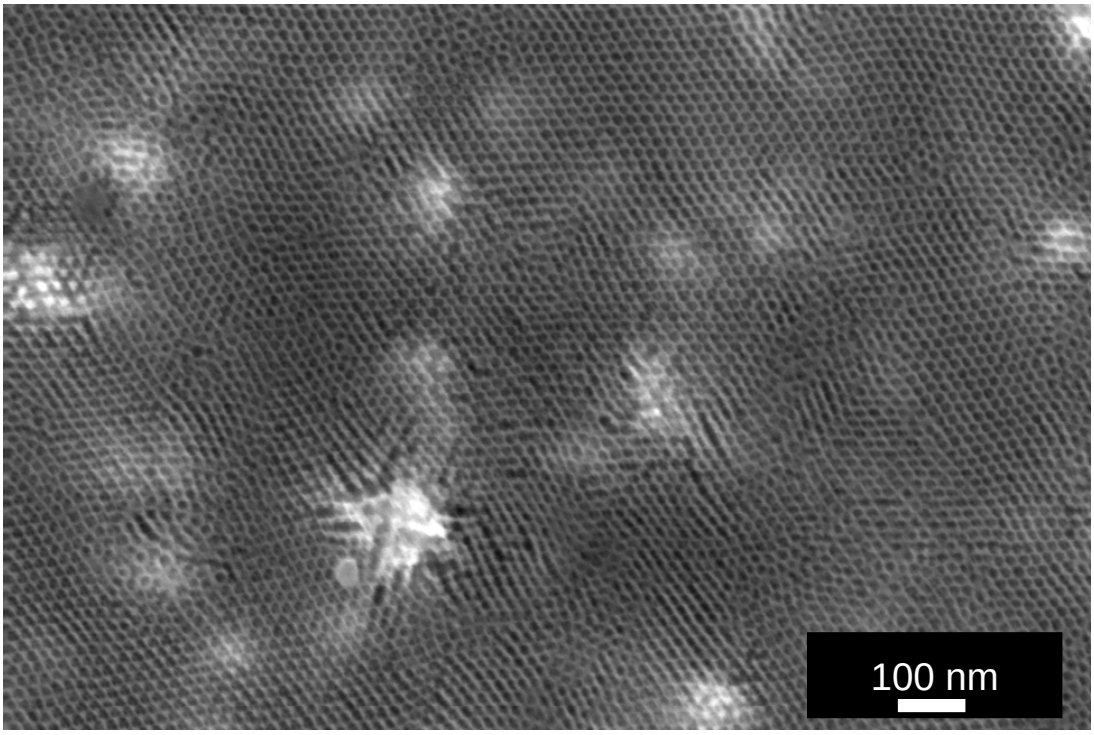

Abb.10: SEM-Aufnahme des mesoporösen TiO_2-Films

Die perfekte langreichweitige und kubische Anordnung der Poren ist deutlich zu erkennen. Dies zeigt die Eignung des Templats sogar in der Synthese von anspruchsvollen kristallinen Materialien. Bereits die Verwendung des PB-PEO Polymers anstelle des kommerziell erhältlichen PEO-PPO-PEO (Pluronics^{TM}), welches einen nur schwach hydrophoben Kern von Poly(Propylenoxid) besitzt, führte zu einer signifikanten Verbesserung des Verfahrens in früheren Experimenten.[22,23] Anwendungen dieses Templats sind zusätzlich in den Artikeln 3 und 4 der Publikationsliste zu finden.

An dieser Stelle ist weiterhin anzumerken, dass die Aggregatgröße der Polymere in der lyotropen Phase ebenfalls nicht zu unterschätzen ist, da bei der späteren thermischen Kristallisation des dünnen TiO_2-Films die Mesostruktur bei zu kleinen Porendurchmessern kollabiert. Auch hier hat das neue verwendete PIB-PEO-Polymer mit einer Aggregatgröße

von 14 nm einen beträchtlichen Vorteil gegenüber Pluronics^{TM}, welches Poren mit ca. 9 nm Durchmesser bildet.

2.3 Die Analyse Lyotroper Modell-Phasen mit Hilfe des Nanocasting

Nachdem die Synthese und Beschreibung von neuen hierarchischen Strukturen und die Charakterisierung und Anwendung neuer Templatphasen erfolgreich demonstriert wurde, werden im Folgenden zwei unterschiedliche hochgeordnete, flüssigkristalline Phasen exemplarisch mit Hilfe des Silica-Nanocastings quantitativ untersucht und verglichen: Die lyotropen Phasen eines Blockcopolymers (Poly(ethylen-*co*-butylen)-Poly(ethylenoxid)), welches im untersuchten Konzentrationsbereich dicht gepackte sphärische Mizellen bildet[24], und eines Alkylimidazoliumsalzes, das zur Ausbildung zylindrischer Aggregate neigt.[25] In diesem Zusammenhang soll besonders die Stärke der Röntgenkleinwinkelstreuung (SAXS) demonstriert werden.

Neben einer einfachen Fitfunktion, die parametrisch an die experimentellen Daten angepasst wird und mit der eine einfache Bestimmung, z.B. der Porengrösse möglich ist, können hierbei aus den Rohdaten der Streukurve, durch ein von Ruland et al.[26,27] entwickeltes numerisches Verfahren, zwei charakteristische Größen für Mesophasen, die Grenzfläche ι und die Krümmung der Grenzfläche κ, gewonnen werden. Mit Hilfe dieser beiden Größen lassen sich Mesophasen in ein generalisiertes Phasendiagramm, das κ-ι-Diagramm, einordnen und bestimmen.[28]

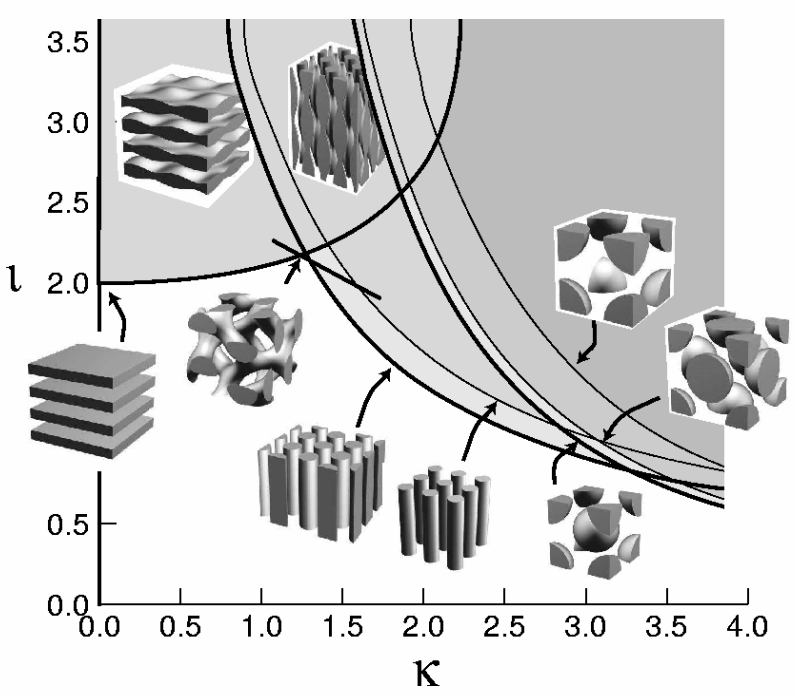

Abb.11: Generelles Phasendiagramm für Blockcopolymermesophasen aus Ref. 28. Die Einteilung erfolgt nach Grenzfläche ι und Krümmung der Grenzfläche κ.

Die folgenden Ergebnisse entstammen einer kooperativen Arbeit mit Dr. B. Smarsly, von dem die numerische Behandlung der Röntgenrohdaten durchgeführt wurde. Die detaillierte Vorgehensweise findet sich in Artikel Nr. 5 (*SAXS-Analysis of Mesoporous Model Materials: A Validation of Data Evaluation Techniques to Characterize Pore-Size, Shape, Surface Area and Curvature of the Interface)* der Publikationsliste.

Generell wird die Streuintensität in SAXS-Kurven durch eine Modulation des Gitterfaktors *Z* mit dem Formfaktor *F,* der das Gitter besetzenden Objekte, beschrieben.

Für ein definiertes Gitter, welches durch polydisperse Objekten besetzt ist, kann unter Annahme eines bestimmten Gittertyps (FCC, BCC, HCP), Form (Kugeln, Zylinder), Größe und Polydispersität eine Funktion aufgestellt werden, die die experimentellen Daten gut beschreibt.[29] Abb.12 zeigt eine solche Funktion im Vergleich mit den experimentell gewonnen Röntgendaten und demonstriert, dass bereits auf diesem Weg eine gute Beschreibung der experimentellen Daten gelingt. So ergibt sich für die sphärischen Poren in

Abb.12 ein Durchmesser von 13.8 ± 0.2 nm und für die Zylinder 2.8 ± 0.2 nm. Diese Werte sind in guter Übereinstimmung mit den TEM-Aufnahmen. Für den Fall der lyotropen Phase mit sphärischen Aggregaten kann die Anpassung der experimentellen Daten sowohl mit dem hier verwendeten FCC-Gitterfaktor als auch mit einem HCP-Gitter erreicht werden, und somit ist keine eindeutige Zuordnung des Strukturfaktors möglich.

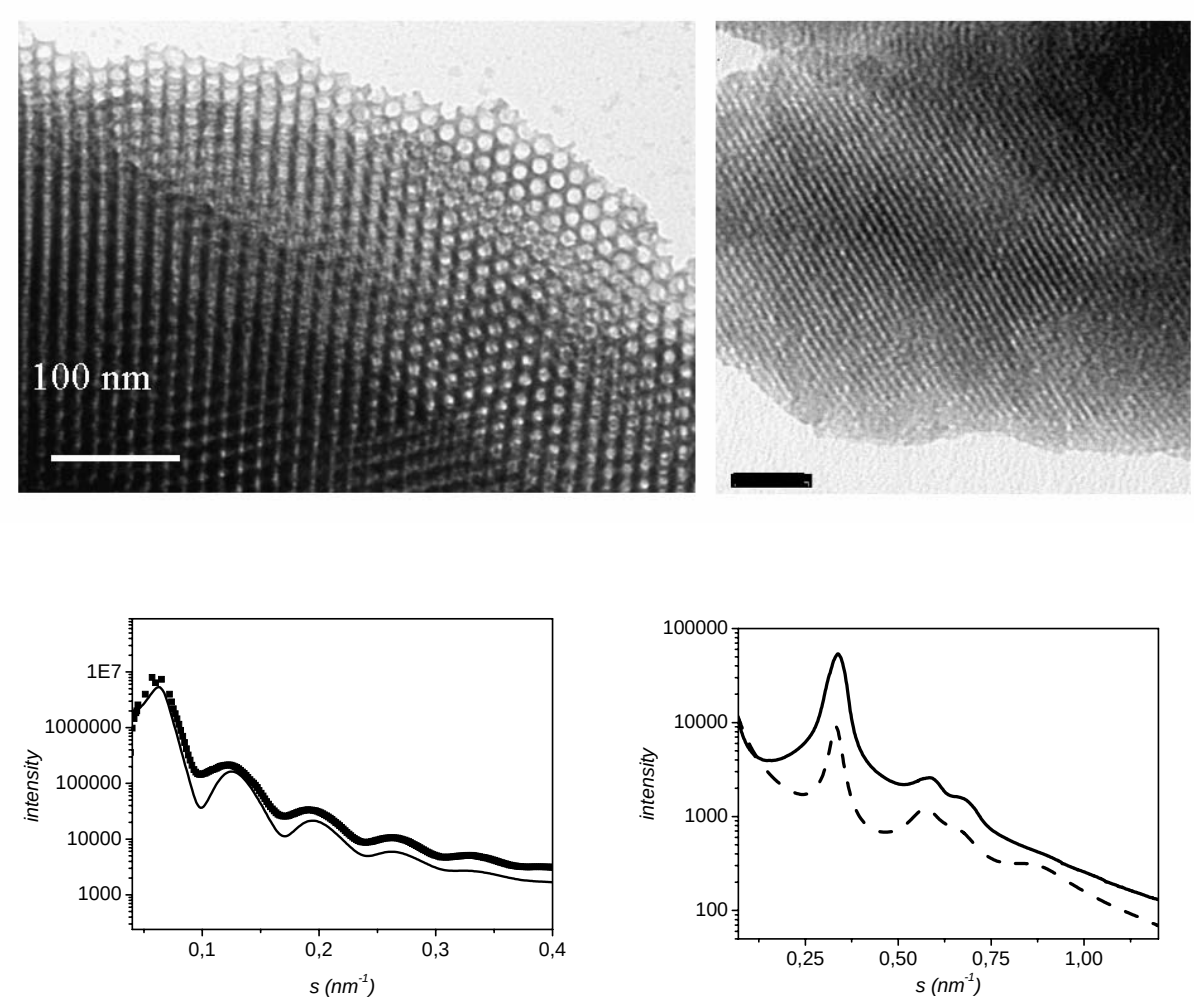

Abb.12: TEM-Aufnahmen (oben) der im Text beschriebenen Mesophasen und die zugehörigen SAXS Daten (unten, Punkte: exp.; Durchgezogen: fit). Der schwarze Balken im rechten TEM-Bild entspricht 25 nm.

Fitparameter für die linke Streukurve (FCC): Porendurchmesser = 13.8 ± 0.2 nm; Gitterparameter d_{111}= 17 ± 0.3 nm.

Fitparameter für die rechte Streukurve (2D-HEX): Porendurchmesser = 2.8 ± 0.2 nm; Gitterparameter d_{10}= 3.5 ± 0.35 nm

Mit der Vorraussetzung, dass mindestens ein Interferenzmaxima in der Streukurve enthalten ist und bei mittleren Streuvektoren das Porod-Gesetz erfüllt wird, können weiterhin Krümmung κ und Grenzfläche ι der mesoporösen Systeme bestimmt werden. Beide Werte sind aus der Segmentlängenverteilungsfunktion („Chord-length-distribution“ CLD)[30,31,32] erhältlich, welche die zweite Ableitung der sogenannten charakteristischen Funktion darstellt und über eine Fouriertransformation mit der experimentellen Streukurve verknüpft ist.
Dies ist besonders im Falle der lyotropen Phase mit der Kugelpackung von Bedeutung, da im Gegensatz zu den Streudaten der zylindrischen Phase, die Reflexe im Verhältnis $1:\sqrt{3}:2$ zeigen und eine hexagonale Zuordnung eindeutig machen, die Anpassung der Streudaten wie oben erwähnt sowohl mit kubischem als auch mit hexagonalem Strukturfaktor möglich ist.
Die beiden numerisch aus den Streudaten der sphärischen Phase bestimmten Parameter von Grenzfläche und Krümmung ergeben ein Wertepaar von (κ=3.3; ι=2.4), welches, eingesetzt im generalisierten κ-ι-Diagramm, das Vorliegen einer kubischen Phase belegt.

3 Mesoporöse Silikate als Nanoreaktoren

3.1 Synthese von Hochtemperaturresistenten Polyimidnanopartikeln

Der Hohlraum poröser Materialien ist aufgrund seiner geometrischen und chemischen Eigenschaften häufig in der Chemie benutzt worden. Einerseits wurden dabei Experimente durchgeführt, die den restriktiven Einfluss dieser Geometrien nutzten; andererseits Synthesen bestimmter Materialien, bei denen das poröse Material als Form zur Replikation verwandt wurde.[33] Bei zeolithischen Materialien stand häufig der Einzelmolekülaspekt im Mittelpunkt, der es erlaubte, z. B. einzelne Farbstoffe in zeolithischen Käfigen spektroskopisch zu untersuchen.[34] Obwohl auch erfolgreiche Experimente zur Replikation durchgeführt wurden[35], blieb die Gast-Wirt-Chemie der Zeolithe, die durch den Sub-Nanometer Bereich

charakterisiert wird, in dieser Hinsicht auf wenige Systeme beschränkt, da sowohl die den Materialien inhärente Größenselektivität als auch Diffusionslimitierungen das chemische „Füllen“ der Materialien mit den Edukten in der Praxis schwierig gestalteten.

Den Durchbruch brachte die Entdeckung der MCM-Materialien mit Kanalsystemen im Nanometerbereich.

Diese Materialien dienten als „Exotemplate“[36] bei der Synthese verschiedenster Verbindungen. Neben Edelmetall-Nanodrähten[37] und leitfähigen Polymersträngen aus Polyanilin[38], wurde eine ganze Reihe von mesostrukturierten Kohlematerialien entwickelt.[39,40,41]

In Zusammenarbeit mit (inzwischen Dr.) Dipl.-Chem. A. Thomas wurden verschiedene monolithische Silikatmaterialien für die Synthese von Polyimidnanopartikeln benutzt. Polyimid ist materialwissenschaftlich wegen seiner hohen Termperaturstabilität von Bedeutung, jedoch außerordentlich schwierig zu verarbeiten.[42]

Durch die Herstellung nanometergroßer Partikel können zum einen Additive für homogene Hybridmaterialien hergestellt werden, zum anderen erleichtert diese Größenlimitierung die Möglichkeit das Material zu sintern und somit für thermische Beschichtungen zu verwenden.

Da es sich bei der gewählten Reaktion (Abb.13) um eine Polykondensationsreaktion handelt, ist die Darstellung nanometergroßer Teilchen auf anderen Wegen, z.B. über Emulsionsreaktionen nicht möglich.

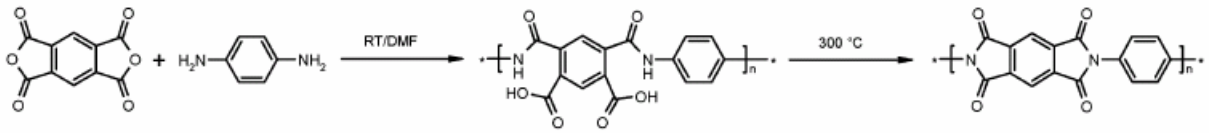

Abb.13: In den mesoporösen Silkaten durchgeführte Polykondensation zu Polyimid

Zwei verschiedene Silikat-Matritzen wurden für die Synthese verwandt; schichtartige mesoporöse Silikate, die durch cholesterische Phasen von Hydroxypropylzellulose hergestellt wurden[43] und kubische Silikate mit sphärischer Porenmorphologie.

Die Ergebnisse dieser Arbeiten sind hier kurz zusammengefasst und werden ausführlich in Artikel Nr.6 (*Nanoparticles and Nanosheets of Aromatic Polyimides via Polycondensation in Controlled Pore Geometries)* der Publikationliste besprochen.

Abb.14 zeigt die gelungene Replikation der Porenmorphologien beider Silikate durch Polyimid.

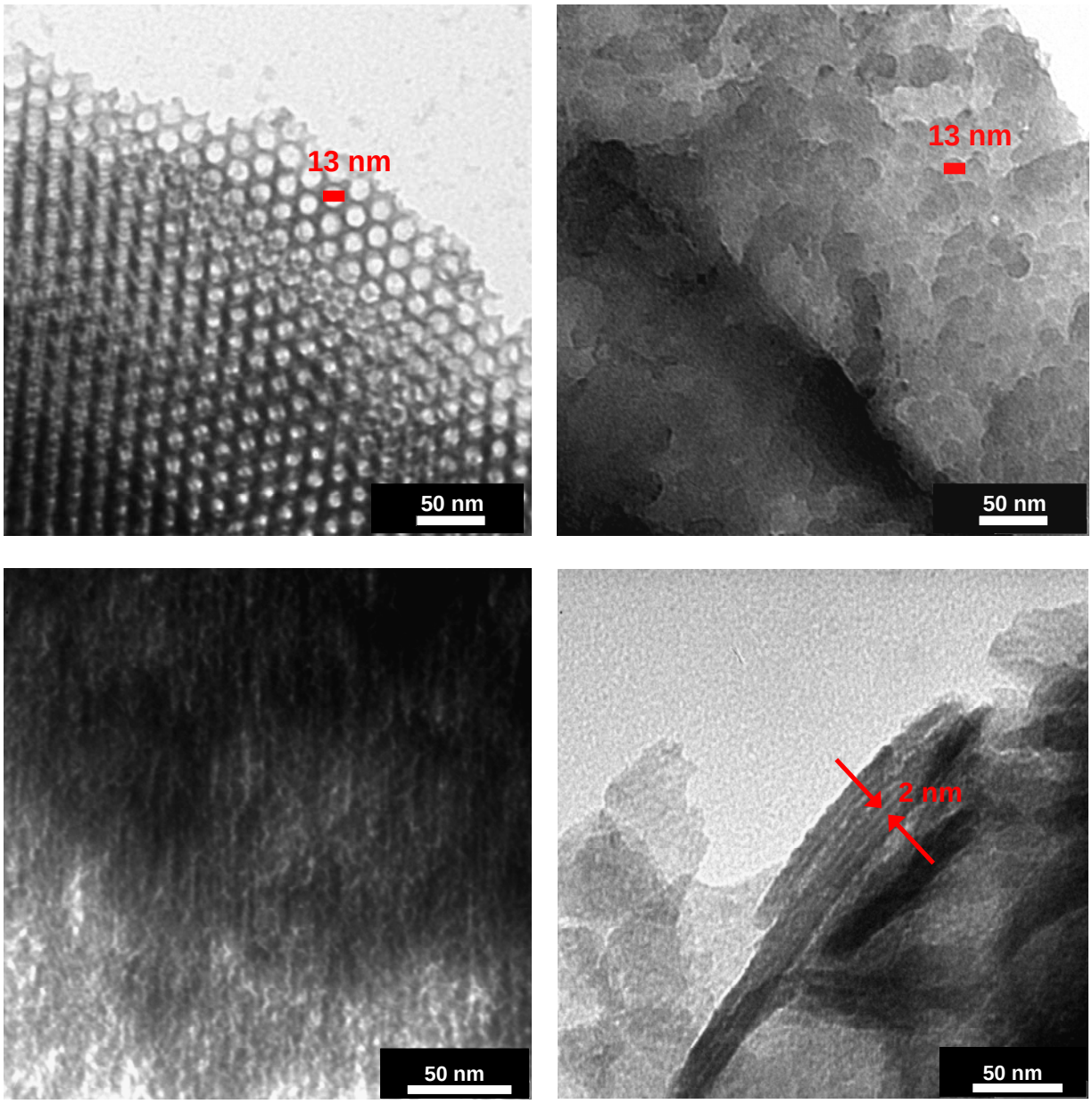

Abb.14: Replikation der Silikate (links) zu Polyimid-Nanopartikeln (rechts). Oben: Das sphärische System führt zu Partikeln mit 13 nm Durchmesser. Unten: Die Verwendung der schichtartigen Silikate liefert Polyimid-Platten mit ca 2 nm Dicke.

Werden sphärische Exotemplate verwendet, erhält man Polyimidkugeln mit einem Durchmesser von 13 nm, bei dem Einsatz der schichtartigen Silikate besteht das Produkt aus Polyimidplatten mit ca. 2 nm Dicke.

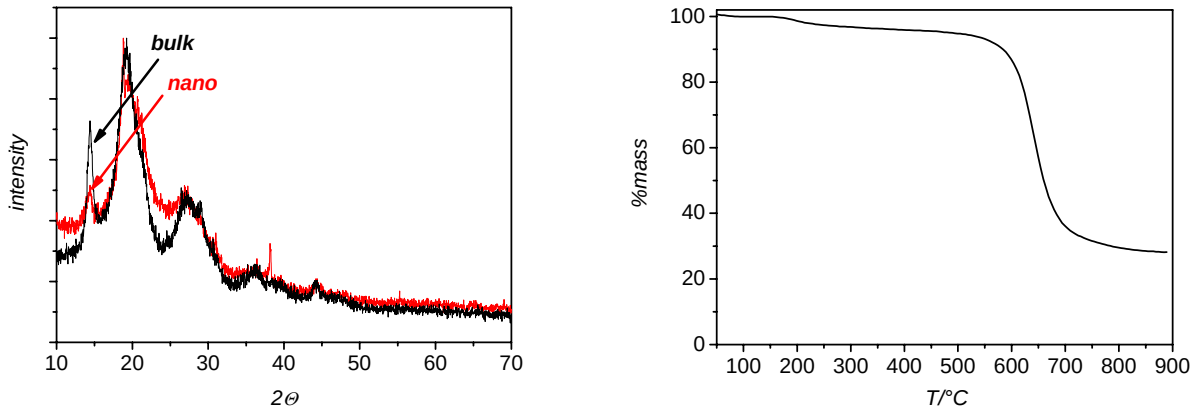

Abb.15: Links: WAXS-Diffraktogramm für die PI-Nanopartikel und die Referenzsynthese. Rechts: Die Thermogravimetrische Analyse der PI-Nanopartikel zeigt, dass diese stabil bis über 500°C sind. Die Restmasse stammt von carbonisiertem PI

Das in Abb.15 gezeigte Röntgendiffraktogramm des Nano-Produkts zeigt ein ähnliches Spektrum wie das Produkt der Referenzsynthese ohne geometrische Beschränkung, mit leichter Verbreiterung der Reflexe durch die nanoskaligen Abmessungen, und belegt die erfolgreiche Synthese von Polyimid-Nanostrukturen. Thermogravimetrische Untersuchungen (Abb.15) zeigen ebenfalls, dass das Material trotz Größenlimitierung seine außergewöhnliche thermische Belastbarkeit erhält. Dieses Experiment demonstriert die potentielle Verwendbarkeit von Polyimid-Nanopartikeln als Hochtemperaturwerkstoff.

3.2 Synthese von Neuen Graphitischen Carbonitridmaterialien: Beschreibung der Referenzreaktion und Anwendung in Mesoporösen Materialien

Nachdem die Herstellung von funktionellen Polymer-Nanopartikeln erfolgreich demonstriert wurde, sollte das Konzept des Nano-Reaktors auch auf keramische Werkstoffe übertragen werden. Eine Skalierung auf Nanometergröße kann hierbei sowohl von synthetischem als auch analytischem Interesse sein. Mit der Verwendung mesoporösen Silikats als Reaktionsmatrix steht ein sinnvolles Instrument zur Verfügung diese Skalierung für grundlegende Untersuchungen zu erreichen.

Von Carbonitriden wird vermutet, dass sie die Eigenschaften von Kohlenstoff in materialwissenschaftlichen Anwendungen verbessern können und somit deren Einsatzspektrum erhöhen. Vor allem bei der Suche nach superharten Materialien stieß man auf das hypothetische β-C_3N_4, isostrukturell mit dem technologisch wichtigen β-Si_3N_4, dem eine ähnliche Härte wie Diamant vorrausgesagt wurde.[44,45] Auch der graphitanalogen Schichtverbindung von C_3N_4, welche bei Normalbedingung die thermodynamisch stabilere Modifikation darstellen sollte, werden eine Reihe interessanter Eigenschaften vom katalytischen Trägermaterial bis zum Gasspeichermedium zugeschrieben.

Außerdem sollten gerade für Schichtverbindungen, wie graphitisches C_3N_4, vergleichende Experimente in restriktiver Geometrie aus mehreren Perspektiven heraus interessant sein. Zum einen, um festzustellen, ob sich überhaupt Schichten in restriktiver Geometrie ausbilden. Falls diese gebildet werden, steht mit den Nanopartikeln ein wirkungsvolles Modellsystem für die Untersuchung von Interkalations- Verbindungen zur Verfügung, bei denen sich die Struktur einzelner Schichten untersuchen lässt. Solche Prozesse sollten durch das hohe Oberflächen/Volumen-Verhältnis bei den Nanopartikeln vermehrt stattfinden. Andererseits sind Kohlenstoff-Stickstoffverbindungen durch die Möglichkeit der C-C-Bindungsknüpfung

unter N-Elimination ideale Precursoren für Kohlenstoffmodifikationen*. Durch die Kompartimentisierung der Materialien auf verschieden große Volumina im nm^3-Bereich wird eine bestimmte Anzahl an Kohlenstoffatomen zur Verfügung gestellt. Abhängig von dieser Zahl sollten sich bestimmte Modifikationen vermehrt bilden.

So ist gezeigt worden, dass durch Pyrolyse von Polypyrol-Nanopartikeln Fullerene synthetisch zugänglich sind, wobei der Anteil höherer Homologen von der Größe der Nano-Partikel abhängig war[46].

Bisherige Synthesen von makroskopischen Mengen graphitischem C_3N_4 (g-C_3N_4) lieferten zumeist schlecht geordnete Produkte. Die meisten Synthesen gingen hierbei von modifizierten Melamin (Triaminotriazin, $C_3N_3(NH_2)_3$) Precursor-Verbindungen aus, die entweder durch Kondensations- oder Methathese-Reaktionen über Stickstoffatome miteinander verknüpft wurden.[47,48,49]

Auch die Synthese von C_3N_4-Nanotubes ist geglückt[50], jedoch ohne kristalline Ordnung. Gemein ist allen Synthesen, dass die Produkte aus N-verbrückten C_3N_3 (Triazin) Heterozyklen bestehen. Theoretisch ist jedoch auch die Verknüpfung von Cyamellureinheiten[51] (Tri-s-Triazin) zu einem kondensierten Netzwerk mit der Summenformel C_3N_4 möglich, welches Hohlräume, die von jeweils 6 Stickstoffen umgeben werden, innerhalb der Schichten enthält. Abb.16 zeigt Strukturausschnitte aus zwei möglichen Allotropen von graphitischem C_3N_4.

* So sind bereits erste interessante Ergebnisse erzielt worden, die bisher noch nicht veröffentlicht wurden.

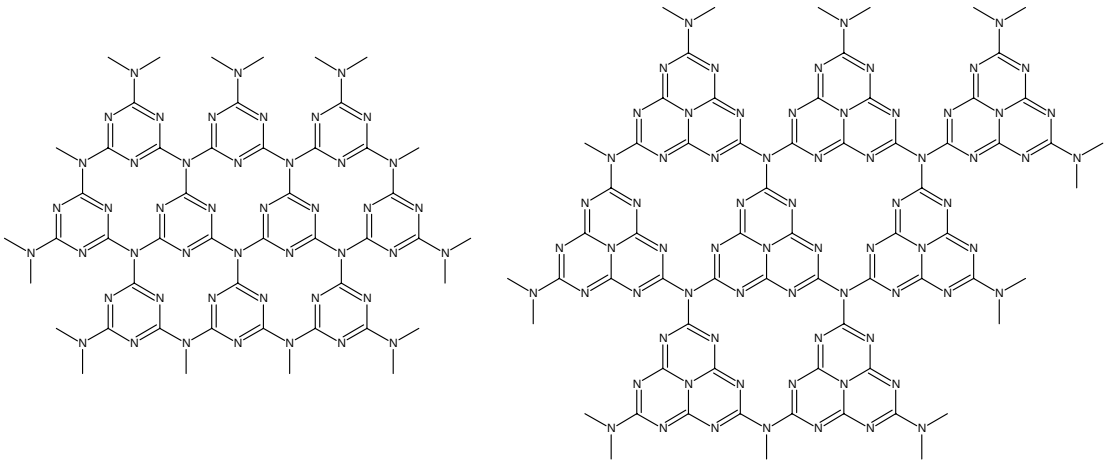

Abb.16: Ausschnitte aus dem C_3N_4-Netzwerk. Links: Basierend auf Melamin (Triazin)- Einheiten. Rechts: Gebildet aus Melem (Tri-s-Triazin)-Einheiten

In dieser Arbeit wurde die kürzlich beschriebene Synthese von Melem[52] ($C_6N_7(NH_2)_3$) abgewandelt, um schichtartige Verbindungen basierend auf dem Tri-s-Triazin (Cyamellur) Heterozyklensystem herzustellen. Nachfolgend werden die wichtigsten Ergebnisse präsentiert, die ausführlich in Artikel Nr. 7 (*Synthesis of g-C_3N_4 based on Cyameluric (C_6N_7) Building Units)* der Publikationsliste beschrieben sind.

Der Reaktionsverlauf ist in Abb.17 schematisiert; thermisch finden zunächst einige Umlagerungen bis zur Stufe des Melamin statt, bevor Kondensationen über die Tri-s-Triazin-Einheiten zu ausgedehnten C_3N_4-Netzwerken führen.

Ausgehend von niedermolekularen Verbindungen wie Cyanamid (1 in Abb.17), welches bei leicht erhöhten Temperaturen schmilzt, ist somit für den Fall der geometrisch restriktiven Synthese ebenfalls eine einfache Beladung des mesoporösen, silikatischen Materials möglich.

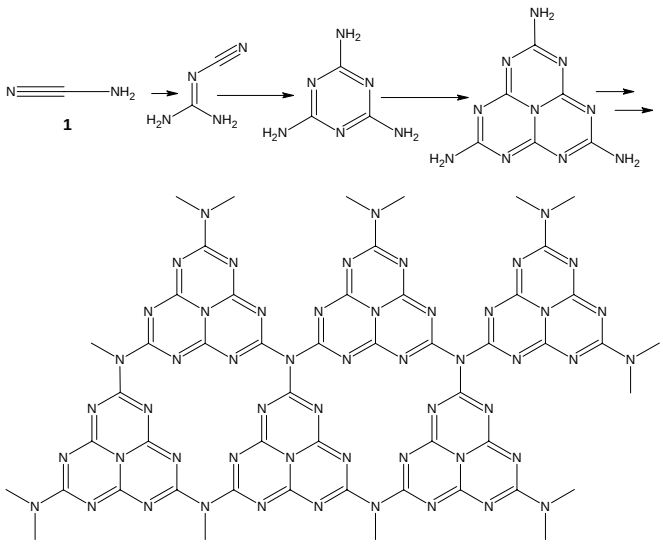

Abb.17: Schematischer Verlauf der Reaktion von Cyanamid über Dicyandiamid, Melamin (Triazin), Melem (Tri-s-Triazin) hin zum g-C_3N_4-Netzwerk

Insgesamt sind verschiedene Edukte auf ihre Eignung in der Synthese überprüft worden, wobei sich herausstellte, dass die Kondensationsreaktion immer über Melamin (Triazin) und teilkondensiertes Melem (Tri-s-Triazin) erfolgt, das sich in endothermer Reaktion bei 380 °C bildet.*

Die kristallographisch bestimmten, relativ geringen Abstände der Aminogruppen im Melem-Molekülkristall, ermöglichen dabei eine Kondensationsreaktion unter Abspaltung von Ammoniak die nur geringfügige Änderungen der relativen Anordnung der Tri-s-Triazin-Einheiten zueinander erfordert.

So bleibt die langreichweitige Ordnung im Bereich von ~0.6 nm in Melem, welche durch die perpendikulare, Zick-Zack-förmige Anordnung der flachen Moleküle untereinander zustande kommt, selbst bei der Auskondensation des g-C_3N_4-Netzwerkes erhalten.

Abb.18 zeigt die strukturellen Änderungen während der Reaktion im Röntgendiffraktogramm bei verschiedenen Temperaturen.

* Wichtig für die Netzwerkausbildung sind alle 3 Aminfunktionen. Wird eine Amineinheit durch einen Alkyl- oder Phenylrest ersetzt, ist die Synthese nicht erfolgreich.

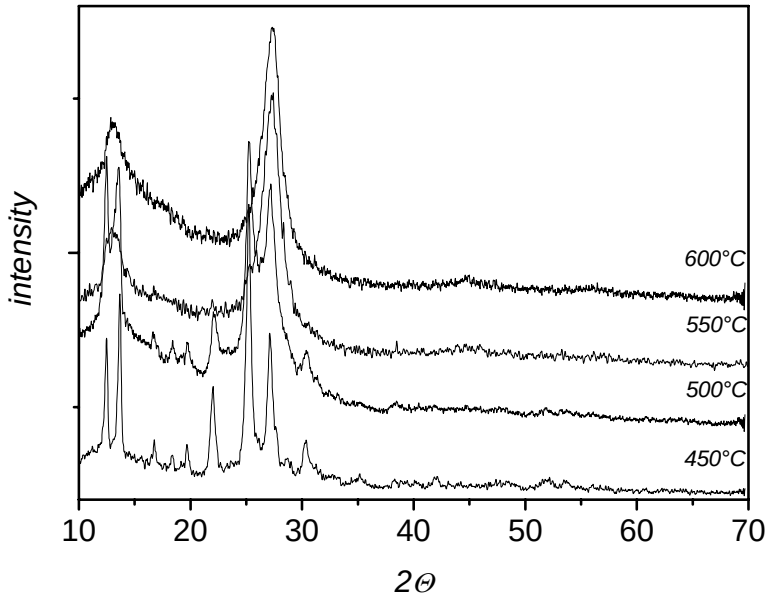

Abb.18: Temperaturabhängiges WAXS-Diffraktogramm für die Reaktion zu g-C_3N_4 von 450°C bis 600°C. Die ankondensierten Tri-s-Triazin-Einheiten (450°C) kondensieren oberhalb 500°C zum g-C_3N_4 -Netzwerk aus.

Die Streukurve bei 450°C entspricht den ankondensierten Tri-s-Triazin-Einheiten mit Fernordnung, angezeigt durch zwei Reflexe im Röntgendiffraktogramm mit Streuwinkeln kleiner 20°, die Wiederholungsperioden von ~0.6 nm entsprechen.

Diese Fernordnung ist auch - wenngleich als breiter Reflex - bei Temperaturen über 500 °C, bei denen die weitere Kondensation zu einem ausgedehnten Netzwerk aus Tri-s-Triazin – Einheiten stattfindet, erhalten. Dies steht im Einklang mit der tetragonalen Konformation des Stickstoffs, der die Einheiten verbindet, und zeigt, dass die Tri-s-Triazin-Einheiten ihre relative Orientierung zueinander während des Kondensationsprozesses beibehalten.

Auch die Reflexe zwischen Streuwinkeln von 20° und 30° münden in einem breiten Reflex bei 27.3°. Dieser Reflex ist typisch für Schichtstrukturen, wie z.B. Graphit, und entspricht einem Interschichtabstand von 0.326 nm, welcher im Vergleich zum Graphit mit 0.335 nm leicht reduziert ist.

Die Verkürzung entspricht einer um ca. 3% dichteren Packung und kann mit der stärkeren Lokalisierung der π-Elektronenwolken erklärt werden. Der Beweis, dass tatsächlich Tri-s-Triazin-Einheiten die Schichtstruktur konstituieren, wird durch XPS-Messungen, die die chemische Umgebung der Elemente anzeigen, erbracht.

Abb.19 zeigt die XPS-Spektren für die 1s-Bindungsenergien des Kohlenstoff- und des Stickstoffatoms.

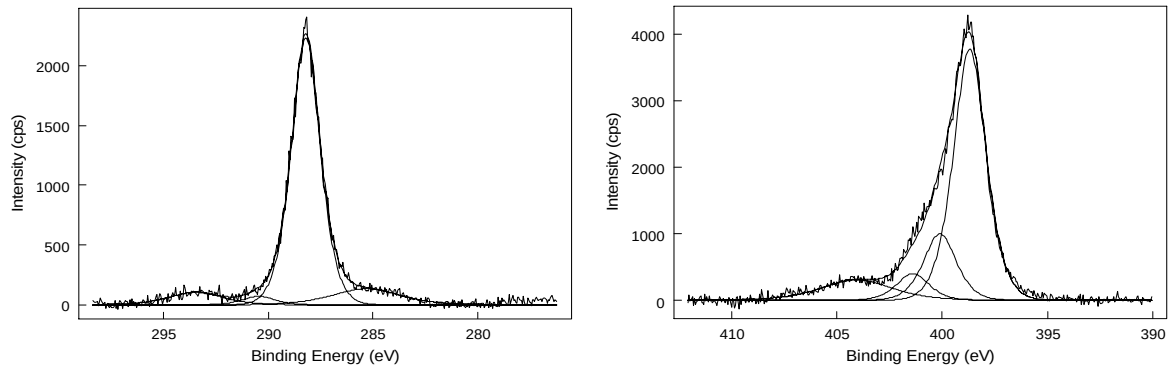

Abb19.XPS-Spektren des g-C_3N_4 für die Bindungsenergie der 1s-Elektronen. Links: Kohlenstoff; Rechts: Stickstoff

Das Kohlenstoffatom zeigt hierbei nur einen Peak, gemäß seiner Bindungsumgebung, welche in jeder Stelle des Moleküls gleich ist, da jedes Kohlenstoffatom trigonal von 3 Stickstoffatomen umgeben ist. Das XPS-Spektrum für das Stickstoffatom zeigt mehrere Signale. Im Vergleich zu den XPS- Daten der in der Literatur beschriebenen g-C_3N_4-Verbindungen, die den gleichen Anteil an tetragonalem (verknüpfendem) Stickstoff und trigonalem (aus den Heterozyklen) Stickstoff enthalten (vgl. Abb.16), sind im g-C_3N_4 (siehe XPS-Spektren in Abb.19), das aus Tri-s-Triazin Einheiten besteht, wesentlich mehr trigonale (398.7 eV) als tetragonale (400.1 eV) Stickstoffatome vorhanden. Zusätzlich zeigt der Fit der experimentellen Daten unkondensierte, H-verbrückte Amine (401.4 eV) an, die die Schichten begrenzen, im Einklang mit dem bestimmten atomaren C/N-Verhältnis von 0.71, das etwas unter dem theoretischen Wert von C/N = 0.75 liegt.

Breite Reflexe, der Interschichtabstand und die Orientierung der Melem-Einheiten untereinander innerhalb einer Schicht weisen somit auf ondulierte, gewellte Schichten im g-C_3N_4 hin.

Abb.20 zeigt ein Modell dieser ondulierten Schichten, aufgebaut aus Tri-s-Triazin- Einheiten:

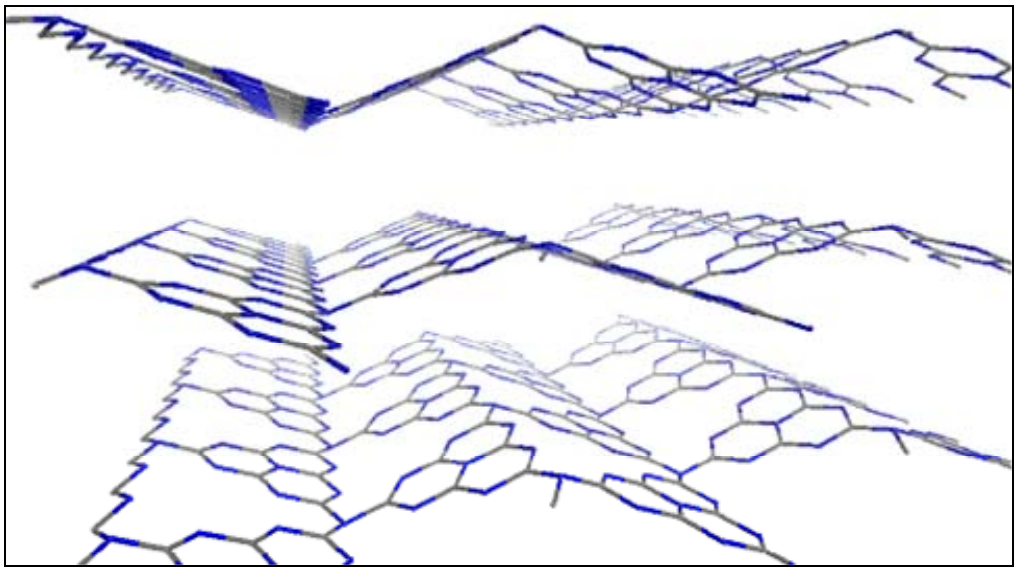

Abb. 20: Modell eines Strukturausschnittes für die ondulierten Schichten des g-C_3N_4

Wenn das Material in einem gasdichten, geschlossenen Behälter weiter auf 600° C erhitzt wurde, konnte ein endothermer Festphasenübergang beobachtet werden. Das Röntgendiffraktogramm in Abb.21 zeigt eine stark erhöhte Kristallinität mit ausgeprägter Schichtstruktur, wobei der Schichtabstand auf 0,319 nm verringert wurde.

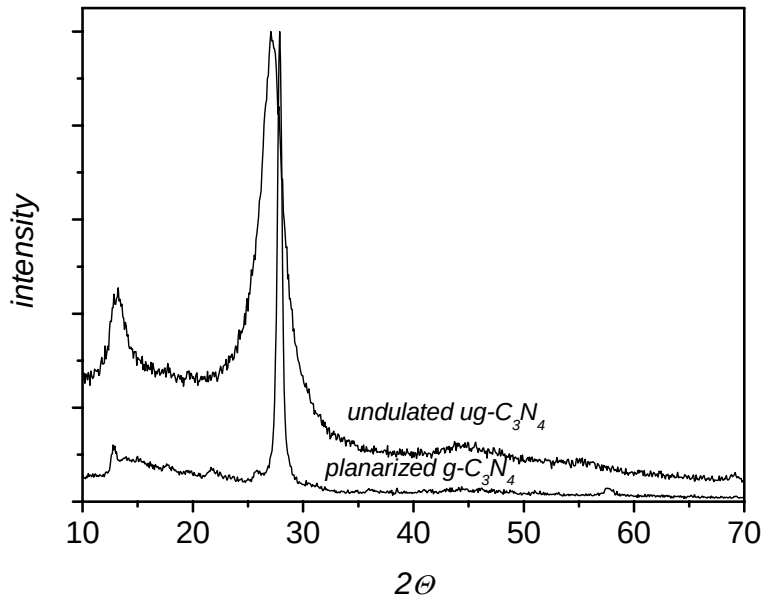

Abb. 21: Röntgendiffraktogramm der ondulierten g-C_3N_4 Phase vor und nach dem Festphasenübergang

Der durch die Ondulationen hervorgerufene Reflex ist jedoch deutlich schwächer. Dies kann mit einer Planarisierung der ondulierten Schichten erklärt werden, bei der die Stickstoffatome ihren elektronischen Zustand von tetragonal hin zu trigonal ändern. Durch die Planarisierung können die Schichten besser gepackt werden und die Ondulation verschwindet. Im Röntgendiffraktogramm bleibt nun die grundsätzliche reguläre Packung, der durch 6 Stickstoffatome gebildeten Hohlräume, innerhalb der Schichten sichtbar, die durch einen schwächeren, aber schärferen, Reflex bei 12.8° angezeigt wird.

Mit Photoluminiszenzmessungen kann die stattfindende Umorientierung der Melem-Einheiten zueinander, auf Grund der Planarisierung bestätigt werden. Abb.22 zeigt das Modell für das graphitische C_3N_4-System nach der Planarisierung.

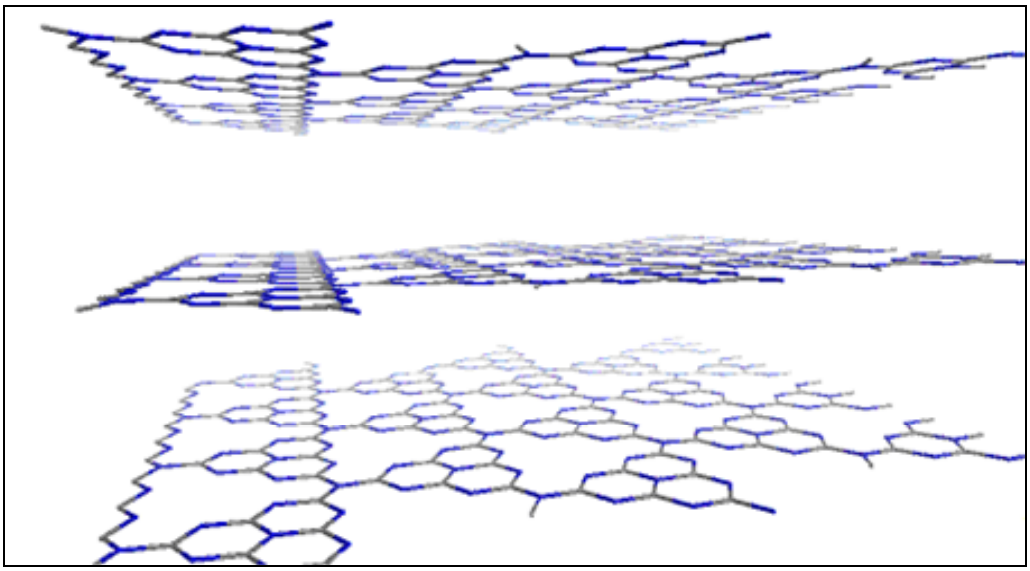

Abb. 22: Modell eines Strukturausschnittes aus dem planarisiertem Material

Der Interschichtabstand von 0.32 nm kann ebenfalls mit hochauflösender Elektronenmikroskopie sichtbar gemacht werden. Abb.23 zeigt ein hochauflösendes TEM-Bild des graphitischen C_3N_4, in dem man die Schichten in Stapelfolge entlang der 002-Richtung deutlich erkennen kann.

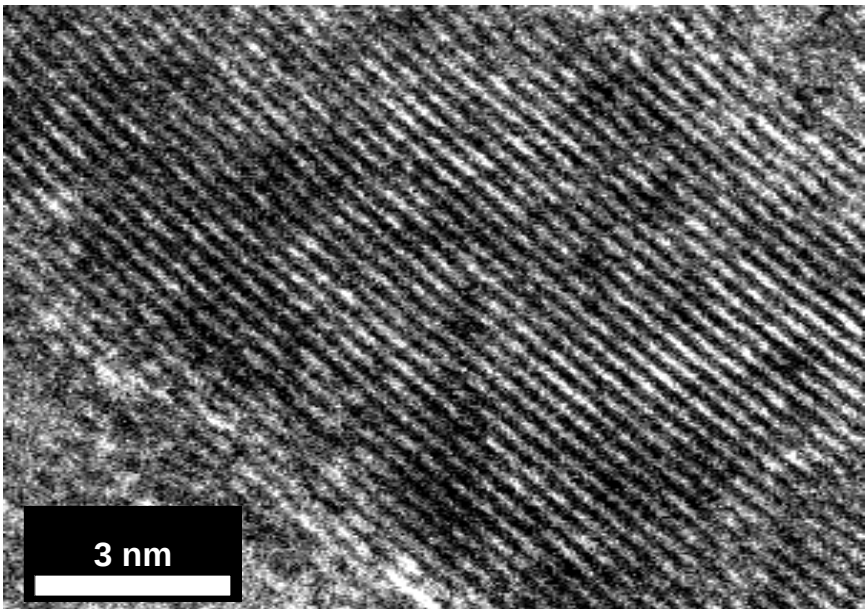

Abb.23: Hochauflösendes (HR) TEM-Bild des graphitischen C_3N_4-Materials. Die hohe kristalline Qualität des Materials und die Schichtabfolge in 002-Richtung mit einem Schichtabstand von 0.32 nm sind deutlich zu erkennen.

Wie bereits weiter oben erwähnt, kann diese Reaktion durch die Verwendung eines molekularen, niedrigschmelzenden Pecursors einfach auf mesoporöse Systeme übertragen werden. Diese Arbeiten sind in Artikel Nr.8 (*Synthesis of g-C_3N_4 –Nanoparticles in Mesoporous Silica Host Matrices*) der Publikationsliste zusammengefasst und werden hier kurz rekapituliert.

Eine thermoanalytische Untersuchung zeigte dieselben Reaktionsstufen in restriktiver Umgebung wie in der makroskalig geführten Referenzreaktion.

Insgesamt wurde die Reaktion in 3 mesoporösen Silikaten mit unterschiedlichen Porendurchmessern untersucht.

In Abb.24 sind die benutzten Silikate mit Porendurchmessern von 5 nm, 13 nm und 60 nm gezeigt.

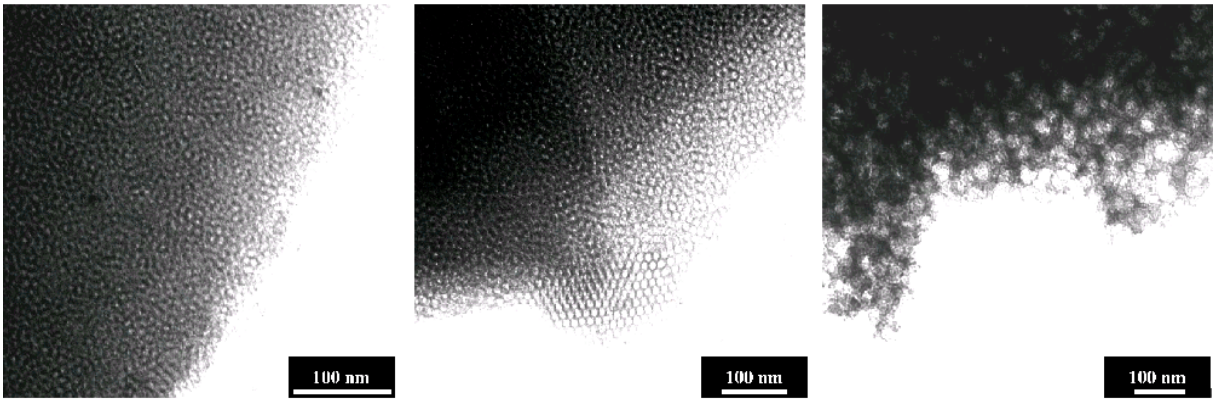

Abb.24: Mesoporöse Silikate, die für die Einführung der restriktiven Geometrie in der Synthese verwendet wurden. Porendurchmesser von links nach rechts: 5 nm, 13 nm, 60 nm

Die gelungene morphologische Transkription ist in Abb.25 zu sehen. Im Silikat sind deutlich sphärische Poren mit einem Durchmesser von ~60 nm zu erkennen, während in dem, von der Matrix befreiten, Carbonitridmaterial sphärische Objekte derselben Größenordnung zu sehen sind.

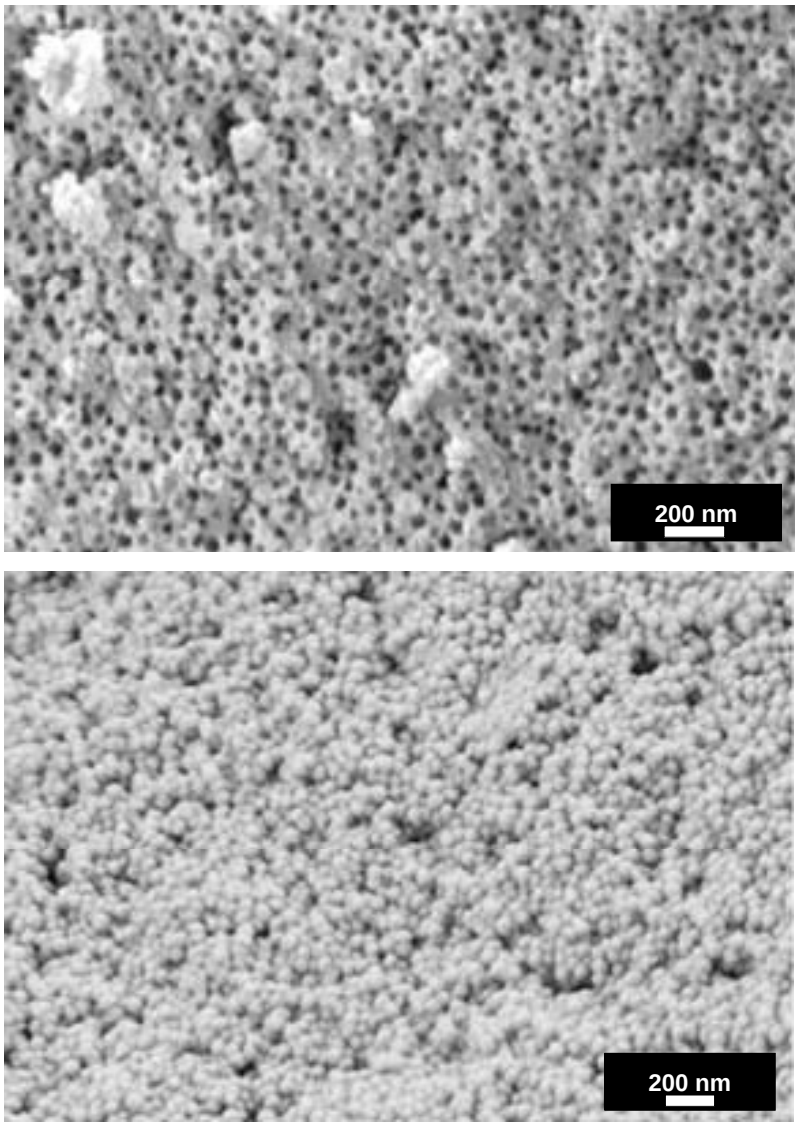

Abb.25: SEM-Aufnahme der Silikatmatrix mit 60 nm Poren (oben). Carbonitrid-Produkt nach Entfernung der Matrix (unten)

Vor allem soll an dieser Stelle betont werden, dass das Carbonitrid nur in den größeren, von den Mesoporen gestellten, Hohlräumen gebildet wird, nicht aber in den Mikroporen, welche die Mesoporen untereinander verbinden[53] und die Füllung des Materials mit dem Precursor erst möglich machen. Alle bisher in der Literatur bekannten Replikationsreaktionen, bei denen mesoporöse Silikate als Exotemplate verwandt wurden, bildeten das vollständige

Kanalsystem inklusive der Mikroporen ab[39,40,41]. Vermutlich wird die Bildung von g-C_3N_4-Stegen in den Mikroporen durch die Größe einer einzelnen Tri-s-Triazin-Einheit verhindert, deren Durchmesser etwas unter 1 nm liegt. Das Vorhandensein isolierter, sphäroider Partikel wird in der AFM-Aufnahme einer redispergierten Lösung in Abb.26 gezeigt, wobei auffällt, dass die Nano-Teilchen oblat, also leicht abgeplattet sind. Dies resultiert aus anisotropem Massenverlust, der ausgehend vom Edukt, welches die Poren vollständig ausfüllt, durch die Kondensation zum Produkt auftritt. Dieser Befund spricht eindeutig für ein „Tortenmodell" mit planaren Schichten und gegen sphärische, konzentrisch angeordnete Schichten im alternativen „Zwiebelmodell". Da kleine Schichten eine höhere Linienspannung besitzen als größere, werden aus energetischen Gründen die radial am weitesten außen liegenden, aus wenigen Tri-s-Triazin-Einheiten bestehenden, Schichten gar nicht erst gebildet, und der Massenverlust findet senkrecht zur Schichtebene statt.

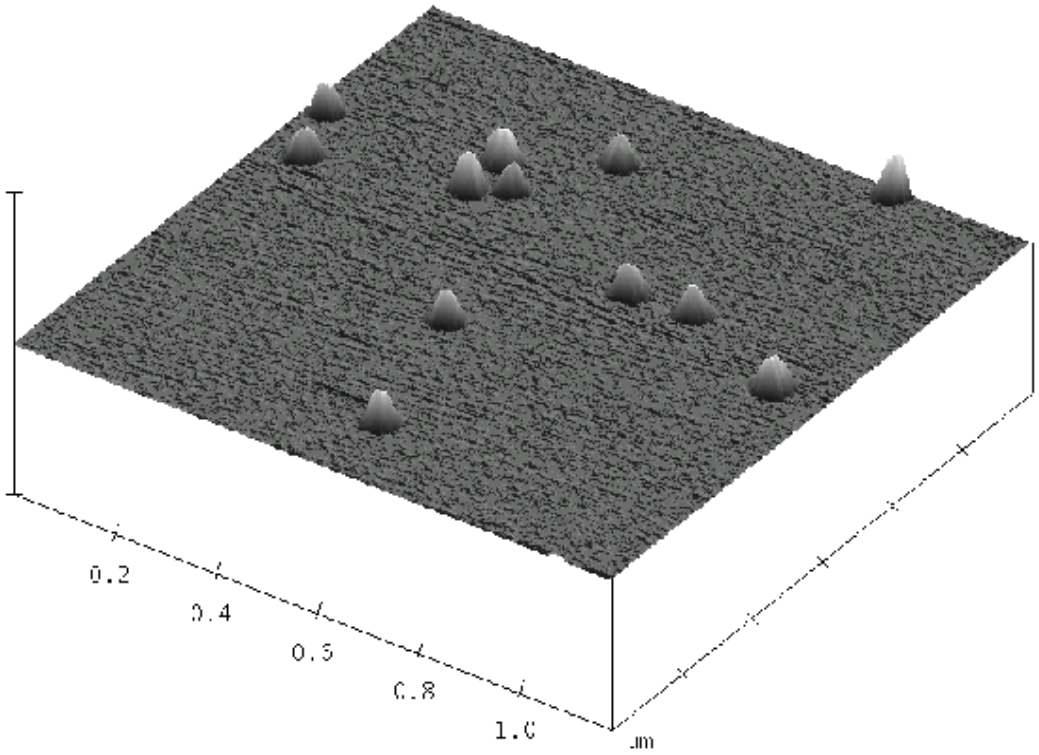

Abb.26: AFM-Aufnahme einer redispergierten Probe von synthetisierten g-C_3N_4-Partikeln. Abmessungen der Aufnahme: 1.18 µm x 1.18 µm x 80 nm. Die Partikel zeigen eine ellipsoide, abgeplattete Form mit einem Durchmesser von ca. 60 nm und einer Höhe zwischen 30 und 40 nm.

Trotz der Größenrestriktion wird bei allen untersuchten Nano-Partikeln die ondulierte g-C_3N_4 Struktur gefunden, wenngleich das Röntgendiffraktogramm (Abb.27) für die Ondulationsperioden starke Verbreiterungen infolge der Nano-Natur der Partikel zeigen. Die Schichtstruktur wird hierbei nicht durch die restriktive Geometrie beeinflusst, wie an dem unveränderten 002 Reflex deutlich wird.

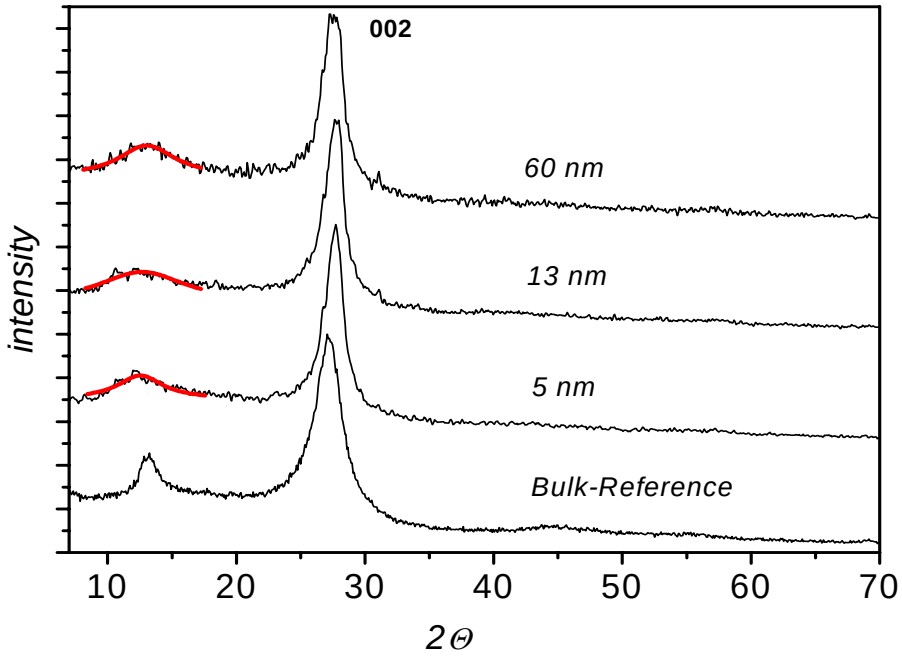

Abb.27: WAXS-Diffraktogramme der g-C_3N_4 Nano-Partikel. Von oben nach unten: 60 nm, 13 nm und 5 nm Partikel. Unten ist das makroskalige Referenzprodukt angegeben. Zur Verdeutlichung sind die stark verbreiterten Reflexe bei Streuwinkeln von etwa 13° durch Lorentzfunktionen gefittet.

In weiteren Experimenten konnte durch die in den Nano-Partikeln gegebene Zugänglichkeit der Tri-s-Triazin-Schichten gezeigt werden, dass im Gegensatz zum makroskopisch synthetisierten Produkt eine Interkalation der Schichten möglich ist, was abermals das Tortenmodell bestätigt. Durch Behandlung des Materials mit fluorierten organischen Säuren ließ sich der Schichtabstand in Abhängigkeit der Kettenlänge der verwendeten Säure aufweiten. Das interkalierte Material zeigte Reflexe bei kleineren Streuwinkeln, die größeren

Schichtabständen entsprechen. Bei der Verwendung einer perfluorierten Decansäure (C10-Kette) ist diese Aufweitung signifikant größer als bei Trifluoressigsäure (C2-Körper). Da die Reflexe wieder schärfer werden spricht dies gleichzeitig für eine Reorganisation des interkalierten Materials auf größeren Skalen. Somit ist dieses Experiment ein weiterer Beweis dafür, dass das Material auch in den Nano-Partikeln aus delaminierbaren, planaren Schichten besteht. In den einzelnen Schichten sind dann die 6-Stickstoffatome der runden Hohlräume innerhalb der einzelnen Schichten (Abb.28) zugänglich und können von den Säuren besetzt werden.

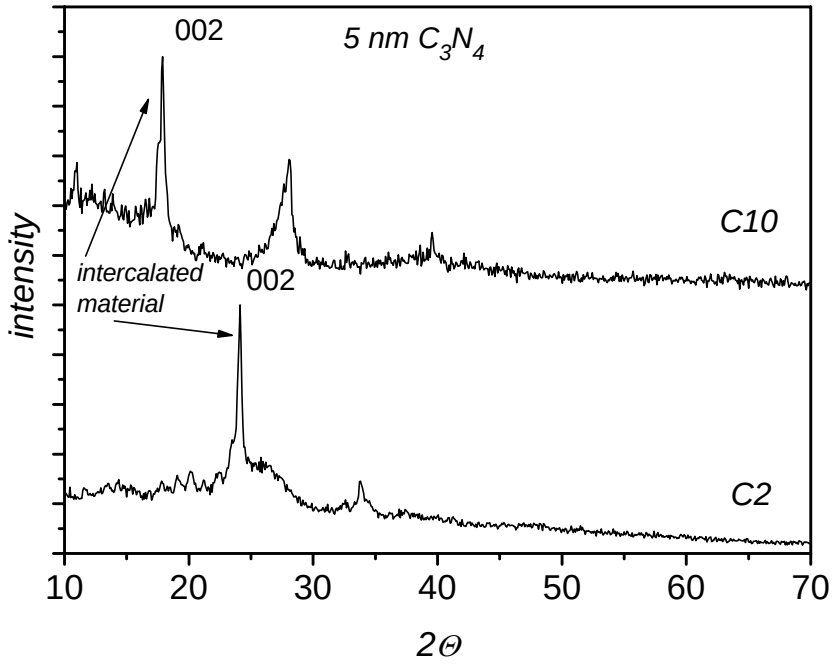

Abb.28: 5 nm Partikel g-C_3N_4, welche mit perfluorierter Dekansäure (oben) und Trifluoressigsäure (unten) behandelt wurden. Obwohl die Interkalation nicht vollständig ist (sichtbar an den immer noch breiten Reflexen an der ursprünglichen Position), zeigt das WAXS deutlich, dass eine Verschiebung des 002-Reflexes zu kleineren Streuwinkeln (größeren Schichtabständen), abhängig von der verwendeten Kettenlänge der Säure, stattgefunden hat.

Erfolgreich wurde in diesem Kapitel gezeigt, wie die Synthese von nanometergroßen Modellpartikeln einer Verbindung zur Charakterisierung beitragen kann. Vorausgesetzt, die Reaktion findet analog der Referenzreaktion statt, können wertvolle Informationen sowohl

über strukturellen Aufbau als auch über die chemischen Eigenschaften einzelner struktureller Bauelemente, hier die Basizität einzelner Schichten durch Hohlräume, die von Stickstoffatomen flankiert werden, erhalten werden.

4 Zusammenfassung

In dieser Arbeit wurden sowohl Beiträge zur Synthese neuer mesostrukturierter, poröser Systeme als auch zum Konzept des Nanoreaktors vorgestellt.

So wurde ein Templatsystem für die Synthese mesoporöser hierarchischer Systeme vorgestellt. Hierarchische Systeme zeigen Verteilungen von verschiedenen Porengrößen und sind von chromatographischem Interesse, da sie eine Abstimmung von Durchsatz und Trennleistung erlauben.

Das Templat besteht aus zwei unmischbaren Blockcopolymeren, die Aggregate unterschiedlicher Größe in lyotropen Phasen ausbilden. Durch die Transkription der lyotropen Strukturen in eine anorganische Matrix wird eine bimodale Verteilung im mesoporösen Produkt erreicht. Verschiedene relative Anteile an Templat wurden untersucht und die korrespondierenden lyotropen Phasen mit Hilfe des Silikat-Nanocastings untersucht.

Des Weiteren wurde ein neues Templat, bestehend aus einem Blockcopolymer mit ultrahydrophobem Kern, welches sich durch die Bildung äußerst robuster lyotroper Phasen auszeichnet, vorgestellt. Gerade bei der Synthese dünner Metalloxidfilme spielt diese Eigenschaft eine große Rolle.

Das Phasenverhalten des Templats wurde mit Hilfe des Nanocastings bei verschiedenen Konzentrationen untersucht. In einem definierten Konzentrationsbereich wurden dabei äußerst hochgeordnete flüssigkristalline Monodomänen gefunden, welche die Eignung dieses Polymers bei der Darstellung hochgeordneter mesoporöser Systeme demonstrieren. Anschließend wurde gezeigt, dass das Templat auch in der Synthese von mesostrukturierten dünnen Übergangsmetalloxidfilmen erfolgreich eingesetzt werden kann. Hierzu wurden hoch geordnete, kristalline Titandioxidfilme synthetisiert.

Schließlich ist demonstriert worden, dass mit Hilfe des Nanocastings auch eine quantitative Beschreibung von lyotropen Phasen möglich ist. Hierzu wurden exemplarisch zwei Modellphasen, eine dichte Packung von Mizellen und eine zylindrische Phase, verglichen.

Von beiden Phasen wurden silikatische Abdrücke mittels Nanocasting hergestellt, die quantitativ mit Röntgenmethoden beschrieben wurden. Die erhaltenen Daten lassen Rückschlüsse auf die flüssigkristalline Phasenmorphologie und die Porengröße und -Gestalt zu.

Der zweite Teil der Arbeit befasste sich mit der Nutzung mesoporöser Silikate als Nano-Reaktoren. Durch die Verwendung mesostrukturierter Silikate als Matrix ist die Synthese von Partikeln einer durch die Matrix vorgegebenen Morphologie möglich.

So wird die Darstellung von morphologisch verschiedenen, funktionellen Polymer-Nanopartikel vorgestellt, die auf anderem Wege nicht zu erhalten sind. Anhand dieses Modellsystems wurde gezeigt, dass das verwendete polymere Material trotz seiner geometrischen Dimensionen keinerlei Leistungseinbußen zeigt.

Anschließend wurde das Konzept des Nano-Reaktors auf die Synthese von keramischen Werkstoffen übertragen. Hierzu wurde zunächst eine makroskopische Synthese für neue schichtartige Carbonitridmaterialien entwickelt, die als Referenz benutzt wurde. Diese Schichtverbindungen sind sowohl von akademischem als auch von technologischem Interesse. So wird die Verwendung von graphitischem Carbonitrid, g-C_3N_4, als Speichermedium für Gase und als katalytisches System diskutiert. Ausgehend von niedermolekularen Verbindungen gelang die Darstellung eines neuen Allotrops dieser Stoffklasse, welches sich durch poröse ondulierte Schichten, die analog zu Graphit gepackt sind, auszeichnet. Auf die Ondulation und Kristallinität des Materials konnte hierbei postsynthetisch Einfluss genommen werden.

Durch die Verwendung niedermolekularer Edukte war die Anwendung dieser Reaktion in mesoporösen Silikaten möglich.

Eine Analyse der Reaktion zeigte, dass diese auch innerhalb eines strukturierten Silikats analog der Referenzreaktion abläuft. Das Produkt dieser Reaktion waren sphäroide, graphitische Carbonitrid-Nanopartikel mit verschiedenen Durchmessern. Die Partikel selbst waren dabei aus planen Schichten aufgebaut waren und nicht, wie alternativ denkbar, aus konzentrischen Sphären. Weiterhin konnte anhand dieses Modellsystems der chemische Charakter einzelner, graphitischer Schichten beschrieben werden.

So erlaubte die nanoskalige Abmessung Interkalation der einzelnen Schichten, deren poröse Natur demonstriert wurde. Abhängig von der Größe der interkalierenden Verbindungen konnte der Schichtabstand eingestellt werden.

Hierdurch wurde besonders deutlich demonstriert, dass die Skalierung von Verbindungen auf Nanometer-Größe von analytischer Bedeutung sein kann.

5 Publikationsliste

In dieser Arbeit sind die Ergebnisse folgender Veröffentlichungen enthalten:

[1] Mixed Micellar Phases of Nonmiscible Surfactants: Mesoporous Silica with Bimodal Pore Size Distribution via the Nanocasting Process
Groenewolt, M.; Antonietti, M.; Polarz, S.;
Langmuir; 2004, 20(18), 7811-7819.

[2] Polyisobutylene-*block*-poly(ethylene oxide) for robust Templating of Highly-Ordered Mesoporous Materials
Groenewolt, M.; Brezesinski, T.; Schlaad, H.; Antonietti, M.;
Advanced Materials, angenommen

[3] The Generation of Mesostructured Crystalline CeO_2, ZrO_2 and CeO_2-ZrO_2 Films using EISA
Brezesinski, T.; Antonietti, M.; Groenewolt, M.; Pinna, N; Smarsly, B.
New Journal of Chemistry, angenommen

[4] The Generation of Mesostructured CeO_2 with Crystalline Pore Walls Using Novel Block Copolymer Templates
Brezesinski, T.; Smarsly, B.; Groenewolt, M.; Antonietti, M.; Grosso, D.; Boissiere, C., Sanchez, C.;
Studies in Surface Science and Catalysis, angenommen

[5] SAXS Analysis of Mesoporous Model Materials: A Validation of Data Evaluation Techniques to Characterize Pore-Size, Shape, Surface Area, and Curvature of the Interface
Smarsly, B.; Groenewolt, M.; Antonietti, M.;
Eingereicht bei: *Progress in Colloid and Polymer Science,* angenommen

[6] Nanoparticles and Nanosheets of Aromatic Polyimides via Polycondensation in Controlled Pore Geometries
Groenewolt, M.; Thomas, A.; Antonietti, M.;
Macromolecules; 2004, 37(12), 4360-4364.

[7] Synthesis of g-C_3N_4 based on Cyameluric (C_6N_7) Building Units
Groenewolt, M.; Antonietti, M; Schlögel, R.;
Eingereicht bei: *Journal of the American Chemical Society*

[8] Synthesis of g-C_3N_4 –Nanoparticles in Mesoporous Silica Host Matrices
Groenewolt, M.; Antonietti, M;
Advanced Materials, angenommen

Thematisch außerhalb dieser Arbeit ist folgende Publikation entstanden:

[9] Zirconium and hafnium oxoclusters as molecular building blocks for highly dispersed ZrO_2 or HfO_2 particles in silica matrix
Armelao, L.; Di Noto, V.; Eisenmenger-Sittner, C; Groenewolt, M; Gross, S.; Sada, C.; Schubert, U.; Tondello, E.; Zattin, A.;
Chemistry of Materials, angenommen

6 Referenzen

[1] Corma A *Chem. Rev.* **1997, *97***, 2373.

[2] Antonietti M, Ozin GA *Chem. Eur. J* **2004**, *10*, 29.

[3] Stucky GD, MacDougall JE *Science* **1990**, *247*, 669.

[4] Attard GS, Glyde JC, Göltner CG *Nature* **1995**, *378*, 366.

[5] Göltner CG, Antonietti M, **1997**, *Adv. Mater.* **1997**, *9*, 431.

[6] Göltner CG, Henke S, Weissenberger MC, Antonietti M *Angew.Chem.* **1998**, *110*, 633.

[7] Porlarz S, Antonietti M, *Chem. Commun.* **2002**, 2593.

[8] Kresge CT, Leonowicz ME, Roth WJ, Vartuli JC, Beck JS *Nature* **1992**, *359*, 710.

[9] Zhao DY, Sun JY, Li QZ, Stucky GD *Chem. Mater* **2000**, *12*, 275.

[10] Antonietti M, Berton B, Göltner CG, Hentze HP *Adv. Mater.* **1998**, *10*, 154.

[11] Zhou Y, Antonietti M, *Chem. Commun.* **2003,** 2564.

[12] Weberskirch, R.; Nuyken, O. *J. Macromol. Sci., Pure Appl. Chem.***1999**, *A36*, 843.

[13] Stähler K, Selb J, Candau F *Langmuir* **1999**, *15*, 7565.

[14] Barthelemy P, Tomao V, Selb J, Chaudier Y, Pucci B.*Langmuir* **2002**, *18*, 2557-2563.

[15] Grosso D, Soler-Illia GJDA, Crepaldi EL, Cagnol F, Sinturel C, Bourgeois A, Brunet-Bruneau A, Amenitsch H, Albouy PA, Sanchez C *Chem. Mater.* **2003**, *15*, 4562.

[16] Crepaldi EL, Soler-Illia GJDA, Grosso D, Cagnol F, Ribot F, Sanchez C *J. Am. Chem. Soc.* **2003**, *125*, 9770.

[17] Crepaldi EL, Soler-Illia GJDA, Grosso D, Sanchez C. *New J. Chem.* **2003**, *27*, 9.

[18] Bagshaw SA, Prouzet E, Pinnavaia TJ *Science* **1995**, *269*, 1242.

[19] Tanev PT, Pinnavaia TJ *Science* **1995**, *267*, 865.

[20] Prouzet E, Pinnavaia TJ *Angew. Chem.* **1997**, *109*, 533.

[21] Kennedy, J. P.; Iván, B. *Designed Polymers by Carbocationic Macromolecular Engineering: Theory and Practice*, Hanser Publishers, 1992.

[22] Smarsly B, Grosso D, Brezesinski T, Pinna N, Boissière C, Antonietti M, Sanchez C. *Chem. Mater.* **2004**, *16*, 2948

[23] Grosso D, Boissière C, Smarsly B, Brezesinski T, Pinna N, Albouy PA, Amenitsch H, Antonietti M, Sanchez C *Nature Materials* **2004**, in press

[24] Thomas A, Schlaad H, Smarsly B, Antonietti M *Langmuir* **2003,** *19*, 4455.

[25] Zhou Y, Antonietti M *Chem. Mater.* **2004**, *16*, 544.

[26] Burger C, Ruland W *Acta Crystallographica Section A* **2001,** *57*, 482.

[27] Smarsly B, Wolff T, Antonietti M *J. Chem. Phys.* **2002,** *116*, 2627.

[28] Micha MA, Burger C, Antonietti M *Macromolecules* **1998,** *31*, 5930.

[29] Smarsly B, Göltner C, Antonietti M, Ruland W, Hoinkis E *J. Phys. Chem* **2001**,*105*, 831.

[30] Méring J, Tchoubar C J. Appl. Crystallogr. **1968,** *1*, 153.

[31] Tchoubar-Vallat D, Méring J *C. R. Hebd. Seances Acad. Sci.***1965,** *26*, 3096.

[32] Méring J, Tchoubar-Vallat D *C. R. Acad. Sci. Paris* **1966,** *262*, 1703.

[33] Göltner CG, Weissenberger MC *Acta Polym.* **1998,** *49*, 704.

[34] Seebacher C, Hellriegel C, Bräuchle C, Ganschow M, Wöhrle D *J. Phys. Chem. B* **2003**, *107*, 5445.

[35] Johnson SA, Brigham ES, Ollivier PJ, Mallouk TE *Chem. Mater.* **1997**, *9*, 2448

[36] Schüth F, *Angew. Chem.***2003**, *115*, 3730.

[37] Huang MH, Choudrey A, Yang P *Chem. Commun.* **2000**, 1063.

[38] Wu CG, Bein T *Science* **1994**, *264,* 1757.

[39] Ryoo R, Joo SH, Kruk M, Jaroniec M. *Adv. Mater.* **2001**, *13*, 677.

[40] Ryoo R, Joo SH, Jun S *J. Phys. Chem. B* **1999**, *103*, 7743.

[41] Lu AH, Schmidt W, Matoussevitch N, Bonnemann H., Spliethoff B, Tesche B, Bill E, Kiefer W, Schuth F *Angew. Chem. Int. Ed.* **2004**, *43*, 4303.

[42] Sroog CE *Prog. Polym. Sci.* **1991**, *16*, 561.

[43] Thomas A, Antonietti M *Adv. Funct. Mater.* **2003**, *13*, 763.

[44] Cohen ML,*Phys.Rev*. **1985**, *B32*, 7988.

[45] Liu AL, Cohen ML, *Science* **1989**, *245*, 841.

[46] Jang J, Oh JH *Adv. Mater.* **2004**, *16*, 1650.

[47] Kouvetakis J, Bandari A, Todd M, Wilkens B, Cave N *Chem.Mater*. **1994**, *6*, 811

[48] Montigaud H, Tanguy B, Demazeau G, Alves I, Courjault S, *J .Mat. Sci*. **2000**, *35*, 1547.

[49] Gu Y, Chen L, Shi L, Ma J, Yang Z, Qian Y, *Carbon* **2003**, *41*, 2674.

[50] Guo Q, Xie Y, Wang X, Zhang S, Hou T, Lv S, *Chem.Comm*. **2004**, 26.

[51] Pauling L, Sturdivant JH, *Proc.Nat.Acad.Sci.ISA* **1937**, *23*, 615

[52] Jürgens B, Irran E, Senker J, Kroll P, Müller H, Schnick W, *J.Am.Chem.Soc*. **2003**, *125*, 10288.

[53] Smarsly B, Göltner C, Antonietti M, Ruland W, Hoinkis E, *J. Phys. Chem. B.* **2001**, *105*, 831.

Danksagung

An dieser Stelle möchte ich mich bei allen bedanken, die wesentlich zum Gelingen der Arbeit beigetragen haben:

Prof. Dr. Markus Antonietti für die geschaffene Möglichkeit meine Promotion an diesem fruchtbaren Institut durchführen zu dürfen und die vielen konstruktiven und spannenden Diskussionen in allen Bereichen der Nanochemie. Auch die sehr gute soziale Atmosphäre innerhalb dieses Instituts hat das Promovendendasein stets sehr bereichert.

Dr. Bernd Smarsly für die Hilfe in komplexen Fragen der Streutheorie und die gute Kooperation.

Torsten Brezesinski, für die gute Zusammenarbeit und gedankliche Zerstreuung auch außerhalb der Chemie.

Dr. Arne Thomas, ebenfalls für gute Zusammenarbeit und die Einführung in Labor und Institut.

Rebecca Voß und Hartmut Rettig für ein immer angenehmes Arbeitsklima im Büro.

Selbstverständlich danke ich auch allen Anderen im Institut, die mir geholfen haben und für mich da waren.

Meinen Eltern, die mich immer unterstützt haben.

Nachfolgend sind die in der Publikationsliste aufgeführten Publikationen bzw. Manuskripte enthalten:

Mixed Micellar Phases of Nonmiscible Surfactants: Mesoporous Silica with Bimodal Pore Size Distribution via the Nanocasting Process

Matthijs Groenewolt and Markus Antonietti*

Max Planck Institute of Colloids and Interfaces, Research Campus Golm, D-14424 Potsdam, Germany

Sebastian Polarz

Ruhr Universität Bochum, Chemistry Department, D-44780 Bochum, Germany

Received April 2, 2004. In Final Form: June 2, 2004

Highly organized mesoporous silica monoliths were reproducibly prepared by nanocasting mixtures of fluorinated nonionic surfactants and micelles of two hydrocarbon block copolymers. It is the special feature of this fluorocarbon/hydrocarbon template mixture that they form not mixed micelles but individual micelles instead. By careful analysis of the pore architectures by gas sorption measurements and transmission electron microscopy in dependence on the relative template concentration, two different situations could be identified: (a) mesoscopically demixed samples and (b) mixed micellar phases where the two different micelles are packed in some type of organized alloy phase. Besides identification of such mixed phases for the first time for fluorocarbon/hydrocarbon mixtures, the resulting porous systems with controlled bimodal pore size distribution might be interesting from a materials perspective.

Introduction

The synthesis of porous matter, omnipresent in nature for structural and functional reasons, has recently experienced enhanced interest in materials chemistry, for a number of reasons. This started from the observation that micelles and lyotropic phases can be used as templates to generate mesoporous silica with a variety of textures (the so-called MCM materials, see refs 1 and 2). Meanwhile, the range of organic supramolecular templates has been significantly extended (polymers, block copolymers, polysaccharides, cyclodextrines, and polymer latexes; for a review, see ref 3), and practically any pore size and pore architecture can be rationally accessed. The precision of the replication, especially in the so-called nanocasting process, is sometimes so high that one can even learn from the pore structure about the assembly structure of the template in it, as for instance delineated for the packing of spherical micelles[4] or the mutual arrangement of cyclodextrine moieties.[5]

A problem we regard as still interesting is the construction of materials with hierarchical or multimodal pore architectures. Here the big pore system accomplishes optimized transport, whereas the small pores provide the surface area and the size selectivity, without the possibility that the channel system can be efficiently blocked. The natural attempt to achieve bimodal pore size distributions in mesoporous silica is to use templates of different size which do not interfere with each other. This is rather simple when using rigid latex templates[6,7] but is demanding for soft self-organizing systems as such systems usually form mixed aggregates. In addition, latex templates are restricted toward smaller pore sizes to about 30−50 nm in size.

In this study, hydrocarbon block copolymer templates which are known to generate 9 and 13 nm large spherical pores, respectively, are mixed with a fluorinated hydrocarbon for simultaneous nanocasting. The fluorocarbon/hydrocarbon situation is known to form separated micelles even in complex mixtures,[8−10] as long as both surfactants have sufficient size. Since fluorinated porogens promise specific advantages (such as new, fluorocarbon-specific phase morphologies[11] or the potential for templating organically modified silica precursors), their usefulness was first investigated in the pure state.

By characterization of the samples with small-angle X-ray scattering (SAXS), nitrogen sorption, and transmission electron microscopy (TEM) analysis, we expect to reveal a quite detailed picture of structure formation and template compatibility.

Experimental Section

The fluorinated surfactants Fluowet OTN and Fluowet OTL (for structures, see Figure 1) were kind gifts from Clariant. The SE3030 polymer was obtained from Goldschmidt, and the KLE3935 polymer was synthesized by a procedure described elsewhere.[4] Tetramethoxysilane (TMOS) was purchased from Aldrich. All commercial chemicals have been used without further purification.

(1) Beck, J. S.; Vartuli, J. C.; Roth, W. J.; Leonowicz, M. E.; Kresge, C. T.; Schmitt, K. D.; Chu, C. T. W.; Olson, D. H.; Sheppard, E. W.; McCullen, S. B.; Higgins, J. B.; Schlenker, J. L. *J. Am. Chem. Soc.* **1992**, *114*, 10834−10843.

(2) Kresge, C. T.; Leonowicz, M. E.; Roth, W. J.; Vartuli, J. C.; Beck, J. S. *Nature* **1992**, *359*, 710−712.

(3) Polarz, S.; Antonietti, M. *Chem. Commun.* **2002**, 2593−2604.

(4) Thomas, A.; Schlaad, H.; Smarsly, B.; Antonietti, M. *Langmuir* **2003**, *19*, 4455−4459.

(5) Polarz, S.; Smarsly, B.; Bronstein, L. M.; Antonietti, M. *Angew. Chem., Int. Ed.* **2001**, *40*, 4417−4421.

(6) Antonietti, M.; Berton, B.; Göltner, C. G.; Hentze, H.-P. *Adv. Mater.* **1998**, *10*, 154−159.

(7) Zhou, Y.; Antonietti, M. *Chem. Commun.* **2003**, 2564−2565.

(8) Weberskirch, R.; Nuyken, O. *J. Macromol. Sci., Pure Appl. Chem.* **1999**, *A36*, 843−857.

(9) Stähler, K.; Selb, J.; Candau, F. *Langmuir* **1999**, *15*, 7565−7576.

(10) Barthelemy, P.; Tomao, V.; Selb, J.; Chaudier, Y.; Pucci, B. *Langmuir* **2002**, *18*, 2557−2563.

(11) Burger, C.; Micha, M.-A.; Oestreich, S.; Förster, S.; Antonietti, M. *Europhys. Lett.* **1998**, *42*, 425−429.

10.1021/la049147k CCC: $27.50
Published on Web 08/05/2004

$CF_3[CF_2]_{6\text{-}16}C_2H_4\text{-}EO_{4\text{-}5}$ $CF_3[CF_2]_{6\text{-}16}C_2H_4\text{-}EO_{7\text{-}8}$

Fluowet OTN ™ **Fluowet OTL ™**

Figure 1. Formulas of the used fluorinated surfactant templates.

Preparation of the Porous Silica Materials Based on Pure Fluorinated Surfactant. In a typical synthesis, 0.30 g of fluorinated surfactant was dissolved in 1.0 g of TMOS. 0.5 g of a 0.01 M aqueous HCl solution was added, and the mixture was slightly heated and treated with ultrasound for 5 min. The homogenized mixture was exposed to a gentle vacuum to remove the methanol formed due to the hydrolysis of the TMOS. The homogeneous and highly viscous solution is poured into a Petri dish, and formation and conservation of the lyotropic phase are controlled during the condensation via a polarization microscope. After 24 h, the resulting hybrid material is calcined by heating the samples up to 550 °C with a temperature ramp of 5 K/min, followed by isothermal treatment at 550 °C for 4 h. The combustion gases were washed with concentrated $Ca(OH)_2$ solution in order to remove HF.

Preparation of the Porous Silica Materials Based on the Binary OTN−SE3030 Polymer System. SE3030 (0.12 g) was dissolved in 1.0 g of TMOS. After homogenization of the mixture, 0.5 g of a 0.01 M aqueous HCl solution was added, and the mixture was homogenized again using slightly elevated temperature and ultrasound.

The mixture was divided into appropriate portions (e.g., 0.30 g; contains 7.3% or 0.022 g of SE3030), and the required amount of fluorinated polymer (OTN) was added for the desired OTN/(SE3030 + OTN) ratio (e.g., 0.027 g to achieve a OTN/(SE3030 + OTN) ratio of 35%; sample SE-4). Again complete homogenization was achieved using slightly elevated temperature and ultrasound. The reaction mixtures were freed from methanol by a gentle vacuum and allowed to complete gelation overnight in a 1 mL open tube.

The resulting monolithic gels were calcined by the same procedure described above.

Preparation of the Porous Silica Materials Based on the Binary OTN−KLE3935 Polymer System. For the KLE3935 mixture, 0.33 g of KLE3935 was mixed with 3.3 g of a 1/1 mixture of TMOS/ethanol. After addition of 0.8 g of a 0.01 M aqueous HCl solution, the mixture was homogenized. A second mixture was prepared by dissolving 0.30 g of OTN in 1.0 g of TMOS. After adding 0.8 g of a 0.01 M aqueous HCl solution, the mixture was also homogenized.

These two solutions were mixed and homogenized to get the different OTN/KLE3935 ratios (e.g., 200 mg of KLE3935 solution (contains 7.5% or 0.015 g of polymer) and 20 mg of OTN solution (contains 14.3% or 0.003 g of polymer) give a polymer ratio of OTN/(KLE3935 + OTN) = 17%; sample KLE-1). Evaporation and calcination are carried out in the same manner as for the SE3030/OTN system.

Characterization of Mesoporous Materials. TEM images were taken using a Zeiss EM 912Ω at an acceleration voltage of 120 kV. Samples were ground in a ball mill and dispersed in acetone. One droplet of the suspension was applied to a 400 mesh carbon-coated copper grid and left to dry in air.

SAXS patterns were recorded employing a Kratky camera.

Nitrogen sorption data were obtained with a Micromeritics Tristar 3000.

Results

First, we analyzed the products of the nanocasting procedure for the pure fluorocarbon surfactant phases. For that, we employed two commercial, nonionic surfactants which differ only in the length of the hydrophilic oligo(ethylene oxide) moiety (see Figure 1).

The surfactants, in short OTN and OTL, were chosen due to their commercial availability and the fact that they show pronounced lyotropic phases with strong birefringence even in the precondensed reaction mixture, as illustrated by the two polarized optical microscopy (POM) pictures shown in Figure 2.

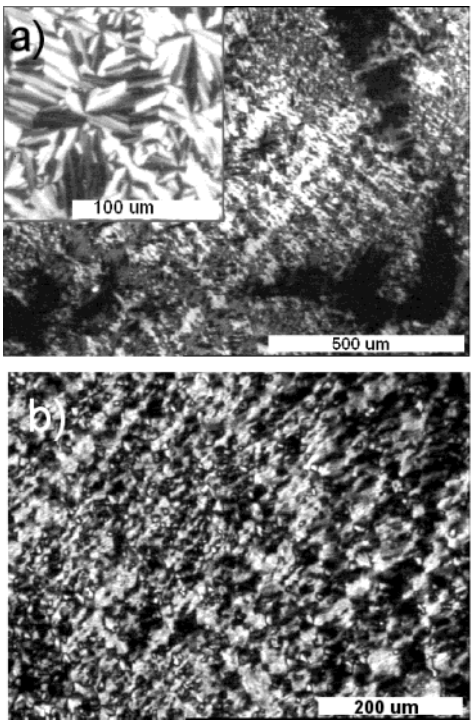

Figure 2. (a) POM image of the mesophase of sample OTN-3 prior to condensation and after evaporation of the alcohol, containing silicic acid. A hexagonal texture with extended domains can be identified, better seen in the inset. (b) POM image of sample OTL-2, under similar conditions. The domains are not as marked as for OTN, but the texture shows hexagonal features, too.

The high stability and pronounced formation of long range ordered phases even in the presence of the hydrolyzed silica precursor make both fluorinated surfactants good candidates as porogens. During the writing of this article, we found out that Blin et al. have proven this point by reporting the preparation of mesoporous hexagonal silica[12] using a nonionic fluorinated surfactant similar to our templates but employed a hydrothermal, SBA-like synthesis. In the Blin case, the surfactant/silica molar ratio was kept constant at 0.5, which corresponds to a template content of 88 wt % of the final condensed material. As our aim is the synthesis of a precise, monolithic replica of the lyotropic phase via the nanocasting route, we decided, without knowledge of the other work, to use much lower ratios of surfactant/silica.

The prepared samples were allowed to gel completely and were calcined afterward, while the amount of template was varied in a systematic fashion. The compositions under examination are summarized in Table 1.

In nanocasting, it is possible to replicate even dilute micellar phases, but materials templated in this way are usually hard to calcine, as the organic material can hardly leave the silica matrix and is partly transferred into carbon or black condensates. This is why a white, carbon-free monolith is usually a signature for the percolation of the template structures and formation of a continuous channel system.

Referring to Table 1 and judging by the color, percolation of the ethylene oxide (EO) brushes of the micelles within the silica starts at about 40 wt % polymer content, as

(12) Blin, J. L.; Lesieur, P.; Stebe, M. J. *Langmuir* **2004**, *20*, 491−498.

Table 1. Mesoporous Materials Synthesized with Different Ratios of Fluorinated Surfactants Relative to the Final Amount of SiO

sample code	OTN/g	OTL (40 wt %)/g	mL HCL, pH = 2	TMOS/g	SiO_2/g	wt % template in completely condensed material	POM texture	carbon-free after calcination?
OTN-1	0.25		1.3	2.56	1	20	no	no
OTN-2	0.50		1.3	2.56	1	33	weak	no
OTN-3	0.77		1.3	2.56	1	44	strong	yes
OTN-4	1.00		1.3	2.56	1	50	no	yes
OTL-1		1.23 (0.51)	0.7	2.56	1	34	weak	no
OTL-2		2.50 (1.00)	0.3	2.56	1	50	strong	yes
OTL-3		3.90 (1.56)	0.3	2.56	1	61	strong	yes

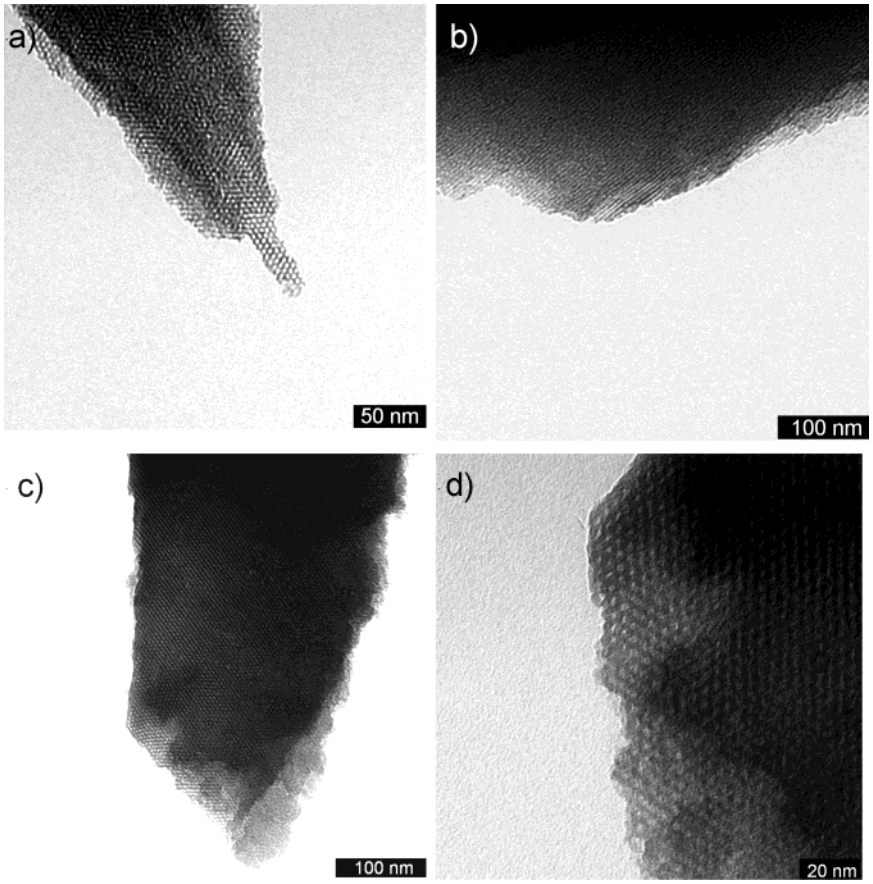

Figure 3. TEM pictures of OTN-3 (a,b) and OTL-2 (c,d). Both samples show nicely ordered hexagonal mesophases (a,c,d), as indicated by the silica replicas.

calculated for the completely condensed material (SiO_2). Both polymers do form a birefringent lyotropic phase in the present reaction system around a concentration of about 30−50 wt % related to silica.

The TEM pictures of the samples with strong polarization textures also show, for both surfactants, clearly well ordered domains with a hexagonal arrangement of the single pores, as depicted in Figure 3.

From the TEM pictures, the pore width is estimated to be around 2.6 (±0.3) nm for OTL and 2.8 (±0.5) nm for the OTN-based material.

The Brunauer−Emmett−Teller (BET) measurements of the synthesized materials (Figure 4) exhibit a typical adsorption isotherm for mesoporous materials, with relatively small micropore content. Capillary condensation takes place at reduced pressures of $P/P_0 < 0.4$, which is pointing to pores with an average pore width of about 3 nm. The difference of the position of the steepest slope, that is, where capillary condensation occurs, is slightly shifted toward higher relative pressures in the OTL-based material, which refers to bigger pores in this material. This is verified by density functional theory (DFT) calculations; that is, the pores in the OTN material are determined to be 2.7 nm, whereas the OTL material possesses 3.1 nm big pores. This is in good agreement with the TEM observations.

The fact that OTN- and OTL-based silicas have a slightly different pore size, although their hydrophobic part, for example, the fluorinated tail, is the same, was similarily found for nonionic hydrocarbon surfactants and was explained by the so-called three-phase model;[13] that is, parts of the hydrophilic tail also contribute to the mesopore volume.

All these results underline that the pure fluorinated surfactants are in general also nicely suited as porogens for silica; the two sets of data on the pure fluorosurfactants are however also relevant as a reference to judge the binary systems under discussion below.

(13) Smarsly, B.; Polarz, S.; Antonietti, M. *J. Phys. Chem. B* **2001**, *105*, 10473−10483.

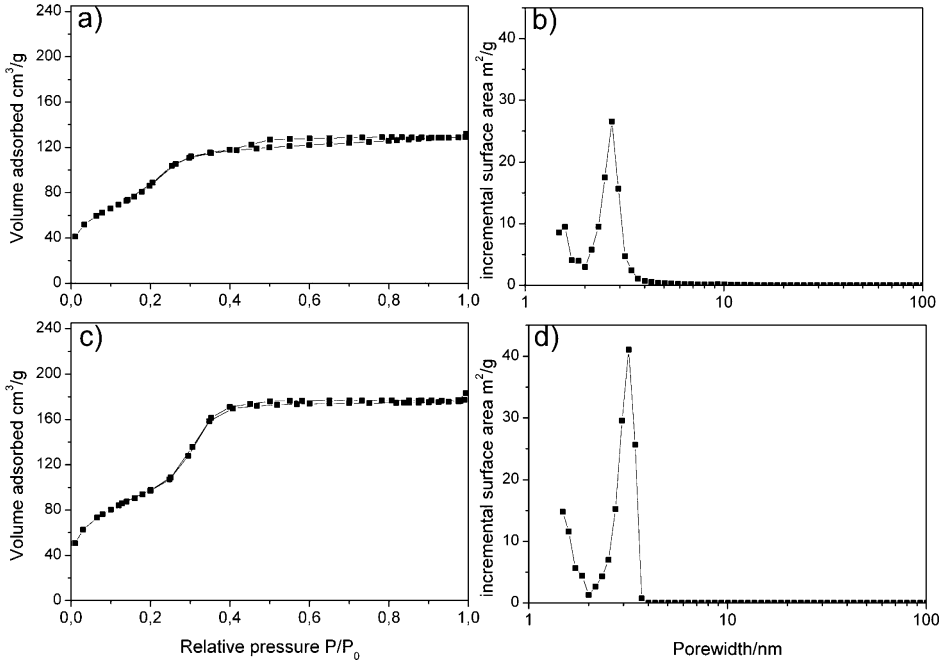

Figure 4. BET isotherm (a) and corresponding DFT calculation (b) for OTN-3. The DFT calculation shows a narrow pore size distribution with an average value of 2.7 nm. BET isotherm (c) and corresponding DFT calculation (d) for OTL-2. The DFT calculation shows a narrow pore size distribution with an average value of 3.1 nm.

Table 2. SE-Based Mixed Mesoporous Materials Synthesized with Different Ratios of OTN to SE3030, Increasing the Amount of Fluorocarbon Pores in Addition to the Hydrocarbon Pores

sample code	SE3030/g	OTN/g	% template giving small pores	HCl, pH = 2/g	TMOS/g	SiO_2/g	wt % template in completely condensed material
SE-1	0.30	0.03	9	1.25	2.56	1	25
SE-2	0.30	0.08	21	1.25	2.56	1	28
SE-3	0.30	0.18	37	1.25	2.56	1	32
SE-4	0.30	0.37	55	1.25	2.56	1	40
SE-5	0.30	0.69	70	1.25	2.56	1	50
SE-6	0.30	1.52	84	1.25	2.56	1	65

Binary Template Systems of Fluorinated Surfactants and Amphiphilic Hydrocarbon Block Copolymers

To simplify analysis and to ensure the absence of miscibility between fluorinated and hydrocarbon species, we decided to use two block copolymer templates with sufficient molecular weight whose phase behavior was already examined in previous publications.[4,14] SE3030 is a polystyrene-*b*-ethylene oxide block copolymer with a molecular weight of 3000 g/mol for each block, whereas KLE3935 is a hydrogenated polybutadiene-*b*-ethylene oxide block copolymer with molecular weights of 3935 g/mol (the KratonLiquid based hydrogenated polybutadiene) and 3460 g/mol (poly(ethylene oxide)).

Nanocasting of the SE3030/OTN System. Six different compositions of SE3030/OTN were used as templates in the standard procedure in order to get a bimodal pore size distribution. OTN was used, as OTL micelles and phases turned out to be too incompatible to reveal homogeneous systems. The compositions are summarized in Table 2. All samples turned out to be carbon-free after calcination, that is, exhibited an open pore structure.

The materials rich in block copolymer, SE-1 to SE-3, show the typical texture of the pure block copolymer (Figure 5). The samples look homogeneous, although macroscopically demixing into pure SE3030 and OTN micelles already starts for sample SE-3 at some spots of the sample.

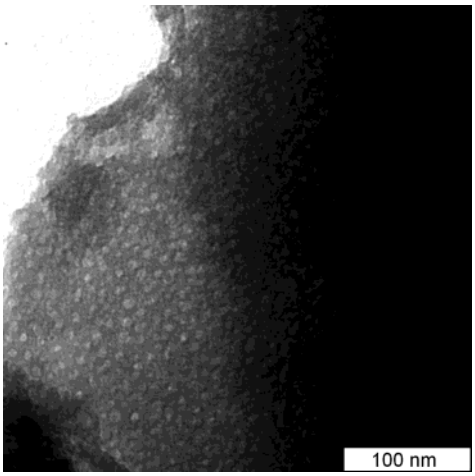

Figure 5. TEM picture of calcined SE-2. The typical SE structure is reproduced. The OTN pores are weakly detectable since their relative importance is low.

Figure 6 shows the adsorption/desorption isotherms of the synthesized materials SE-1 to SE-3. In comparison to the reference, which is the corresponding pure SE3030 silica with 10 wt % polymer template (with respect to the silica matrix), additional surface is created. Interestingly, the isotherms show no significant gain of microporosity with increasing concentration of OTN. The additional

(14) Göltner, C. G.; Henke, S.; Weissenberger, M.; Antonietti, M. *Angew. Chem., Int. Ed.* **1998**, *37*, 613−616.

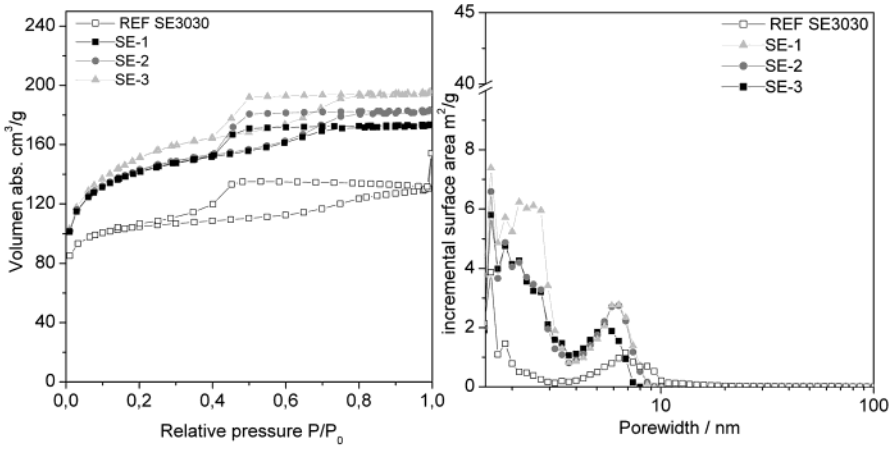

Figure 6. BET isotherms of the calcined materials SE-1 to SE-3. The DFT calculations for SE-1 and SE-2 are mainly sensitive to the pores generated by the SE3030 template. For SE-3, the smaller OTN pores can be numerically separated and show up in the pore size distribution.

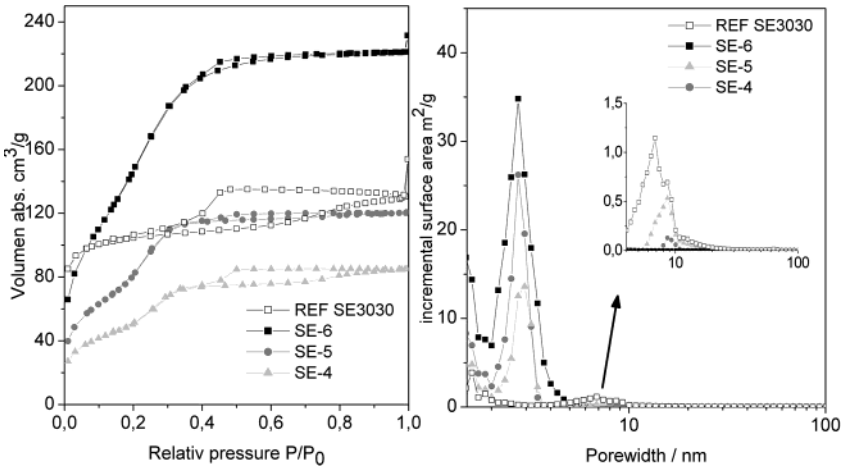

Figure 7. Isotherms of the materials SE-4 to SE-6. The shape of the isotherm is now dominated by the small pores formed by the OTN polymer. DFT calculations show clearly the shift of the SE pore distribution toward higher values, as compared to the SE pores in the materials SE-1 to SE-3 and the reference material.

Table 3. Surface and Overall Porosity of the Calcined Materials in Dependence on Added OTN Content

	SE3030	SE-1	SE-2	SE-3	SE-4	SE-5	SE-6
BET surface [m^2/g]	354	488	492	527	184	299	565
porosity [cm^3/g]	0.20	0.27	0.28	0.30	0.13	0.19	0.34

porosity is mainly seen in the range up to 0.3 relative pressure. The shape of the hysteresis loop changes only slightly and still exhibits type IV behavior, according to IUPAC nomenclature.

DFT calculations (Figure 6b) reveal this additional porosity to be similar to that of pure OTN phases, but the two types of pores cannot be deconvoluted. Just for SE-3, a distinct pore size starts to become visible. The corresponding BET surface areas are listed in Table 3. The expected linear increase of surface area from sample SE-1 to SE-3 goes well with the additional mesopore volume created by OTN micelles.

Obviously, up to this concentration, the two type of micelles stay separated but do form a common phase, with the smaller OTN micelles being embedded in the interstitial sites between the block copolymer micelles. To the best of our knowledge, this is the first manifestation of such a mixed micellar phase.

Both the BET surface area and the shape of the adsorption/desorption isotherms change dramatically with still increasing OTN content, as seen in Table 3 and shown in Figure 7. Despite the increased amount of template, the surface area and the overall porosity have decreased, speaking for the fact that parts of the surfactant are lost for the micellar casting. The DFT calculations show the dominance of the OTN pores but also the suppression of the SE3030 pores, the leftovers of which in addition exhibit an increased size.

Electron microscopy reveals the reason for these changes: the samples demix in two micellar phases. For SE-4, still mixed micellar regions are found, but the majority of the sample is demixed into fine, homomicellar regions (data not shown). For SE-5 (Figure 8a,b), the demixing is getting more pronounced, whereas the size of the demixing regions is largest for the SE-6, the sample with the highest fluorocarbon concentration (data not shown).

A careful observation of the pictures reveals the reason for the drop of surface area. In addition to the already mentioned incomplete access to the pore system of the pure OTN phase and the dispositional loss of surface area and porosity, the pore size of the SE structures has been significantly increased, partly to structures of up to 20 nm. Presumably, the two micellar phases compete for the

Table 4. Compositions of the Mixed Micellar KLE3935-Based Materials under Discussion

sample code	KLE3935/g	OTN/g	% template giving small pores	HCl, pH = 2/g	TMOS/g	SiO_2/g	wt % template in completely condensed material	carbon-free after calcination?
KLE-1	0.45	0.09	17	1.37	2.56	1	35	no
KLE-2	0.31	0.29	48	1.78	2.56	1	38	no
KLE-3	0.22	0.43	66	1.51	2.56	1	39	yes
KLE-4	0.14	0.55	80	1.81	2.56	1	41	yes
KLE-5	0.04	0.72	95	1.99	2.56	1	43	yes

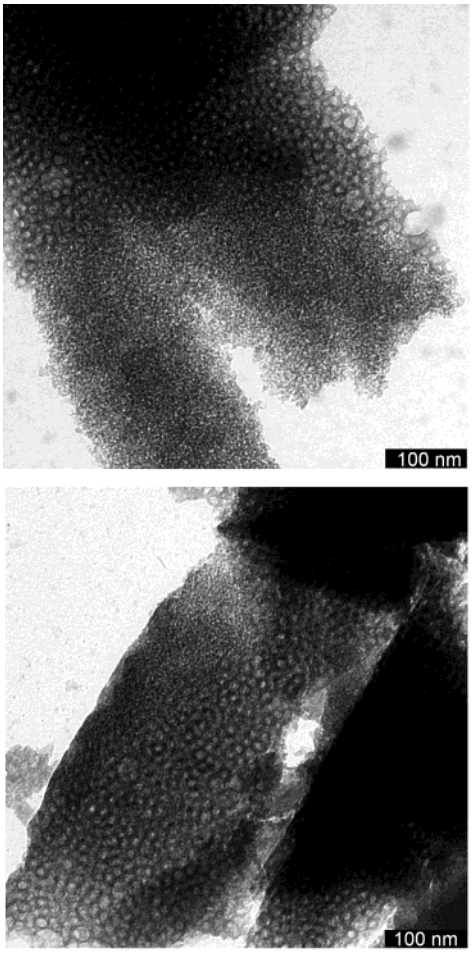

Figure 8. TEM of sample SE-5 showing only demixed regions of the two different pore systems.

solvent, with the fluorinated micelles obviously having the higher osmotic pressure. Because of that, the SE3030 phase is higher in template concentration, and larger aggregates or even vesicular or droplet structures do form. Due to the difference in osmotic pressure, the coexistence with a mixed micellar phase is excluded. With increasing OTN content, the surface area is increasing again, however just based on the OTN-type pores. The phase boundary between one-phase and two-phase regions seems to be located at about 40 wt % OTN content with respect to the organic phase.

The advantage of nanocasting and the ability to depict the detailed phase structure is illustrated by comparing those results with the X-ray data of the calcined material. Figure 9 shows the SAXS data for two of the synthesized materials with different contents of OTN in the demixed region. The curve is essentially dominated by the form factor of the big pores, with some Percus−Yevick-like interference function at small angles due to the mutual packing. The richness of the structure or even the much weaker scattering due to the OTN structure however

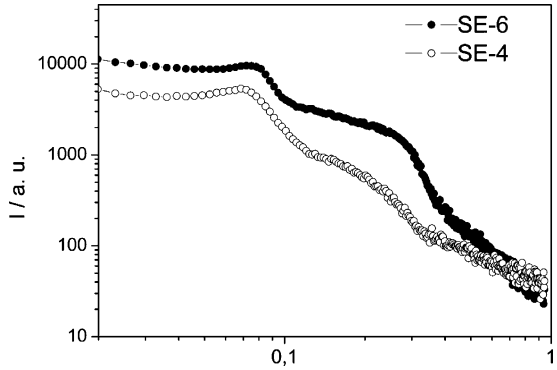

Figure 9. SAXS data of two different materials synthesized with SE3030 and OTN. The maximum of the scattering curve at low scattering values is a property of the SE pores, whereas the shoulder at higher scattering angles belongs to the pores generated by the fluorinated surfactant.

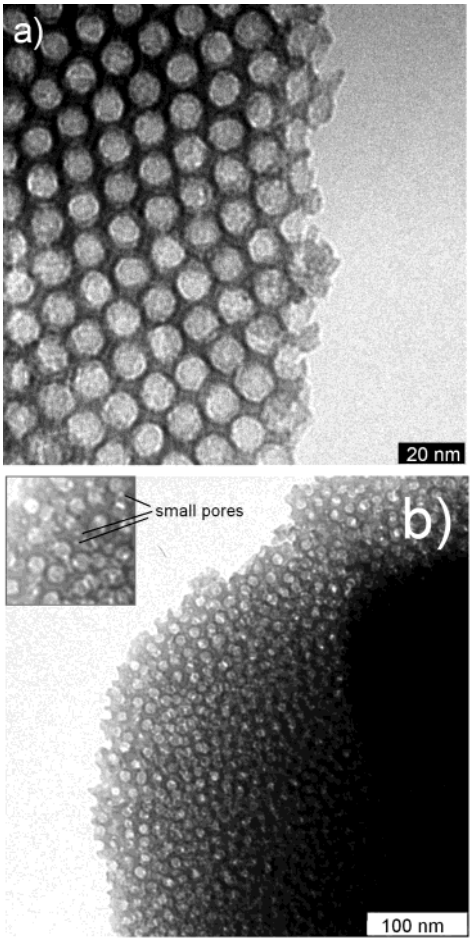

Figure 10. TEM pictures of samples KLE-1 (a) and KLE-2 (b). As the OTN content increases, the ordering of the sample decreases (b). For the sample KLE-2, the small pores generated by the OTN oligomer can be visualized between the KLE pores (see the inset).

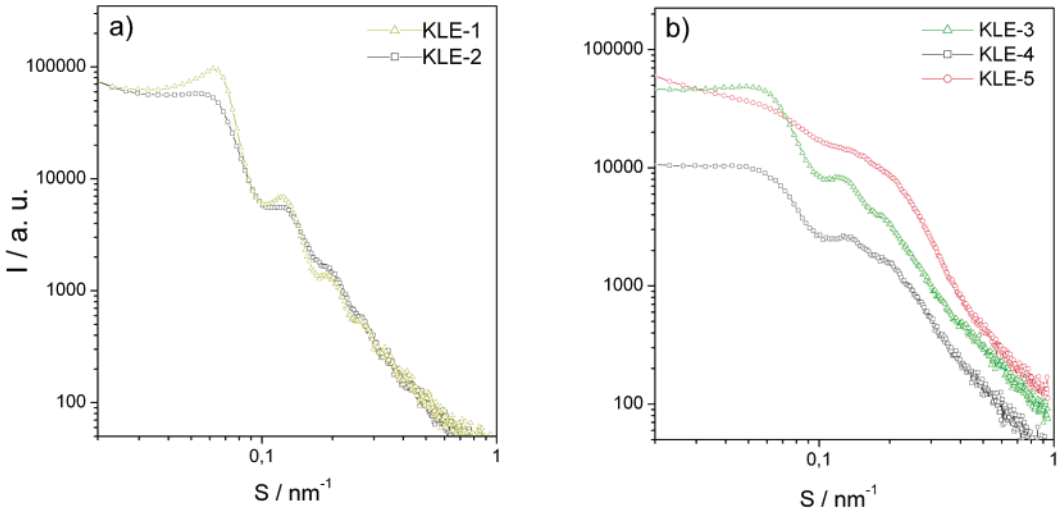

Figure 11. The SAXS curve of sample KLE-1 reflects the highly ordered fcc-type arrangement of the monodisperse pores generated by the template (a). With increasing content of OTN, the samples loses the order of the big pores, and a shoulder of the smaller pores due to OTN micelles at higher scattering values starts to grow (samples KLE-3 to KLE-5) (b).

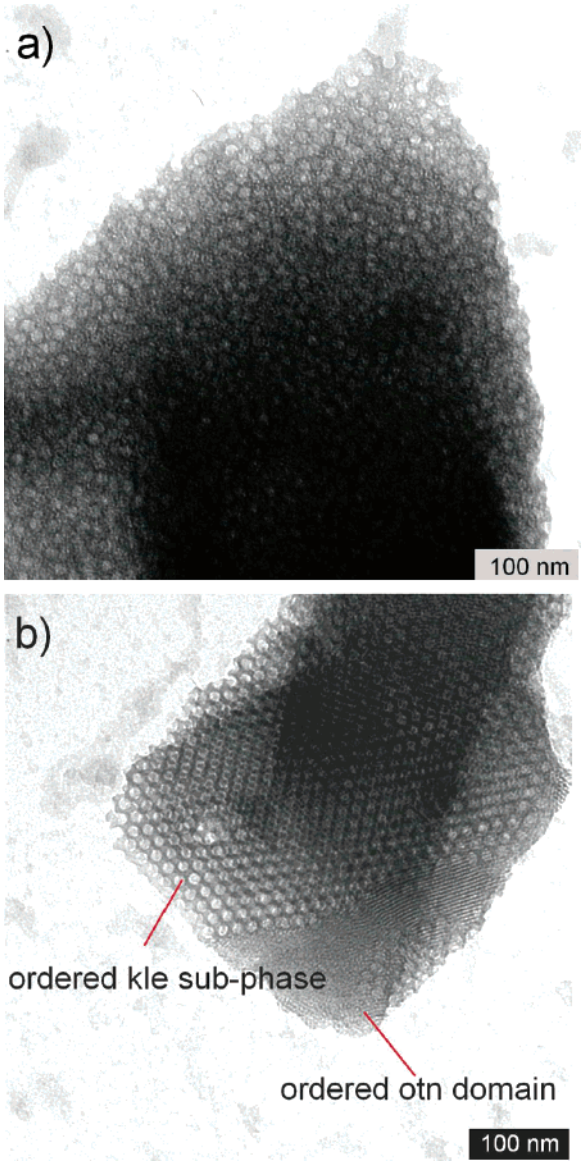

Figure 12. TEM characterization of sample KLE-3: (a) metastable homogeneous mixed micellar phase; (b) demixed double liquid crystalline phase.

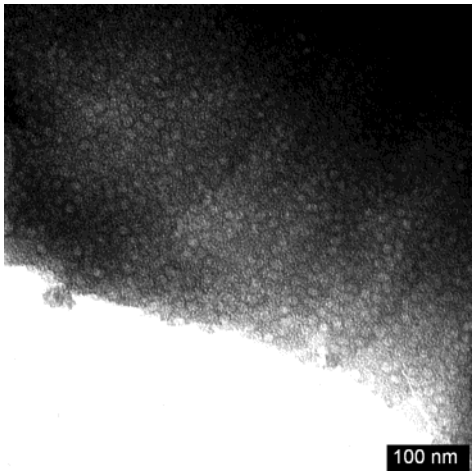

Figure 13. KLE-4 shows perfect miscibility of the two different micelles. The big pores generated by the KLE3935 micelles are statistically distributed in a matrix of the small micelles formed by OTN.

remains unseen. This is why SAXS cannot be employed to reveal quantitative information for this more complex system.

Nanocasting of the KLE3935/OTN System. As osmotic pressure around the micelle and size (because of depletion and packing effects) obviously play an important role for such micelle mixtures, system specificity is to be expected. Therefore, we applied this approach to a second nonionic fluorocarbon/hydrocarbon system, where OTN was mixed with KLE3935, a system forming regular spherical pores with 13 nm diameter with a strong tendency for cubic micellar packing.[4] Five porous silicas based upon OTN and KLE3935 with systematic variation of composition have been synthesized. The resulting compositions of the systems are summarized in Table 4.

For these systems, the compatibility between the two micellar species seems to be higher. For the samples with high hydrocarbon polymer micelle concentration, KLE-1 and KLE-2, respectively, almost clear KLE3935 behavior, only differing by the degree of order, is found. This is depicted in Figure 10.

The sample with the very low fluorosurfactant content is nicely ordered (face-centered cubic (fcc)), whereas

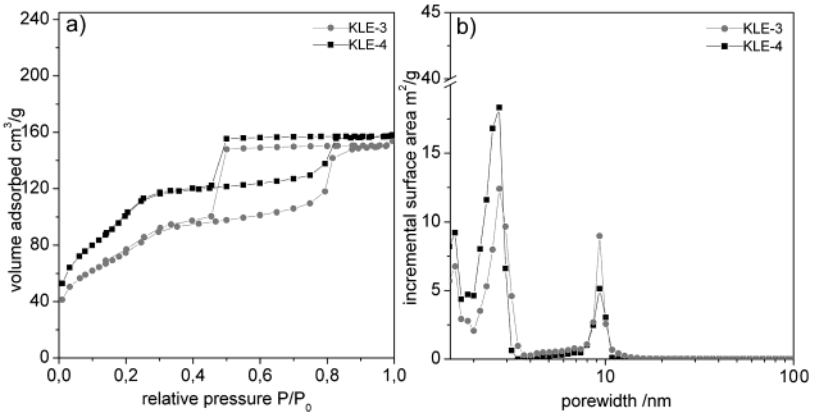

Figure 14. BET isotherms of samples KLE-3 and KLE-4. The relative amount of OTN and KLE3935 template, respectively, is reflected in the relative probabilities of finding the respective pore sizes in the DFT calculations.

increase of the content of fluoromicelles in the mixed micellar phase from 17% to 48% (relative to the total template) promotes disorder. The existence of pure OTN phases, which are usually quite easily identified (see the first set of experiments), can be denied on the basis of the TEM observations. Therefore, all the fluoromicelles must be located in the walls between the big pores, where TEM however can only give weak indications (see the zoom in Figure 10b).

Indirect evidence for this co-localization can also be taken from the fact that samples KLE-1 and KLE-2 were homogeneously black after calcination, whereas both pure reference materials with similar compositions would be certainly white. Obviously the presence of the fluorocarbon micelles in the regions between the block copolymer micelles suppresses percolation of the stabilizing PEO chains; that is, they are depleted onto the micellar cores. This assumption is supported by sorption measurements, which show no significant surface for both samples.

Also, the SAXS experiments go nicely with the TEM observations, as depicted in Figure 11a. In both cases, the scattering curves are dominated by the form factors due to the near monodisperse spherical pores, while the high fcc order of sample KLE-1 amplifies the maxima and minima of the curve.

For the sample with intermediary composition, KLE-3 (66 wt % fluorosurfactant of the total template content; note that the fluorosurfactant has a significantly higher density), an exciting metastability shows up. Depending on the fine details of preparation, either a stable mixed micellar phase (Figure 12a) or a mixture of the two pure liquid crystalline phases (Figure 12b) is obtained. This situation can be compared with the classical case of crystallization from an alloy: whereas the disordered phases are miscible, the crystalline phases are not, and demixing into microdomains of the pure compounds can take place. The fact that in the present case two liquid crystalline phases are concerned changes not the underlying physics but the time scale of metastability. This is an interesting model case of colloidal crystallization from the starting situation of a binary blend.

In contrast to the SE3030/OTN system, the KLE3935/OTN system is stable and miscible again at high OTN content. The TEM pictures of KLE-4 (Figure 13) and KLE-5 (not shown) show nicely the mixed micellar phases with two different pore sizes, where the abundance of each micelle type goes with the stoichiometry.

The presence of two different pore sizes is also clearly seen in the gas sorption measurements shown in Figure 14, where the results for samples KLE-3 and KLE-4 are shown. The two different regimes of sorption are also nicely separated by the DFT calculations revealing two distinct pore populations with incremental surface areas reflecting the stoichiometry. It must be underlined that the gas sorption of KLE-3 does not depend on the metastability of the sample structure, as the mixed micellar and the demixed double liquid crystalline state are practically indistinguishable in the gas sorption experiments.

Contrary to the SE system, the larger mesopores do not change their size even at very high OTN concentration, again underlining that this system is much better balanced with respect to mutual osmotic pressure.

The question is left of why the KLE3935 shows much better compatibility as compared to the SE system. If mixing were mainly entropic, the larger system would be less compatible, which is however not the case. Also, we do not observe any specific size effects, as they are found for metal alloys. We can only speculate that mutual recognition and acceptance of the micelles is due to the density of the nonionic PEO chains on both micelles and the coupled local osmotic pressures, which have to be balanced.

Conclusion

It was shown that micelles of fluorinated nonionic surfactants can be employed as templates in the nanocasting process to generate mesoporous silica. Depending on composition and the relative surfactant composition, highly organized hexagonal phases were identified with transmission electron microscopy. As fluorocarbons usually do not mix with hydrocarbons, those templates are also promising to promote the organization of hydrophobically modified monomer mixtures.

The mixture of those micelles with two amphiphilic hydrocarbon block copolymers allowed templating of silica with two independent, self-organized templates at the same time. The special feature of this fluorocarbon/hydrocarbon template mixture to form two individual micellar species under all conditions was confirmed: in not a single case did we find evidence for mutual structural cross-influence. By careful analysis of the pore architectures by gas sorption measurements and transmission electron microscopy of the final porous silica in dependence on the relative template concentration, parts of the phase diagrams could be revealed.

For the mixture between the polystyrene-*b*-poly(ethylene oxide), essentially macroscopically demixed samples, that is, the coexistence of two lyotropic phases, were found. Just in the case of high hydrocarbon and low fluorocarbon template content, a mixed micellar phase

was identified. This however turned out to be a closed pore structure: the coronas of the two micellar species do not percolate. In the coexistence region, the two lyotropic phases compete for the water, and the mesophase structure of the hydrocarbon block copolymer is altered by strong dehydration.

For the mixture between KLE3935 and OTN, miscibility over the whole composition space was identified. For high KLE contents, a mixed micellar phase where the two different micelles are packed in some type of organized alloy was identified. For all other compositions, the mutual presence lowers the order, and mixed micellar phases with liquid structure are observed. Close to symmetric composition, this liquid mixture can undergo "crystallization", and the coexistence of two highly organized liquid crystalline phases is clearly identified with the TEM experiments.

The nanocasting toward porous silica indeed serves in these experiments as an analytical tool, as such structural details of mixed micellar phases were previously not accessible. In addition, the obtained porous systems with controlled bimodal pore size distribution might be interesting from a materials perspective.

Acknowledgment. We thank the Clariant AG for providing us with the fluorinated surfactants. Steady support by the Max Planck Society is gratefully acknowledged.

LA049147K

Polyisobutylene-*block*-poly(ethylene oxide) for robust templating of highly-ordered mesoporous materials

Matthijs Groenewolt, Torsten Brezesinski, Dr. Helmut Schlaad, and Prof. Dr. Markus Antonietti*

Max Planck Institute of Colloids and Interfaces, Research Campus Golm,

Am Mühlenberg 1, D-14476 Potsdam-Golm, Germany.

Péter Werner Groh and Prof. Dr. Béla Iván

Department of Polymer Chemistry and Material Science, Institute of Materials and Environmental Chemistry, Chemical Research Center, Hungarian Academy of Sciences,

H-1525 Budapest, Puztaszeri u. 59-67, P.O. Box 17, Hungary.

Graphical Abstract

Robust self-assembly with very high order is demonstrated by a polyisobutylene-*block*-poly(ethylene oxide) (PIB-PEO) copolymer tailor-made by combining living cationic and anionic polymerization. A cubic micellar phase with long-range order and a glassy phase consisting of deformed spheroids were identified. Application of PIB-PEO in the synthesis of porous titanium oxide yielded perfect anatase crystalline films with high regularity (see Figure).

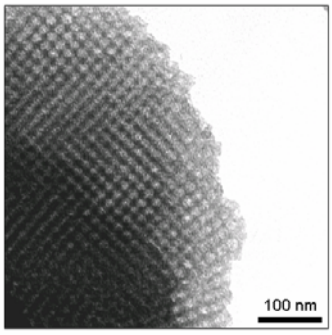

Introduction

Nanocasting, the 3D-transformation of self-assembled organic nanostructures into hollow inorganic replicas under preservation of fine structural details, has recently turned out to be a versatile tool for the synthesis of porous media with new pore topology. In the classical synthesis of mesoporous inorganics,[1,2] a route called "synergistic precipitation", the order of the starting and end situation are not related to each other. Nanocasting or the “true lyotropic liquid crystal approach”,[3-7] as introduced by Attard and Göltner, is different. Here, the starting high concentration template phase is solidified by chemical gelation reactions. In the early work it was shown already, that this technique offers the possibility to make an 1:1 imprint or negative copy of organic mesophases. X-ray measurements, performed throughout the process, showed that the solidified hybrid inherits all structural features of the original matrix. In order to enable nanocasting, the cast structure must be compatible with both the liquid precursor phase as well as the final solidified replica. If this is not the case, the enormous interfaces involved (up to 1000 m^2/g) will add up unfavorable interface energies and replication breaks down.

This is why most work is done on sol-gel silica,[8] the surface chemistry of which is easy to address. Handling surface energies via poly(ethylene oxide) (PEO) tails, first demonstrated by Pinnavaia et al.,[9-11] is presumably the most frequently applied tool. Here, the formation of hydrogen bridges between the silicic acid framework and the ether oxygens of the PEO chain stabilize the interface. The gelation of the SiO_2 network is preferentially done at about pH 2, close to the isoelectric point of silicic acid.

More recent work on the generation of mesoporous films made of other, crystalline inorganic materials by evaporation-induced self-assembly (EISA)[12] indicates that a second property of the templates severely influences the quality of the formed mesoporous films. This is the “robustness” of the self-assembly process against processing conditions, such as temperature, alcohol content, or moisture level in the gaseous headspace.[13-15] Ozin et al. were able to produce mesoporous crystalline titania films on the base of the commonly used pluronics^{TM} block copolymers, but relied

on the specific replacement of ethanol by the more hydrophobic butanol in their recipes.[16,17] Already the switch from the just moderately hydrophobic poly(propylene oxide) (constituting) to the more hydrophobic poly(ethylene-*co*-butylene) significantly improved the process and allowed the generation of more complex mesoporous materials under a wider range of conditions with improved structural quality, such as titanium oxide[18] or even perovskites.[19]

The scope of the present work is therefore to synthesize and explore the applicability of a template with extreme hydrophobic contrast, composed of polyisobutylene (PIB) and PEO. PIB is an easily accessible, utmost hydrophobic hydrocarbon polymer[20], which can be easily removed by calcination without health and security risks (especially compared to other polymers with similar hydrophobicity, namely siloxanes and fluorine-based polymers). The aggregation and the mutual packing motifs of the aggregates of a selected PIB-PEO are analyzed in detail by transmission electron microscopy (TEM) and of the silica replicas in dependence of template concentration. Small-angle x-ray scattering (SAXS) was also applied. Since the solubility of PIB in water and water/alcohol mixtures is so low that equilibration is highly hindered, we also analyzed the effects of different sample processing. Finally, we will describe the applicability of our new polymer in the synthesis of mesoporous ordered crystalline systems. For a proof of principle, we used our template in the synthesis of mesostructured crystalline titania films via the EISA route. The titanium oxide films were prepared using a dip-coater in a humidity chamber, calcined afterwards and studied by TEM. Wide-angle x-ray scattering (WAXS) was performed to analyze the crystallinity of the films.

Results and Discussion

Application of quasiliving carbocationic and anionic polymerization techniques (see the Experimental Section) enabled the synthesis of a PIB_{85}-PEO_{79} block copolymer (subscripts denote the average number of repeating units) of very high purity. The PIB-PEO exhibits a monomodal molecular-weight distribution with an apparent polydispersity index of 1.06 (size-exclusion chromatography (SEC), calibrated with polystyrene standards) and is free of homopolymer. The ^{1}H NMR spectrum and the SEC trace of the sample are shown in Figure 1.

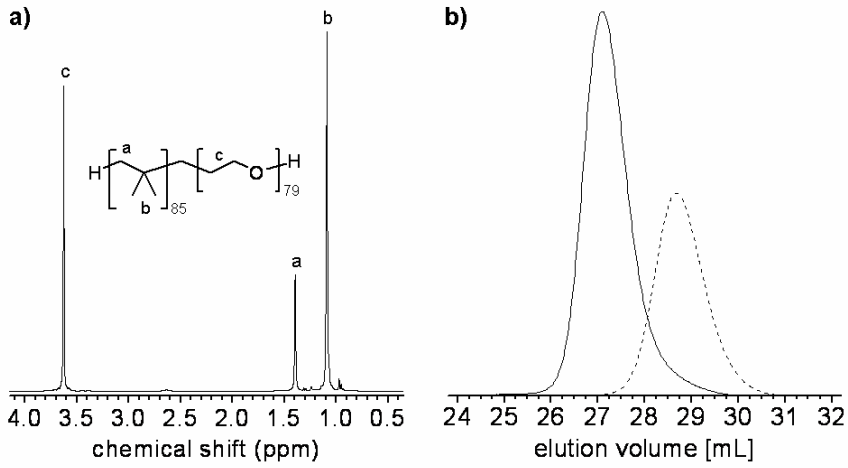

Figure 1: ^{1}H NMR spectrum (400.1 MHz, $CDCl_3$, 25 °C) (a) and SEC chromatogram (solid line; eluent: THF at a flow rate of 1 mL/min, 25 °C, stationary phase: SDV polystyrene gel, detector: RI) (b) of the synthesized PIB-PEO block copolymer. The dashed line in (b) corresponds to the SEC trace of the PIB precursor.

This block copolymer, which is soluble in water or ethanol, was used as a template for the generation of mesoporous hybrid materials (SiO_2 and TiO_2). The most appealing aspect of using PIB-PEO is the ultrahydrophobicity of the PIB segment. Owing to its chemical structure, a fully saturated backbone with two methyl groups per monomer unit, PIB is considered as one of the most hydrophobic hydrocarbon polymers.[20]

All as-made silica hybrids **1**-**4**, experimental details are given in Table 1, are in monolithic form and transparent homogeneous materials, indicating the absence of demixing throughout the silica solidification process. After calcination, the samples are either black (**1** and **2**) or turbid white (**3** and **4**), which in the latter case is due to the increasing difference in refractive index. The black color of the first samples is indicative for isolated polymer aggregates, which lead to trapped carbonization fragments in the silica matrix during the process of calcination. This is a quite typical phenomenon when template concentration is low and the resulting pore system is non-percolating. Polarization microscopy reveals in all cases the absence of birefringence, indicating the presence of either a cubic or disordered micellar structure.

Table 1: Experimental composition of the set of silicas under investigation (see Experimental section for details).

Sample code	PIB_{85}-PEO_{79} (5 wt % in ethanol) [mg]	$HCl_{aqueous}$ (pH 2) [mg]	tetramethoxy orthosilicate [mg]	wt % template in the final silica cast*
1	154	103	203	9
2	346	101	192	18
3	980	113	224	35
4	1540	88	193	50

* mass (polymer) / [mass (polymer) + mass (SiO_2)]

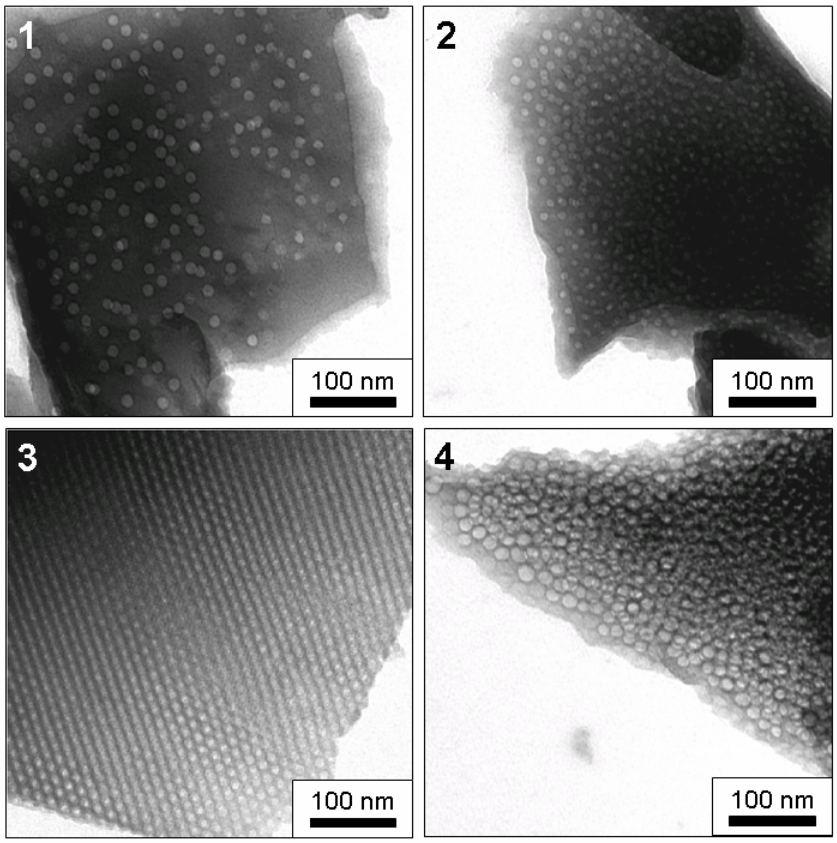

Figure 2: TEM micrographs of the calcined silica nanocasts **1**-**4** obtained for different concentrations of the PIB_{85}-PEO_{79} template (see Table 1).

The TEM images of the structures of calcined silica nanocasts, as obtained in dependence on the concentration of the template (weight percentage of the template in the silica cast before calcination), are depicted in Figure 2. At lower concentrations (**1** and **2**), only spherical micelles with a diameter of ~14 nm can be seen, distributed in a statistical way. Light scattering performed on solutions with a similar preparation history revealed micelles with a corresponding molecular weight, indicating that nanocasting indeed depicts the original structure. At about 35 wt % (**3**), a cubic FCC-type micellar phase with extraordinarily high long-range order, i.e. exclusively liquid crystalline monodomains, is found. This order is even improved as compared to the poly (ethylene-*co*-butylene)-*block*-PEO system described earlier.[21] The perfection of the spherical pores and the FCC-type ordering can be supported by SAXS measurements on those samples, as shown in Figure 3. It should be mentioned that FCC and HCP packing are hard to differentiate by scattering, but that only FCC motifs were found in TEM.

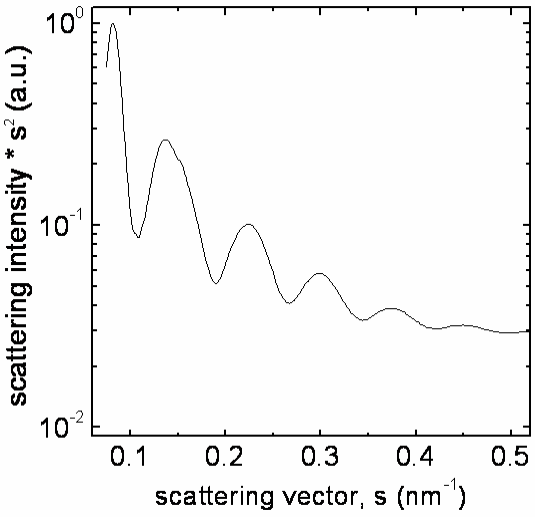

Figure 3: SAXS diffractogram of sample **3**. The curve is typical for practically monodisperse spherical pores with an FCC/HCP (as indicated by the fine structure of the second peak of the form factor) packing.

At the highest concentration investigated (50 wt %, **4**), we observe a glassy-disordered, high-density phase which involves also deformed particles. This phase, which presumably is kinetically trapped, was already discussed in detail in a previous work.[21] The size of micelles has increased to about 20

nm, and the aggregates become quite polydisperse and slightly ellipsoidal. In certain spots of the sample, this glassy phase coexists with some pseudo-cubic liquid crystalline phase (picture not shown), which involves stronger deformation of the single spherical micelles. As those regions do not occur in a systematic fashion, they will not be discussed in further detail. The ease of deforming the shape of micelles at high concentrations is to our experience quite unusual. It seems evident that the system is at the border to a lamellar phase, i.e. a slight change of molecular composition towards a more hydrophobic polymer would presumably result in lamellar aggregation in the whole concentration range.

Noteworthy is the sensitivity of the system to the protocol of sample preparation. This phenomenon is well known for systems undergoing self-assembly and having an extremely low solubility in the continuous phase, e.g. lipids. Any starting situation may be kinetically trapped and may not relax into the equilibrium state. Here, the intermediary presence of alcohol increases the solubility of block copolymer chains and promotes a more efficient equilibration on the timescale of the experiments. For a demonstration of this effect, we made a silica replica of a pure aqueous solution of the template. The aqueous template solution was added to the (weakly condensed) aqueous silica precursor after the removal of alcohol. After complete gelation, the mixture was treated like the other samples (cf. Experimental Section). For this processing pathway, multilamellar vesicles and aggregates (see Figure 4) with a periodicity in the range of 15–20 nm, but no spherical micelles, are obtained. Powder fragments coexist with a larger number of non-porous silica fragments, indicating the structural heterogeneity of the system. The vesicular aggregates are considered to be a metastable, not fully equilibrated species, which are however stable over months. This observation highlights the great impact of metastability of self-assembled structures of block copolymers which are very flexible (note: the glass transition temperature of PIB is about –70 °C)[22, 23] but also very hydrophobic. Hence, special care on the proper experimental conditions seems to be essential when dealing with ultrahydrophobic systems.

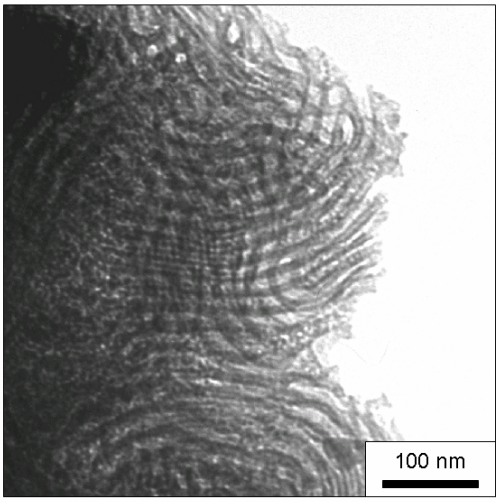

Figure 4: Silica nanocast of a 1 wt % aqueous solution obtained by direct dissolution the PIB_{85}-PEO_{79} template in the absence of alcohol.

Finally, we applied the PIB_{85}-PEO_{79} (weight fraction of the template before calcination: 34 wt %) for the generation of porous titanium oxide via the EISA process. The importance of optimizing length scales and crystallinity in mesoporous titanium oxide films have been discussed in a recent paper[18] and are out of the scope of the present work. After the temper cycle described in the Experimental Section, the crystalline titanium oxide film is composed of anatase nanocrystals as confirmed by WAXS measurements (not shown). The high quality of the mesostructured films can be seen in TEM picture in Figure 5a. It is interesting to note that the SAXS pattern (Figure 5b) is dominated by the lattice factor of a BCC monodomain, (110) resp. (220) peak. The irregular arrangement of titania crystals around the pores leads to polydispersity and hence a less pronounced fine structure (undulations) of the SAXS curve as compared to the amorphous silica.

These results highlight the advanced applicability of this polymer template in the synthesis of complex mesostructured crystalline materials.

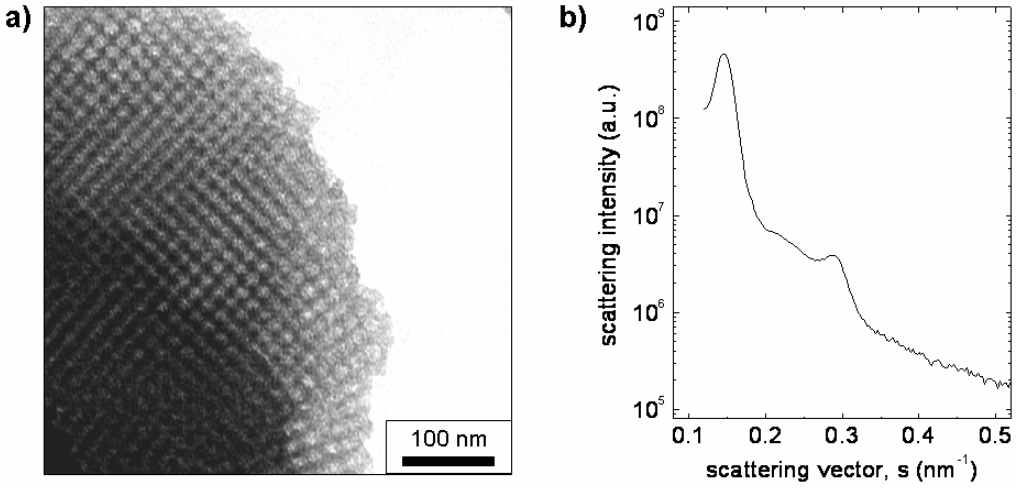

Figure 5: Representative TEM picture (a) and SAXS curve (b) of the calcinated titanium oxide film made via EISA processing.

Conclusion

A new amphiphilic block copolymer was introduced for templating applications, namely PIB-PEO, made by a convenient combination of quasiliving cationic and anionic polymerization techniques. Starting from an isotropic micellar arrangement at <20 wt % of the template, a cubic FCC-type packing of spherical micelles (diameter: ~ 14 nm) with a huge long-range order is found at 35 wt %. We attribute this rather unusually high level of ordering to the ability of the system to undergo easy deformation. At about 50 wt %, a disordered glassy packing of deformed spheroidal micelles is found with an increased average assembly size of about 20 nm diameter.

Equilibration, however, turned out to be a crucial point because the solubility of the core-forming PIB block in water is so low that metastable aggregation structures can be easily trapped and persist on the timescale of months. This, for lipids well known feature, was shown by analyzing the product of “direct dissolution” of the block copolymer in water, which turned out to be a lamellar mesophase coexisting with pure solvent.

From the perspective of materials science and technology, the very robust self-assembly of PIB-PEO block copolymers is very appealing, because it enables generation of very homogeneous porous crystalline materials with an interesting intermediate pore size in the range of 10-20 nm and high structural order. Experimental conditions are feasible under which traditional block copolymer

templates usually fail to assemble, for instance in the presence of larger amounts of alcohols or polar organic solvents.

Acknowledgments

We like to thank Ines Below for the help with block copolymer synthesis, Rona Pitschke for the technical help throughout TEM studies, and Dr. Stefano Bruzzano (Fraunhofer IAP, Golm) for VPO measurement. Erich C. is especially acknowledged for keeping the creative atmosphere. The Max Planck Society is acknowledged for financial support. Partial support by the Hungarian Scientific Research Fund (OTKA T046759) for P. W. Groh and B. Ivan is also acknowledged.

Experimental Section

Polymer synthesis and characterization

ω-Hydroxy-polyisobutylene (PIB-OH) was synthesized by quasiliving cationic polymerization as follows: the polymerization of isobutylene was initiated with 2-chloro-2,4,4-trimethylpentane in conjunction with $TiCl_4$ in the presence of a nucleophile,[20] and the polymerization was quenched with allyltrimethylsilane[24,25] leading to allyl-ended PIB. Hydroboration of the terminal double bonds with 9-borabicyclo[3.3.1]nonane (9-BBN, 0.5 M in THF; Aldrich) and subsequent oxidative cleavage of the carbon-boron bonds with alkaline H_2O_2 resulted in PIB-OH.[22,23] In order to remove cyclooctane-1,5-diol, a by-product formed during the treatment with 9-BBN, the crude product was dissolved in hexane and precipitated three times by the drop-by-drop addition of methanol under vigorous stirring. Finally, the polymer was re-dissolved in hexane, precipitated into acetone, filtered, and dried in vaccum. Thin layer chromatography (TLC) and ^{1}H NMR analyses showed that the product was free of contaminants and exhibited a 100 % endfunctionality.[24,25] According to vapor-pressure osmometry (VPO) and SEC, the number-average molecular weight of the sample is 4850 g/mol (corresponding to 85 isobutylene repeating units) and the apparent polydispersity index (PDI) is 1.07.

Polyisobutylene-*block*-poly(ethylene oxide) (PIB-PEO) was synthesized according to a procedure described elsewhere.[26] Briefly, to a ~20 wt % solution of PIB-OH in tetrahydrofuran (THF) were added 0.5 equivalents of the phosphazene base *t*-BuP_4 (1 M solution in hexane, Fluka) via a syringe. The solution was cooled to –30 °C and ethylene oxide (Fluka) was cryo-distilled into the reactor. The reaction mixture was

stirred at that temperature for 1 hour, then slowly heated to 50 °C and stirred for 2 days under a dry argon atmosphere. After quenching the polymerization with acetic acid, the reaction solution was concentrated and the crude product was precipitated into cold acetone (–30 °C). The polymer was re-dissolved in distilled water, washed with the strongly acidic cation exchanger DOWEX 50WX4-100 to remove traces of protonated *t*-BuP_4, filtered, and freeze-dried. The chemical composition and numbers of repeating units of the sample were determined by ^{1}H NMR: PB_{85}-PEO_{79} (number-average molecular weight: 8330 g/mol). SEC indicated a monomodal molecular-weight distribution with PDI = 1.06.

Silica Nanocasting

A set of different template concentrations was prepared as follows (cf. Table 1). About 200 mg organic silica precursor (tetramethyoxyorthosilicate, TMOS) were taken for each entry, to which appropriate amounts of a 5 % ethanolic solution of the PIB-PEO block copolymer were added drop by drop. After the addition of ~100 mg aqueous hydrochloric acid of pH 2, samples were treated with ultrasound for 5 minutes, and then the alcohol was evaporated under gentle vacuum. The resulting gels were aged at 60 °C in a drying oven for 10 hours. The silica casts were finally calcined in air at 550 °C for 5 hours.

EISA-film casting of mesoporous titanium oxide film

An ethanolic solution of the PIB-PEO block copolymer (95 mg polymer + 3.0 g ethanol) was added to the precursor solution containing 430 mg $TiCl_4$, 350 mg H_2O, and 8.0 g ethanol. The mixture was stirred for 1 hour. The mesoporous thin film was prepared by dip-coating at a constant speed (6 mm/s) and relative humidity (10–20 %). After storing the sample at 60 °C for 12 hours, it was heated up to 300 °C with a heating rate of 3 K/min and kept at this temperature for 1 hour. Finally, the porous crystalline anatase film was obtained through controlled crystallisation by heating to 450 °C with a temperature ramp of 3 K/min and consecutive isothermal treatment for 1 hour.

Analytical instrumentation and methods

TEM images were taken with a Zeiss EM 912Ω at an acceleration voltage of 120 kV. Samples were ground in a ball mill and taken up in acetone. One droplet of the suspension was applied to a 400 mesh carbon-coated copper grid and left to dry in air. SAXS measurements were carried out using a Nonius rotating anode (Cu K_α radiation, λ = 0.154 nm) with pinhole collimation and image plates. With the image plates placed at a distance of 40 cm from the sample, a scattering vector range of s = 0.07-1.6 nm^{-1} was available. 2D

diffraction patterns were transformed into 1D radial averages, and the data noise was calculated according to Poisson statistics. WAXS measurements were performed in reflection mode on a Bruker D8 diffractometer.

References

[1] J. S. Beck, J. C. Vartuli, W. J. Roth, M. E. Leonowicz, C. T. Kresge, K. D. Schmitt, C. T. Chu, D. H. Olson, E. W. Sheppard, S. B. McCullen, J. B. Higgins, J. L. Schlenker, *J. Am. Chem. Soc.* **1992**, *114*, 10834-10843.

[2] C. T. Kresge, M. Leonowicz, W. J. Roth, J. C. Vartuli, J. S. Beck, *Nature* **1992**, *359*, 710.

[3] G. S. Attard, C. G. Göltner, J. M. Corker, S. Henke, R. H. Templer, *Angew. Chem.* **1997**, *109*, 1372-1374.

[4] G. S. Attard, J. G. Glyde, C. G. Göltner, *Nature* **1995**, *378*, 366.

[5] C. G. Göltner, S. Henke, M. C. Weißenberger, M. Antonietti, *Angew. Chem.* **1998**, *110*, 633-636.

[6] C. G. Göltner, M. Antonietti, *Adv. Mater.* **1997**, *9*, 431.

[7] S. A. Bagshaw, T. J. Pinnavaia, *Angew. Chem.* **1996**, *108*, 1180-1183.

[8] C. J. Brinker, G. W. Scherer, *Sol-Gel Science: The Physics and Chemistry of Sol-Gel Processing.*, 1 ed., Academic Press Inc, **1990**.

[9] S. A. Bagshaw, E. Prouzet, T. J. Pinnavaia, *Science* **1995**, *269*, 1242-1244.

[10] P. T. Tanev, T. J. Pinnavaia, *Science* **1995**, *267*, 865-867.

[11] E. Prouzet, T. J. Pinnavaia, *Angew. Chem.* **1997**, *109*, 533-536.

[12] Y. F. Lu, R. Ganguli, C. A. Drewien, M. T. Anderson, C. J. Brinker, W. L. Gong, Y. X. Guo, H. Soyez, B. Dunn, M. H. Huang, J. I. Zink, *Nature* **1997**, *389*, 364-368.

[13] D. Grosso, G. Soler-Illia, E. L. Crepaldi, F. Cagnol, C. Sinturel, A. Bourgeois, A. Brunet-Bruneau, H. Amenitsch, P. A. Albouy, C. Sanchez, *Chem. Mater.* **2003**, *15*, 4562-4570.

[14] E. L. Crepaldi, G. Soler-Illia, D. Grosso, F. Cagnol, F. Ribot, C. Sanchez, *J. Am. Chem. Soc.* **2003**, *125*, 9770-9786.

[15] E. L. Crepaldi, G. Soler-Illia, D. Grosso, M. Sanchez, *New J. Chem.* **2003**, *27*, 9-13.

[16] S. Y. Choi, M. Mamak, N. Coombs, N. Chopra, G. A. Ozin, *Adv. Funct. Mater.* **2004**, *14*, 335-344.

[17] S. Haseloh, S. Y. Choi, M. Mamak, N. Coombs, S. Petrov, N. Chopra, G. A. Ozin, *Chem. Commun.* **2004**, 1460-1461.

[18] B. Smarsly, D. Grosso, T. Brezesinski, N. Pinna, C. Boissière, M. Antonietti, C. Sanchez, *Chem. Mater.* **2004**, *16*, 2948-2952.

[19] D. Grosso, C. Boissière, B. Smarsly, T. Brezesinski, N. Pinna, P. A. Albouy, H. Amenitsch, M. Antonietti, C. Sanchez, *Nature Materials* **2004**, *3*, 787-792.

[20] J. P. Kennedy, B. Ivan, *Designed Polymers by Carboncationic Macromolecular Engineering: Therory and Practice*, Hanser Publisher, **1992**.

[21] A. Thomas, H. Schlaad, B. Smarsly, M. Antonietti, *Langmuir* **2003**, *19*, 4455-4459.

[22] Y. C. Bae, R. Faust, *Macromolecules* **1998**, *31*, 2480-2487.

[23] G. Erdodi, B. Ivan, *Chem. Mater.* **2004**, *16*, 959-962.

[24] B. Ivan, J. P. Kennedy, *J. Polym. Sci. Part A, Polym. Chem.* **1990**, *28*, 89-104.

[25] B. Ivan, J. P. Kennedy, V. S. C. Chang, *J. Polym. Sci. Part A, Polym. Chem.* **1980**, *18*, 3177-3191.

[26] H. Schlaad, H. Kukula, J. Rudloff, I. Below, *Macromolecules* **2001**, *34*, 4302-4304.

The generation of mesostructured crystalline CeO_2, ZrO_2 and CeO_2-ZrO_2 films using EISA

Torsten Brezesinski, Markus Antonietti*, Matthijs Groenewolt, Nicola Pinna, and Bernd Smarsly

Max Planck Institute of Colloids and Interfaces, Research Campus Golm, D-14424 Potsdam, Germany.
Fax: +49-331-567-9502, Tel: +49-331-567-9501, E-mail: pape@mpikg.mpg.de

Mesostructured thin films of CeO_2 and CeO_2-ZrO_2 mixed oxides with highly crystalline pore walls and ordered arrays of mesopores were obtained by a straightforward fabrication process employing evaporation-induced self-assembly (EISA) and a well-designed temperature treatment, taking advantage of a novel type of amphiphilic block copolymers as a template. The mesostructure and crystallinity were studied in detail using small-angle and wide-angle x-ray scattering and electron microscopy. The mesostructured CeO_2 films are crack-free, possess a final pore size of ca. 10 nm, and the mesopores are surrounded by an almost completely crystalline matrix of nanoparticles of ca. 5-7 nm in size, as revealed by high-resolution electron microscopy. Additionally, the mesoscopic order (bcc structure) shows high thermal stability. The crystallization of the walls is usually accompanied by stresses and strong uniaxial structural shrinkage, which however can significantly be diminished by making mixed CeO_2-ZrO_2 mesostructured systems. Here, the crystallites represent "solid solutions" of both binary oxides which exhibit an even higher thermal stability, while the constituting nanocrystals are smaller compared to the pure CeO_2.

Introduction

Recent progress in the synthesis of mesoporous materials by in-situ characterization of the involved complex kinetic processes and their optimization,[1] but also the development of more suitable and more "phase-robust" block copolymer templates[2] enabled the synthesis of practically fully crystalline mesoporous titania[3] and diverse perovskite films.[4] As a further advantage, both the mesopore size (ca. 10 nm) and the thickness of the crystalline walls (ca. 6-10 nm) were tuned to be significantly larger compared to previous studies, thus leading to improved physicochemical properties and mechanical stability. For the first time, this new type of mesoporous materials now allows the study of dielectric and other properties as a function of the nanoparticle size. The resulting films, fabricated by the "evaporation-induced self-assembly" (EISA) process,[5] were shown to have good optical quality and to possess a uniform tunable thickness between 100 nm and 500 nm, so that they could be employed directly for the respective purpose of the functional oxides, e.g. for sensors or solar energy conversion.

Several studies report the fabrication of mesoporous crystalline ceria. However, usually the ceria mesostructure undergoes a severe breakdown throughout the final crystallization step,[6a,b,c] leading to rather ill-defined porosity without controlled nanocrystallinity in the pore walls in terms of the spatial distribution and the size of the oxide nanocrystals. For instance, Morris et al. reported the preparation of crystalline mesoporous ceria,[6d] but the pore sizes were rather small (ca. 2 nm) and the nanocrystals quite large, pointing to mesostructural collapse and a leftover intergrain porosity. In general, in previous reports it still remained ambiguous to conclude that indeed the crystalline regions, detected by x-ray diffraction, originate from polycrystalline mesopore walls and not from non-porous domains created my mesostructural collapse. Since in all cases small template molecules were used, the mesostructural collapse in these studies can be attributed to the geometric incompatibility of the primary nanocrystal size and the mesopore size determined by the template, in other words one cannot set-up a finer tectonic with larger crystals. Just recently, Sanchez et al. reported the first successful procedure to generate mesostructured ZrO_2-CeO_2 (rich in Zr) thin films using Pluronics polymers as template.[10] To the best of our knowledge, no well-defined mesoporous structures (e.g. with cylindrical or spherical pore shape) of pure crystalline CeO_2 thin films and films with at least balanced CeO_2/ZrO_2 ratios have been reported so far.

The continued search for a procedure to make pure mesoporous CeO_2 films or mixed CeO_2-ZrO_2 species with improved structure is motivated by the interesting functional properties of these materials.[7] Compared to other metal oxides, Ceria and Zirconia are known to be chemically and thermally extraordinarily stable and therefore used as catalyst supports and in ceramic membranes for catalysis and sensing.[7,8] In particular, mesoporous CeO_2 is highly interesting for redox processes, and the control over the nanocrystallite size on the nanometer scale was reported to optimize sensing properties.[8g]

Ceria only has one polymorph (a cubic fluorite structure) and can easily switch in this structure between Ce^{4+} and Ce^{3+},

Table 1 Chemical compositions of the initial solution and critical temperatures of crystallisation and mesostructure degradation

	CeO_2	ZrO_2	CeO_2-ZrO_2
"KLE"	**0.075 g**	**0.090 g**	**0.090 g**
M1	**0.875 g ($CeCl_{3*}7H_2O$)**	**0.5 g ($ZrCl_4$)**	**0.480 g ($CeCl_{3*}7H_2O$)**
M2	**-**	**-**	**0.3 g ($ZrCl_4$)**
EtOH	**7.59 g**	**7.59 g**	**8.86 g**
THF	**1.12 g**	**-**	**-**
H_2O	**0.2 g**	**0.7 g**	**0.4 g**
Crystallisation	**250 °C**	**450 °C**	**350 °C**
Mesostructural collapse	**> 660 °C**	**> 650 °C**	**> 700 °C**

balancing the charge difference with oxygen vacancies, that is it can mediate oxidation. This distinct property makes it highly attractive in high temperature solid oxide fuel cells. In general, CeO_2 based systems have been extensively studied, and excellent reviews are available, which discuss the different aspects from structural properties to catalytic application.[9] The binary system CeO_2-ZrO_2 exhibits solid solution formation over a wide range of compositions.[7] Doping of zirconia with ceria stabilizes its tetragonal and cubic phase at room temperature.

It is the purpose of the present paper to describe the conditions under which thin films with mesopores of up to 10 nm can be fabricated using evaporation-induced self-assembly, starting from metal chloride solutions, and to characterize their structural features in detail by transmission electron microscopy (TEM), high resolution TEM (HRTEM), small- and wide-angle x-ray scattering (SAXS and WAXS). As one of the key aspects, a novel block copolymer template is used, which significantly facilitates both the self-assembly process and the pore wall crystallisation under preservation of the mesostructure.

By thorough x-ray diffraction study of the development of the crystallinity in the pore walls and the mesostructure changes as a function of the heat treatment, it is possible to optimize the mesopore structure and crystallinity simultaneously. Minimization of structural shrinkage by optimized processing and structural adjustment of template and primary nanocrystal size allows in addition securing of flat, crack free films, which are required for most applications.

Experimental part

Experimental condition of film processing and treatment:

The starting inorganic precursors were $CeCl_{3*}7H_2O$ and $ZrCl_4$. The block copolymer ($H(CH_2CH_2CH_2CH(CH_3)CH_3)_{89}(OCH_2CH_2)_{79}H$) (referred to as "KLE") was used as surfactant template. Initial solution were prepared by dissolving inorganic precursor into the selected solvent, before the block copolymer template "KLE" is added with the proper amount of EtOH/THF to dissolve it (cf. table 1). The mesoporous thin films were prepared by dip-coating at constant speed (6 mm/s) and constant relative humidity (10-20 %). For CeO_2 a fast transfer to a chamber at 100 °C directly after dip-coating is necessary to prevent local crystallisation of $CeCl_{3*}7H_2O$. Stabilisation of networks before crystallisation was achieved by thermal consolidation (dehydration) at 300 °C under air for 60 min. The desired materials were obtained through controlled crystallisation provided by heating with a ramp of 3 °C/min under air up to 660 °C for CeO_2, 650 °C for ZrO_2 and 700 °C for CeO_2-ZrO_2.

The WAXS experiments and SAXS measurements in reflection were performed using a D8 diffractometer from Bruker instruments (wavelength 0.154 nm). A Philips CM200 FEG microscope, 200 kV, equipped with a field emission gun was used for HRTEM. Transmission electron microscopy (TEM) images with high contrast were taken with a Zeiss EM 912Ω at an acceleration voltage of 120 kV. The GISAXS experiments were carried out at the synchrotron beamline at ELETTRA (Trieste, Italy) at the SAXS beamline of the Austrian Academy of Sciences.

Results and Discussion

1. Mesostructured CeO_2

As pointed out recently,[1,3] the fabrication of mesostructured films of metal oxides with optical quality requires the precise control of parameters such as the external humidity, solvent, dip-coating speed, etc. As one of the major advantages, the KLE polymer employed in the present set of experiments showed to be less sensitive against changes in these parameters. However, still each metal oxide needs optimized fabrication conditions depending on the special nature of the metal salts used. Compared to our recent work on titania,[3] the films have to be exposed to an elevated temperature (at least 100 °C) directly (within seconds) after dip-coating, otherwise $CeCl_3{*}7H_2O$ crystallization takes place (indicated by film turbidity) and the mesostructure is lost. The fast heat treatment also removes major parts of the formed HCl and fixes the mesostructure. The ability of the KLE polymer for rapid self-assembly turned out to be essential in this step, thereby avoiding the insufficient build-up or loss of mesostructure usually observed in previous studies.

Transmission electron microscopy (TEM) on films removed from the Si-support already demonstrates the high quality of the generated mesostructure. Fig. 1 depicts a pure Ceria film, indicating that it is homogeneously mesoporous throughout large domains. The film thickness is ca. 170-200 nm, as determined by spectral ellipsometry.

The TEM images are consistent with a cubic array of spherical pores with an average diameter of about 9-10 nm, as determined on the base of various different TEM images. Also, this morphology is in full agreement with our previous work on mesoporous silica and titania, performed with the same block copolymer template.[2,3]

High resolution TEM of the same sample provides a more detailed view of the construction principle. Selected area electron diffraction (SAED) (Fig. 1b) of such a zone displays diffraction rings characteristic of a structure composed of little domains with crystallographic axis randomly oriented with respect to each other. The d-spacings measured from the diffraction rings are in good agreement with the cerianite structure (JCPDS 34-394). HRTEM of a square of 20 nm side length (Fig. 1c) shows several nanocrystallites with well defined lattice planes, proving the high crystallinity of the sample. From such pictures, the primary nanocrystallite size is estimated to be about 6-8 nm, and no significant amorphous fraction between the single particles could be identified. The crystallites are randomly oriented towards each other, as seen from the lattice fringes. This is further demonstrated by the power spectrum (PS) of this image (Fig. 1d), which is smeared out to narrow rings without preferential orientation. It is also seen that the pore size (ca. 10 nm) is still larger as the primary crystal size, which is a crucial prerequisite for the mechanical stability of the mesopore framework. Taking into account the problems reported to obtain crystalline mesostructured ceria, our case seems to represent a borderline case where the crystallite and template size are still in a region that the mesostructure is maintained during the crystallization. Larger primary nanocrystals (as they would result from a lower nucleation or growth rate) would certainly destroy the present mesopore structure, and reconstitution to a porous powder material with an interstitial pore system would take place.

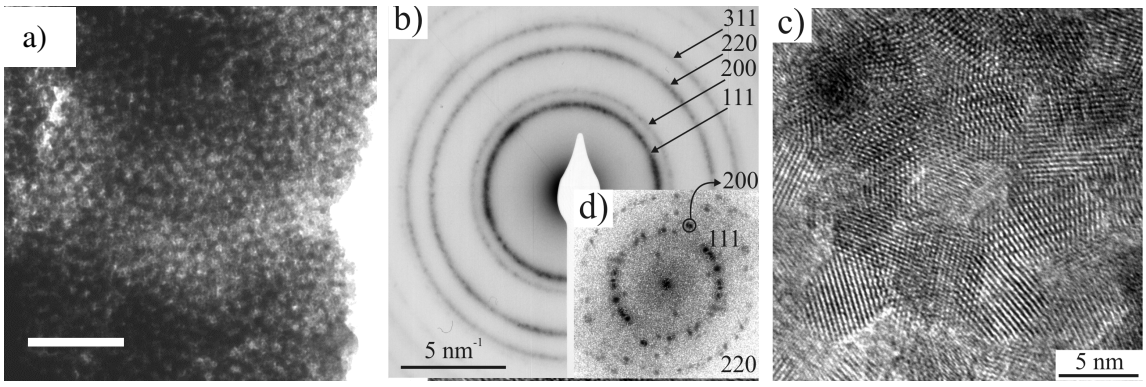

Fig. 1 TEM image (a) of a Ceria film (the scale bar is 100 nm). b) HRTEM: selected area electron diffraction of a zone of 250 nm diameter. c) HRTEM image of a zone of 20 nm side length (c) and its power spectrum (d).

WAXS measurements performed after the different steps of the temperature treatment confirm the TEM results (Fig. 2). Already at 300 °C, the pure ceria system shows a certain degree of crystallinity, however with small nanoparticles of ca. 2 nm and coexisting amorphous regions. Treating the sample to 450 °C completes crystallization, and after a treatment for 10 min at 550 °C the WAXS peaks correspond to a primary crystal size of 7.6 nm, as calculated from the Scherrer equation. The 550 °C data allow to give an upper estimate of the amorphous part of 5 vol% max, not contradicting even a fully crystallized system. The limited growth of the nanocrystals even at high temperatures is prerequisite to maintain the mesopore structure.

The mesostructure was furthermore studied by both grazing incidence small-angle x-ray scattering (GISAXS) and SAXS in symmetric reflection as a function of the heat treatment (Fig. 3). While GISAXS in combination with a 2D detector allows the study of the mesostructure orientation, SAXS in symmetric reflection only shows the interferences in the z-direction (lattice planes parallel to the substrate). It is remarkable that the mesostructure is still present at 600-650 °C, as revealed by GISAXS. The GISAXS pattern is indicative of a distorted bcc structure in [110] orientation, as already observed recently for other cubic systems.[1a, 10] A second order reflection in the 1D SAXS curves is found even for substantially crystallised samples up to T = 450°C (Fig. 3a), suggesting a high degree of mesostructural order. It has to be emphasized that SAXS experiments in reflection on a diffractometer are more sensitive

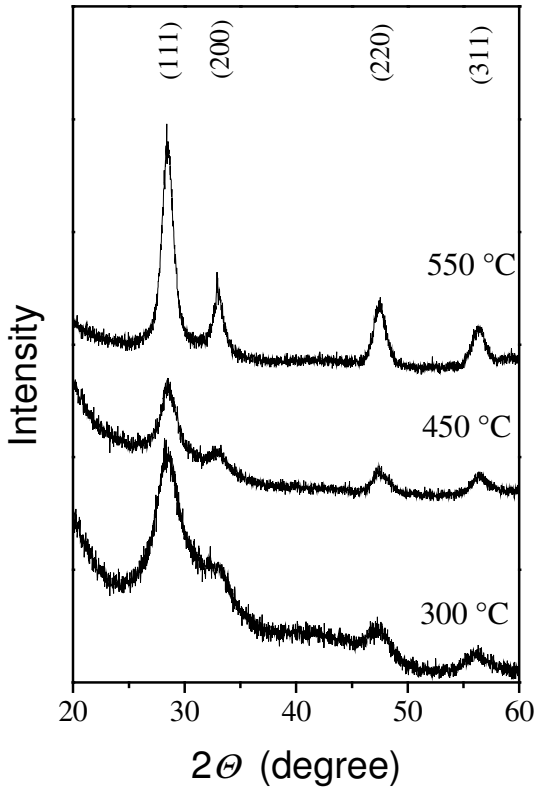

Fig. 2 WAXS diffractograms of the pure ceria film, obtained after annealing at different temperatures.

to weak diffraction peaks than the CCD camera used for GISAXS. From the GISAXS and SAXS experiments, we obtain a lattice parameter for the structure of a = 16 nm, assuming a

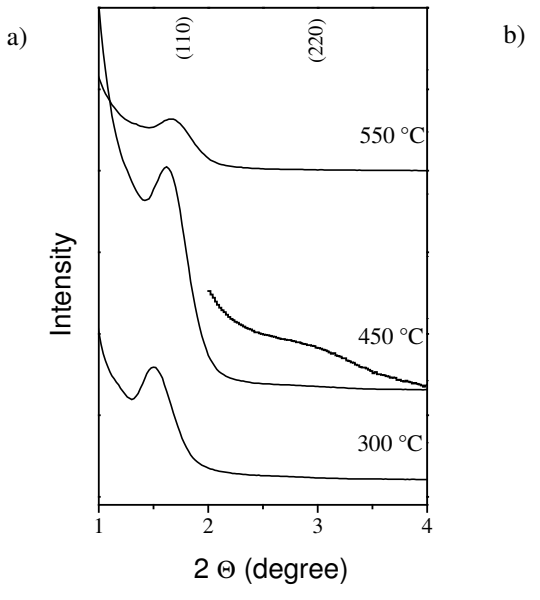

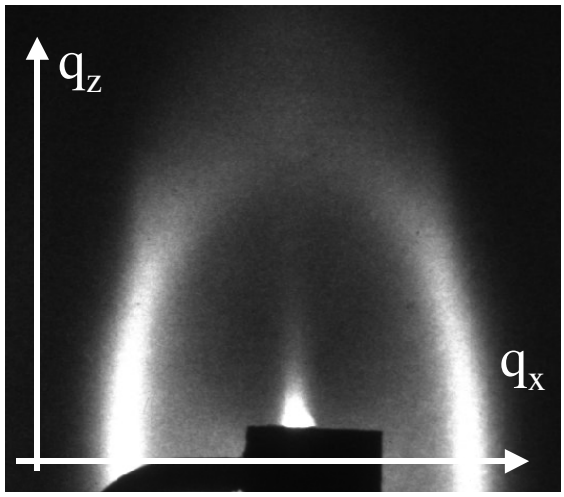

Fig. 3 1D SAXS (reflection, a) as a function of temperature treatment and b) GISAXS (taken at 600 °C) of mesostructured CeO_2 thin films.

distorted bcc structure (see Fig. 3). The relatively large width of the interferences (Fig. 3a) is explained by the small film thickness (ca. 200 nm), corresponding to only ca. 12 layers of pores perpendicular to the surface.

Interestingly, the shrinkage of the mesostructure induced by heat treatment is moderate, because we find an overall uniaxial shrinkage (in the [110] direction) of 20 %. It is noteworthy that the lattice parameter of the mesostructure does not change significantly even up to temperatures of 650 °C (data not shown). Thereby, these mesostructured CeO_2 films show high promise for applications involving even elevated temperatures.

2. Mesostructured ZrO_2

In order to verify the general applicability of our procedure and to test the other pure counterpart, thin films of ZrO_2 were prepared. Interestingly, the crystallization takes place at about 450 °C, which is significantly higher than for CeO_2. The mesoporous structure is retained, however with a more pronounced shrinkage.

As seen in Fig. 4, the mesostructure is not as well organized as in case of CeO_2. WAXS as a function of temperature (Fig. 4c) characterizes the crystallization as a function of the heat treatment. Also, a nanocrystal size of 10 nm (at 450 °C) is obtained from WAXS, being much larger than in the case of CeO_2.

Systems with a primary crystal size of the order of the mesopore size are to our experience critically close to a possible structural collapse. As these mesostructures were also less ordered and showed a high shrinkage, they were not further analysed in the present context.

3. Mixtures of CeO_2 with ZrO_2

Mixed oxides of ZrO_2 and CeO_2 were studied accordingly with respect to the changes in mesostructure and nanocrystallinity induced by high temperature treatment. Sanchez et al. just recently reported that ceria/zirconia thin films can be obtained over a certain range of compositions without phase separation.[10] In the present study, the preparation and crystallization conditions were optimized with respect to the mesostructure quality, in particular with the expectation that a mixed system

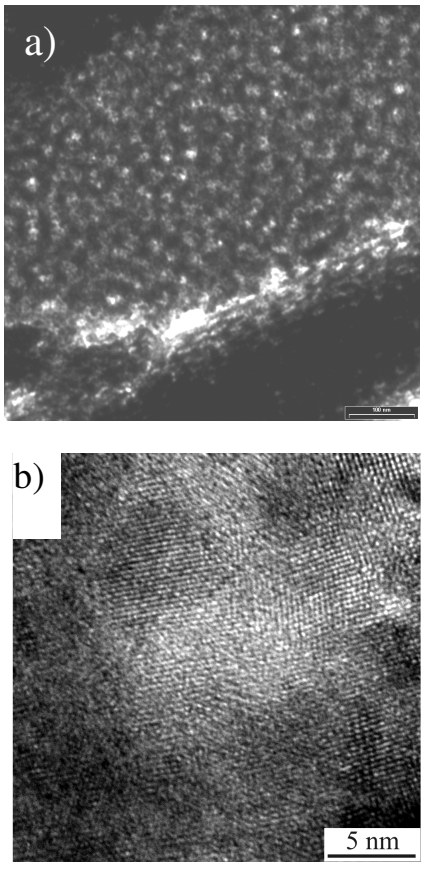

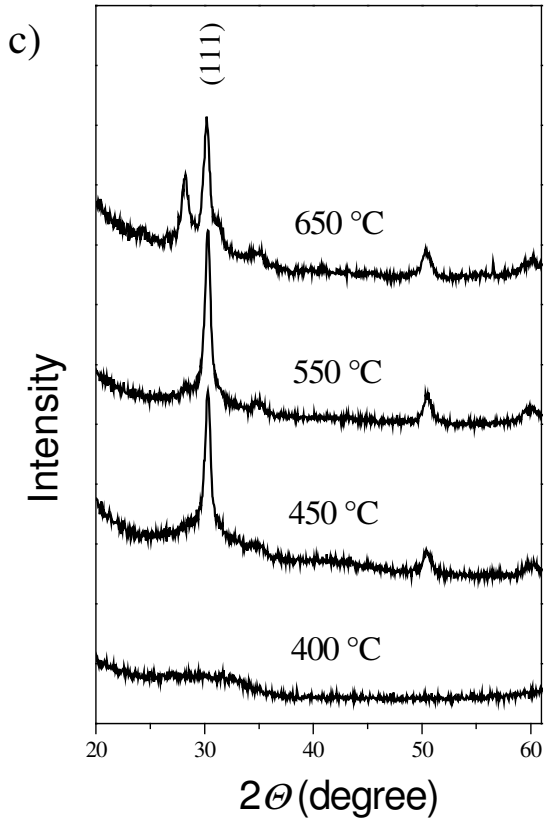

Fig. 4 TEM (a) , HRTEM (b), and WAXS (c) of ZrO_2 thin films (the electron microscopy images were taken of a film treated at 450 °C). The scale bars correspond to 100 nm (a) and 5 nm (b). The WAXS pattern is consistent with the monoclinic modification of ZrO_2.

undergoes slower crystallization because of the formation of solid solutions.

Also in this case, the use of KLE block copolymer as a template provided mesostructured films with crystalline pore walls.

TEM of the symmetric mixed system (tempered at 550 ^{o}C) already indicates that this material has a better structural definition and lower shrinkage than the CeO_2 films (Fig. 5a). High resolution electron microscopy of single pores (Fig. 5b) confirms the concept of using mixed oxides for smaller nanoparticles and better mesopore definition: The primary crystal size has dropped markedly to 2-4 nm compared to ceria, and each pore is now surrounded/constituted by a larger number of nanoparticles, thus allowing their arrangement around the mesopores and, thereby, replicating original micelle shape more precisely than in case of CeO_2. The power spectrum indicates that the present crystals are indeed solid solutions, i.e. each crystal is a mixed species. Furthermore, EDX (energy dispersive x-ray analysis) confirmed the 1:1 molar ratio between Zr and Ce and the absence of chlorides (also for CeO_2 and ZrO_2 films).

The crystallisation behavior was studied in further details by WAXS (Fig. 6), revealing important differences compared to CeO_2.

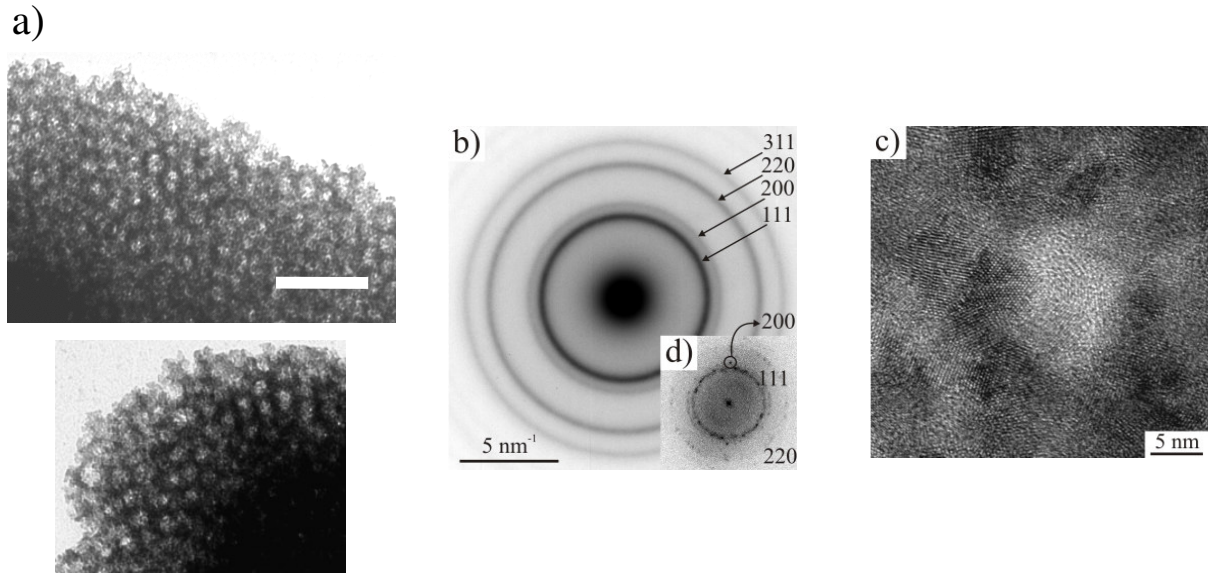

Fig. 5 TEM (a) and HRTEM (b, c, d) of the CeO_2-ZrO_2 mixed oxide film (the scale bar is 100 nm for a). b) HRTEM: selected area electron diffraction of a zone of 250 nm diameter. c) HRTEM image of a zone of 20 nm side length and its power spectrum (d).

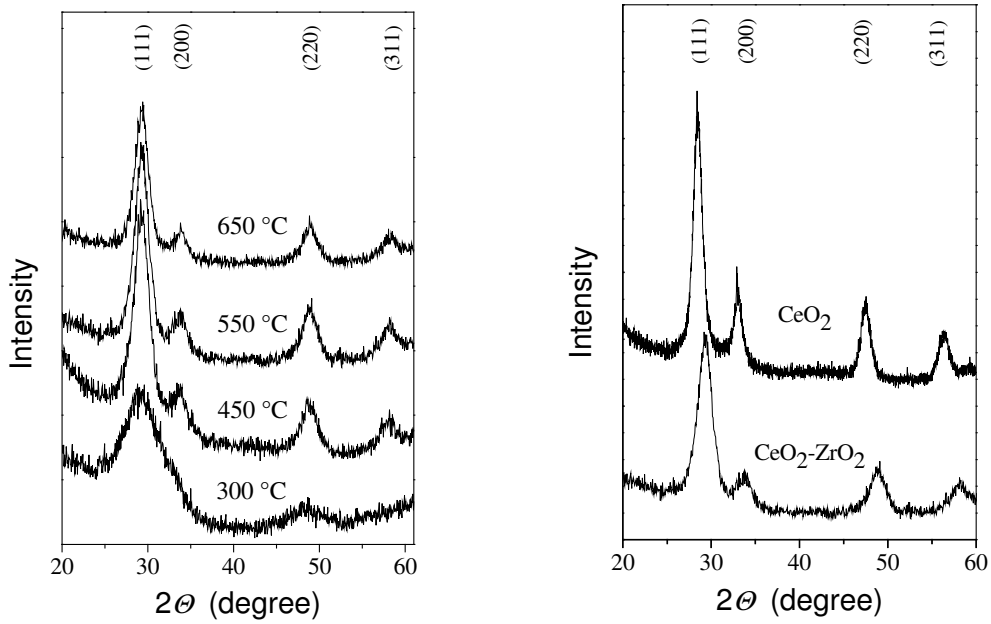

Fig. 6 WAXS diffractograms of the mixed ceria/zirconia species (molar ratio Zr/Ce = 1:1). a) Development of the crystallinity as a function of the temperature. b) Comparison between CeO_2 and CeO_2-ZrO_2 mixed oxide film indicating the presence of solid solutions.

First, it is seen that the onset of the crystallization (defined by the occurrence of the reflections) is shifted to a significantly higher temperature of ca. 350 °C. Second, as an important feature for practical applications, this structure does not undergo changes even at significantly elevated temperatures, that is the primary mixed nanocrystals keep their size and do not easily recrystallize. Fig. 6b compares the WAXS patterns of pure ceria and the mixed symmetric species, both mesoporous and tempered at 550 °C. It is seen that the structures of CeO_2 and CeO_2-ZrO_2 are isomorphous (i.e. cubic fluorite-type), while substitution with zirconia only shifts all peaks to higher angles (cell contraction). Also, the reflections are broader, confirming the smaller primary particle size (4.5 nm as determined by the Scherrer equation) already observed in electron microscopy. Fig. 7 presents the corresponding SAXS patterns (performed as a function of the temperature treatment) and GISAXS measurements.

It is noteworthy that even at 600 °C the mixed oxides still show a well-defined mesostructure, which is more defined than in the case of CeO_2. Based on the GISAXS pattern, the primary structure after drying, but prior to crystallization is indicative for an [110] oriented bcc structure with a lattice parameter of 17 nm (550 °C) and 19.3 nm (450 °C), thus being significantly larger than the one of pure CeO_2. The shrinkage upon crystallisation (determined from the positions of the [110] reflection at 300 °C and 450 °C) is below 10 %, and recrystallization at higher temperature of the whole structure (usually accompanied with a density increase of about 20 %) leaves the mesostructure essentially intact with negligible shrinkage. The overall uniaxial relative shrinkage at 650 °C, compared to 300 °C, is below 15 %, which is attributable to the density change between the amorphous and crystalline state. Note that a film confined to a substrate can only shrink uniaxially, as shrinkage along the other directions would lead to delamination. Compared to other crystalline mesoporous materials, where shrinkages of 60 %,[3] 80 %,[10] or 40 % were obtained,[4] or compared even to our own optimized CeO_2 system (20 %), the changes upon crystallisation and recrystallisation are remarkably small.

Such films, when analysed either with SEM or AFM (data not shown), turned out to be comparably flat (rms surface roughness of ca. 2 nm) and crack- and defect-free. This is much harder to obtain for films which undergo higher shrinkage and sometimes show periodic cracking patterns. The concept of avoiding criticality of mesostructure and to make the constituting nanocrystalline elements as small as possible to keep the primary structure has therefore proven valid with these experiments.

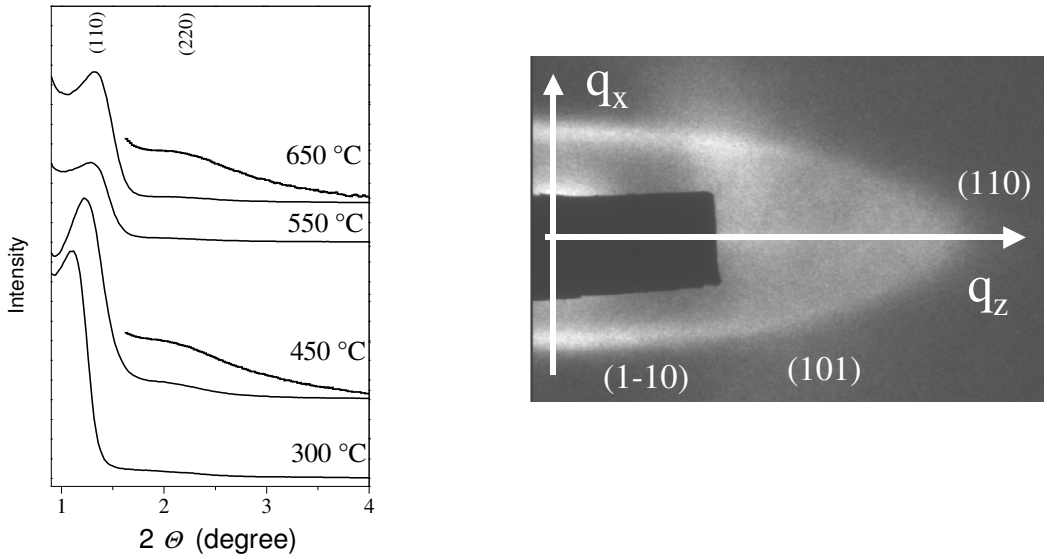

Fig. 7 1D SAXS (a) and GISAXS (taken at 600 °C, b) for CeO_2-ZrO_2 thin films. The white shadow in the GISAXS pattern is due to parasitic scattering of the setup.

Conclusion and Outlook

In the present study, thin films of mesostructured CeO_2 and CeO_2-ZrO_2 with crystalline pore walls were obtained by evaporation-induced self-assembly (EISA), followed by a suitable thermal treatment. In particular, to the best of our knowledge the present study for the first time succeeded to

obtain mesostructured, crystalline CeO_2 films with a well-defined mesopore shape and an overall volume fraction of ca. 30-40 % porosity. The successful preparation of these materials is attributed to the use of the KLE polymer showing several significant advantages compared to the Pluronics polymer family. First, the mesostructure formation during dip-coating proceeds substantially faster[3], thus helping to stabilize the fragile mesohybrid during the metal chloride hydrolysis and, later on, the condensation. Second, the KLE polymer is thermally more stable, thus maintainig the mesostructure even beyond the onset of metal oxide crystallisation.

CeO_2-ZrO_2 mixed oxides show even a smaller primary crystal size and a better preservation of the original template structure. This result is in excellent agreement with recent work on CeO_2-ZrO_2 and also demonstrates the absence of surface/thin film effects in the generation of these solid solutions.[11] In particular, it is important to note that the addition of ZrO_2 significantly improves the thermal stability of the films up in a technologically quite appealing region. Future work has to focus on the application of these films for catalytic applications. Also, these films will be the subject to more detailed studies addressing the accessible mesoporosity, lattice defects and the exact redox state of the CeO_2.

References

1 a) D. Grosso, G. J. D. A. Soler-Illia, E. L. Crepaldi, F. Cagnol, C. Sinturel, A. Bourgeois, A. Brunet-Bruneau, H. Amenitsch, P. A. Albouy and, C. Sanchez, *Chem. Mater.,* 2003, **15**, 4562. b) E. L.Crepaldi, G. J. D. A. Soler-Illia, D. Grosso, F. Cagnol, F. Ribot, and C. Sanchez, *J. Ame. Chem. Soc.,* 2003, **125**, 9770. c) G. J. D. A. Soler-Illia, E. L. Crepaldi, D. Grosso and C. Sanchez, *Curr. Op. Coll. Interf. Sci.,* 2003, **8**, 109. d) E. L.Crepaldi, G. J. D. A. Soler-Illia, D. Grosso and C. Sanchez, *New J. Chem.,* 2003, **27**, 9.

2 A. Thomas, H. Schlaad, B. Smarsly and M. Antonietti, *Langmuir,* 2003, **19,** 4455.

3 B. Smarsly, D. Grosso, D.; T. Brezesinski, N. Pinna, C. Boissière, M. Antonietti and, C. Sanchez, *Chem. Mater.,* 2004, **16**, 2948-2952.

4 D. Grosso, C. Boissière, B. Smarsly, T. Brezesinski, N. Pinna, P. A. Albouy, H. Amenitsch, M. Antonietti, C. Sanchez, *Nature Materials,* 2004, in press.

5 C. J. Brinker, Y. F. Lu, A. Sellinger and H. Y. Fan *Adv. Mater.,* 1999, **11**, 579-585.

6 a) M. Lundberg, B. Skarman, F. Cesar and L. Reine Wallenberg, *Microporous and Mesoporous Materials,* 2002, **54**, 97-103. b) D. Terribile, A. Trovarelli, J. Llorca, C. de Leitenburg and G. Dolcetti, *J. Cat.,* 1998, **178,** 299–308. c) J. A. Wang, J. M. Dominguez, A. Montoya, S. Castillo, J. Navarrete, M. Moran-Pineda, J. Reyes-Gasga and X. Bokhimi, *Chem. Mater.,* 2002**, 14***,* 4676-4683. d) D. M. Lyons, K. M. Ryan and M. A. Morris, *J. Mater. Chem.,* 2002, **12**, 1207-1212.

7 a) M. Yashima, M. Kakihana and M. Yoshimura, *Solid State Ion*., 1996**, 86**, 1131-1149. b) D. Terribile, A. Trovarellia, J. Llorca, C. de Leitenburg and G. Dolcettia, *Catalysis Today,* 1998, **43**, 79-88. c) P. Fornasiero, G. Balducci, R. DiMonte, J. Kaspar, V. Sergo, G. Gubitosa, A. Ferrero and M. Graziani, *J. Catalysis*, 1996, **164,** 173–183.

8 a) S. Logothetidis, P. Patsalas and C. Charitidis, *Mater. Sci. Eng. C*, 2003, **23,** 803–806. b) P. K. Mahendra, Y. Ichihashi , K. Kuraoka, W.-J. Shen and Y. Matsumura, *Catalysis Lett.,* **88**, 83-87. c) P. Jasinski, T. Suzuki and H. U. Anderson, *Sensors and Actuators B*, 2003, **95** 73–77. d) R. Ramamoorthy, P. K. Dutta and S. A. Akbar, *J. Mater. Sci.,* 2003, **38** 4271–4282. e) D. Perednis and L. J. Gauckler, *Solid State Ionics* 2004, **166**, 229–239. f) P. Patsalas, S. Logothetidis, L. Sygellou and S. Kennou, *Phys. Rev. B,* 2003, **68**, 035104. g) N. Izu, W. Shin, I. Matsubara and N. Murayama, *Sensors and Actuators B*, 2003, **94**, 222–227.

9 a) J. Kaspar, P. Fornasiero and M. Graziani, *Catal. Today,* 1999, **50**, 285–298. b) A. Trovatelli, *Catal. Rev. Sci. Eng.,* 1996, **38**, 439–520. c) J. Kaspar, P. Fornasiero and N. Hichkey, *Catal. Today* 2003, **77**, 419–449.

10 E. L. Crepaldi, G. J. D. A. Soler-Illia, A. Bouchara, D. Grosso, D. Durand and C. Sanchez, *Angew. Chem. Int. Ed.* 2003, **42**, 347.

11 A. S. Deshpande, N. Pinna, P. Beato, M. Antonietti and M. Niederberger, *Chem. Mater.,* 2004 **16**, 2599-2604.

The Generation of Mesoporous CeO_2 with Crystalline Pore Walls Using Novel Block Copolymer Templates

T. Brezesinski[a], B. Smarsly[a,*], M. Groenewolt[a], M. Antonietti[a], D. Grosso[b], C. Boissière[b] and C. Sanchez[b]

[a] Max Planck Institute of Colloids and Interfaces, Am Mühlenberg 1, D-14476 Potsdam Golm (Germany), smarsly@mpikg.mpg.de

[b]Laboratoire Chimie de la Matière Condensée, Université Pierre et Marie Curie, 4 place Jussieu 75252 Paris Cedex 5,France

Mesoporous thin films of cerium oxide with spherical pores and crystalline pore walls were prepared using evaporation-induced self-assembly (EISA), taking advantage of a novel type of block copolymer. The films were characterized by various techniques, in particular electron microscopy, small-angle x-ray scattering (SAXS), wide-angle x-ray scattering (WAXS) and krypton sorption. The evaluation of SAXS in symmetric reflection allowed for a quantification of the pore dimension perpendicular to the film and revealed a significant degree of ellipsoidal deformation of the pores during the crystallisation. Detailed WAXS studies as a function of the temperature showed that the crystallite size can be finely tuned as a function of the heat treatment.

1. INTRODUCTION

The fabrication of porous transition metal or rare earth oxide thin films has been studied by many groups due to their diverse properties (e.g. optical, electronic, magnetic) [1]. Among these materials ceria is of particular interest for a wide range of applications. It is known that ceria is chemically and thermally extraordinarily stable, and therefore it is of interest in ceramic membranes for catalysis and sensing and as catalyst support. Furthermore, ceria has just one polymorph (cubic fluorite structure) and can easily switch between Ce^{4+} and Ce^{3+} simply by balancing the charge with oxygen vacancies, which makes the system promising for redox processes (e.g. high temperature solid oxide fuel cells).

There are several studies reporting the fabrication of porous crystalline ceria. However, usually the structure (mesoscale) undergoes a severe breakdown throughout the final crystallization step [6], leading to rather ill-defined porosity without controlled nanocrystallinity in the pore walls in terms of the spatial distribution and the size of the oxide nanocrystals.

To the best of our knowledge, no well-defined mesoporous structures of pure crystalline CeO_2 thin films have been reported by other groups so far. Our group has managed to obtain mesoporous titania and diverse perowskite thin films, taking advantage of evaporation-induced self-essembly (EISA), using a special type of diblock copolymer template [3-5]. Based on these studies, very recently we have succeeded to prepare mesoporous ceria thin

films, starting from a solution of cerium chloride [6]. The present paper focuses on an improved preparation of thin CeO_2 films with a long range order of mesopores, addressing the crystallisation of the nanoparticles. Furthermore, small-angle scattering in symmetric reflection (SR SAXS) is applied to determine the mesopore size and degree of deformation, while SAXS in asymmetric reflection is used to quantify the degree of preferred orientation of the mesostructure with respect to the substrate.

2. EXPERIMENTAL

Cerium(III)chloride hydrate was used as starting inorganic precursor. Poly(ethylene oxide)- based block copolymer ($H(CH_2CH_2CH_2(CH)CH_2CH_3)_{89}$ $(OCH_2CH_2)_{79}OH$), referred to as "KLE" (ref. 3), was used as structural-directing agent. The initial solution was prepared as follows. The appropriate amount of "KLE" (80 mg) dissolved in Ethanol (3 ml) was added dropwise into an ethanolic solution (6 ml) of $CeCl_3{*}7H_2O$ (600 mg) and H_2O (0.2 ml). The resulting sol was stirred for 1h at room temperature. The thin films were prepared at 273 K by dip-coating silicon substrates at constant withdrawal rate (6 mm/s) and constant relative humidity (15-20 %). A fast transfer to a chamber at 200 °C directly after dip-coating is indispensable to prevent local crystallisation of $CeCl_3{*}7H_2O$. The desired crystalline, mesoporous CeO_2 films were obtained through controlled crystallisation by heating with a ramp of 5 °C/min under air up to 650 °C.

Small- and wide-angle x-ray scattering were performed using a D8 diffractometer from Bruker instruments (wavelength 0.154 nm). Transmission electron microscopy (TEM) images with high contrast were taken with a Zeiss EM 912Ω at an acceleration voltage of 120 kV. The surface area (BET) was determined by Krypton sorption at 77 K using Autosorb-1 from Quantachrome instruments.

2. RESULTS AND DISCUSSION

2.1. Transmission Electron Microscopy

Fig. 1 shows a representative TEM image taken from a ceria film calcined at 450 °C. The image clearly reveals the presence of a well-ordered array of spherical mesopores of ca. 8 nm in diameter. Also, it is seen that the degree of mesostructural order is significantly improved compared to our previous formula [6].

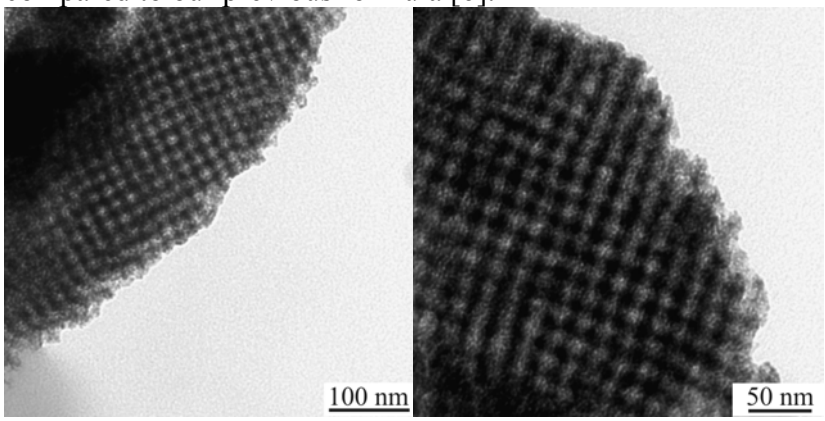

Figure 1. Mesoporous CeO_2 film, heat treated at 450 °C.

3.2. SAXS in symmetric reflection

The ceria films were studied in detail by small-angle x-ray scattering (SAXS) in symmetric reflexion (abbreviated as SR SAXS in the following). The principal experimental setup of SR SAXS is illustrated in Scheme 1. Fig. 2 shows SR SAXS data as a function of the heat treatment. The observed reflections can be assigned as (110) and (220) of a bcc lattice of the mesostructure. It is noteworthy that even at 300 °C still a second order interference is observable, indicating a high degree of regularity. The SR SAXS data were then analyzed in order to determine the pore size and the wall thickness. Due to the preferred orientation of the mesostructure, it is important to mention that the values obtained from this analysis only reflect the geometry in the z-(s_3)-direction, while no information is obtained regarding the lateral dimension.

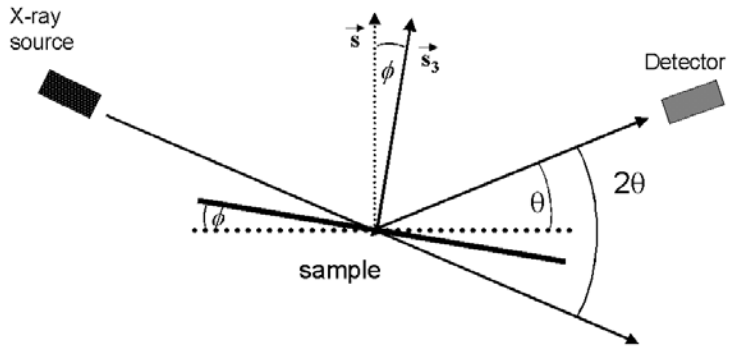

Scheme 1: Schematic representation of SAXS measurements in symmetric and asymmetric reflection (see ref. 7).

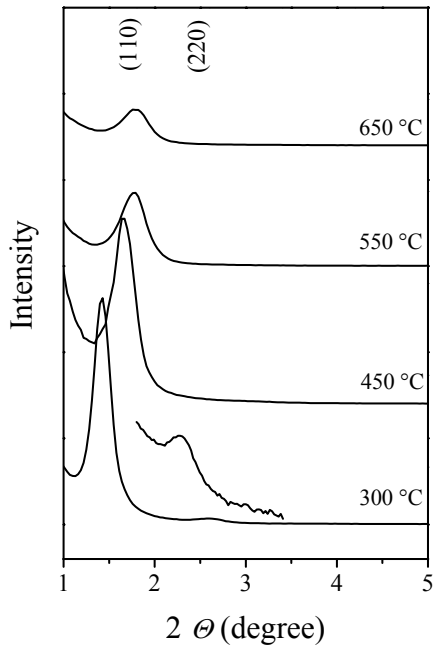

Figure 2. SAXS in symmetric reflection of CeO_2 mesostructured films as a function of the heat treatment temperature.

In general, the underlying idea of our evaluation approach is to fit the experimental data by scattering functions obtained for reasonable structure models, described by geometrical parameters, in particular the average pore radius R_{av}, its variance σ_R, the average long period d_{110}, its variance σ_d and the average stack height L. For the theoretical SAXS of finite stacks of oriented polydisperse spheres we follow a similar approach for lammellar nancomposite thin films and mesoporous powder materials [7,8]. A suitable SAXS approach to take into account polydisperse spheres is similar to the one presented in ref. 8 and given by

$$I_{sphere}(s) = \left(\left\langle \left| F(s) \right|^2 \right\rangle + \left| \left\langle F(s) \right\rangle \right|^2 \left(\left| Z_{1D} \right|^2 (s) - 1 \right) \right) \qquad (1)$$

with $s = 2/\lambda \sin\theta$. $\langle\ \rangle$ stands for number average. For the form factors F we have chosen the approach described in ref. 8, using a gamma distribution for the size distribution of spheres. For the lattice factor Z_{1D}/N we use an approach for a 1D point lattice of finite extention with periodicity d_{110} [7]. If the finite width of the interface between ceria and the micelles/pores cannot be ignored, a suitable approach is given by multiplying eq. (1) by the function $H_z^{\,2}(s) = \exp(-2\pi d_z^2 s^2)$ [7], where d_z is the thickness of the interface boundary. Taking into the absorption correction A and an additive constant background scattering I_B (3D density fluctuations) we obtain for the final fitting curve

$$I_{fit}(s) = k\, A(s)\, \left[I(s)\, H_z^2(s) + I_B \right]. \qquad (2)$$

This expression was additionally corrected for the slit-smearing of our in-house diffractometer.

Fig. 3 shows the SR SAXS data together with an analysis based on eq. 2. Although the data cannot be fitted in terms of a complete coincidence of the experimental data and the theoretical curve, the shape of the curve is reasonably described by our approach. As fitting parameters we obtain for the sample treated at 300 °C (that is prior to template removal) R_{av} = *2.0 nm,* σ_R *=0.5 nm,* d_{110}*= 8.8 nm,* σ_d *= 0.3 nm, L = 40 nm.* For the sample treated at 450 °C, which is indeed mesoporous, we obtain R_{av} *= 1.9 nm,* σ_R *= 0.5 nm,* d_{110}*=7.2 nm,* σ_d *= 0.6 nm, L = 35 nm.*

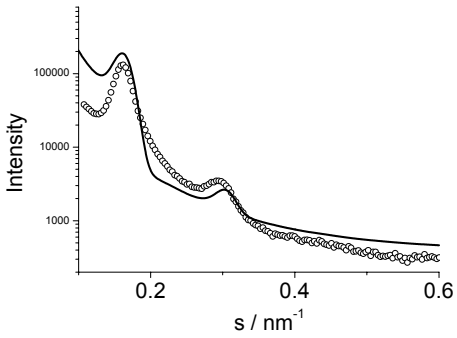

Figure 3. SR SAXS of the sample treated at 300 °C and the corresponding fit (solid line). $s = 2/\lambda \sin\theta$.

The porosity was also studied by Krypton sorption at 77 K. Since we were not able to perform the experiment at 87 K, it was only possible to carry out a BET analysis, but no complete isotherm could be obtained. However, the BET analysis clearly revealed a significant degree of porosity and a surface area of 100-150 m^2/g, taking into account the density of crystalline cerium oxide and an average film thickness of 200 nm. Thereby, it is clearly demonstrated that the spherical pores are indeed accessible.

Interestingly, similar values are obtained for the samples treated at higher temperatures, supporting the finding that mesostructured crystalline ceria films undergo only moderate shrinkage once the matrix is crystalline. In conclusion, the SR SAXS analysis reveals several interesting features. First, the pore size is in marked difference to the apparent pore size as determined from TEM. This discrepancy can be explained by the deformation of the mesostructure during the preparation, especially the heat treatment. The TEM images probably show flake-like parts of the films, observed from the top, while SR SAXS detects the dimensions perpendicular to the substrate. From SR SAXS we obtain a pore "height" (in the direction perpendicular to the film) of ca. 4 nm, while the lateral extention of these ellipsoidal mesopores is ca. 7-8 nm (based on TEM and GISAXS [6], thus indicating a significant degree of deformation.

Aside from the pore sizes and the deformation of the mesopores, a further important structural parameter is the degree of preferred orientation with respect to the substrate. It was demonstrated recently that SAXS measurements performed in so-called "asymmetric reflection" represent an ideal tool to quantitatively determine the degree of preferred orientation. Fig. 4 shows a SAXS curve measured in asymmetric reflection of the film treated at 300 °C, determined at the position of the second interference maximum. A pronounced maximum is seen around $\varphi = 0°$, clearly proving preferred orientation. Furthermore, the degree of preferred orientation is quite high, because the integral width is around 0.05°.

3.2. WAXS analysis

The crystallization process was studied by wide-angle x-ray scattering (WAXS). As already demonstrated in our previous publication, indeed the matrix separating the mesopores consists of an almost fully crystalline framework of ceria. However, the development of crystallinity remained unclear. In order to follow the crystallization, WAXS analysis was performed at various temperatures (Fig. 5).

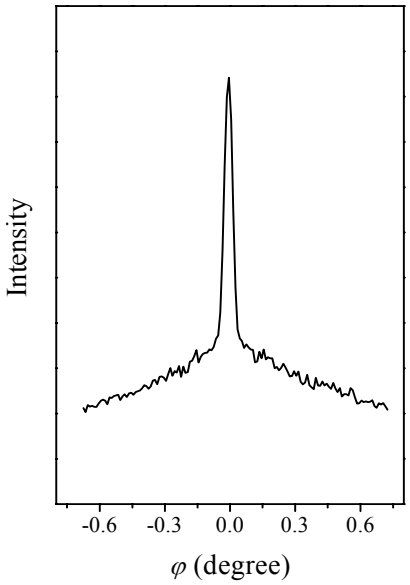

Figure 4. SAXS in asymmetric reflection of a cerium oxide film treated at 300 °C.

Already at 300 °C diffuse maxima appear, indicating a semicrystalline framework of small ceria nanoparticles of ca. 3 nm in size, as determined from the Scherrer equation. With increasing heat treatment temperature, the crystallite size increases almost linearly up to 7 nm at 650 °C (Fig. 6). It is important to emphasize that, in spite of the significant increase in the crystallite size, the material is still mesostructured, i.e. no mesostructural collapse occurs. In particular, these results demonstrate that the crystallite size can be finely tuned between 3 nm and 7 nm, keeping the mesopores intact. This finding goes well with our previous studies on titania, suggesting that the use of the KLE polymers enables the formation of larger nanocrystallites compared to previously polymer templates such as Pluronics.

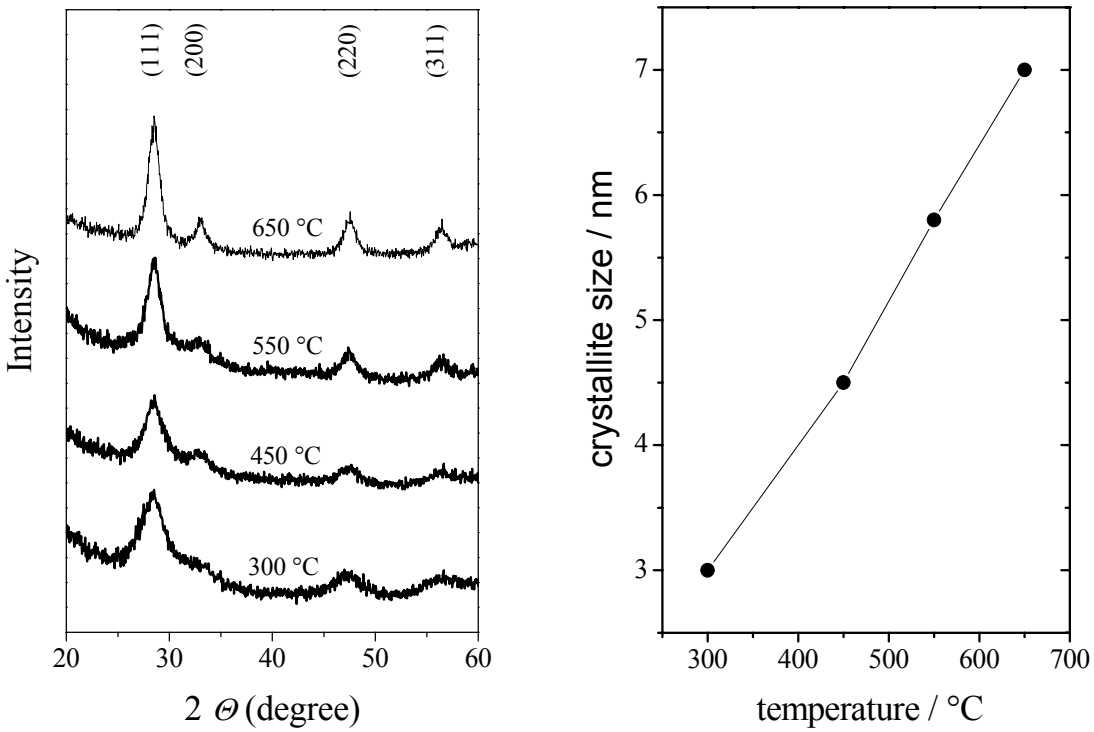

Figure 5. A: WAXS patterns of a cerium oxide mesostructured film as a function of the heat treatment temperature. B: Dependence of the crystallite size, determined by the Scherrer equation, as a function of the heat treatment temperature.

CONCLUSIONS

A simple EISA routine was shown to produce highly ordered mesoporous ceria thin films (thickness ca. 200 nm) with the walls between the mesopores highly crystalline, as revealed by WAXS and, recently, also by high-resolution TEM [6]. While in our recent study [6] the mesopore structure was similar to a disordered arrangement of spherical mesopores, we have optimized this formula to obtain a well-defined bcc mesopore morphology, showing even a second order interference in SAXS in symmetric reflection, thereby significantly exceeding previous studies in the mesostructural regularity of mesoporous, crystalline ceria. The main improvement was achieved by optimiziting the ratio between the block copolymer and cerium oxide.

In addition, the present study confirms our previous works on mesoporous crystalline titania films [1,4]. It was concluded that the choice of a suitable template such as the one used in the present study significantly improves the quality of the films in terms of the crystallinity and the mesostructural stability. In particular, the generation of substantial wall thickness of ca. 5 nm requires the use of sufficiently large block copolymers, also showing a sufficiently high hydrophobic contrast between the two blocks. This interpretation is fully supported by the present study, in that the crystallite size can be tuned between 3 nm and 7 nm by a suitable heat treatment, without destroying the mesostructure. Further work will be devoted to an improvement of the analysis of SR SAXS data of mesoporous thin films to obtain more accurate for the pore sizes, etc. Also, it is attempted to bring together the quantification of SR SAXS and physisorption, in particular krypton sorption.

REFERENCES

1 a) D. Grosso, G. J. D. A. Soler-Illia, E. L. Crepaldi, F. Cagnol, C. Sinturel, A. Bourgeois, A. Brunet-Bruneau, H. Amenitsch, P. A. Albouy and C. Sanchez, Chem. Mater., 15 (2003) 4562. b) E. L.Crepaldi, G. J. D. A. Soler-Illia, D. Grosso, F. Cagnol, F. Ribot, and C. Sanchez, J. Ame. Chem. Soc., 125 (2003) 9770. c) G. J. D. A. Soler-Illia, E. L. Crepaldi, D. Grosso and C. Sanchez, Curr. Op. Coll. Interf. Sci., 8 (2003) 109. d) E. L. Crepaldi, G. J. D. A. Soler-Illia, D. Grosso and C. Sanchez, New J. Chem., 27 (2003) 9.

2 a) M. Lundberg, B. Skarman, F. Cesar and L. Reine Wallenberg, Microporous and Mesoporous Materials, 54 (2002) 97. b) D. Terribile, A. Trovarelli, J. Llorca, C. de Leitenburg and G. Dolcetti, J. Cat., 178 (1998) 299. c) J. A. Wang, J. M. Dominguez, A. Montoya, S. Castillo, J. Navarrete, M. Moran-Pineda, J. Reyes-Gasga and X. Bokhimi, Chem. Mater., 14 (2002) 4676. d) D. M. Lyons, K. M. Ryan and M. A. Morris, J. Mater. Chem., 12 (2002) 1207.

3 A. Thomas, H. Schlaad, B. Smarsly and M. Antonietti, Langmuir, 19 (2003) 4455.

4 B. Smarsly, D. Grosso, D.; T. Brezesinski, N. Pinna, C. Boissière, M. Antonietti and C. Sanchez, Chem. Mater., 16 (2004) 2948.

5 D. Grosso, C. Boissière, B. Smarsly, T. Brezesinski, N. Pinna, P. A. Albouy, H. Amenitsch, M. Antonietti and C. Sanchez, Nature Materials, 2004, in press.

6 T. Brezesinski, M. Groenewolt, N. Pinna, M. Antonietti, B. Smarsly, New Journal of Chemistry, in press.

7 W. Ruland and B. Smarsly, J. Appl. Cryst. 37 (2004) 575.

8 B. Smarsly, C. Göltner, M. Antonietti, W. Ruland, E. Hoinkis, J. Phys. Chem. B 105 (2001) 831.

SAXS analysis of mesoporous model materials: a validation of data evaluation techniques to characterize pore size, shape, surface area, and curvature of the interface

BERND SMARSLY*, MATTHIJS GROENEWOLT, MARKUS ANTONIETTI

Max Planck Institute of Colloids and Interfaces, Am Mühlenberg 1,

D-14476 Potsdam-Golm

smarsly@mpikg.mpg.de, Tel. +49 – 331 567 9508, Fax: +49 – 331 567 9502

Abstract

Two model mesoporous silicas with cylindrical and spherical mesopore architectures were analyzed with SAXS, using evaluation principles introduced by Ruland. The comparison with sorption measurements and transmission electron microscopy revealed that suitable SAXS analysis methods are a very precise technique to determine a whole range of structural properties of two-phase systems with mesostructure, namely the characteristic size of both phases, the surface area, the curvature of the phase boundary, and – applying the so-called κ- ι formalism - even the type of mesophases under consideration.

Keywords

SAXS, Porod-law, curvature, kappa-iota, silica, mesopores

Introduction

In the recent decade, mesostructured materials with structural units on the nanometer scale have attracted a great deal of attention, both because of potential applications and the fundamental interest in the special properties of matter (confinement effects), etc. [1]. Among the most prominent representatives of this new class of materials are the mesophases of block copolymers, nanoparticulate composites, and mesoporous materials. Another way which leads to an illustrative understanding of the partial exceptional physical properties of such materials is to point to the large internal interfacial area, amounting easily up to 1000 m^2/g, i.e. such material can be regarded as interface-dominated. Most of the macroscopic properties are therefore in delicate dependence on the size and shape of the constituting objects (pores, particles or aggregates) and their interfacial properties (especially energy and curvature), and suitable characterization techniques are inevitably needed.

The most important analytical techniques for the structural characterization of mesostructured materials are transmission electron microscopy (TEM), small-angle scattering (SAXS, SANS for x-rays and neutron, respectively) and – for porous materials- physisorption, and many of papers in the last decade have shown that analysis of such materials is incomplete without one of them. However, it is also regularly observed that a thorough TEM analysis suffers from the instability of soft matter in the electron beam, which restricts special resolution to some nanometers, and that sorption measurements are plagued by unspecific adsorption (e.g. on the outer grain) and the inaccessibility of significant parts of the pore system.

In conclusion, SAXS often represents the only feasible technique for structural analysis. Up to now, SAXS is mostly used in the most simple mode: if several well-defined interference maxima ("Bragg peaks") are observed, the data are evaluated in terms of basic concepts of classical crystallography, that is the assignment of the corresponding space group and unit cell content. If SAXS data lack pronounced features, the data are mostly not further used. This is a waste of accessible information, as it was already demonstrated decades ago by Méring/Tchoubar and by Ruland that for various materials of different chemical nature the concept of the chord-length distribution *g(r)* provides a suitable tool for a reasonable characterization of nanostructured materials, especially for those lacking a high degree of mesoscopic order [2-4]. The approaches developed by Ruland were shown to be suitable for the SAXS evaluation of semicrystalline polymers with lamellar superstructures [5], microporous carbon [6-8], block copolymers [9] and polymer fibers [10,11]. The calculation of *g(r)* from the raw scattering data is however not too simple, but Burger and Ruland [12] and later Smarsly [13] developed a novel and stable evaluation approach, which is based on the regularization of SAXS data by suitable analytical functions.

Beside characteristic length information, such as the thickness of both subphases, *g(r)* also contains important topological information. It was shown by Kirste and Porod as early as 1951 that the serial expansion of the "characteristic function" $\gamma(r)$ can reveal the absolute surface area, a measure of the curvature of the interface, plus potentially the genus of the mesostructure [14,15].

By normalizing those quantities to the characteristic length scales (also accessible from *g(r)*), Burger et al. generalized this principle to the κ-ι concept where even on the base of one single broad scattering peak the scale invariant relative interface area ι and the scale invariant relative curvature κ could be determined

[16]. As usually any κ-ι couple corresponds to one specific mesophase structure (except at phase boundaries), this principle inevitably allowed the determination of phase structure on the base of ill-defined scattering curves. Grafically spoken, the κ-ι concept makes use of the fact that curvature and interface are local properties which quickly relax in their local energetic minima, whereas classical crystallography relies on larger ordered domains the formation of which might even be kinetically hindered.

The κ-ι concept was applied in several recent studies, e.g. on polypeptide-containing block copolymers [17,18], and showed its usefulness, but a strict validation of this method with ideal model materials has not been performed. The accuracy of κ and ι especially depends on a correct evaluation of the asymptotic behavior of SAXS data at large scattering vectors. However, in this region of SAXS curves the scattering intensity is low and affected by several complex scattering effects. The importance of these scattering effects was demonstrated by Ruland in several detailed studies, especially on carbon [19,20] and block copolymers [21-24]. One important factor is the finite transition region between the two phases, leading to a multiplication of the theoretical curve by $H_z^2(s) = \exp(-2\pi^2 d_z^2 s^2)$ with the width d_z of the transition region, where an error function is used to describe the transition [21]. Interdigitation of the two interfaces leads to complex additive scattering contributions I_{inter} [9, 23]. Another important contribution are density fluctuations within the nanodomains (1D, 2D or 3D) leading to an additive scattering contribution [20,21]. As demonstrated by Ruland for the case of block copolymers, all these contributions are important and are to be appropriately considered. Hence, the general asymptotic behavior of SAXS

curves of two-phase systems ("Porod-law", ignoring higher exponents of 1/s for simplicity) for an ideal pin-hole collimation is given by

$$I_{asym}(s) = H_z^2(s)\, a/s^4 + I_{fluct} + I_{inter.} \qquad (1)$$

It is evident that these factors can massively modify SAXS curves in the asymptotic regions and that any numerical analysis which is based on the asymptotic behavior has to carefully take into account these effects in determining κ and ι.

A suitable approach to test the general applicability and practicability of the κ-ι-concept is the SAXS investigation of materials for which the SAXS asymptote in eq. (1) is only weakly influenced by the effects described above. These requirements are quite ideally fulfilled by well-defined mesoporous materials with distinct pore morphologies (e.g. spherical or cylindrical pores), in particular mesoporous silicas. Since these systems consist of pores distributed in compact silica, they can be regarded as almost perfect "two-phase systems". The scattering contribution I_{inter}, which is significant for block copolymers, can be neglected, and the maximum width d_z of the interface between mesopores and silica is on the order of the size of a silica tetrahedron at maximum, i.e. < 0.3-0.4 nm. Furthermore, I_{fluct} is just a constant in case of SiO_2, because silica can be treated as an isotropic glass [20,21]. It has to be pointed out that the aforementioned aspects do not apply for fractal-like silica aerogels with porosities of up to 99.9% because of the absence of real interfaces.

Meanwhile mesoporous silica is accessible in a practically complete range of pore sizes and pore geometries. The process which allows the best adjustment is called "nanocasting" and works via solification of the silica around an organic template with predescribed size and symmetry [25]. It was also shown that this technique

allows adjustment and replication with Angstrom precision, i.e. this is presumably the most appropriate biphasic model system for the validation of high precision SAXS techniques [26].

In the present study, two types of high-quality mesoporous silicas were prepared using nanocasting. A mesoporous silica with cylindrical mesopores of ca. 2.5 – 3 nm on a 2D hexagonal lattice was obtained an ionic-liquid template (called "CYL" in the following) [27]. Using a novel block copolymer, porous silica with spherical mesopores of ca. 13-14 nm in diameter was obtained (sample "SPHERE"), placed on a distorted cubic lattice [28-30]. These materials were studied in detail by nitrogen sorption, TEM and SAXS. The SAXS curves were then analyzed, using the algorithm described in ref. 13, to determine κ and ι. Because of the well-known mesostructures, their theoretical scattering curves and, thus, κ and ι can be predicted based on the lattice parameter, the pore size distribution and the porosity (i.e. volume fraction of pores). These theoretical values were then compared with those obtained from the SAXS analysis to check the validity of the evaluation. Furthermore, the SAXS curves were analyzed by fitting with scattering functions based on a Ruland-approach [31]. It will be validated with our model systems that this approach also allows for a precise determination of pore sizes and a meaningful comparison with the pore sizes obtained from nitrogen sorption and TEM. With such high precision SAXS data, it will then become possible to improve the adaption of sorption theories to such materials.

SAXS of two-phase systems – Theory

In general, the SAXS of a two-phase system is given by the Fourier-Transform of the characteristic function $\gamma(\vec{r})$

$I(\vec{s}) = k \quad \mathbb{F}(\gamma(\vec{r}))$,

where $\vec{s}$ represents the scattering vector with $|s| = \frac{2}{\lambda}\sin(\theta)$ (λ wavelength, 2θ scattering angle). For a two-phase system, the radially averaged characteristic function is given by

$$\gamma(\vec{r}) = \gamma(r) = 1 - \frac{|\vec{r}|S}{4\phi(1-\phi)V} + \ldots = 1 - \frac{r}{l_p} + \ldots,$$

where l_p is the "Porod-length" (average chord-length). l_p is related to the porosity ϕ and the interfacial area S/V via

$$l_p = \frac{4\phi(1-\phi)V}{S}. \qquad (2)$$

l_p is determined by the average segment lengths l_i of the two phases by

$$\frac{1}{l_p} = \frac{1}{l_1} + \frac{1}{l_2} = \frac{1}{\phi_1 l_2} = \frac{1}{\phi_2 l_1}.$$

The latter relationship allows the calculation of pore sizes (independently of a specific geometric model) and wall thicknesses on the basis of l_p.

The Porod-length itself is related to SAXS data via

$\lim_{s\to\infty} s^4 I(s) = \frac{k}{2\pi^3 l_p}$, where k is the Porod invariant.

It was demonstrated by Méring, Tchoubar and Ruland that a suitable approach to describe the pore structure of materials with substantial disorder is the concept of

the "chord-length distribution" *g(r)*, which is proportional to the second derivative of $\gamma(r)$: $g(r) = l_p \gamma''(r)$

$$g(r) = -8\int_0^\infty \left[1 - 2\pi^3 s^4 l_p k^{-1} I(s)\right] \frac{d^2}{dz^2}\frac{\sin(z)}{z} ds, \quad z = 2\pi r s. \quad (3)$$

If the higher orders of *r* in $\gamma(r)$ are taken into account, one obtains

$$\gamma(r) = 1 - \frac{r}{l_p} + \frac{r^3}{8\, l_p}\left(\left\langle H^2 \right\rangle_S - \frac{1}{3}\left\langle K \right\rangle_S\right) + O(r^5) \qquad (4)$$

where $\left\langle H^2 \right\rangle_S$ and $\left\langle K \right\rangle$ are the mean and Gaussian curvature, respectively.

with $H^2 = (c_1 + c_2)^2 / 4 \qquad K = c_1 c_2 \qquad (5)$

where c_i are the principal curvatures.

It is the idea of the κ and ι- phase diagram to classify the various morphologies (lamellar, 2D hexagonal, bcc, etc.) in terms of two normalized parameters, namely the parameter ι (interface area) and κ (curvature) [16]. The only precondition of the applicability, aside from the determination of the Porod asymptote, is the presence of at least one interference with long period *L*.

The parameters are defined by

$$\iota = \frac{S}{V} L$$

$$\kappa = L\sqrt{\left\langle H^2 \right\rangle_S} = L\sqrt{8\, b}\,, \qquad (6)$$

where *b* is the so-called "Kirste-Porod parameter".

It is evident that the parameter κ defined by the latter relationship is only related to the mean curvature, but does not take into account the Gaussian curvature. While for lamellar and cylindrical morphologies (even with undulations) $K = 0$

(Gauss-Bonnet theorem), *K* does not vanish for cubic morphologies. In general, *b* then has to be renormalized by

$b = b^* + \frac{1}{3*8}\frac{4\pi(1-\Gamma)}{\iota V}$, where Γ is defined as the Genus per unit cell. For the renormalization a specific type of unit cell has to be defined. For instance, if two spheres are within the unit cell, Γ = -1, while a single sphere has Γ = 0. The procedure for the renormalization is described in detail in ref. 16 and 32.

In conclusion, the parameters κ and ι can be extracted from *I(s)* (providing *L*) and *g(r)* (providing l_p as the first moment of *g(r)*) and *g'(0)*).

The κ -ι -diagram is shown in Scheme 1, illustrating the values for various morphologies.

Experimental

The SAXS measurements were performed using a CuK_α rotating anode device (Nonius) with 3-pinhole collimation, equipped with a 2D image plate detector.

Nitrogen sorption isotherms were obtained from a Micromeritics ASAP instrument.

Transmission electron microscopy (TEM) images were taken with a Zeiss EM 912Ω at an acceleration voltage of 120 kV. Samples were ground in a ball mill and taken up in acetone. One droplet of the suspension was applied to a 400 mesh carbon-coated copper grid and left to dry in air.

Preparation of sample SPHERE: A solution of the block copolymer (see ref. 25) was prepared by dissolving 100 mg of the block copolymer in 1g of ethanol. 500 mg of the organic silica precursor tetramethoxysilane (TMOS) was added. After

the dropwise addition of 250 mg aqueous hydrochloric acid (pH=2), the sample was treated with ultrasound for 5 minutes, and then the alcohol was evaporated under gentle vacuum. The resulting gel was aged at 60 °C in a drying oven for 10 hours. Finally the dried silica gel was calcined in air at 550 °C for 5 hours.

Sample CYL: In a typical synthesis with C_{16}mimCl as template (see ref. 24), tetramethylorthosilicate (TMOS) was used as the sol-gel precursor. 0.36 g (1.05 mmol) of C_{16}mimCl was dissolved into 2 ml of EtOH, then mixed with 2.0 ml of TMOS under mild magnetic stirring. After homogenization of the mixture, 1.0 ml of aqueous solution of 0.01 M HCl as an acid catalyst was added dropwise. The resulting mixture was stirred for 30 min. Complete gelation was accomplished by leaving the sample in an open flask at room temperatureC_{16}mimCl was removed from the silica by calcination of the sample at 550 ^{o}C for 5 h with a temperature ramp of 100 ^{o}C h^{-1} from room temperature to 550 ^{o}C. The final product was ground into powders for further characterization.

Results and Discussion

1. TEM analysis

TEM images of the samples SPHERE and CYL are shown in Fig. 1. For SPHERE, a highly ordered array of almost close-packed spherical mesopores of ca. 13 nm in diameter is found, and the mesophases domains extend over several hundred nanometers each. Accordingly, the TEM images of CYL indicate regular arrays of long cylindrical mesopores with a pore diameter of ca. 2-3 nm and a length above 100 nm. Thereby, the microscopic study shows that the pore

morphologies are well-defined in each case, being spheres for sample SPHERE and cylinders for sample CYL.

2. Nitrogen sorption

The porosities of CYL and SPHERE were analyzed by nitrogen sorption at T = 77 K (see Fig. 2), the data are summarized in Table 1. For physisorption data of sample CYL, see also ref. 24.

Based on the TEM and SAXS results, the sorption data were evaluated by the BJH approach in case of sample CYL and in terms of a recently developed NLDFT approach in case of sample SPHERE [33]. The sorption data of both materials support the interpretation that they are well-defined mesoporous materials with distinct pore sizes. From the overall porosities, the volume fraction of mesopores was calculated assuming a density of amorphous silica of 2.2 g/ml.

3. SAXS analysis

3.1. SAXS fitting based on model scattering functions

Fig. 3 shows the SAXS curves of the samples CYL and SPHERE. The SAXS pattern of CYL is characteristic of a 2D hexagonal lattice with the interference maxima obeying the theoretical ratio 1: sqrt(3): 2. While weak higher order peaks are visible at higher magnification, the bare SAXS data already indicate a certain degree of lattice distortion. However, the SAXS pattern is ideal for a detailed κ-ι analysis, because the curve shows an extended Porod asymptote at larger s. Similarly, the SAXS curve of SPHERE reveals a sequence of several interference maxima, attributable due to a cubic pore arrangement, while it is not possible to distinguish between an fcc or hcp packing. Also in this case, the asymptote of the SAXS curve is in almost perfect agreement with the Porod law, thus representing

an ideal candidate for a mesoporous model system with spherical pores. The presence of the Porod-law behavior at moderate values of *s* in both cases proves the high quality of these mesosporous silicas in terms of the pore uniformity and, additionally, excludes the presence of significant amounts of undesirable micropores, which are frequently observed in mesoporous materials and which would aggravate the SAXS analysis [34,35].

The SAXS data were then fitted using an approach used already previously by Ruland [31,34] for the evaluation of SAXS data of mesostructured materials, constituted of objects with a finite size distribution ("polydispersity"), placed on a certain lattice (cubic, 2D hexagonal etc.)

$$I(s) \propto \left(\left\langle \left| F(s) \right|^2 \right\rangle + \left| \left\langle F(s) \right\rangle \right|^2 \left(\frac{\left| Z \right|^2}{N}(s) - 1 \right) \right) \qquad (6)$$

F are the form factors of the corresponding objects (spheres, cylinders) and $\frac{\left| Z \right|^2}{N}$ is the lattice factor. For $\frac{\left| Z \right|^2}{N}$, Ruland developed suitable approaches to include the effects of both lattice distortions and finite domain sizes. $\langle\ \rangle$ stands for the number average of the object sizes. While this expression corresponds to the so-called "Laue-scattering" in general, it was Ruland who developed suitable evaluation procedures for the SAXS of mesoscopic materials and applied them to mesoscopic materials such as block copolymers [31] and mesoporous materials [34]. The principal idea is to fit experimental SAXS data by eq. 6, using physically meaningful parameters such as the average diameter $\overline{R}$ of the objects, its variance σ_R, the average lattice parameter $\overline{a}$ and its variance σ_a. Also, it should be emphasized that Ruland developed suitable approximations, faciliting the computational implementation of the polydisperse form factors *F* [22]. Fig. 4

shows the evaluation of the SAXS of SPHERE using eq. 6, similar to ref. 31 and ref. 34, using an fcc lattice for $\frac{|Z|^2}{N}$ and Lorentz profiles for the shape of the interferences. Since the TEM study indicated a large size of the mesostructured domains, it was assumed that the integral width of the interferences is only determined by lattice imperfections, thus increasing with *s* (see the procedure described below for CYL). It has to be pointed out that the fitting is similarly good using an hcp lattice model. It is clearly seen that the approach in eq. 6 is able to describe the experimental data reasonably over the full range of scattering vectors in terms of a system of spherical pores with finite size distribution, providing a pore diameter of 13.9 nm and σ_R = 0.2 nm. For the interferences of the lattice factor Lorentz profiles were used with $\bar{d}_{111}$ = 17 nm and a variance σ_{111} = 0.3 nm. Evidently, this analysis is in excellent agreement with the sorption analysis, thereby proving the applicability of the approach.

A comparable approach was used to evaluate the SAXS data of sample CYL. In this case, it has to be taken into account that 2D hexagonal array of cylinders is anisotropic, thus requiring the calculation of the radial average for the SAXS of such mesopores. If I_2 denotes the SAXS in the plane s_{12} (perpendicular to the cylinder axis), for sufficiently long cylinders the radially averaged SAXS is given by

$$I(s) \propto \frac{1}{s} I_2(s) .$$

Hence, *I(s)* can be calculated similarly to eq. 6, using expressions for the form factors according to ref. 14. Compared to sample SPHERE, the interferences are separated more distinctly. For the lattice factor, a suitable approach was used to

take into account that the integral with of the reflections is determined both by the finite domain size and also lattice distortions: for the shape of the interferences I_{hk} constituting we have chosen

$$I_{hk}(sj) = \frac{B_{hk}(s_j)}{B_{hk}(s_j)^2 + \pi^2 s^2},$$

and the integral width B_{hk} of the interferences at $s = s_j$ was calculated by

$$B_{hk}(s_j) = \frac{1}{d_{10} N} + s_j^2 \pi^2 \sigma_{10}^2 / d_{10}^3,$$

where σ_{10} is the variance of $d_{10} = a$ 2/sqrt(3) with a being the lattice constant of a 2D hexagonal lattice.

It is seen (Fig. 4) that also in this case the approach in eq. 6 provides a reasonable evaluation of the experimental SAXS data ($\bar{a}$ = 3.5 nm, σ_{10} = 0.35 nm), the values for the pore sizes of both CYL and SPHERE are shown in Table 1.

3.2. κ-ι analysis of the SAXS data

In the following, the SAXS data of samples CYL and SPHERE are further analyzed using the concept of the chord-length distribution, aiming at both the verification of pore sizes and the determination of κ-ι curvature parameters. As pointed out, the κ-ι formalism requires the presence of the Porod law and a reasonable statistics in the high s region. The validity of the experiment and the analysis is demonstrated in Fig. 5. The s^4-I- plot levels off to a plateau at large s, after substraction of a small additive background scattering I_{fluct}. Obviously, the rotating anode device used was able to produce scattering data of reasonable intensity also at high s. It is important to note that the strong SAXS intensity at large s is also attributable to the significant electron density contrast between the matrix and the pores, thus further indicating that the present materials are highly

suitable for this kind of analysis. This asymptotic behavior is in good agreement with the ideal Porod asymptote s^{-4}, thus allowing for a meaningful κ-ι analysis.

In principle, the κ-ι formalism is only applicable if $g(0) = 0$, because otherwise $\gamma(r)$ would contain an r^2 term. Without the constraint $g(0) = 0$, for the two samples under study $g(0)$ was slightly positive ($g(0) < 0.01$). Within the margin of errors, it was therefore justified to assume $g(0) = 0$ to allow for the calculation of κ. Fig. 6 shows the chord-length distribution $g(r)$ of sample SPHERE, obtained from the algorithm in ref. 13. It is seen that the first maximum at $r = 6.4$ nm is attributable to the pore wall thicknesss, which is in reasonable agreement with the value obtained from the lattice parameter and pore size from the SAXS fitting in section 3.1. If the second maximum is interpreted as originating from the mesopores themselves, one obtains a mesopore size of ca. 12.5 nm, which is in relatively good agreement with the analysis shown above. Hence, it is even possible to extract meaningful pore sizes from $g(r)$ itself, if the two contributions are separable. In this context, it has to be emphasized that the determination of mesopore sizes above 10 nm by physisorption can still have an error of 20%.

In the following, we are mainly interested in the κ-ι.analysis. As described recently, the Porod length l_p (which is required for the determination of κ and ι.) can be obtained with good precision as the first moment of $g(r)$ based on ref. 13. On the contrary, κ (determined from $g'(0)$) might be more heavily affected by numerical uncertainties. In the present case, $g'(0)$ was obtained directly from $g(r)$ by determining the slop of at $r = 0$. Based on this procedure, for sample SPHERE we obtain $\kappa = 3.3 \pm 0.5$ after renormalization for an fcc lattice and $\iota = 2.6 \pm 0.2$. If the renormalization is not carried out, κ has an unrealistically small value. It was

pointed out by Burger that this procedure provides a suitable criterion to exclude other morphologies (cylindrical) [16]. Taking into account the consideration concerning the mean and average curvature, as pointed out in ref. 16, these values correspond to a cubic phase in the κ-ι diagram and strongly deviate from any other pore structure, which is in agreement with TEM and the aforementioned SAXS analysis. However, based on the renormalization of the Kirste-Porod parameter according to ref. 16, it is not possible to unambiguously determine the nature of the cubic phase (bcc, fcc, hcp), because a major uncertatinty originates from the numerical determination of *g'(0)*.

In order to obtain theoretical values for κ and ι for sample SPHERE, first these two values were theoretically calculated assuming monodisperse spheres and an fcc/hcp lattice without distortion, based on the average size of the spheres and the lattice parameter. From this simple calculation, we obtain ι = 0.8 and κ = 3.1. Evidently, especially the ι deviates significantly from the values obtained from *g(r)*. In order to take into account the polydispersity and the lattice distortions, the fitting curve in Fig. 4 was numerically transformed to the corresponding *g(r)*, which was then evaluated as described above to obtain κ and ι.. By this procedure, the effects of polydisperse pores and lattice disorder on κ and ι were automatically taken into account. Interestingly, the theoretical *g(r)* obtained in this way differs slightly at r < 20 nm in the general shape of the curves. These differences might be due to fine deviations of the real mesopores from a perfectly spherical shape. The corresponding values for κ and ι are listed in Table 2. Obviously, a reasonable agreement is observed with the experimentally determined values, showing a deviation of only ca. 10-15%. Therefore we speculate that the

aforementioned deviation in κ assuming monodisperse pores could be attributable to the finite polydispersity of the mesopores.

A similar procedure was carried out for sample CYL (see Table 2). Although *g(r)*, calculated from the transformation of the fitted *I(s)* curve in Fig. 3 [13], is slightly different a small *r*, the agreement between both curves is reasonable. The deviation between the curves in the region of the first maximum in *g(r)* can be attributed to uncertainties of the algorithm a large *s* or deviations from a perfect cylindrical shape. Similar to sample SPHERE, already the bare shape of the chord-length distribution allows for a semi-quantitative determination of pore sizes and wall thicknesses. From *g(r)* of sample CYL we obtain a pore size of ca. 2.6 nm (second maximum) and a wall thickness of ca. 1.2 nm, both being in good agreement with the aforementioned SAXS analysis and sorption data.

Summarizing the results of the application of the κ-ι formalism, interesting trends can be observed for the two samples. In both cases, the ι -values are relatively high, indicating higher surface area than theoretically expected. Possible reasons are undulations of the cylinders parallel to the cylinder axis or additional micropores in the matrix. Since the sorption data did not reveal any hint for micropores, we speculate that the cylinders may not be perfectly smooth, but might show certain variations of the cylinder radius along its axis. Similarly, local deformations of the spherical mesopores would contribute to a higher surface area in case of sample SPHERE.

Conclusions

Analyzing the data of two model mesoporous silica with cylindrical and hexagonal symmetry, it was shown that SAXS using evaluation principles introduced by Ruland is a very precise technique to determine a whole range of structural properties of two-phase systems with mesostructure, namely the characteristic size of both phases, the surface area, the curvature of the phase boundary, and – applying the κ- ι formalism- even the type of mesophases under consideration. Comparison of the data determined with SAXS with data of sorption isotherms and electron microscopy gave an almost perfect perfect agreement, thus validating the applied technique also for systems with lower structural definition. It is interesting to note that even the surface areas can be reasonably extracted from the analysis in terms of the concept of chord-length distributions.

We regard this tool to be of extraordinary importance for all nanocomposite materials where application of electron microscopy is restricted, e.g. for beam sensitive materials or systems with structural elements below TEM resolution.

As the evaluation of sorption data of mesoporous materials in certain ranges of pore size is also heavily under discussion, well defined silica materials fully characterized by SAXS are expected to be of great use as reference standards to improve numerical evaluation processes.

References

1. Antonietti M, Ozin GA (2004) Chem. Eur. J. 10: 29

2. Méring J, Tchoubar C (1968) J. Appl. Crystallogr. 1, 153

3. Tchoubar-Vallat D, Méring J (1965) C. R. Hebd. Seances Acad. Sci. 26:3096

4. Méring J, Tchoubar-Vallat D (1966) C. R. Acad. Sci. Paris 262: 1703

5. Stribeck N, Ruland W (1978) J. Appl. Cryst. 11:535

6. Perret R, Ruland W (1968) J. Appl. Cryst. (1968) 1:308

7. Perret R, Ruland W (1969) J. Appl. Cryst. (1969) 2: 209

8. Perret R, Ruland W (1971) J. Appl. Cryst. (1972) 5: 183

9. Wolff T, Burger C, Ruland W (1994) Macromolecules 27:3301

10. Perret R, Ruland W (1970) 3:525

11. Thüneman AF, Ruland W (2000) Macromolecules 33: 2626

12. Burger C, Ruland W (2001) Acta Crystallographica Section A 57:482

13. Smarsly B, Wolff T, Antonietti M (2002) J. Chem. Phys. 116:2627

14. Porod G (1951) Kolloid Z. Z. Polym. 124: 83; Porod G (1952) Kolloid Z. Z. Polym. 125:108.

15. Porod G, Kirste R. (1962) Kolloid Z. Z. Polym. 184:1

16. Micha MA, Burger C, Antonietti M (1998) Macromolecules 31:5930

17. Schlaad H, Kukula H, Smarsly B, Antonietti M, Pakula T (2002) Polymer 43:5321

18. Schlaad H, Smarsly B, Losik M (2004) Macromolecules 37:2210

19 Ruland W (2001) Carbon 39:232

20. Ruland W (1974) J. Appl. Cryst. 7:383

21. Ruland W (1971) J. Appl. Cryst. 4:70

22. Siemann U, Ruland, W (1982) Coll. Polym. Sci. 260:999

23. Ruland W (1987) Macromolecules 20:87

24. Ruland W (1977) Colloid and Polymer Science 255:417

25 Polarz S, Antonietti M (2002) Chemical Communications 22:2593

26 Smarsly B, Polarz S, Antonietti M (2001) J. Phys. Chem. B 105:10473

27 Smarsly B, Kuang D, Antonietti M (2004) Coll. Polym. Sci. 282:892

28 Thomas A, Schlaad H, Smarsly B, Antonietti M (2003) Langmuir 19:4455

29 Groenewolt, M, Thomas A, Antonietti M (2004) Macromolecules 27:4360

30 Groenewolt M, Antonietti M, Polarz S (2004) Langmuir 20:7811

31 Brandt M, Ruland W (1996) Acta Polymer. 47:1996

32 Micha MA, PhD Thesis, 1997.

33 Ravikovitch PI, Neimark AV (2001) Microporous Mesoporous Mat, 44-45: 697

34 Smarsly B, Göltner C, Antonietti M, Ruland W, Hoinkis E (2001) J. Phys. Chem. 105:831

35 Goltner CG, Smarsly B, Berton B, Antonietti M (2001) Chem. Mater. 13:1617

Table 1: Porosity parameters for the two samples under study. The SAXS surface areas were obtained from eq.

Sample	Pore size (adsorption) [nm]	Pore size SAXS fitting, and variance σ_R [nm]	BET surface area [m^2/g] / SAXS	Pore volume [cm^3/g]	Pore volume fraction ϕ
CYL	2.6	2.8 ± 0.2	1600 / 1450	0.76	0.62
SPHERE	13.8	13.9 ± 0.2	320 / 250	0.59	0.56

Table 2: κ and ι values for the two samples. The κ value for sample SPHERE is normalized for an fcc lattice. The "theoretical" values of the parameters were obtained from transforming the fitted curves in Fig. 4 to *g(r)*.

Sample	$l_{p,exp}$[nm] / $l_{p,theo}$	κ_{exp} / κ_{theo}	ι_{exp} / ι_{theo}	Phase
CYL	0.97 / 1.1	2.7 / 2.8	2.6 / 2.1	2D hex
SPHERE	5.23 / 5.5	3.3 / 3.0	2.4 / 2.2	fcc - hcp

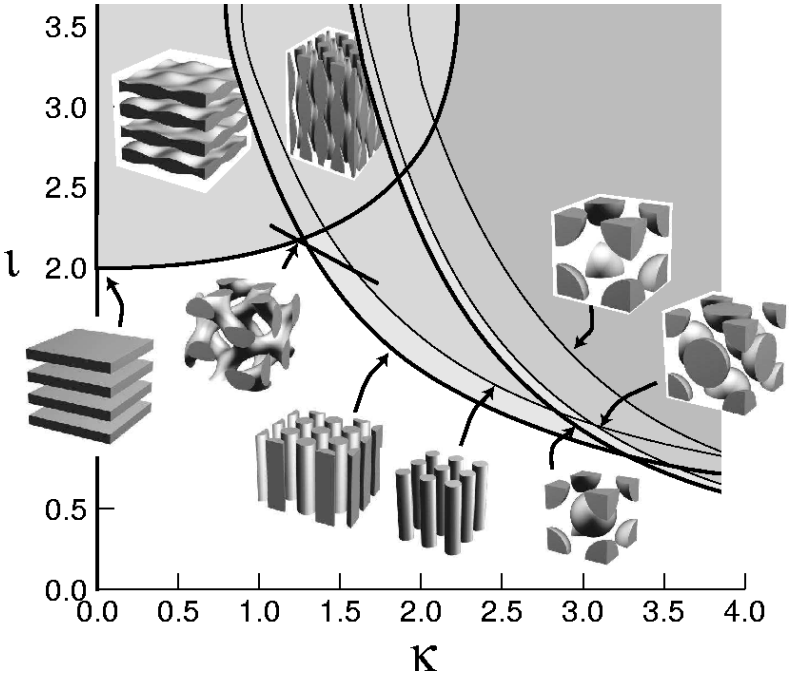

Scheme 1: κ -ι-diagram according to ref. 16.

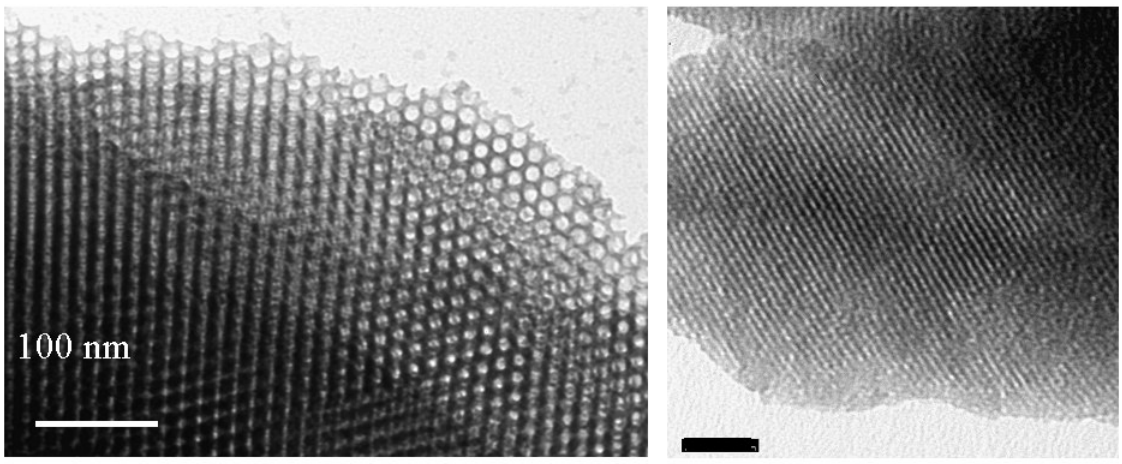

Figure 1: TEM images of SPHERE (left image) and CYL (right image). The scale bar for sample CYL is 25 nm.

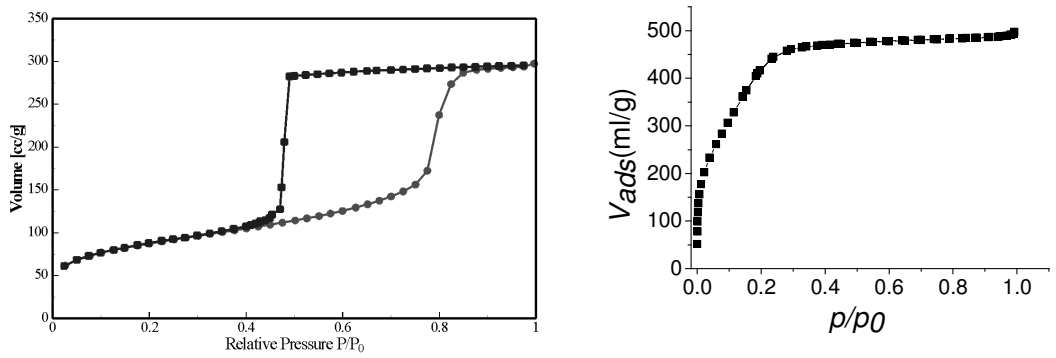

Figure 2: Nitrogen sorption isotherm at 77 K for sample SPHERE (left) and CYL (right).

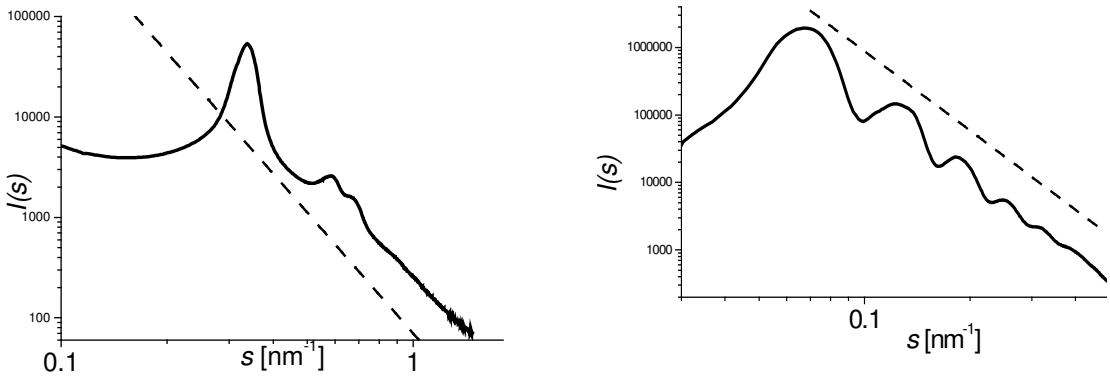

Figure 3: SAXS curves of samples CYL (left) and SPHERE (right). The porod asymptote is indicated by dashed lines in both cases.

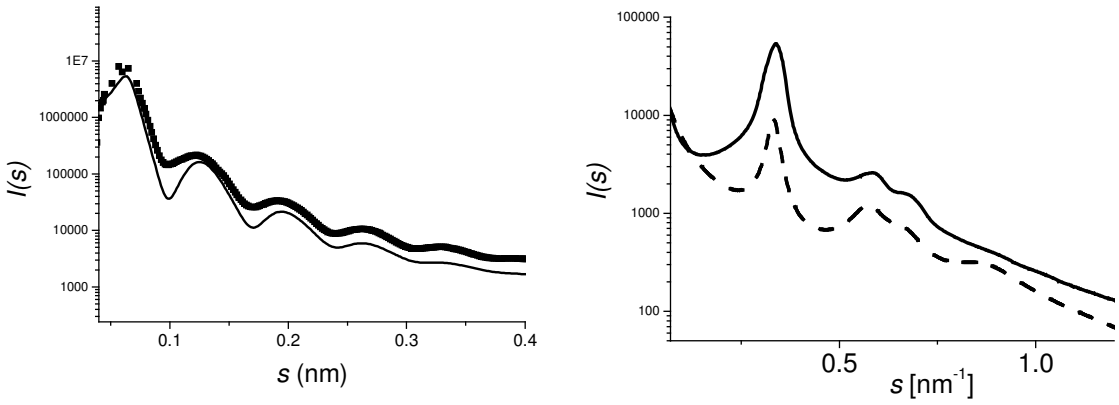

Figure 4: SAXS analysis of sample SPHERE (left) and CYL (right) using eq. 6.

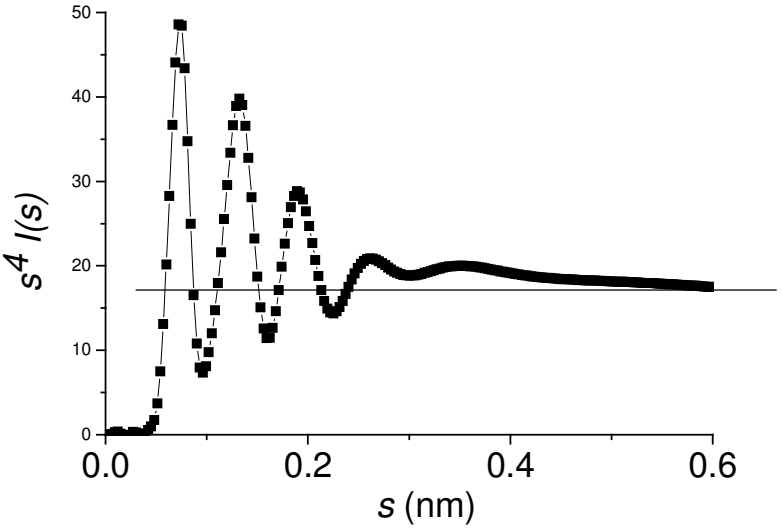

Figure 5: s^4-I plot for sample SPHERE. Squares: experimental data. Solid line: Fitted curve according to the regularization algorithm in ref. 13.

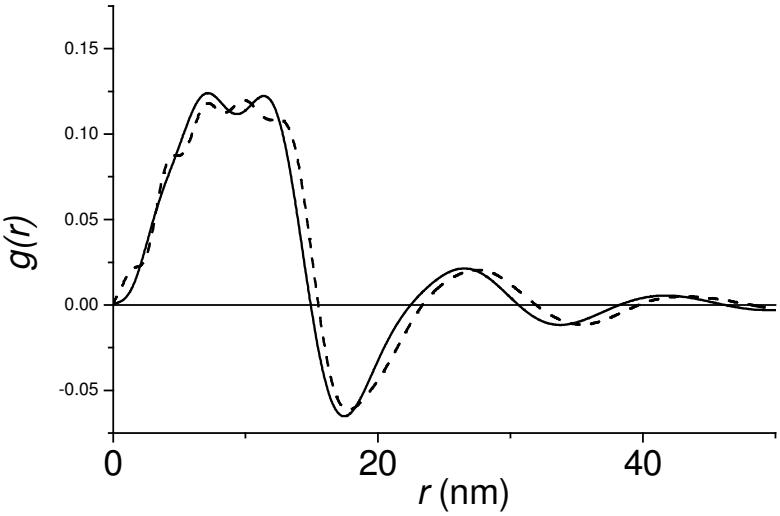

Figure 6: Chord-length distribution *g(r)* of sample SPHERE, obtained from the algorithm in ref. 13 (solid line). Dashed line: *g(r)* obtained as the transform according to eq. 3 of the fitting in Fig. 4.

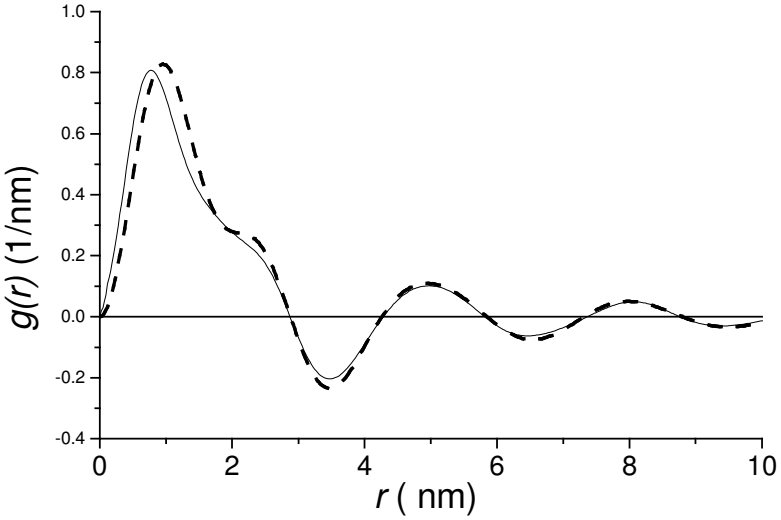

Figure 7: Chord-length distribution *g(r)* of sample CYL (solid line), obtained from the algorithm in ref. 13. Dashed line: *g(r)* obtained as the transform according to eq. 3 of the fitting in Fig. 4.

Nanoparticles and Nanosheets of Aromatic Polyimides via Polycondensation in Controlled Pore Geometries

Matthijs Groenewolt, Arne Thomas, and Markus Antonietti*

Max Planck Institute of Colloids and Interfaces, Research Campus Golm, Am Mühlenberg 1, D-14476 Golm, Germany

Received December 1, 2003; Revised Manuscript Received April 1, 2004

ABSTRACT: Nanoparticles and nanosheets of a high-performance aromatic polyimide can be synthesized via a simple monomer adsorption/polycondensation process inside the pores of specially selected mesoporous silica monoliths. The morphology of the pores directly controls the shape of the resulting polymer nanostructures. About perfect replication was found for both silicas under consideration: one a mesoporous silica with spherical pores with a diameter of 13 nm and another with a lamellar pore morphology with ca. 2 nm thickness. The resulting polymer structures were analyzed by TEM, SFM, thermogravimetric analysis, IR spectroscopy, and X-ray scattering, and the generation of a pure nanocrystalline polyimide was verified.

Introduction

Starting from the invention of mesoporous silica in 1992[1] and due to their availability with a wide range of regular pore sizes and connectivities, experiments to use their pore system as a mold to nanostructure a third type of material have become increasingly popular. Early work of Mallouk[2] started with the replication of zeolithic pore structures into phenol−formaldehyde type resins, whereas Göltner and Attard shaped polystyrene/divinylbenzene resins to mesoporous polymers by silica templated by nonionic surfactants.[3,4] Using appropriate carbon precursor polymers, Ryoo and Joo et al. were able to generate nicely ordered mesoporous carbon replicas by a replication/carbonization sequence.[5,6] Another class of experiments highlighting the potential of such replication techniques was the generation of oriented fibers of a conducting polymer, polyaniline, within the oriented hexagonal channels of a MCM41 host,[7] leading to nanowires with high conductance. Tolbert et al.[8,9] were able to extend this principle to photoluminescent conducting polymers, leading to oriented optoelectronic properties.

In the present paper, we want to make use of this "pore replication" (or "nanoreactor") principle for building nanostructures of another interesting class of polymers, the aromatic polyimides. Those polymers are thermally stable until 500 °C and chemically very inert in most conditions and show extraordinary mechanical properties. They are ideal polymer candidates for a number of nanotechnology applications but are hardly processable.[10] This is why colloidal polyimide particles, either spheres (for the sintering toward coatings or as fillers) or nanorods/nanoplates (as fillers and for composite materials), would be highly attractive. Nanopore replication is currently out of range to become an industrial process, but the resulting structures may serve as models to learn about the behavior of those crystalline/liquid crystalline polymers when single dimensions are reduced toward the scale of a few nanometers.

This is why we report on the synthesis of narrowly distributed polyimide nanospheres with 13 nm diameter and of polyimide nanosheets with 2 nm thickness; polyimide formation will be proven by IR spectroscopy, X-ray analysis, and thermogravimetry, whereas the nanostructure is confirmed by transmission electron microscopy (TEM) and atomic force microscopy (AFM).

Experimental Section

The polyimide was synthesized by polycondensation of *p*-phenylenediamine and pyromellithic dianhydride (benzene−1,2,4,5-tetracarboxylic dianhydride) in DMF. In the first polymerization step a polyamide is formed which can be converted into the polyimide by heating to 300 °C in the second step. The polymerization steps are shown in Scheme 1.

Keeping the reaction spatially confined, all polymerization steps were carried out in the pores of mesoporous silica. The synthesis of the silica materials is described elsewhere.[11,12] Both are synthesized via the nanocasting route,[13] using an organic self-organizing template and a liquid silica precursor. For the silica with spherical pores, poly(ethylene-*co*-butylene)-*block*-poly(ethylene oxide) was used as template. After removal of the template through calcination, a mesoporous silica with spherical pores ordered in a face-centered-cubic (fcc) type arrangement is obtained.

For the silica with regular slit pores, the cholesteric phases of hydroxypropylcellulose were used as a template. Here, the cellulose chains form ca. 2 nm thick layers, which are quite stiff and regularly packed.[11] It is important to note that those slit pores, presumably due to rare pillar defects, do not collapse throughout calcination and removal of the template.

In a typical polymer synthesis a 1.0 M solution of the amine is cooled to −60 °C, and the same amount of a 1.0 M solution of the anhydride in DMF and the monolith of the mesoporous silica are added together simultanously. After 10 min it was assumed that the pores are filled with the monomers and the solvent molecules, and the monolith was taken out of the solution and washed two times by dipping it in pure DMF for 30 s to remove surface adsorbed polymer. After tempering the polymer−silica hybrid at 80 °C for 3 h for polyamide precondensation, the monolith was heated to 300 °C to remove the DMF and to form the polyimide. The silica material was removed with hydrofluoric acid solution (48 wt % in water) at room temperature. A more efficient removal of the silica was observed by grinding the hybrid material before the HF treatment. After removing the silica material, glossy yellow powders of polyimide are obtained.

The obtained polyimide was characterized by TEM, AFM, TGA, WAXS, and IR spectroscopy.

Transmission electron microscopy (TEM) images were taken with a Zeiss EM 912Ω at an acceleration voltage of 120 kV. Samples were ground in a ball mill and taken up in acetone.

10.1021/ma035804o CCC: $27.50
Published on Web 05/11/2004

Scheme 1

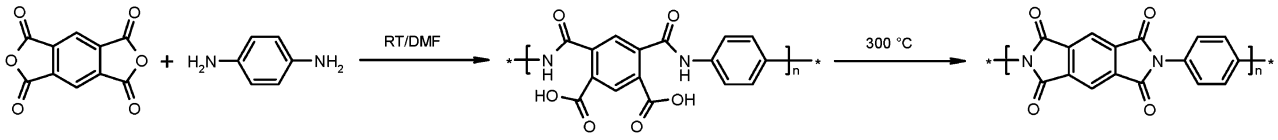

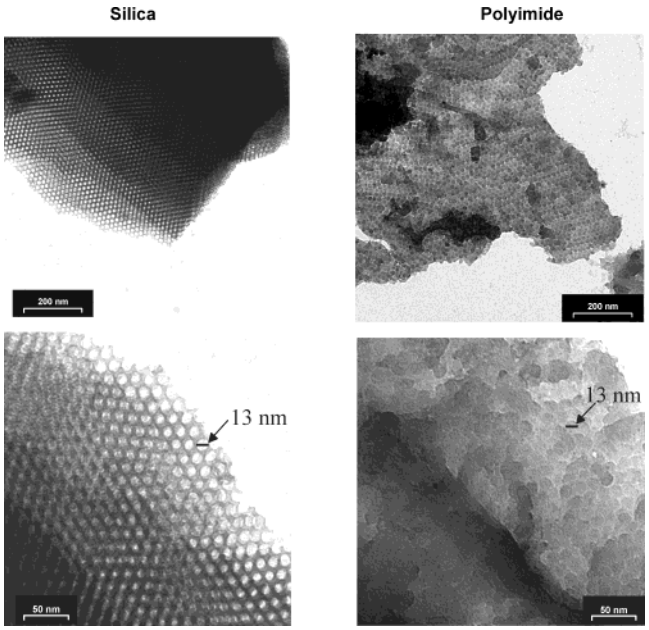

Figure 1. TEM micrographs of the pore structure of the silicas synthesized with block copolymer micelles as template (left) and the resulting polyimide replicas (right).

One droplet of the suspension was applied to a 400 mesh carbon-coated copper grid and left to dry in air.

Tapping mode atomic force microscopy (AFM) images were recorded with a multimode AFM from Vecco Instruments employing Olympus microcantilevers (resonance frequency: 300 kHz; force constant: 42 N/m). The samples were redispersed in water with ultrasonication, and one droplet was spin-coated on a freshly prepared mica substrate.

X-ray data were recorded with a Siemens D8 diffractometer equipped with a Sol X, SI solid-state detector, using Cu Kα radiaton in a symmetric reflection setup.

The IR spectrum was collected with a BIORAD FTS 6000 FTIR spectrometer, equipped with a attenuated total reflection (ATR) setup.

Thermogravimetric analysis has been carried out using a NETZSCH TG209. The heating rate was 20 K/min. The measurements were carried out under an air atmosphere.

Results and Discussion

The described preparation yields in a fine, free-flowing, glossy yellow polymer powder. The nanometric texture of this powder is revealed in TEM experiments. Figure 1 compares the structure of the original template and the structure of the resulting colloidal polyimide replicas. The TEM micrographs clearly indicate that the spherical shape and the diameter of the pores are reflected into polyimide particles of similar size. This provides in general the possibility to tailor the particle diameter and shape by varying the silica matrix only. As shown in the micrographs, the adjacent pore arrangement seems to be reproduced in the packing of the particles. On the basis of these micrographs, it is uncertain whether the particles are separated and only closed-packed (as it could be expected for spherical particles of that small dispersity) or whether the pore interconnections have been replicated, too. As the mesopores of the silica are connected via smaller micropores,[14] which also are involved while filling the pores with the reactants, polymerization in these pores could in principle lead to particles' interconnections. This was for instance found for carbon replicas of SBA15. The diameter of these micropores ($d < 2$ nm) in our case is on the scale of hydrated poly(ethylene glycol) chains; i.e., connections, if they exist, should be constituted of single polyimide chains. The fact that the isolated product is a powder and did not adopt the shape of the monolith indeed proves that those interconnections, if existing, are rare.

To get additional information about the structure of the particles, AFM was used. The AFM pictures indicate regions of isolated particles, beside regions where the particles are close-packed. The dense regions show the standard fcc arrangement of 13 nm sized particles, plus an additional species which sits on top as well as on the steps of the structure. These look like "oily" nanodroplets, being definitely more deformed then the other nanoparticles. We can only speculate about the origin of those species; they might be low molecular weight species trapped in the micropore system which underwent coalescence after removal of the templates or fractured polyimide shells, as delineated below. The "dilute" regions of the AFM pictures show both single spheres as well as smaller aggregates with constant height. A quantitative evaluation of the smaller dots gives a size of 13 ± 0.2 nm, with a height of ca. 1.6 ± 0.3 nm. This is certainly not consistent with a model of massive nanospheres that are fused or connected, as might be inferred from the TEM micrographs in Figure 1. It also must be stated that the morphology of the isolated spheres is in general less defined than the one of the tightly packed counterparts, which indicates a potential problem with sampling, as spheres of different quality are deposited at different places of the film. This is, however, not unusual for polymer colloids. We can, however, excluded impurities and contaminations to be responsible for this effect, as the structures are found in all samples with a rate much higher than we know from the standard impurity artifacts.

A quantitative discussion is somewhat hindered that we have impregnated the monolith with the monomers, which certainly will enrich due to adsorption onto the silica surface, as it was also observed for the anilinium species.[7] As we started with a 1 M solution, the filling of the pores is at least with 14.8 wt % monomer, after condensation revealing at least 14.0 wt % polymer. One explanation for the observed particle size and morphologies could be that the monomers are preferentially located at the pore walls, so that the polymerization occurs mainly on the silica surface. This process would lead to hollow polyimide particles with a minimal molecular weight of 101 500 g/mol, a diameter of 13 nm, and a minimal numerical shell thickness of 0.3 nm; this is the cross section of a single PI chain. As we observe the aromatic stacking peak at $2\Theta = 27°$, it can be assumed that the PI chains sit nematically ordered within the surface (Figure 4).

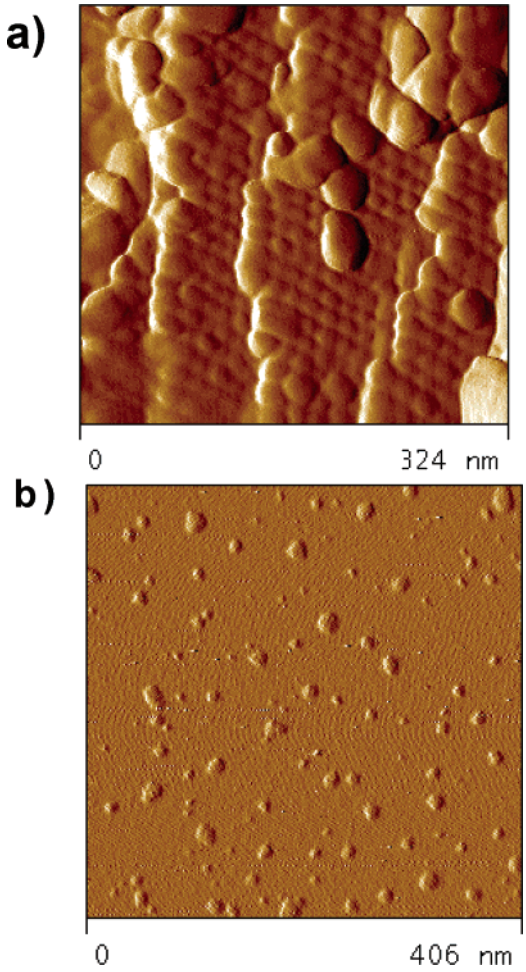

Figure 2. AFM pictures of the spherical polyimide particles: (a) densely packed regions; (b) isolated particles (shown are the amplitude pictures).

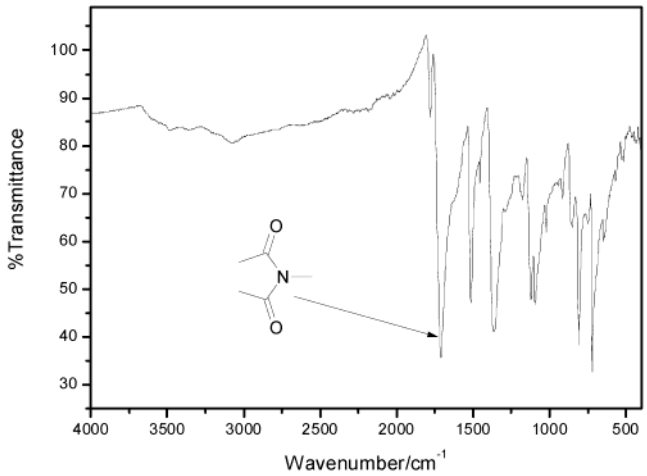

Figure 3. IR spectra of the polyimide particles. Pointed out is the peak of the imide group at 1700 cm^{-1}.

We, however, also cannot exclude the possibility that, at the applied very high temperatures, after removal of the solvent the formed oligomers undergo redistribution and pore condensation in special regions of the silica only. In this case, we would end up with massive spheres and hollow, nonreplicated pores.

The chemical architecture of the polymer can be analyzed by IR spectroscopy of the isolated powder. The IR spectra (Figure 3) show the typical peaks for an aromatic polyimide and confirm the proposed structure. The given aromatic polyimide is expected to be semicrystalline in the bulk. This could be confirmed by WAXS measurements which were carried out to detect the crystallinity in the particles (Figure 4). The WAXS diffractogram also supports the polyimide structure. The found scattering peaks overlap with a reference sample prepared in the bulk. The peaks are slightly broadened, as it is well-known for nanoparticles. The width of the peaks also prevents a more detailed discussion of local arrangements.

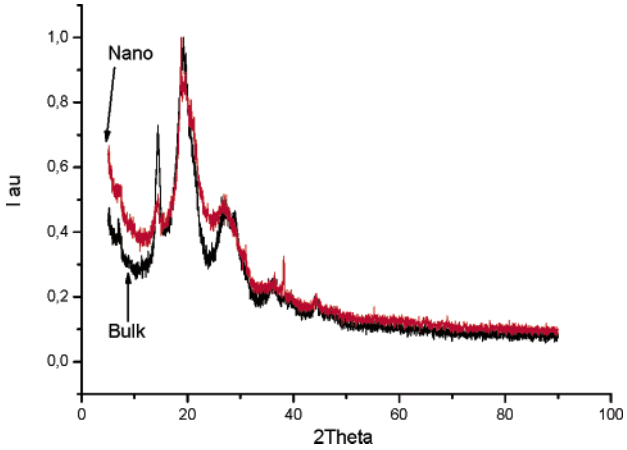

Figure 4. WAXS diffractograms characterizing the crystallinity of the bulk and the nanometer-sized polyimide.

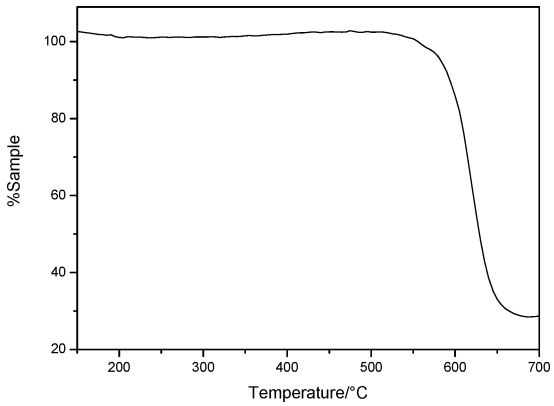

Figure 5. TGA of the polyimide polymerized in a porous silica.

The high-temperature stability of the resulting nanoparticles can be quantified by TGA (Figure 5). The TGA shows that the particles are thermically stable up to 550 °C. The decomposition starts between 560 and 580 °C. This indicates that the high-temperature resistance, one relevant property for the application of this type of polymer, is also maintained in the nanosized particles. In the present sample, TGA also shows a nondegradable fraction of 30 wt % which is essentially carbon from the polyimide plus some adsorbed silica. Because of the risks involved while working with more aggressive versions of HF, we refrained from strictly removing silica.

The most extended structures of the present set of experiments have been produced in the lamellar, sheetlike pores of the hydroxypropylcellulose-templated silica. Figure 6a shows the original silica (where the highly parallel channel structure is hardly visible due to its small size) compared to the structure of the isolated polyimide replicas depicted in Figure 6b,c.

Polyimide sheets with an average thickness of 2.0 nm become visible in the side view. This is in good agree-

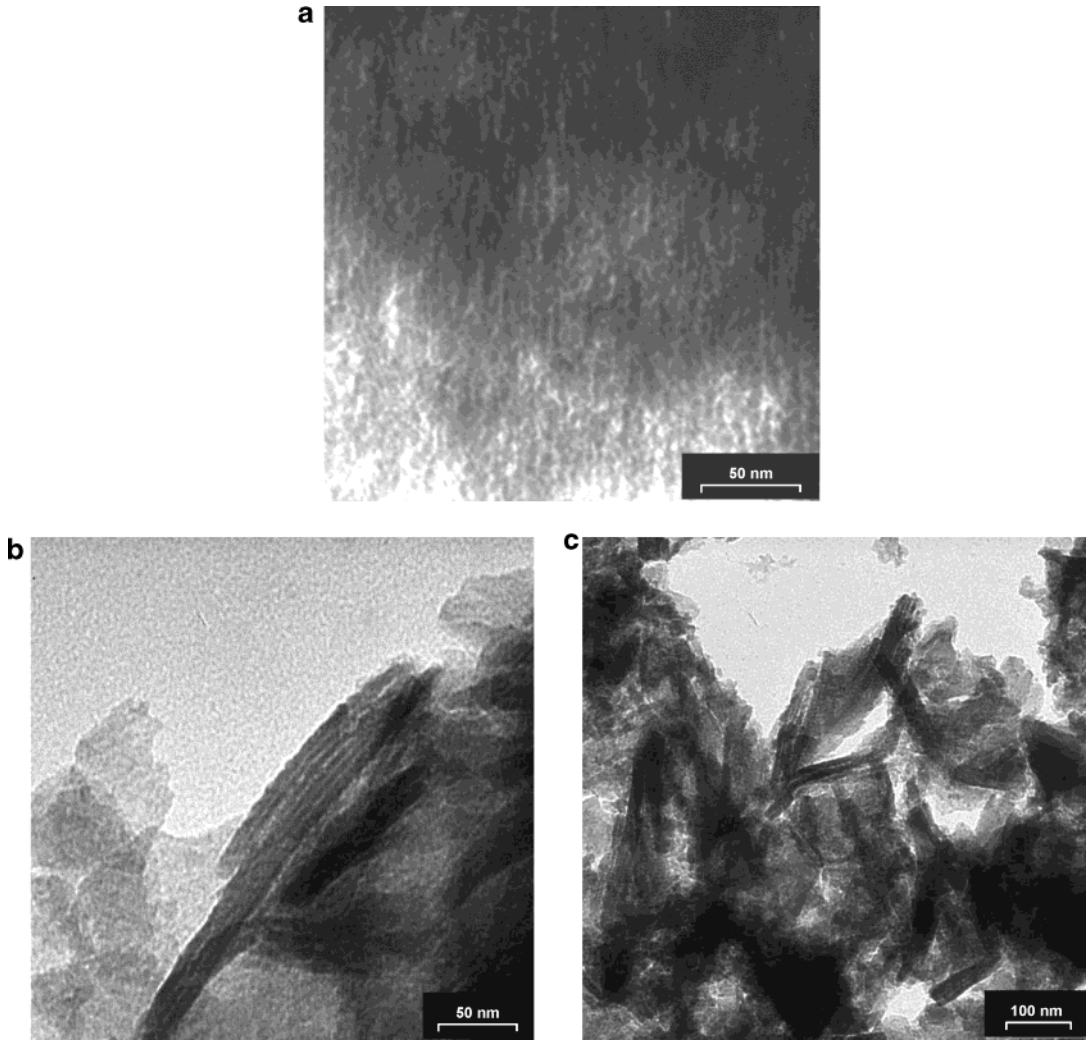

Figure 6. TEM micrographs of polyimide layers synthesized in the slitlike lamellar pores of a porous silica made by replication of the cholesteric phases of hydroxypropylcellulose as template: (a) original silica; (b, c) different micrographs of the resulting sheet like polyimide.

ment with the preceding template structure. Since only aggregates of sheets were observed, we could not decide whether the layers are covalently interconnected by rare topological defects or not. The yellow material obtained after etching with HF showed quite the same macroscopic shape as the original monolithic template, making a conclusion on the microscopic connectivity situation difficult.

WAXS measurements indicated only a slightly higher crystallinity than in the nanosphere situation, and TGA gave an even increased thermal stability of the two-dimensional system.

Conclusion

Nanoparticles and nanosheets of an aromatic polyimide were synthesized via a very simple monomer adsorption/polycondensation reaction inside the pore systems of some different mesoporous silica monoliths. The resulting nanoparticles were found as about perfect replications for both silicas under consideration: one a mesoporous silica with spherical pores with a diameter of 13 nm and another with a lamellar pore morphology with an approximately 2 nm thickness.

All analytical data as well as the thermogravimetric behavior indicated that indeed a quite pure polyimide was produced, with a somewhat lowered crystal size due to the nanoconfinement of the synthesis.

On the basis of AFM observations, the question was raised if at least some of the polyimide spheres were hollow due to incomplete loading with monomer. This question could not finally be answered in the present context.

As the nanosheet structures seemed to be cohesive and quite extended, it is promising to extend the present work to the replication of three-dimensional nanostructures, e.g., membranes or separation gels by nanocoating,[15] for the controlled design of high-performance membranes and filters with structural features on the nanoscale.

References and Notes

(1) Beck, J. S.; Vartuli, J. C.; Roth, W. J.; Leonowicz, M. E.; Kresge, C. T.; Schmitt, K. D.; Chu, C. T. W.; Olson, D. H.; Sheppard, E. W.; McCullen, S. B.; Higgins, J. B.; Schlenker, J. L. *J. Am. Chem. Soc.* **1992**, *114*, 10834−10843.

(2) Johnson, S. A.; Brigham, E. S.; Ollivier, P. J.; Mallouk, T. E. *Chem. Mater.* **1997**, *9*, 2448−2458.

(3) Frisch, H. L.; West, J. M.; Goltner, C. G.; Attard, G. S. *J. Polym. Sci., Part A: Polym. Chem.* **1996**, *34*, 1823−1826.

(4) Göltner, C. G.; Weissenberger, M. C. *Acta Polym.* **1998**, *49*, 704−709.

(5) Jun, S.; Joo, S. H.; Ryoo, R.; Kruk, M.; Jaroniec, M.; Liu, Z.; Ohsuna, T.; Terasaki, O. *J. Am. Chem. Soc.* **2000**, *122*, 10712−10713.

(6) Ryoo, R.; Joo, S. H.; Kruk, M.; Jaroniec, M. *Adv. Mater.* **2001**, *13*, 677−681.
(7) Wu, C. G.; Bein, T. *Science* **1994**, *264*, 1757−1759.
(8) Nguyen, T. Q.; Wu, J. J.; Doan, V.; Schwartz, B. J.; Tolbert, S. H. *Science* **2000**, *288*, 652−656.
(9) Wu, J. J.; Gross, A. F.; Tolbert, S. H. *J. Phys. Chem. B* **1999**, *103*, 2374−2384.
(10) Sroog, C. E. *Prog. Polym. Sci.* **1991**, *16*, 561−694.
(11) Thomas, A.; Antonietti, M. *Adv. Funct. Mater.* **2003**, *13*, 763−766.
(12) Thomas, A.; Schlaad, H.; Smarsly, B.; Antonietti, M. *Langmuir* **2003**, *19*, 4455−4459.
(13) Polarz, S.; Antonietti, M. *Chem. Commun.* **2002**, 2593−2604.
(14) Göltner, C. G.; Smarsly, B.; Berton, B.; Antonietti, M. *Chem. Mater.* **2001**, *13*, 1617−1624.
(15) Caruso, R. A.; Antonietti, M. *Chem. Mater.* **2001**, *13*, 3272−3282.

MA035804O

A low pressure route to various forms of graphitic-C_3N_4 compounds based on cyameluric C_6N_7-building blocks

Matthijs Groenewolt, Markus Antonietti*

Max Planck Institute of Colloids and Interfaces, Research Campus Golm,

Am Muehlenberg 1, D-14476 Golm, Germany. e-mail: pape@mpikg.mpg.de

Robert Schlögl, Christian Hess, Dangsheng Su

Fritz-Haber-Institute of the Max-Planck-Society, Department of Inorganic Chemistry

Faradayweg 4-6, D-14195 Berlin, Germany

Abstract

Graphitic carbon nitride, g-C_3N_4, has been synthesized by temperature induced condensation of cyanamide or dicyandiamide or 2,4,6-triamino-1,3,5-triazine. The reactions and structures were characterized using TGA, DSC, WAXS, XPS, HRTEM, EELS, FTIR and photoluminescence.

In a first step, a polymeric or dendritic C_3N_4–network with pendant amino groups can be isolated. Further condensation with precise temperature steps leads to two graphitic C_3N_4 allotropes. Both species turned out to be composed of tri-*s*-triazine (C_6N_7) units, bridged by a nitrogen, and not the (usually discussed) system based on single triazine (C_3N_3) rings.

1. Introduction

Carbon nitride is presumably the most promising (and the most searched-for candidate) to complement carbon in materials applications. The diamond-like ß-C_3N_4 is predicted to be of similar hardness and low compressibility then diamond.[1,2] However, it has to be assumed that similar to carbon, at ambient conditions a graphitic-C_3N_4 (g-C_3N_4) is presumably the most stable allotrope, and there is a larger number of reports in the literature approaching the synthesis of different modifications of this material. Physical and chemical vapor deposition methods to synthesize thin films are described most often (e.g., ref. 3-5) but all of them are dogged by the elimination of the very stable N_2, which results only in local order and is accompanied by a shift of the composition towards carbon-rich materials. This is why we regard chemical approaches as more promising, as they also can be scaled-up more easily.

Related to the present work, Kouvetakis et al. decomposed triaminotriazine (melamine) precursors at 400 °C-500 °C and obtained an amorphous carbon nitride with about correct composition and a broad graphitic stacking peak.[6] Montigaud et al. reported on the solvothermal condensation of melamine with cyanurchloride, which indeed worked at larger scales.[7] Condensation performed at

250 °C and 130 Mpa however revealed only a badly condensed product with weak order and many pendant amino groups. Heating melamine in presence of hydrazine to 800 °C at 2.5 Gpa resulted in carbonitrides with about perfect graphitic stacking, but a large excess of carbon and no in-plane order of the nitride pores were found. This work was resumed by Qian et al. who synthesized g-C_3N_4 by condensing cyanurchloride and calcium cyanamide[8] and identified only a very small temperature window between 500 °C – 600 °C to optimize order and composition.

Wolf et al. used 2-amino-4,6-dichlorotriazine as a precursor and obtained in a high pressure-high temperature approach a close-to-crystalline graphitic-C_3N_4 derivative, where the generated HCl played the role of a template to fill the nitridic in-plane pores.[9] The structure of these materials was - until then - most refined, as the system exhibited both, a regular in plane packing of the nitridic triazine-based pores as well as x-ray diffractograms which could be quantitatively assorted.

Another benchmark-step towards better defined and organized graphitic C_3N_4 systems was published by Schnick et al.[10] who were able to isolate and solve the crystal structure of another potential building block of g-C_3N_4, 2,5,8-triamino-tri-*s*-triazine, or melem ($C_6N_{10}H_6$). Melem was found to be stable until 560 °C, but further heating only resulted in badly defined amorphous graphitic-C_3N_4, as reported by the authors.

The list of these references which are closely related to the present work however reflects the attraction of the field only incompletely, and especially solvothermal synthetic routes seem to have some extra promise. Xie et al. were able to make g-C_3N_4 from cyanurchloride and sodiumamide solvothermally in benzene by heating to about 200 °C for 8 – 12 h.[11] The same group also produced carbon-nitride nanotubes by a similar reaction from cyanurchloride and sodiumazide.[12] Graphitic packing in those samples was less pronounced, which however can also be due to the nanostructure.

As g-C_3N_4 is a potentially useful substitute for amorphous and graphitic carbon in a variety of applications, e.g. as a thermally stable catalytic support or for gas storage,[13] novel procedures for more defined carbon nitrides and a better understanding of the building mechanism are still eagerly wanted.

It is the purpose of the present paper to analyze the reaction path during the self-condensation of cyanamide, dicyandiamide and melamine to generate g-C_3N_4. In particular, we will focus on the different condensation steps during the reaction, mainly on a highly condensed functionalized CNH polymer. The polymeric or dendritic C_3N_4 first to isolate at 400 °C is essentially a highly amine-functional, incompletely condensed version of the g-C_3N_4 structure. It might be interesting as an alternative for hyperbranched polymers in engineering plastics, since the formed network is inflammable, cheap due to the low cost of the precursors and bears a lot of functionalities, which guarantees compability in a lot of hybrid materials.

For the fully condensed g-C_3N_4, triazine and tri-s-triazine (also called cyameluric nucleus after Pauling[14]) are discussed as tectonic units to constitute potential allotropes of g-C_3N_4 , which differ in their stability - due to the different electronic environment of the N atom - and the size of the nitride pores, as seen in scheme 1:

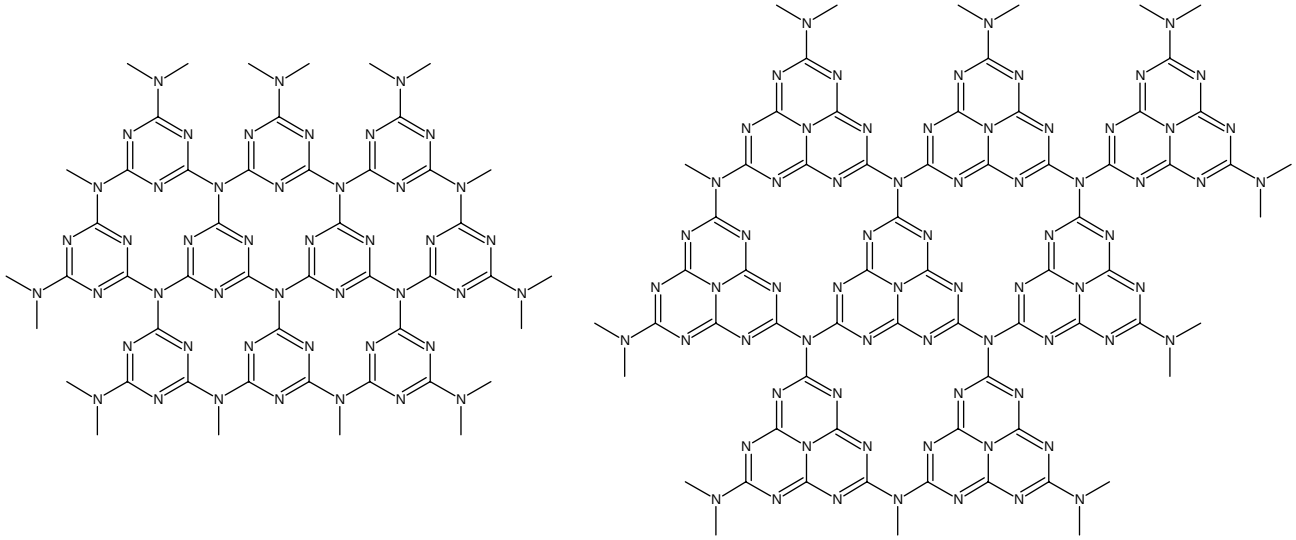

Figure 1: triazine- (left) and tri-*s*-triazine- based (right) of g-C_3N_4

These structures and their energetical differences were first discussed by Kroke et al. [17], who also revealed by DFT calculations that the tris-s-triazine based structure is by 30 KJ/mol more stable. It will be shown that all g-C_3N_4 synthesized by our approach are based on cyamelluric tri-*s*-triazine building blocks, indicating that this allotrope is the most stable species under the given reaction conditions. Additional regularity, possibly due to the periodicity of in-plane undulations - originating from the introduction of the tetrahedral bridging nitrogen atoms - is evidenced by additional scattering peaks.

Finally we describe a solid-solid phase transition of this in-plane organized graphitic carbonitride into the fully densified g-C_3N_4 allotrope with increased interlayer order, the latter being a structural isotype to graphite.

2. Materials and Methods

Materials

Cyanamide, dicyandiamide and melamine were supplied by Aldrich and used as received.

Calcination was done in quartz dishes or tight but not sealed steal tubes using a programmable muffle type furnace (Nabertherm).

Two heating rates were applied (2 K/min and 5 K/min), and in some experiments isothermal temper steps at 350 °C, 400 °C and 450 °C (5 h each) were inserted. As the changes of such steps were

mostly only minor, as evidences by XRD, we will discuss the reaction conditions only in context with specific products.

The yellowish compounds **M1-M4** were isolated and characterized without further washing and processing. Content of adsorbates was checked by TGA, which showed that approx. 2-5 wt% adsorbed species could be released until 150 °C. Sample pathways **M1-M3**, made from different starting products in an open reaction geometry, gave essentially the same product, and differ only by their yields. The tempered material **M4** will be differentiated in the discussion.

In the case of melem synthesis, the white product - obtained after opening the ampule - was freed from starting material and formed melamine by isothermal treatment at 300 °C for 1 h. Purity was checked by TGA and XRD.

Table 1 summarizes the experimental details, reaction conditions and the yields of all samples under discussion.

Table 1: Experimental details of the samples under discussion

Educt	**Initial weight /mg**	**Yield / mg**	**Temperature, Heating ramp, Isothermal treat.**	**Conditions**	**Sample code**
cyanamide	734	459 (63 wt%)	450 °C, 2 K/min, 10 h	sealed quartz ampoule	melem
cyanamide	612	225 (37 wt%)	550 °C, 5 K/min, 10 h	N_2	M 1
dicyandiamide	535	285 (53 wt%)	550 °C, 5 K/min, 10 h	N_2	M 2
melamine	578	180 (31 wt%)	550 °C, 5 K/min, 10 h	N_2	M 3
M1	139	106 (76 wt%)	600 °C, 5 K/min, 10 h	sealed quartz ampule	M 4

Measurements

TGA and DSC measurements were carried out under flowing air, applying a heating rate of 5 K/min and samples weights of about 5 mg.

High-resolution imaging and EELS (electron energy-loss spectroscopy) were performed in a Philips TEM/STEM CM 200 FEG transmission electron microscope equipped with a field-emission gun and a GATAN GIF 200 image filter. The acceleration voltage is set to 200 kV.

FTIR-spectra were collected using a BIORAD FTS 6000 spectrometer equipped with an attenuated total reflexion (ATR) setup.

Steady state fluorescence spectra were recorded on a Perkin-Elmer LS50B luminescence spectrometer. Emission spectra were recorded in the range of 325 to 650 nm with an excitation wavelength exc = 300 nm (melem) and exc = 340 nm (M1-M4). The excitation and emission bandwidths were both 2.5 nm

Elemental analyses (C, H, N, S) were performed on a Vario EL Elementar (Elementar Analysen-systeme, Hanau, Germany)

X-ray photoelectron spectroscopy (XPS) measurements were carried out using a modified LHS/SPECS EA200 MCD system equipped with a Mg K_α source (1253.6 eV, 168 W). The pass energy of the analyzer was fixed to 48 eV. The binding energy scale of the system was calibrated using Au $4f_{7/2}$ = 84.0 eV and Cu $2p_{3/2}$ = 932.67 eV from foil samples. The powder samples were mounted on a stainless steel sample holder. The base pressure of the UHV chamber was 1×10^{-10} mbar. All binding energies were referenced to the sharp C1s peak in >C=N- which was set to 288.2 eV in accordance with the literature [18]. Quantitative data analysis was performed by subtracting a stepped background and using empirical cross sections [19].

The results of the XPS data fitting is summarized in table 2:

Table 2: Results of the XPS-fits characterizing local binding situations

C 1s			N 1s		
Energy / eV	FWHM / eV	Rel. Freq	Energy / eV	FWHM / eV	Rel. Freq
285.3	4.2	11.3 %	398.7	2.0	64.5 %
288.2	1.8	78.8 %	400.1	2.0	17.1 %
290.4	2.0	2.9 %	401.4	2.0	6.8 %
293.5	3.4	7.0 %	404.1	4.4	11.6 %

3. Results

Thermoanalytical methods (TGA, DSC) in combination with XRD are used to characterize the intermediate steps along the condensation of the molecular precursors (cyanamide, dicyandiamide, melamine) into g-C_3N_4. The resulting diagrams are shown in Figure 2.

Note that the DSC has some inertness of heat flow which shifts the temperatures of the significant points (e.g. weight loss due to evaporation) to higher temperatures as compared to the corresponding TGA event (e.g. endothermic peak for melting). Another reason for minor

differences are that the different crucibles (DSC: closed Al pan with pierced lid; TGA: open Al_2O_3 pan), also resulting in smaller weight loss in the DSC-measurement due to sublimation. This is the reason for observing peaks at 383 °C and 513 °C in the DSC curve of c), although the material has already sublimed at these temperatures in the TGA-setup.

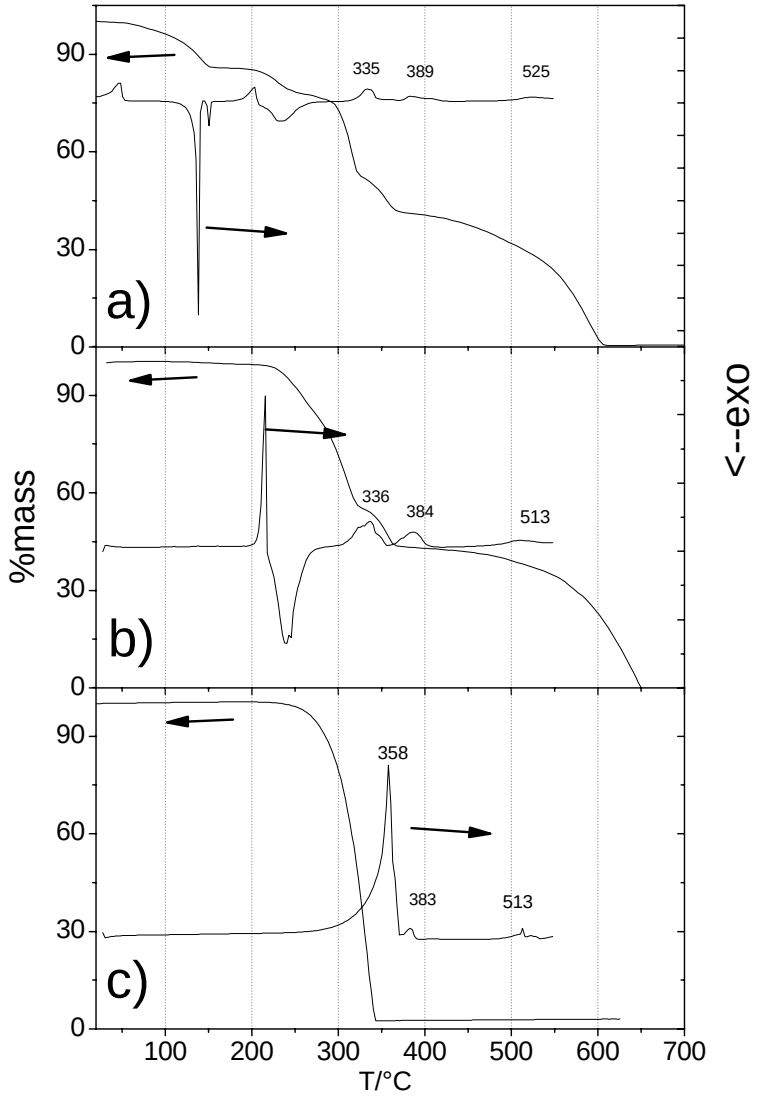

Figure 2: Combined DSC and TGA thermograms for the formation of C_3N_4 from the different precursors. The heating rate is 5 K/min, sample mass is about 5 mg. a) cyanamide; b) dicyandiamide; c) melamine

The corresponding transitions of the three data sets are also summarized in table 3:

Table 3: transitions identified by TGA and DSC and the processes attributed to those transitions

Temperature in Thermogram (**a**, **b** or **c**):	Related process
47 °C (**a**)	Melting point (mp) of cyanamide
137 °C (**a**) & 151 °C (**b**)	Reaction of cyanamide into dicyandiamide
203 °C (**a**), 216 °C (**b**)	mp of dicyandiamide
234 °C (**a**), 239 °C (**b**)	Reaction of dicyandiamide into melamine
335 °C (**a**), 336 °C (**b**), 358 °C (**c**)	Sublimation point (sp) of melamine
389 °C (**a**), 384 °C (**b**), 383 °C (**c**)	Formation of the cyameluric core, C_6N_7, from melamine followed by partial condensation
525 °C (**a**), 513 °C (**b**), 513 °C (**c**)	Formation of the C_3N_4 - Network

The lower temperature transitions both in the cyanamide as well as in the dicyandiamide systems are easy to explain: cyanamide melts and dimerizes to dicyandiamide which has finished at about 160 °C. Dicyandiamide itself melts slightly above 200 °C, followed by the exothermic trimerization reaction into melamine, which takes place at 240 °C. For the melamine track, consequently no transitions are found up to this temperature. Stopping the reaction at this point reveals a powder which is X-ray equivalent to melamine (data not shown) for both, cyanamide and dicyandiamide.

The melamine present or generated in all three reactions starts to sublimate at around 340 °C. In addition to the strong endothermic peak seen in the DSC curve, a weight loss of 30 % relative to the formed melamine in case of the cyanamide and dicyandiamide tracks is observed. In the case of melamine as starting material, the sublimation in the used open heating geometry is almost quantitative. Melamine can only be further condensed in closed or nearly-closed reaction vessels or under pressure. Sublimation is the major source of inefficiency in the described process and can be reduced quite efficient by using one of the two other starting products - maybe due to strong H-bridge interactions with other condensation motifs. It is therefore recommended to employ cyanamide and dicyandiamide as a precursor for the simple condensation reaction leading to g-C_3N_4 with higher efficiency.

At about 380 °C , the cyameluric nucleus - C_6N_7 - forms out of 3 melamine units, as already reported by Schnick et. al. in the synthesis of melem.[10] The observed mass loss of 23 % relative to the remainder is significantly higher than the 13 % calculated for this reaction, that is melem itself undergoes further condensation, as depicted in scheme 3.

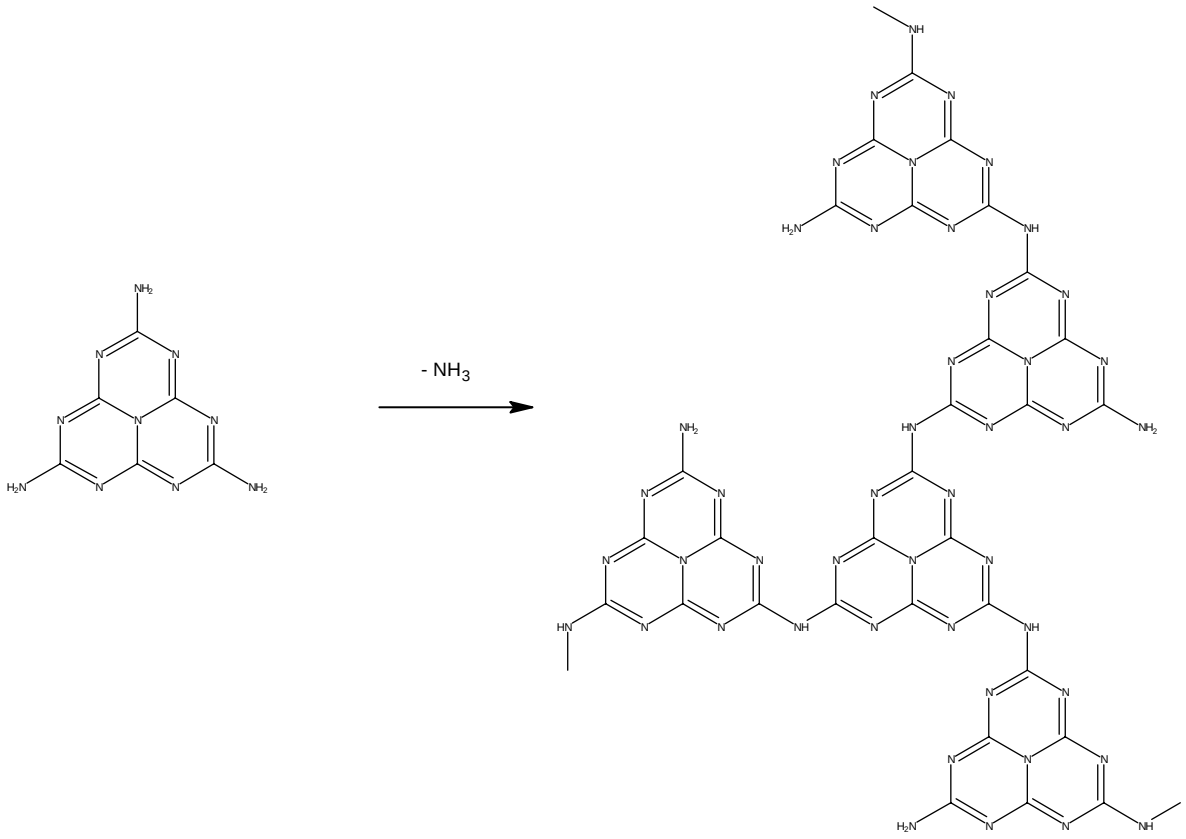

Figure 3: further condensation of melem units

The corresponding plateau in the TGA curve also points out that this condensation stage, the cyameluric nucleus, is a rather stable intermediate in the formation of g-C_3N_4. Also the condensed/cross-linked polymeric melem can be savely produced by stopping the reaction at 400 °C in a gas-open environment. Note that Schnick et al. performed their reaction towards melem in closed glass tubes, which is under high ammonia partial pressures, whereas our reaction processing is always pure in ammonia at ambient pressure, which shifts the equilibrium to the more condensed polymeric species. The formation of the cyameluric nucleus, C_6N_7, under these conditions can however also be detected by a DSC experiment within a tight steel crucible. In this setup, cyamelur forms at a slightly higher temperature, 414 °C, characterized by a very well defined endothermic peak.

To compare both products, melem and our condensation polymer isolated at 400 °C, we also synthesized pure melem according to the Schnick procedure. Fig. 4 compares the x-ray diffractograms of the species condensed at 400 °C and melem. Both systems share nicely the long range order of the atomic periodicities, while differences mainly occur in the intensities, which we attribute to slight differences in orientation due to condensation. It is noteworthy that in the crystalline melem, the free amino groups are very close to each other,[10] which obviously supports further ammonia elimination under minor structural changes. The peaks attributed to the aromatic stacking are shifted to lower angles for the condensation product, indicating some restrictions of the

packing due to connectivity. We regard these facts as a proof that also the polymeric C_3N_4 structure is essentially composed of cyamelluric units packed in a related fashion to melem.

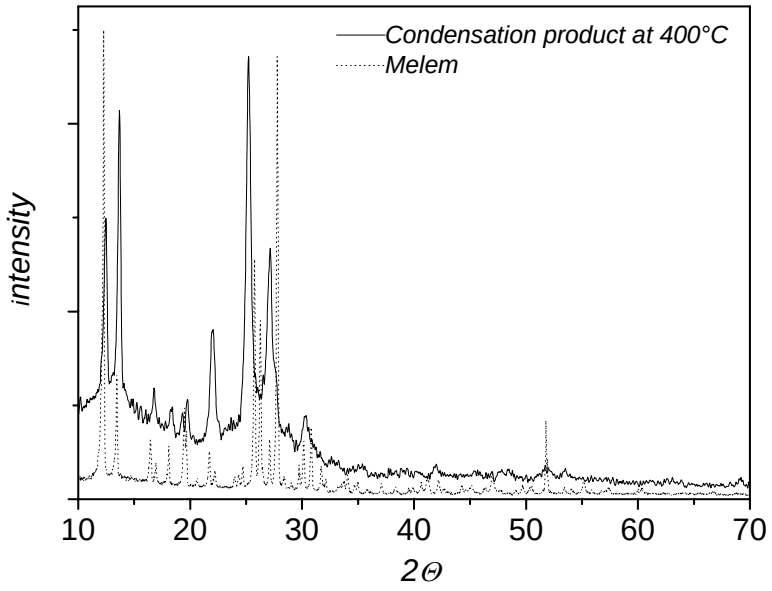

Figure 4: WAXS diffractograms of the 400 °C condensation product, which is regarded as a polymer of cyameluric building units, and melem, synthesized by the Schnick procedure.

Heating of the precondensed melem over 500 °C results in further elimination of ammonia and the formation of a practically condensed C_3N_4 - network (cf. table 2). The coupled structural changes of this phase transition are nicely followed by temperature dependent WAXS experiments, depicted in Figure 5:

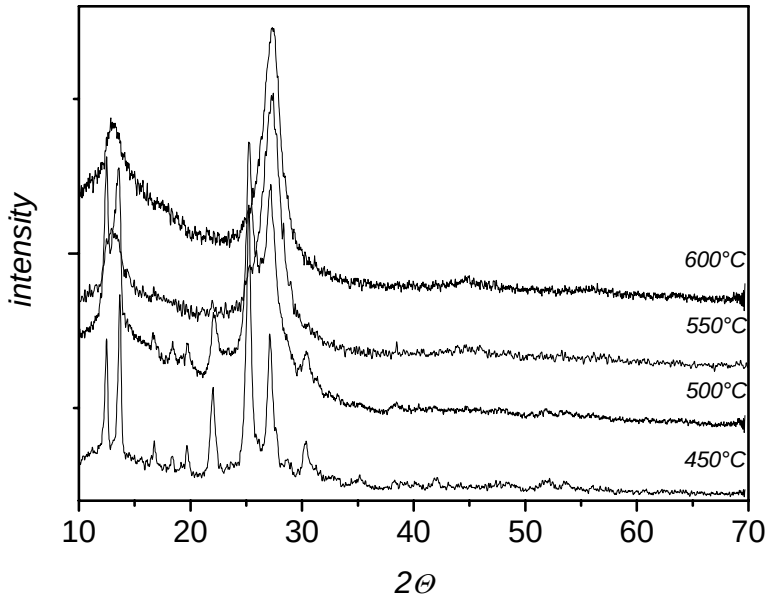

Figure 5: WAXS measurements characterizing the transition from polymeric C_3N_4 to the first g-C_3N_4 phase. The reaction was stopped immediately after the given temperature was reached.

It is seen that the peaks typical for the aromatic packing of the melem type structure at 23° - 27° merge to one single peak at 27.3°. This is usually identified as the (002) peak of graphitic C_3N_4 and corresponds to a stacking distance of the aromatic units of d = 0.326 nm. This stacking is significantly more dense than the packing in carbon with graphene units (d = 0.353 nm) and even 3 % denser than the packing in crystalline graphite, which possesses d = 0.335 nm.[15] The higher packing density perpendicular to the layers is well understood and can be attributed to the localization of the electrons by the heteroatomar substitution pattern. This peak position is also in agreement with previous reports on high quality g-C_3N_4.

A pronounced additional peak is found at 13.1°, corresponding to a distance d = 0.675 nm. This peak was already reported in previous work [11,20], however with lower intensity and definition and interpreted as the (001) peak [20], with the system having a marked A-B-A type sheet packing. However, as observed from our temperature dependent WAXS measurements, this peak originates from the formal fusion of the two peaks of melem attributed to the mutual distance of the single units along their maximal molecular extension, that is essentially an in-plane order (see Figure 3 of ref.10). This in-plane order becomes smeared in the condensed product to a broader peak with internal structure, which however does not shift, that is the mutual arrangement of the cyamellur units is essentially preserved. We feel inclined to follow the very precise Schnick-observations and address the 13.1° small angle peak to an in-plane structural packing motif. From these observations, it is also concluded that in this carbonitride species the cyamellur units are not necessarily coplanar

with each other. Note that the bridging nitrogen between three cyamellur units in all previous drawings was depicted in a tetrahedral single bonded state, that is such an electron configuration would result in an undulated lamellar structure.

XPS measurements (Fig. 6) also demonstrate that the material consists out of cyamellur units, C_6N_7, contrary to the usually postulated C_3N_4 materials. The 1s C binding energy shows mainly one carbon species with a binding energy of 288.2 eV, corresponding to >C=N- fragments. In the 1s N spectrum several binding energies can be separated. The main signal shows clearly the increased ratio of imino groups, =N- (398.7 eV), to amines >N- (400.1 eV), compared to the energies determined for condensed melamin units in the literature, where this ratio is closed to 1. However, we detected also groups from hydrogen-bridged amines at 401.4 eV. This indicates that the network is not fully condensed, but still has amino functions forming hydrogen bonds. The peak at 404.1 eV is attributed to π- excitations. Integration of the C and N signals gave an atomic C/N ratio of 0.71, indicating 5 % of nitrogen excess compared to the theoretical value, which can be attributed to uncondensed amino groups.

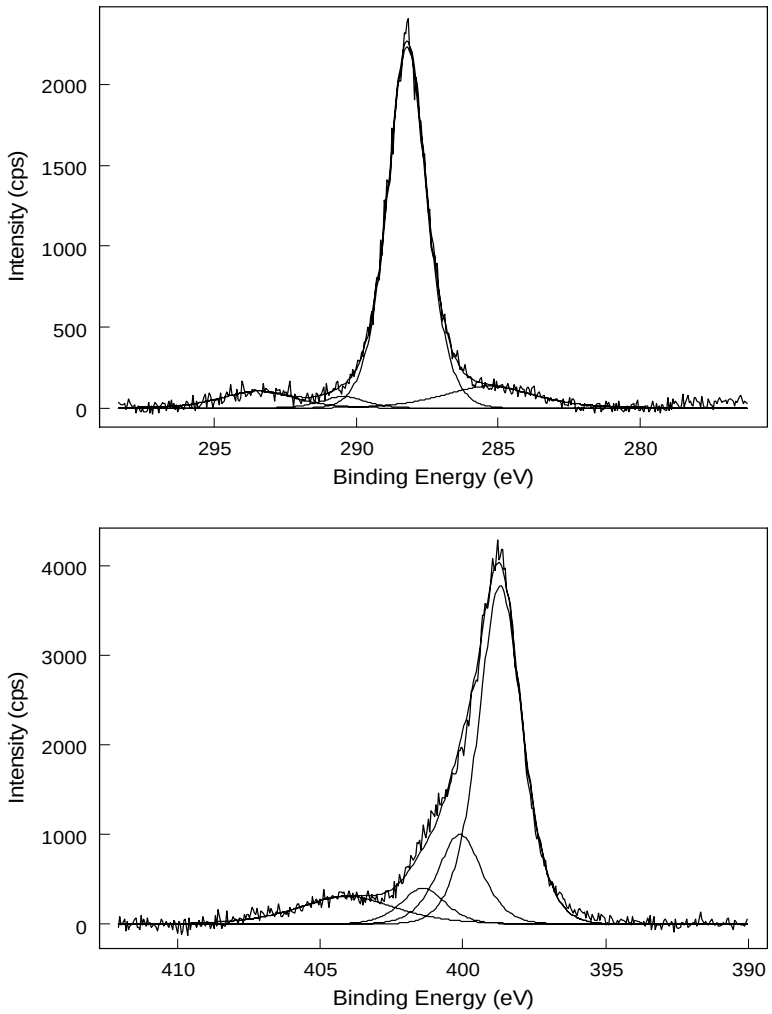

Figure 6: XPS spectrum of the g-C_3N_4 synthesized at 500°C. Shown are the 1s binding energies of carbon (top) and nitrogen (bottom).

As XPS is essentially a surface sensitive technique and surfaces rely on structural termination additional functional groups, we regard the obtained data as a worst case description of the structural quality and the degree of condensation. Elemental analyses have been performed several times on different batches of the prepared material. An average value of 0.71 was determined for the atomic C/N ratio (theoretical value of C_3N_4: 0.75), in agreement with the XPS measurement. Additionally small amounts of hydrogen (2 %) from uncondensed amino-functions and little amounts of adsorbed water have been detected.

The g-C_3N_4 compound was also investigated by FTIR-spectroscopy. We found several strong bands in the 1200-1600 cm^{-1} region, which are the typical stretching modes of CN heterocycles, also found in melamine and melem. Additionally the characteristic breathing mode of the triazine units at 800 cm^{-1} is found. Absorption above ~3000 cm^{-1} indicates still the presence of uncondensed amino groups. Since this band is quite strong, even if the total hydrogen content is very low, as reported by Guo et al.,[12] we decided to attribute this absorption to terminating aminogroups of the extended layers of the material rather to structural protons in the network.

The photoluminescence spectrum (Fig.7) shows a bathochromic shift of M1 – M3 compared to pure melem (λ_{max} = 366 nm), to λ_{max}= 472 nm in agreement with lowering the optical band gap by condensation of single molecules to an extended solid material. These simple measurement also prove that all the polymeric modifications are chemically sufficiently different from melem, and are especially not only disordered versions of it.

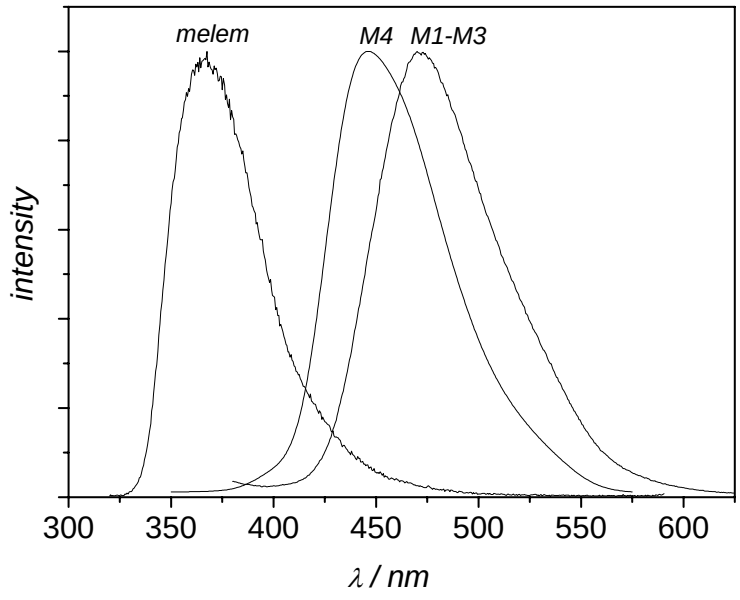

Figure 7: Photoluminescence spectra of the synthesized materials M1-M3 and the final g-C_3N_4 (M4, see text) in comparison to the spectrum of melem.

Since temper steps and variation of the heating rate did not affect the structure of this in-plane organized carbon nitride significantly, and the maximum operation window without depleting the structure in nitrogen was found to be limited to 600 °C, we tried to improve the order of the material obtained at 550 °C in an ambient pressure atmosphere by tempering it in a sealed quartz ampule at 600 °C for 10 h.

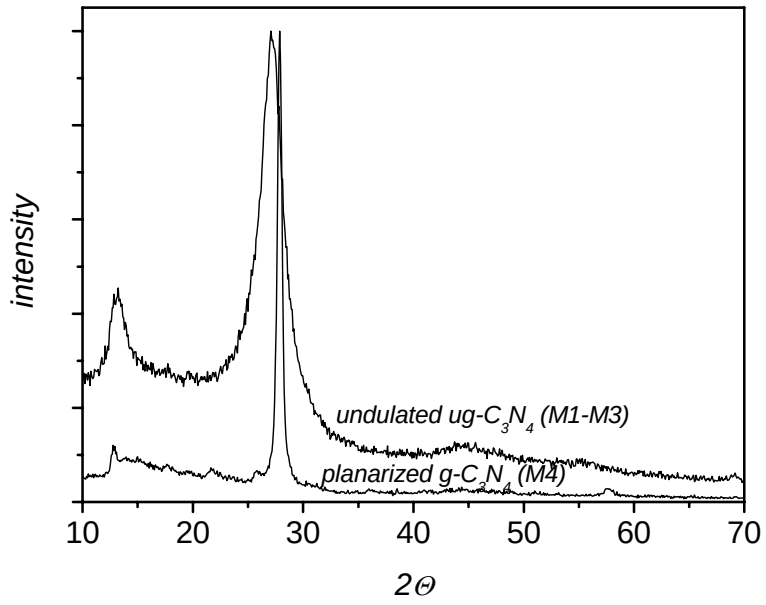

Figure 8: XRD patterns of the synthesized g-C_3N_4 materials (M1-M3, undulated) and M4 (planarized)
The 002 reflex has shifted to higher angles in the planarized structure, and additional but weak intralayer order is found.

Interestingly, we observed a significant structural change of the material (Fig. 8). One the one hand, a much better (002) interlayer organization is found, accompanied by a compression of the average interlayer distance towards still smaller d-values (d = 0,319 nm). This is about the smallest value for the packing of aromatic units ever found. In addition, the in-plane peak is also narrowed, has relatively weakened and is shifted to larger distances (from 0.675 nm to 0.689 nm). To our experience, such shifts are not typical for a better organization of the system and the increase of correlation length, but speak for a structural change of the system.

Based on the elaborated structure of melem [10], we speculatively attribute this to the final planarization of the system (scheme 9). The single layers composed of bridging tetrahedral N atoms and tectonic C_6N_7- units, which contain defects, undulations, and differently oriented melem units, can obviously densify and “snap” into a new electronic configuration where the bridging nitrogen atoms are more heavily involved in the electronic exchange of the aromatic system.

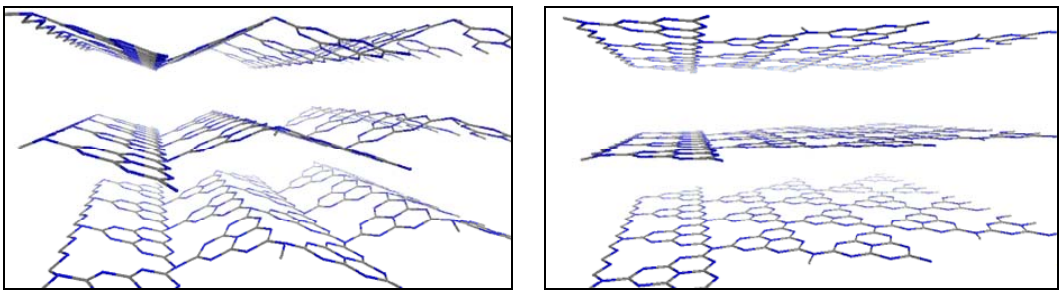

Figure 9: the temperature induced proposed planarization of the single layers consisting out of melem-units: the defect rich, undulated structure (left) densifies to a planar structure (right) by the heat treatment in a sealed quartz ampoule

This structural change, contrary to simple expectation, is accompanied with a slight blueshift in the PL-spectrum (Fig. 6). This can be due to different electronic interaction between the layers introduced by the geometric change due to the planarization, analogous to H-aggregate formation in dyes.[16] H–aggregates, which consists of vertical stacks of molecules, show a blue shifted emission maximum in the PL spectrum. Also the stretching modes of the skeletal g-C_3N_4 network in the FTIR-spectrum are better resolved in the final planar material, probably due to a decoupling of the vibrational modes by the planarization.

This final material is stable enough to allow HRTEM and EELS measurements (note that all other species undergo structural transformations in the intense electron beams). Figure 10 shows nicely the perfect layered order of the g-C_3N_4 materials along the 002 direction with d = 0.32 nm.

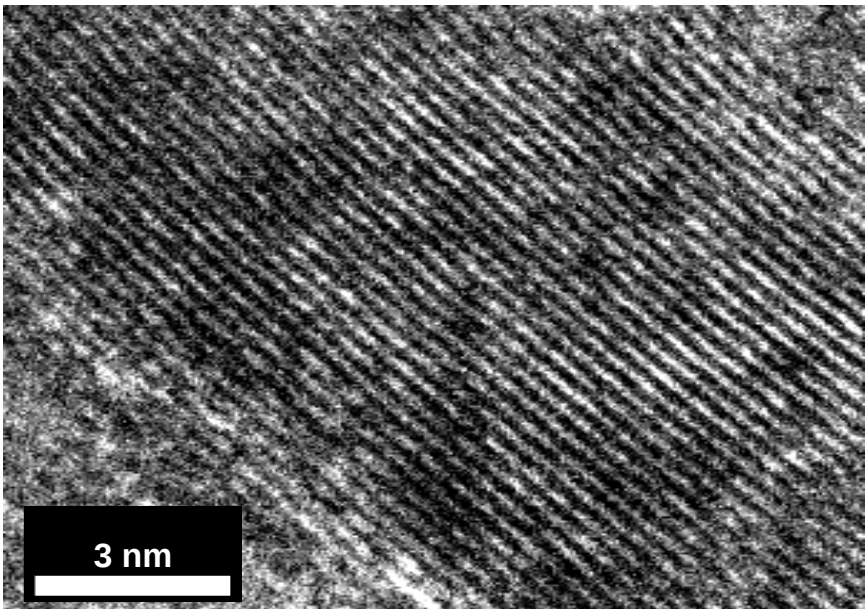

Figure 10: HRTEM of the material showing the graphitic layering of g-C_3N_4

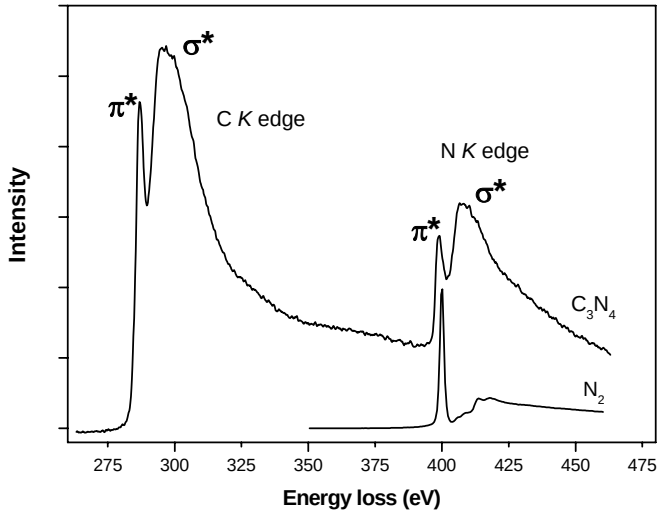

Figure 11: EELS spectrum of carbon and nitrogen K edges recorded in crystalline g-C_3N_4 synthesized at 550 °C. For comparison, the nitrogen K edge of N_2 is also presented.

In addition, the core-level EELS spectrum in Figure 11 shows the presence of sp^2-hybridized carbon and nitrogen by the existence of the $1s \rightarrow \pi^*$ resonance for both elements, in agreement with the proposed structure. The carbon K edge and nitrogen K edge show the same near edge structure indicating the same threefold coordination and electronic environment of carbon and nitrogen in the synthesized material. These results nicely confirm the proposed structure model.

4. Conclusion

A set of carbon nitrides, including a polymelem, an in-plane structured C_3N_4 and a graphitic C_3N_4, have been synthesized by a simple self-condensation process based on cyanamide. All obtained materials consist of condensed cyamellur/C_6N_7-units, supporting the calculations of Kroke et al. [17], but contradicting the usual previous structure assumption based on condensed triazine/C_3N_4-building blocks.

The first C_3N_4-derivative formed at 550°C is at least metastable and shows pronounced in-plane ordering with a broad additional peak corresponding to 0.675 nm repeat period. As this peak develops from very similar peaks of melem with its known crystal structure characterizing the distance of the mutually tilted aromatic melem stacks, we interpret this as evidence for the presence of planar distortions or undulations in the graphitic layers of this C_3N_4, which also allows at least some of the bridging nitrogen atoms to stay in a tetrahedral conformation.

By a solid-solid phase transition above 550 °C, this material transforms into the more densely packed, planar g-C_3N_4 with an interlayer distance of d = 0.319 nm, as evidenced by WAXS, HRTEM, and EELS.

Future work will focus on the use of these carbon nitrides for catalysis and the possibility to create intercalation compounds, analogous to graphite.

Acknowledgments

We like to thank Rona Pitschke for technical help throughout electron microscopy, Ute Wild for help with the XPS measurements and Pablo Beato for raman measurements during this project. The Max Planck Society is acknowledged for financial support.

References

1. Cohen, M. L. *Phys. Rev.* **1985**, *B32*, 7988.
2. Liu, A. L.; Cohen, M. L. *Science* **1989**, *245*, 841.
3. Niu, C.; Lu, Y. Z.; Lieber, C. M. *Science* **1993**, *261*, 334.
4. Guo, L. P.; Chen, Y.; Wang, E.G.; Li, L.; Zhao Z. X. *Chem. Phys. Lett.* **1997**, *268*, 26–30.
5. Chowdury, A. K. M. S.; Cameron, D. C.; Hashmi, M. S. J.; Gregg, J. M. *J. Mater. Res.* **1999**, *14*, 2359-2363.
6. Kouvetakis, J.; Bandari, A.; Todd, M.; Wilkens, B.; Cave, N. *Chem. Mater.* **1994**, *6*, 811.
7. Montigaud, H.; Tanguy, B.; Demazeau, G.; Alves, I.; Courjault, S. *J. Mat. Sci.* **2000**, *35*, 1547-2552.
8. Gu, Y.; Chen, L.; Shi, L.; Ma, J.; Yang, Z.; Qian, Y. *Carbon* **2003**, *41*, 2674-2676.
9. Zhang, Z.; Leinenweber, K.; Bauer, M.; Garvie, L. A. J.; McMillan, P. F.; Wolf, G. H. *J. Amer. Chem. Soc.* **2001**, *123*, 7788.
10. Jürgens, B.; Irran, E.; Senker, J.; Kroll, P.; Müller, H.; Schnick, W. *J. Amer. Chem. Soc.* **2003**, *125*, 10288-10300.
11. Guo, Q.; Xie, Y.; Wang, X. M.; Lv, S.; Hou, T.; Liu, X. *Chem. Phys. Lett.* **2003**, *380*, 84-87.
12. Guo, Q.; Xie, Y.; Wang, X.; Zhang, S.; Hou, T.; Lv, S. *Chem. Commun.* **2004**, 26-27.
13. Bai, X. D.; Zhong, D. Y.; Zhang, G. Y.; Ma, Y. C.; Liu, S.; Wang, E. G.; Chen, Y.; Shaw, D. T. *Appl. Phys. Lett.* **2001**, *79*, 1552-1554.
14. Pauling, L.; Sturdivant, J. H. *Proc. Nat. Acad. Sci. ISA* **1937**, *23*, 615.
15. Ruland, W.; Smarsly, B. *J. Appl. Cryst.* **2002**, *35*, 624–633.
16. a) Jelley, E. *Nature* **1936**, *138*, 1009; **1937**, *139*, 631. b) Scheibe, G. *Angew. Chem.*, **1936**, *49*, 563; **1937**, *50*, 212.
17. Kroke E., Schwarz M., Horath-Bordon E., Kroll P., Noll B., Norman AD., New.J.Chem. **2002**, *26*, 508 – 512
18. Carbon 40 (2002) 597
19. Briggs, D., Seah, M.P., *Practical Surface Analysis*, Wiley, Chichester, 1990

Graphic for Table of Contents

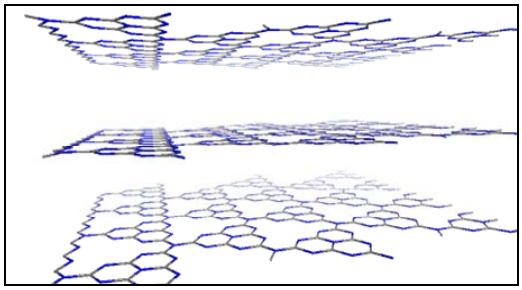

Different modifications of high quality graphitic carbonitride were prepared by a controlled thermal condensation route from different precursors. Characterization revealed that all modifications are composed of cyamellur-trirings and that stacking is much tighter then in crystalline graphite.

Synthesis of g-C_3N_4 –Nanoparticles in Mesoporous Silica Host Matrices

Matthijs Groenewolt, Markus Antonietti*

Max Planck Institute of Colloids and Interfaces, Research Campus Golm, Am Mühlenberg 1, D-14476 Golm, Germany.

Abstract/TOC

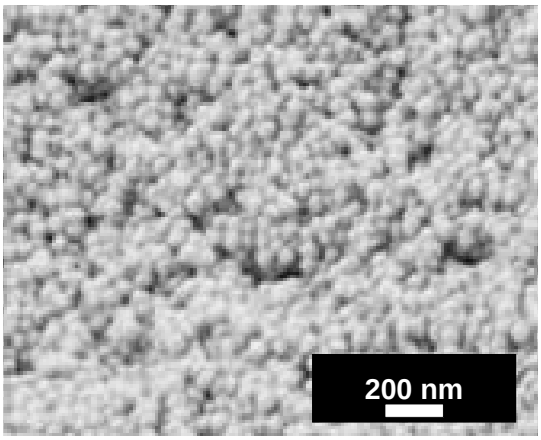

g-C_3N_4 nano particles of high crystallinity have been synthesized from molecular precursors via a polycondensation reaction, using mesoporous silica-materials with different pore sizes as a host matrix.

The particles isolated after removal of the host matrix were characterized using WAXS, TEM, SEM, IR, BET and photoluminescence. Structural and electronic size effects were identified by comparing nanoparticles with 5, 13 and 60 nm diameter .

Article

Nanoparticles and nanostructures materials which are otherwise not accessible can be made by casting/replication of ordered mesoporous silica matrices. Pioneering work in replication of inorganic host matrices with nanometer precision was done with carbon. Precursors were used to fill the channel system, followed by carbonisation of the guest material and subsequent removal of the silica matrix (1,2). Our own work in this direction was related to the polymerisation of unconventional polymers and unusual morphologies. By using solutions of monomers and – contrarily to the high temperature treatment in the carbonisation process -

modest temperatures, we were for instance able to synthesize spherical high- temperature-resistant (HTR) polyimide nanoparticles and polyimide nanoplates (3).

In this work we report on the synthesis and morphology control of novel nanoparticles with different diameters made of graphitic carbon nitride or g-C_3N_4. g-C_3N_4 is a novel, rarely examined material which however has extraordinary perspectives, e.g. in catalysis or as filler particles. The replication of pore structures is made using a reaction/condensation scheme recently employed for the synthesis of melem (4) and for the synthesis of highly organized g-C_3N_4 in the bulk (5). The underlying reaction sequence was clearified for the bulk synthesis of g-C_3N_4 in previous (5) work by means of x-ray analysis and differential scanning calorimetry and is shown in scheme 1:

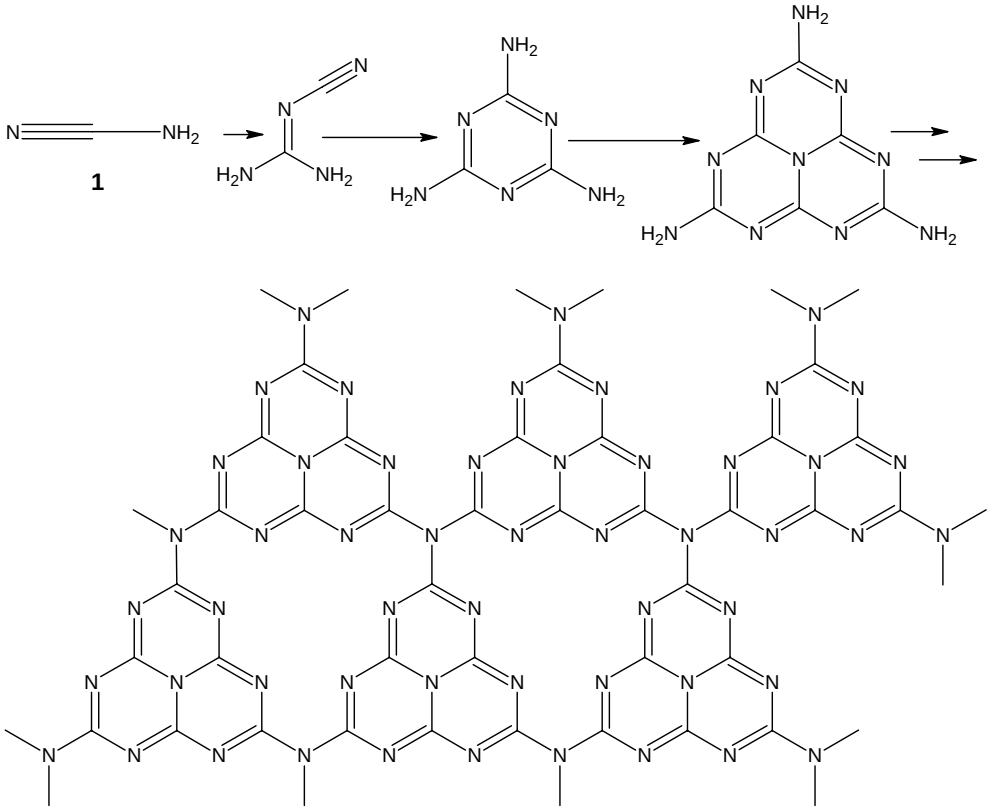

Scheme 1: Reaction path for the formation of graphitic C_3N_4 out of cyanamide (**1**)

The layered C_3N_4 material consists out of condensed melem (4) / cyamelluric (C_6N_7) units, contrary to how g-C_3N_4 materials in the literature are usually described where a network of condensed cyanuric cores (C_3N_3) is postulated (6).

To check whether the condensation steps of the reaction take place in the same fashion in the nano confinement as in the bulk conditions, we analyzed the heat flow during the reaction of a

monolithic particle (at least 2 mm in size) of **M13** soaked with cyanamide and compared it to the corresponding unconfined reaction (fig 1). The DSC thermogram shows clearly that both reactions exhibit the same features, that is the endothermic melting of cyanamide at 45°C, the exothermic dimerisation towards dicyandiamide at 150°C, the endothermic melting of dicyandiamide at 200°C followed by the exothermic reaction to melamin at 240°C, which partially sublimates at 350°C . Only the formation of the cyamelluric core (C_6N_7-unit) at around 390 °C is more defined in the bulk reaction. Finally the g-C_3N_4 network is formed at around 520°C.

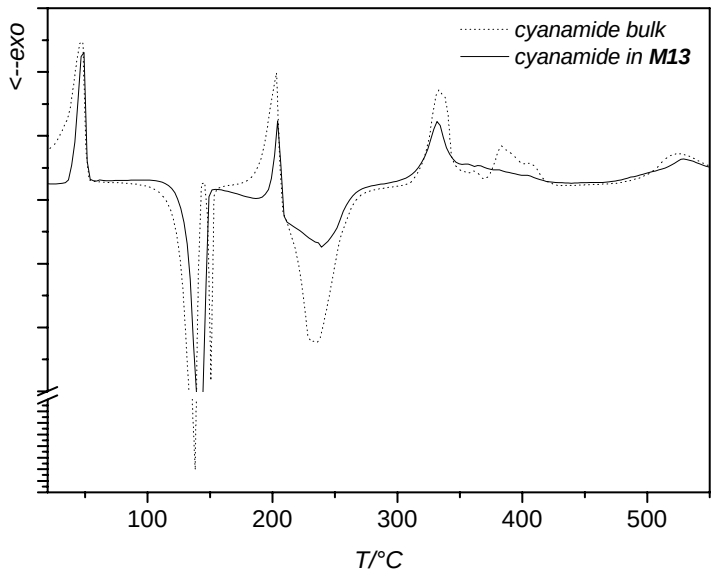

Fig. 1: DSC-thermogram of the condensation reaction of cyanamide into g-C_3N_4. The reaction in the nanostructured **M13** matrix shows the same features as the bulk reaction

The different mesoporous silica matrices with different pore sizes were made via "nanocasting"(see refs in the experimental part) using either block copolymers (**M5** and **M13**) or a polystyrene latex (**M60**) as a template.

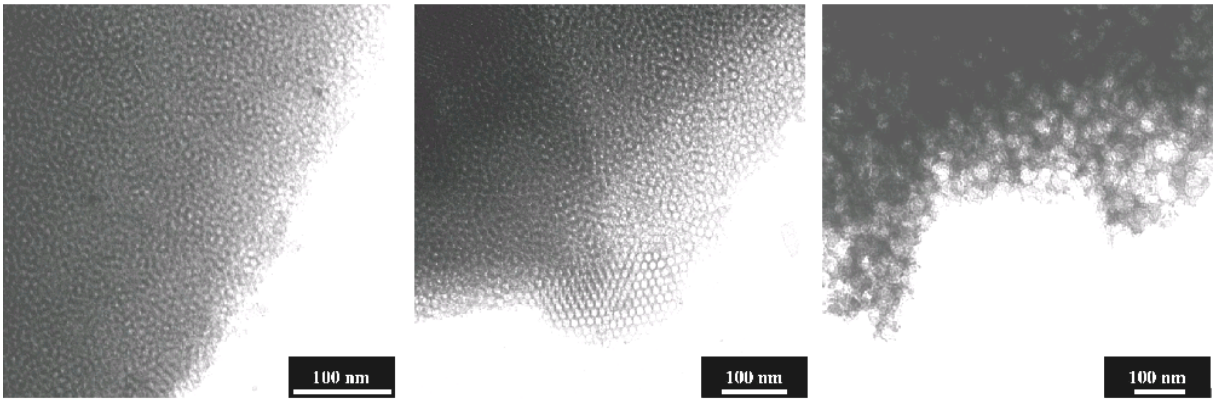

Fig 2. TEM pictures of the silica hosts **M5** (left), **M13** (middle) and **M60** (right) used as inorganic matrices

In the TEM pictures (fig.2) of the prepared matrices the high homogeneity of the materials becomes evident. **M5** has an average pore diameter of 5 nm, **M13** one of 13 nm and **M60** one of 50-70 nm. All used materials were examined by means of nitrogen sorption, to provide accessibility of the mesoporous channel system for the liquid C_3N_4 – precursor. The quite low specific surface in the final product can be explained that it is a dense materialsd (loss of micropores), which are not replicated as discussed below.

The resulting characterization data are summarized in table 1:

	pore size / nm (TEM)	**A /m^2*g^{-1} (BET)**	**wt% loading with C_3N_4 (TGA)**	**A /m^2*g^{-1} (BET) of C_3N_4-spheres after etching with HF and washing**
M5	5	582	22	~100
M13	13	320	20	~100
M60	~ 50-70	445	26	~100

Table 1. Characteristics of the used mesoporous matrices. The determined surface of the etched particles are approximate values, since the measurement is affected by ca 2-5% residual silica which could not be removed.

The successful morphological transcription of the spherical pore-system was proven by TEM for samples **M5** and **M13** (data not shown), and with SEM for sample **M60**. Fig. 3 shows exemplary SEM-images of the used silica matrix **M60** and the C_3N_4-product found after etching the matrix. The material consisted out of spherical, partly ellipsoidal particles with mainly 50-70 nm diameter, although smaller pores and corresponding carbonitride spheres can be detected in both pictures.

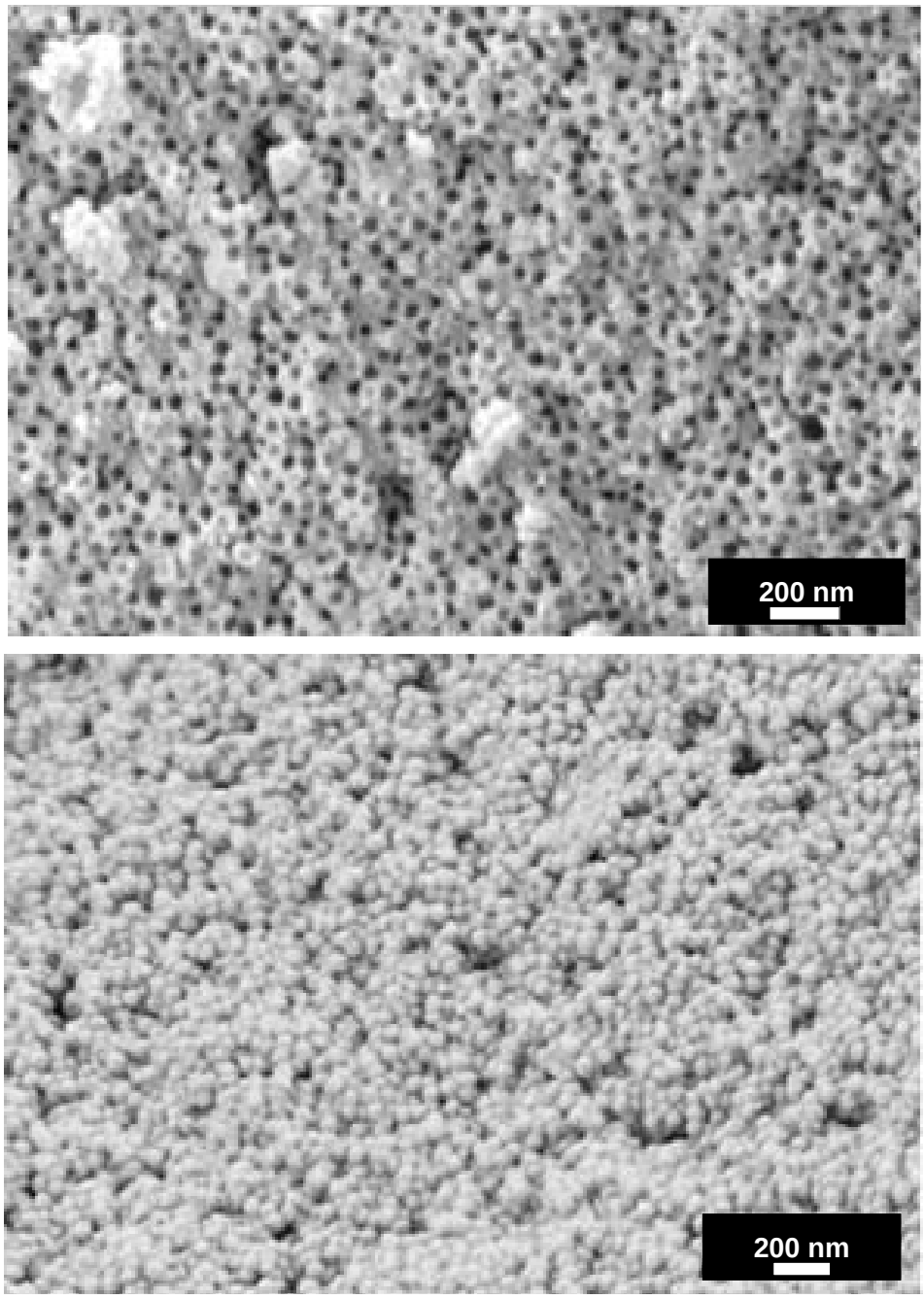

Fig.3 SEM pictures of the used silica matrix (top) and the C_3N_4-spheres (bottom) after etching the matrix

As indicated above, we do not observe the formation of "catwalks" between the particles, owing to the fact that such materials usually contain micropores which connect the big pores of the matrix with each other (7). The resulting carbon nitride powder is free flowing and just consists of isolated spheres. In previous replication experiments, the micropores of the mesoporous silica were always present in carbon replicas (1, 2), resulting in a monolithic 1:1 copy and not in isolated objects. We speculate that the reason for this peculiarity lies in the

very special architecture of g- C_3N_4 which is composed of ca 1 nm sized cyamellur units. These are simply too big to be formed in the micropores.

The sample could be redispersed by applying ultrasound to a mixture of the material **M60** in water. Fig 4 shows the AFM height image of such a dried aqueous **M60** dispersion. Several isolated particles with ~ 60 nm horizontal diameter and a height of ~ 30 - 40 nm are identified, in agreement with the SEM images. The reaction product is obviously not perfect spherical, but has an oblate shape, corresponding to the mass loss and the densification throughout the condensation process. One has to remind that g-C_3N_4 is a layered material, that is we have to assume that the structure looks like a stack of pancakes (the C_3N_4- planes) filling the center of the spherical pores, with the volume at the poles simply left out for energetical reasons (the formation of very small sheets is handicapped by a high line tension).

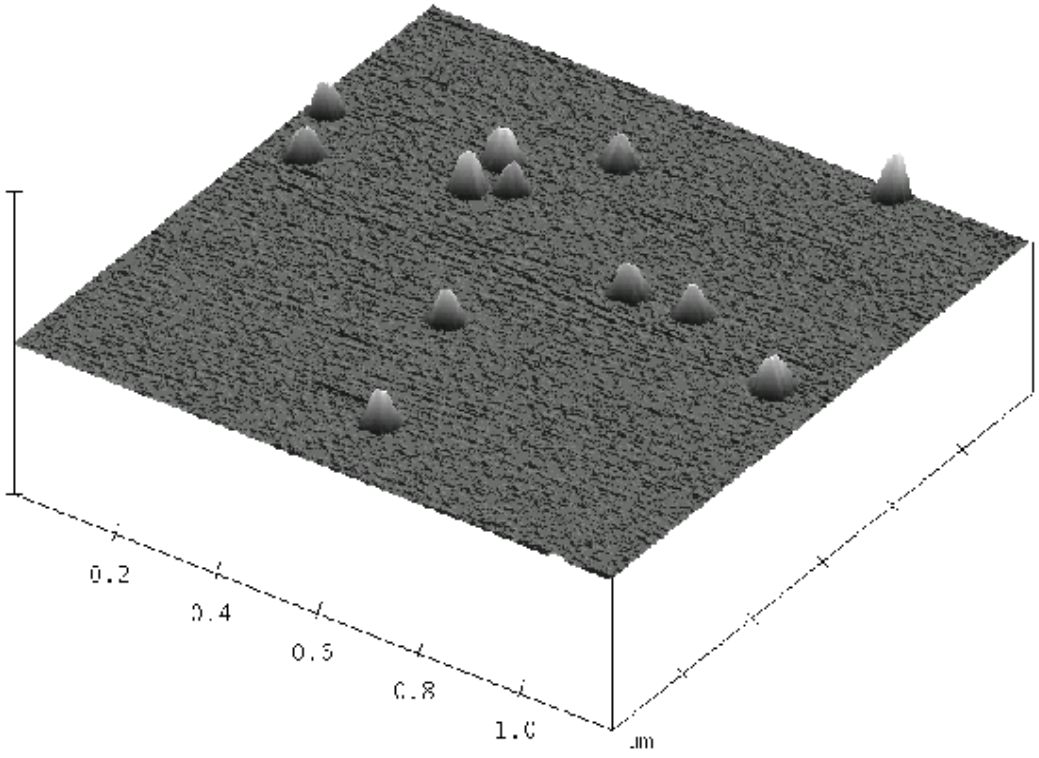

Fig 4.: 1.18 µm x 1.18 µm area of a C_3N_4 dispersion (sample **M60**) on a mica substate (height is 80 nm) The image shows isolated particles indicating the absence of interconnecting catwalks

FTIR-spectroscopy (see ESI) implies the existence of condensed CN heterocycles, showing the typical breathing mode of CN heterocyles at 800 cm^{-1} as well as the stretching mode of these rings between 1300 and 1600 cm^{-1} which were found also in the low molecular weight

heterocycles melamin ($C_3N_6H_6$) and melem ($C_6N_{10}H_6$). This confirms the formation of heterocycles as predicted for the structural model of g-C_3N_4 . We also found bands in the 3000 cm^{-1} regime pointing to uncondensed amino-groups in agreement with the E.A. result (C/N = 0.64 vs C/N = 0.71 for the bulk reaction (5) and the theoretical value of C_3N_4, C/N = 0.75). As the product is a nanoscaled material, we have to assume that the surface is densely terminated with amino-groups, due to connectivity reasons.

XRD (fig. 5) reveals the graphite like structure of the different materials, showing the typical 002 interlayer stacking peak, corresponding to an interlayer distance of d = 0.321 nm, in agreement with the literature (8). In the nano-confined reaction conditions, the 002 reflex is shifted to slightly higher angles, as compared to the bulk material (d = 0.326), indicating a minimal shortening interlayer distance of 0.05 Å. , As described earlier for the bulk material (5), the single layers are potentially undulated (thus explaining the width of the (002) peak), but could be planarized by further heating, resulting in a very narrow peak and a more dense packing.

The periodicity of the ondulations corresponds to the size of the cyamelluric cores, and gives rise to a second reflex with a d-spacing of around 0.68 nm. No broadening of the interlayer reflex due to size effects is observed. The better packing in the nanomaterial sound somewhat unusual, but is not unusual and is simply due to a relatively smaller influence of structural defects on the nanoscale. Even the 5 nm particles seem to be quite perfectly packed perpendicular to the layer direction.

The scattering peak at small angles (corresponding to an in-plane structure as aforementioned) is however significantly broadened in the nanoparticles case (fig. 5, pointed out by thick, red lines). This is also reasonable, since reflexes at lower angles correspond to larger d-values and are therefore more affected by the geometric confinement.

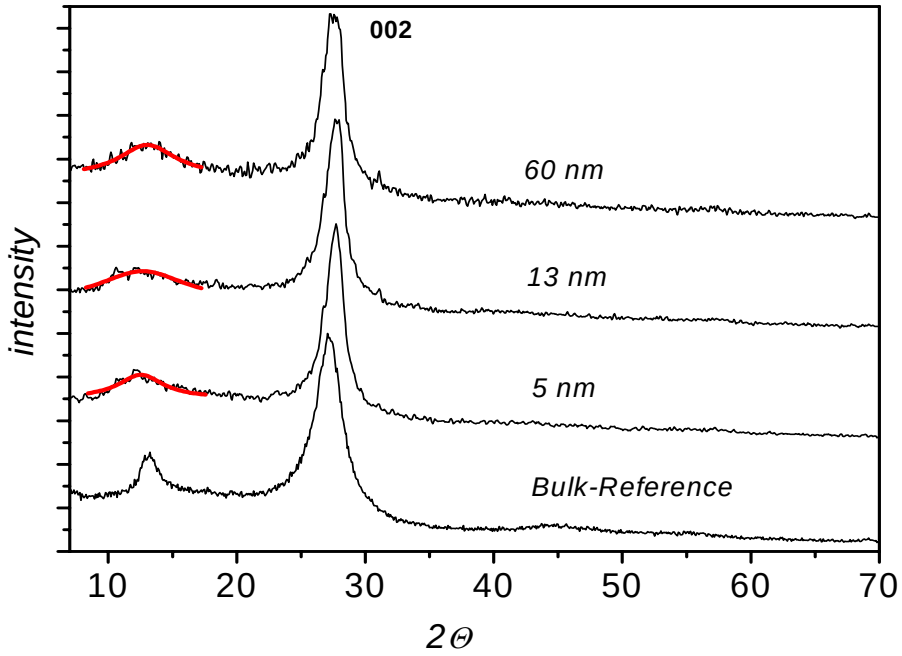

Fig 5. XRD of the synthesized nano-scaled C_3N_4-materials with different diameters. The interlayer spacing (002) is only weakly affected, but the intralayer periodicity (reflex at $2\Theta \sim 13°$, d = 0.68 nm) is broadened due to the geometric confinement. To point out this reflex, we fitted the experimental data in this range with a lorentz-function (thick, red line).

A confinement effect on the electronic structure can be identified by the photoluminescence spectra (fig. 6). It is seen that the optical bandgap is shifted towards higher energies for the nanoparticles, which is however the same for all synthesized particles. We are currently analyzing this effect in more detail.

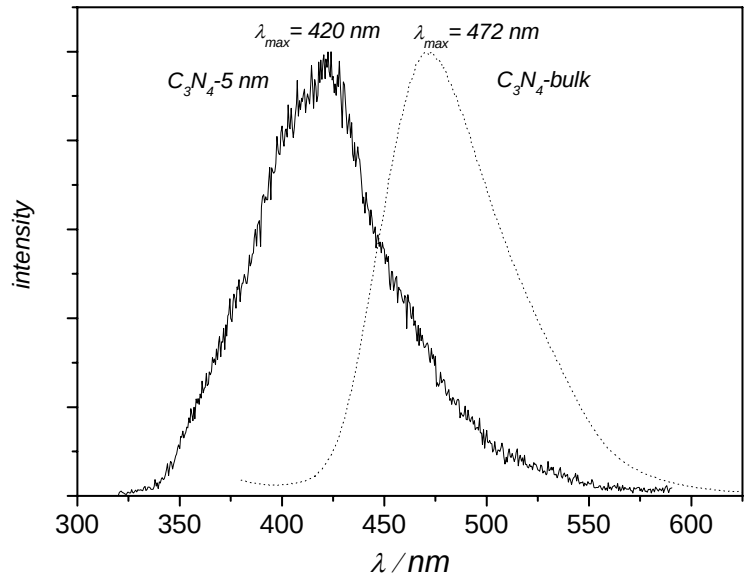

Fig. 6 Photoluminescence spectra of the bulk compared to the nano material **M5**. The emission maximum is shifted towards higher energies in the confined material.

The fact that these particles are indeed composed of single, non connected C_3N_4–layers can be shown by intercalation experiments. The basic nature of g-C_3N_4 enables the intercalation of organic moieties by simple stirring with strong acids, in our case fluorinated carboxylic acids with two different tail lengths. Fig. 7 shows the XRD patterns of the intercalated materials:

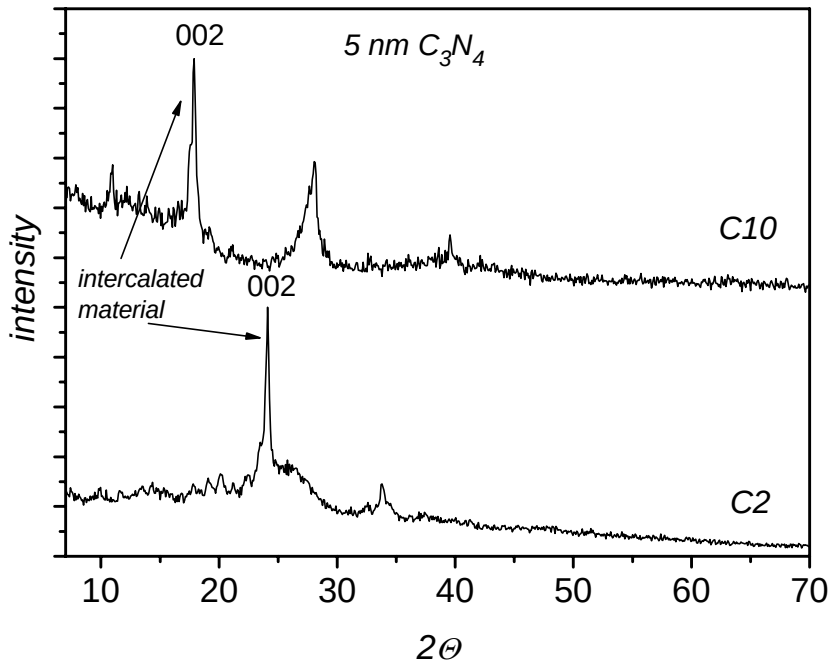

Fig. 7: XRD of the intercalated compounds. Perfluoro decanoic acid (C10, top) and trifluor acetic acid (C2, bottom) were used as intercalating agents

It is nicely seen that the (002) stacking peak is indeed shifted to smaller angles corresponding larger distances, which in addition depends on the tail length of the acid. This proves that the single nanolayers are indeed not connected and can expose their chemical functionality, i.e. their six-nitrogen base pots. A broad peak at the former stacking position however indicates that the delamination is still not perfect.

In summary, it was shown that nanoparticles of graphitic C_3N_4 with different diameters could be synthesized by carrying out a simple polycondensation process inside the confinement of mesoporous silica host matrices. The powder, consisting out of slightly flattened nano-spheres, could be redispersed to larger extents, indicating the absence of possible connections between the spheres. This was attributed to the special molecular structure of g- C_3N_4.

Future work will focus on a better understanding of the electronic processes in such materials and graphite-like intercalation compounds based on the nanoscaled g- C_3N_4.

Acknowledgements

We like to thank Ines Below for the help with block copolymer synthesis, Rona Pitschke for technical help throughout electron microscopy and Dr. Klaus Tauer for providing us with the latex dispersions. The Max Planck Society is acknowledged for financial support.

Experimental

Synthesis of the mesoporous silica matrices: Three different templates were used to prepare the mesoporous silica host matrices with different pore sizes: A polystyrene-block-poly(ethyleneoxide) (SE1010) provided by Goldschmidt for the material **M5** (made as described in 7), a hydrogenated polybutadiene-block-poly(ethyleneoxide) (PBPEO20) for the material **M13** (made as described in 9), and an aqueous polystyrene latex dispersion (LAT) with a solid content of 9 % for the material **M60** (made analogous to ref 10).

The dried and aged silica gels were calcined in a muffle type furnace at 550°C for 6 h. The resultant mesoporous matrices where characterized by transmission electron microscope (TEM) and nitrogen sorption measurements (BET).

Table 1 summarizes the composition of the synthesized materials:

Material:	**Used Template**	**Template / g**	**Ethanol /g**	**HCL (pH=2) / g**	**TMOS**	**wt% template in final silica**
M5	SE1010	1,0	-	2,5	5,0	33
M13	PBPEO20	1,7	5,0	2,5	5,0	46
M60	LAT, 9%	19,0	-	2,5	5,0	46

Table 1: composition of the synthesized materials

Synthesis of the g-C_3N_4 nano spheres: Cyanamide (CH_2N_2) was used as a molecular precursor because its low melting point (47°C) allows us convenient filling of the silica matrices by soaking at slightly elevated temperatures. The monolithic silica-material was brought into liquid cyanamide at 70°C and kept there for 30 min. Then the monoliths were taken out, dried in air, and the surface adsorbed cyanamide molecules were washed away by dipping in ethanol.

After the hybrid material was dry again, the reaction was carried out by heating the monolith under flowing N_2 up to 550°C with a heating ramp of $5K*min^{-1}$. 3h of isothermal treatment completed the reaction.

The monoliths were then crashed into a fine powder with a ball mill and treated with an excess of fluoric acid (HF, 5%) two times for 24 h to free the C_3N_4 spheres from the silica matrix. The centrifuged C_3N_4 powder was separated from the HF solution and washed with distilled water. Note that working with HF gives rise to special security measures

The purity of the samples and the silica leftovers were determined by TGA. Samples were temperature stable up to 550°C and contained 2-5% silica residues.

Characterisation of the materials:

Transmission electron microscopy (TEM) images were taken with a Zeiss EM 912Ω at an acceleration voltage of 120 kV.

Scanning electron microscopy (SEM) was performed on a Zeiss DSM 940 A.

Tapping mode atomic force microscopy (AFM) images were recorded with a multimode AFM from Vecco Instruments employing Olympus microcantilevers (resonance frequency: 300 kHz; force constant: 42 N/m). The samples were redispersed in water with ultrasonication and one droplet was spin coated on a freshly prepared mica substrate.

X-ray data were recorded with a Siemens D8 diffractometer equipped with a Sol X, SI solid state detector, using CuK_α radiaton in a symmetric reflexion setup.

Sorption measurements (BET) were obtained with a Micromeritics Tristar 3000.

Elemental analyses (C, H, N, S) were performed on a Vario EL Elementar (Elementar Analysen-systeme, Hanau, Germany).

The IR spectrum was collected with a BIORAD FTS 6000 FTIR-spectrometer, equipped with a attenuated total reflexion (ATR) setup.

Steady state fluorescence spectra were recorded on a Perkin-Elmer LS50B luminescence spectrometer.

Thermogravimetric Analysis (TGA) was performed on a Netzsch TG 209.

Differential Scanning Calorimetry (DSC) was performed on a Netzsch DSC 204.

References :

1 a) Ryoo, R., Joo, S. H., Kruk, M., Jaroniec, M., *Adv. Mater.* **2001**, *13*, 677. b) Ryoo, R., Joo, S. H., Jun, S., *J. Phys. Chem. B* **1999**, *103*, 7743.

2 Lu, A. H., Schmidt, W., Matoussevitch, N., Bonnemann, H., Spliethoff, B., Tesche, B., Bill, E., Kiefer, W., Schuth, F., *Angew. Chem. Int. Ed.* **2004**, *43*, 4303.

3 Groenewolt, M., Thomas, A., Antonietti, M., *Macromolecules* **2004**, *37,* 4360.

4 Jürgens, B., Irran, E., Senker, J., Kroll, P., Müller, H., Schnick, W., *J. Am. Chem. Soc.***2003**, *125*, 10288.

5 Groenewolt, M., Dangsheng, S., Schlögl, R., Antonietti, M. *submitted.*

6 a) Teter, D. M., Hemley, R. J., *Science* **1996**, *271,* 53. b) Guo Q., Xie Y., Wang X., Zhang S., Hou T., Lv S., *Chem.Comm.* **2004**, 26.

7 Smarsly, B., Göltner, C., Antonietti, M., Ruland, W., Hoinkis, E., *J. Phys. Chem. B.* **2001**, *105*, 831.

8 a) Alves, I., Demeazeau, G., Tanguy, B., Weill, F., *Solid State Communication* **1999**, *109*, 697.

b) Zhang, Z., Leinenweber, K., Bauer, M., Garvie. L. A. J., McMillan, P. F., Wolff, G. H., *J. Am. Chem. Soc.* **2001**, *123,* 7788.

9 Thomas, A., Schlaad, H., Smarsly, B., Antonietti M., *Langmuir* **2003**, *19*, 4455.

10 Antonietti, M., Berton, B., Göltner, C., Hentze, H. P., *Adv. Mater.* **1998,** *10*, 154.

Corresponding author:

Silvia Gross

CNR–ISTM and INSTM

Department of Chemical Sciences

University of Padova

Via Marzolo, 1

35131 Padova, Italy

E-Mail: silvia.gross@unipd.it

Phone ++39-049-8275736

Fax ++39-049-8275161

Zirconium and hafnium oxoclusters as molecular building blocks for highly dispersed ZrO_2 or HfO_2 nanoparticles in silica thin films

Lidia Armelao[a], Christoph Eisenmenger-Sittner[b], Matthijs Groenewolt[c], Silvia Gross[a*], Cinzia Sada[d], Ulrich Schubert[e], Eugenio Tondello[a], Andrea Zattin[a]

a- CNR–ISTM, *Department of Chemical Sciences,* University of Padova and INSTM, via Marzolo, 1- I-35131 Padova, Italy

b- Institut für Festkörperphysik-Vienna University of Technology, Vienna, Austria

c- Max-Planck-Institut für Kolloid- und Grenzflächenforschung, Golm, Germany

d- Department of Physics, University of Padova, Padova, Italy

e- Institute of Materials Chemistry-Vienna University of Technology, Vienna-Austria

---

Abstract

A novel synthetic route to prepare ZrO_2 or HfO_2 nanoparticles homogeneously dispersed in SiO_2 thin films films was developed. This route is based on the copolymerisation of organically modified crystalline oxozirconium or oxohafnium cluster ($M_4O_2(OMc)_{12}$, M= Zr, Hf; OMc = $OC(O)-C(CH_3)=CH_2$) with (methacryloxymethyl)triethoxysilane (MAMTES, $(CH_2=C(CH_3)C(O)O)-CH_2Si(OCH_2CH_3)_3$). The crystalline clusters, which are the precursors for the corresponding metal oxides (MO_2), were prepared via the sol-gel route by reaction of zirconium or hafnium butoxide ($M(OBu)_4$)) with methacrylic acid. The copolymerization of the clusters with the methacrylate-functionalized siloxane was photoinitaited by Irgacure 184 and allowed the anchoring of the cluster to the forming silica network. The solution was cast into films by dip-coating and UV cured (10', 125 W) to promote the copolymerisation of the methacrylate groups of the cluster with those of the silane. Transparent and homogeneous films 200-450 nm thick were obtained after calcination at 800°C in air. This route allowed to yield a very homogeneous dispersion of the MO_2 precursors inside the silica matrix. The surface and in-depth composition of the thin films was investigated through IR, X-Ray Photoelectron Spectroscopy (XPS) and Secondary Ion Mass Spectrometry (SIMS). SIMS and XPS depth profiles evidenced a very homogenous distribution of both zirconium or hafnium within the

whole silica films and sharp film-substrate interfaces. The surface morphology of the coatings was investigated through Atomic Force Microscopy (AFM), which showed smooth, homogeneous and crack-free surfaces. Through X-Ray Diffraction (XRD) the crystallization of hafnium and zirconium oxides was pointed out, while the presence of isolated crystalline nanoparticles having a diameter ranging in the interval 5-10 nm was evidenced by Transmission Electron Microscopy (TEM). Pull-off test pointed out a very good adhesion of the films to the substrate.

Keywords

Multicomponent oxides, sol-gel, ZrO_2, HfO_2, methacryloxytrialkoxysilanes, thin films, nanocomposites, XPS, SIMS

---

1. Introduction

The need for advanced materials endowed with enhanced properties has progressively more focused on composite systems which can involve complex stoichiometries or architectures. In this framework, the development of synthetic strategies which enable a precise control over the evolution of the precursor to give the final solid-state system has become a major concern in many technological and scientific fields. A noticeable attention has been focused on mixed oxide materials and on their preparation via the sol-gel process.[1,2]

For the preparation of multicomponent oxide systems, a major disadvantage is however represented by the different hydrolysis and condensation rates of the precursors, which can lead to heterogeneous mixtures. To circumvent this drawback and to obtain multicomponent materials homogeneous at a molecular level, different strategies have been devised among which the design of suitable precursors represents a key concern. Different hybrid materials containing both silica and other metal oxides have been formerly prepared by mixing metal alkoxides (e.g. Zr, Ti) with methacrylic acid as complexing ligands bearing the polymerisable moiety, and methacryloxysilanes.[3-5] Inorganic-organic hybrid materials in which metal oxide precursors are homogenously embedded into a silica matrix can be conveniently used as "composite precursors" for the preparation of binary oxide systems of the type MO_x: SiO_2 in

which the metal oxide is evenly dispersed in the silica matrix. The thermal calcination at high (> 600° C) temperature of the starting hybrid materials promotes the pyrolysis of the organic parts and the densification of the oxide networks, thus enabling the preparation of pure and homogeneous composite oxide materials, either as bulk or thin films.

Among these oxides, an increasing attention has been devoted to zirconium and hafnium oxides. In particular, mixed zirconia-silica and hafnia-silica materials are potentially useful in a wide spectrum of technological applications, for instance in catalysis,[6-7] as catalyst supports[8] or in optics.[3] It has been reported that Zr/Si binary oxides prepared by the sol-gel route show catalytic activity for the selective formation of isobutene.[9] Sol-gel ZrO_2-SiO_2 materials have been catalytically tested for isopropanol and n-butanol dehydration.[10] Zr/Si binary oxides having strong acid sites have been also found to exhibit catalytic activity for the dehydrogenation of cyclohexanol.[11] These mixed oxides display enhanced physico-chemical properties such as high thermal and chemical stability. Zirconia-silica glasses have been also carefully investigated as structural materials thanks to their low thermal expansion, high fracture toughness and excellent resistance to chemicals.[12,13] Furthermore, binary zirconia-silica and hafnia-silica in the form of thin films are appealing replacements for silicon dioxide as gate dielectric materials for complementary metal-oxide-semiconductor (CMOS) transistors.[14-16] Zirconia and hafnia are known to be thermodynamically stable when in contact with silicon.[14-16] These binary oxide "alloys" are expected to provide enhanced permittivity with respect to SiO_2, while the silica component should impart crystallisation resistance and electrically neutral interface.[17]

As already mentioned, the properties of these binary systems are strongly affected by the composition, the microstructure and the degree of mixing of the two oxide components. Consequently, the choice of a suitable synthetic route enabling a control on the mentioned features would enable a fine tailoring of the final properties. These binary systems have been recently prepared by a chemical solution deposition,[18] by ultrahigh vacuum molecular beam epitaxy[17] and by conventional sol-gel processing starting from the corresponding alkoxides.[2, 20-21]

In this study, we propose the implementation of a method based on the use of methacrylate-substituted transition metal oxoclusters $M_4O_2(OMc)_{12}$ (M = Zr, Hf) and of a

methacryloxysilane to prepare silica thin films embedding hafnia or zirconia. The clusters, which are precursors for the corresponding oxides, are easily prepared by reaction of metal alkoxides with methacrylic acid as reported elsewhere.[22-24] The methacrylate moieties of the cluster and that of the silane are copolymerised, while the alkoxy groups of the silane undergo hydrolysis and condensation reactions to form a silica network. These and similar metal oxoclusters have been already used as inorganic building blocks for the synthesis of a wide variety of inorganic-organic hybrid materials.[24-27] The advantage of the approach reported in this article, compared to the processing of mixtures of metal alkoxides, methacrylic acid and methacrylate-substituted silanes (see above) is that the use of the pre-formed clusters allows a better structural control on the obtained composite materials. Although the final materials are mixed-metal oxides, our approach allows to use polymer processing methods, which is particularly useful for the preparation of composite films.

In the present study, the composition, the morphology, the microstructure of $xZrO_2$-(100-x)SiO_2 and $xHfO_2$-(100-x)SiO_2 (x = molar, $0<x<17$) thin films were investigated. In particular the in-depth distribution of the host zirconium and hafnium oxides in the silica matrix was analysed by performing XPS and SIMS depth profiles.

2. Experimental

Chemicals

Methacryloxymethyltriethoxysilane (purchased from Gelest); methacrylic acid 99%, anhydrous tetrahydrofuran and anhydrous toluene, purchased from Aldrich, were used as received. The photoinitiator Irgacure 184 (I184) was purchased from Ciba. All the chemicals were stored under argon. The clusters $M_4O_2(OMc)_{12}$ (M = Zr, Hf) were synthesised by the previously reported procedure.[22-23]

Precursors solutions

All handlings were performed under argon using standard Schlenk techniques. The preparation of the starting solution used for the film deposition can be described as a three step process, which is schematically sketched in the flow chart in figure 1.

place fig. 1 here

First, (methacryloxymethyl)triethoxysilane (MAMTES) is dissolved in THF and prehydrolysed with water in the presence of HCl as catalyst for 8 h at room temperature. The typical composition of the sol-gel solution is silane: H_2O: HCl 1:4:0.04 molar ratio. The hydrolysis time was chosen on the basis of time-resolved infra-red studies of the hydrolysis rate of the silane, as elsewhere reported.[28] A calculated amount of the crystalline cluster is dissolved in toluene and this solution is then mixed with the prehydrolysed silane and stirred at room temperature for 15 minutes. To this solution, CIBA Irgacure 184 (1-hydroxycyclohexyl-1-phenylketone) is added 1% (w/w with respect to silane) as radical photoinitiator under stirring. When excited to its triplet state by UV radiation, the molecule undergoes α-cleavage to produce benzoyl and 1-hydroxycyclohexyl radicals. The former is primarily responsible for initiating the polymerisation of the methacryloxypropyl group. Different samples were prepared by varying a) the type of cluster (Hf or Zr) and b) the silane:cluster molar ratio. As a reference, the MAMTES silane without addition of hafnium or zirconium clusters was also casted into film and UV cured. Table 1 summarises the different molar ratios used for the preparation of the samples, according to the nominal composition of the solution. In table 1 and in the following, the labels "SiZr" and "SiHf" indicate the specimens prepared by using the zirconium and hafnium oxoclusters, respectively, while the number indicates the Si/M (M = Zr, Hf) atomic ratio.

place table 1 here

Film deposition and UV curing

The prepared solutions were cast into films by dip-coating procedure. Four different materials were used as substrates: silicon wafers (Si 110), Herasil silica slides, supplied by Hereaus, K-glass slides, supplied by EKOPLUS, consisting of soda–lime–silica one side coated with a thin film (<500 nm thick) of fluorine doped tin oxide (supplied by Isoclima, Este, PD, Italy) and

stainless steel plates. Before use, the slides were cleaned and rinsed both in doubly distilled water and 2-propanol. This procedure was repeated several times to remove organic residuals at the surface thus favouring the best adhesion between coating and substrate. The slides were finally dried in air at room temperature.[29]

Dip-coating film deposition was carried out in air at a constant withdrawal speed of 10 cm min^{-1}, at room temperature with a relative humidity of 30-40% by using a home-made equipment. After dip-coating, the films were irradiated under an UV source for 10 min to promote the polymerisation of methacrylate. The irradiation source was a Helios Italquartz s.r.l. lamp with a power of 125 W and an emission range of 250-450 nm. The films were then calcined in air at 800° C for 3 h to remove the organic groups and to yield the final mixed oxides. Homogeneous and well adherent films were obtained on all the substrates. Some selected samples were also calcined at 1000° C for 5 h to investigate their crystallisation behaviour. Transparent and homogeneous films were obtained, having a thickness in the 200-450 nm range. For some selected samples, the thickness was determined by measuring the crater depth made after the SIMS analysis by a Tencor Alpha Step Profilometer. The determined values for some selected samples are reported in Table 2, where the error on the thickness determination contains the contribution of the surface roughness and the profilometer scan error.

place table 2 here

Thin films characterization

FT-IR analyses spectra were recorded in transmission with a Nexus 870 FT-IR spectrometer (Nicolet) in the range from 400 to 4000 cm^{-1}, by using a resolution of 4 cm^{-1}. The films for the analysis were spun onto a one side polished Si wafer.

The composition of the film at the surface and in the bulk was investigated by XPS. Photoelectron spectra were run on a Perkin-Elmer Φ 5600ci spectrometer using non-monochromatized Al-K_α radiation (1486.6 eV). The working pressure was $< 5 \cdot 10^{-8}$ Pa. The spectrometer was calibrated by assuming the binding energy (BE) of the $Au4f_{7/2}$ line at 83.9 eV with respect to the Fermi level. The standard deviation for the BE values was 0.15 eV. The

reported BE were corrected for the charging effects, assigning to the C1s line of adventitious carbon the BE value of 285.0 eV.[30] In the calcined samples, in which no carbon could be detected, charging effects were corrected by assuming that the Si2p peak has the BE typical of silicon in silica, i.e. 103.6 eV. This implies the assumption that silicon experiences mostly an oxygen environment. Considering that, also in the most concentrated sample, the amount of silica is at least 83%, this assumption can be considered reliable in a first approximation. Survey scans were obtained in the 0-1350 eV range. Detailed scans were recorded for the O1s, Si2p, Zr3d, C1s regions in the case of zirconia-silica films and O1s, Si2p, Hf4f, Hf4d, C1s in the case of hafnia-silica films. The atomic composition was evaluated using sensivity factors supplied by Perkin-Elmer.[31] Depth profiles were carried out by Ar^+ sputtering at 3 keV with an Argon partial pressure of $5 \cdot 10^{-6}$ Pa. A specimen area of 2x2 mm^2 was sputtered. A flood gun was used to compensate charging effects on the surface of the irradiated specimens. Samples were introduced directly, by a fast entry lock system, into the XPS analytical chamber.

Glancing incidence XRD patterns were recorded by means of a Bruker D8 Advance diffractometer equipped with a Göbel mirror and a CuK_α source (40 kV, 40 mA), at a fixed incidence angle of 1.5°. The average crystallite dimension was estimated from the most intense diffraction peaks by means of the Scherrer equation.

SIMS measurements were carried on a IMS 4f mass spectrometer (Cameca, Padova, Italy) using a 10 KV Cs^+ primary beam and by negative secondary ion detection (the sample potential was fixed at -4.5 kV) with a final impact energy of 14.5 keV. The SIMS spectra were carried out in ultra-high vacuum conditions at different primary beam intensities (in the range 30-50 nA) rastering over a nominally 125x125 μm^2 area. Beam blanking mode was used to improve the depth resolution, interrupting the sputtering process during magnet stabilization periods. The measurements were performed in high mass resolution-configuration to avoid mass interference artefacts. The charge build-up occurring in insulating samples during the in-depth profiling was compensated by an electron gun without any need to cover the surface with a metal film. The erosion speed was evaluated by measuring the depth of the erosion crater at the end of each analysis by means of a Tencor Alpha Step profilometer with a maximum uncertainty of few nanometers. The dependence of the erosion speed on the matrix composition

was taken into account for each sample by recording various spectra at different depths in each sample.

AFM images were taken using a Park Autoprobe CP instrument operating in contact mode in air. The micrographs were recorded in 3-4 different areas of each sample, in order to test the film homogeneity. The background was subtracted from the images using the ProScan 1.3 software from Park Scientific.

Transmission electron microscopy (TEM) images were taken with a Zeiss EM 912 at an acceleration voltage of 120 kV. Samples were scraped off from the substrate with a razor blade and brought on to a 400 mesh carbon-coated copper grid. Different areas were investigated in order to check the homogeneity of the material.

3. Results and discussion

Before carrying out the deposition of the films, the UV photoinduced polymerisation process was first monitored by FT-IR to optimize the irradiation time. As the polymerisation process proceeds, the intensity of the acrylate ν(C=C) band at about 1638 cm^{-1} decreases due to the C=C double bonds consumption, while the integrated area of the ν(C=O) bands remains constant. Consequently, the ν(C=C)/ν(C=O) area ratio was considered as a measure of the degree of conversion. The conversion of methacrylate moiety was followed by plotting the relative intensity of the double bond vibration versus the irradiation time (Fig. 2).

place fig. 2 here

The degree of conversion shows a trend already observed in similar experiments.[4] While in the early stage of UV irradiation, the C=C bonds are rapidly consumed, a lowering in the reaction rate is observed after about 60' second since the propagation step requires the diffusion of the monomeric species, which are not highly mobile in the reaction mixture. Althought the methacrylate moieties are covalently anchored to an inorganic network already partially crosslinked, a conversion degree of about 70% is reached within about 7 minutes. After this time, no further decrease of the ν(C=C)/ν(C=O) ratio is observed and the curve flattens, thus

indicating that the polymerisation does not proceed any more. On account of these findings, the deposited films were irradiated 10 minutes.

The prepared samples were characterised both *as-prepared* and after the thermal treatment, to investigate the effect of the temperature on their compositional, microstructural and morphological features. The composition of the thin films containing both zirconium and hafnium clusters was at first investigated through FT-IR spectroscopy. In the following, the spectra of the two systems are jointly discussed, since no remarkable difference was pointed out on going from hafnia- to zirconia-based binary oxides. In figure 3 the IR spectra of the sample SiZr21 before (Figure 3a), and after calcination (Figure 3b) are compared.

place fig. 3a-b here

The peak have been assigned according to the values reported in literature[18,32,33] and the main vibration are summarised in the graphs of figure 3a-b.

As it can be seen in the spectrum reported in figures 3a, the typical vibrations of silica are present already in the not calcined samples. In particular, the typical band of silica at 800 cm^{-1} was detected, which is ascribed to the symmetric stretching of oxygen in the Si-O-Si group.[34] This band is in the same region in which the Si-O-Zr vibration would be expected, and whose wavenumbers, according to literature data, should be found at about 802 cm^{-1}.[35] Concerning the *as-prepared* samples, also the intense band at 1118 cm^{-1} is evident, which is ascribed to the ν_{as}(Si-O-Si) asymmetric stretching of the siloxane group. This band shows a shoulder at 1174 cm^{-1}, whose origin has not yet been clarified. In literature, shoulders at about 1200 cm^{-1} have been ascribed to asymmetric stretching in tetranuclear siloxane rings.[36] The band ascribed to Si-O-Si is shifted upon calcination and consequent densification to a lower wavenumber, 1069 cm^{-1}, a value close to that reported in literature, 1080 cm^{-1}. In addition, a further band at 450 cm^{-1} was also detected, which was ascribed to the *rocking* vibrations of the Si-O-Si.[34] The peaks at 2960 e 2930 cm^{-1} are ascribed to the asymmetric stretching $\nu_{as}(CH_3)$ of the not yet completely hydrolysed Si-O-Et groups and to the symmetric ν_s(CH) stretching of the terminal methylene double bonds respectively.

In the *as-prepared* samples, the vibrations typical of the organic components of the matrix are also well evident. In particular, the sharp band of the C=O carbonyl group at 1722 cm^{-1} and that of the C-O ester group of the methacrylate at 1330 cm^{-1} are also clearly detected. Due to the overlapping of the bands, the ν(C=O) vibration of the methacrylate groups of the cluster could not be identified. In addition, at 1635 cm^{-1} the band assigned to the C=C vibration of the methacrylate double bond was pointed out. The fact that this band is still present also after UV curing can be ascribed to the lack of a complete polymerisation of the methacryloxy moieties of the silane. This can in turn be traced back to the hampered mobility of the methacrylate groups, which are covalently linked to the already partially formed silica network. Furthermore, the steric restrictions imposed by the two isostructural clusters, both bearing 12 methacrylate groups, is also expected to play a role in avoiding the complete copolymerisation of the cluster methacrylate groups with the methacryloxysilane, thus explaining the presence of unreacted double bonds.

In the not calcined sample, a broad band at 3450 cm^{-1} is detected. Two different contributions can originate this band: the stretching vibration of the OH groups of water adsorbed on the film surface and the vibration of the Si-OH groups formed upon hydrolysis. In fact, this band disappears upon calcination, which induces a further densification of the matrix through condensation of silanols groups to give Si-O-Si. In the calcined samples, only the bands of silica at 1063, 804 and 447 cm^{-1} are present, while the features typical of the organic parts completely disappeared.

On account of these findings, the IR spectra allowed us to conclude that:

- the formation of a polysiloxane network is observed already in the hybrid thin film;
- the methacrylate groups are not completely polymerised, due to the steric hindrance and to the limited mobility imposed by the silica matrix;
- heating induces a complete densification of the matrix and the complete disappearance of the organic components;
- the presence of vibrations ascribable to mixed Si-O-M bonds could not be ascertained.

The surface and in-depth composition of the films was investigated by XPS and SIMS. For the sake of clarity, XPS and SIMS data are discussed together, since the two methods provide complementary and mutually integrated information arising from different depth resolution, erosion capability and speed. Also in this case, for some selected films, the analyses were repeated on the *as-prepared* as well as on the calcined specimens. For comparison, the surface XPS spectrum of the UV polymerised MAMTES (SiHf0) *as-prepared* was also acquired. This latter sample shows, after calcination, the typical features of a silica network. In particular, the Si2p and O1s regions have the binding energies of 103.6 and 533.0 eV respectively. These values are in good agreement with those typical of silicon dioxide, 103.6 and 532.5 eV respectively.[31] The O/Si atomic ratio in the analysed specimen is higher than the stoichiometric one, i.e. 2. This finding can be ascribed to the presence of hydroxyl groups on the surface of the silica films.

In figure 4, the survey spectra of samples SiZr17, SiHf11 and SiHf0 *as-prepared* are superimposed, while in figure 5 the survey of the calcined SiZr17 and SiHf11 samples are plotted.

place figure 4 and 5 here

For the elements of interest, detailed scans were also acquired. In the *as-prepared* samples, all the expected elements (C, Si, O, Zr, Hf) were detected. The composition of the film was analysed on the surface as well as in-depth. The samples were sputtered and the analysis of the eroded surface was carried out after each sputtering cycle. By using this operation mode, depth profiles were obtained.

In-depth quantitative analysis performed on both *as-prepared* and calcined samples reveals an even distribution of the guest zirconium and hafnium related species. In figure 6, the Si/Zr atomic ratios in the sample SiZr17 before and after the thermal treatment are reported, while in figure 7, the Si/Hf atomic ratios in the sample SiHf25 before and after the thermal treatment are plotted.

place figure 6 here

place figure 7 here

As it can be seen in the plots of the ratio of the atomic percentages *vs*. time of sputtering, which can be in turn related to the eroded depth, the guest species are evenly distributed along the whole film thickness. It should be pointed out, however, that the lateral distribution of XPS is about 5-10 μm, therefore heterogeneities of a smaller dimension cannot be detected by this technique. This even distribution is observed in both the *as-prepared* and calcined specimens. These findings confirm that the calcination treatment does not affect the distribution of the species in the samples on the given scale. A significant difference among the two set of samples concerns the carbon content. While in the crude samples, due to the presence of the inorganic-organic hybrid structure, carbon is detected in a considerable amount (40%), a very low content of carbon (< 1%) is present after calcination.

Assuming that silicon is mostly present as silica, and by giving the Si2p the value of SiO_2, i.e. 103.6 eV,[31] the binding energy value of $Zr3d_{5/2}$, corrected for charging effects, results in 183.5 eV for sample SiZr17, a values higher than bulk zirconium oxide, i. e. 182.2 eV.[31] This finding can be rationalised by considering that in a system consisting of zirconia particles dispersed in a silica matrix, zirconium experiences a chemical environment which is substantially different from that in bulk zirconia. Since Si is more electronegative than zirconium, an Si-O- bond around Zr is expected to withdraw more electron density than a Zr-O environment which would be expected in the case of a pure zirconium oxide. This in turn implies a shift of the Zr3d BE to higher values, as experimentally observed.

A shift to higher binding energies of the Zr3d peak has been already observed for zirconia-silica binary nanocomposite characterised by a zirconia loading < 20% wt.[37] In particular, in this study, a value of 183.1 eV for a sample containing 9.3% wt of zirconia was measured, and the shift to higher value was ascribed to the smaller relaxation energy for highly dispersed zirconium oxide species compared to the powdered ZrO_2. A similar trend was observed also for

the SiHf24 sample, in which the Hf4f is characterised by a BE of 19.3 eV, a value higher than that reported for hafnium oxide, 16.7 eV.[31]

In the zirconium sample, the atomic percentages obtained by XPS are: 1.7% (Zr), 29.5% (Si), 68.8 % (O). These data are in very good agreement with the theoretical ones, i.e. 1.8%, 31.5%, 66.7% for zirconium, silicon and oxygen, respectively. In particular, the experimental Si:Zr atomic ratio results 17, in complete agreement with the calculated ratio (i.e. 17).

Also in the case of the analysed hafnium sample, the measured atomic percentages (3.6% Hf, 66.7% O, 29.4% Si) are in very good agreement with the nominal composition (2.8% Hf, 66.7% O, 30.5% Si).

The in-depth distribution of zirconium and hafnium in the silica matrix along the whole film thickness was further investigated by using SIMS. In particular, SIMS analyses were performed to check the elements in-depth profile and the presence of contaminants in both the *as-prepared* and calcined samples. Fig.8a and Fig.8b report the element SIMS profiles of sample SiHf24 before and after thermal treatment, respectively.

place figure 8a-b here

The film thickness in the case of the *as-prepared* sample was found to be close to 430 nm and significantly decreases after the calcination treatment due to the densification of the film. The film-to-substrate interface is sharp and the element inter-diffusion layer is lower than 50 nm in the *as-prepared* sample but increases up to 100 nm after calcination. SIMS data also pointed out that the calcination process does not influence the film composition since the Hf content appears to remain constant through the film as observed in the *as-prepared* sample. Similar results were found also in the case of zirconium samples, which are extensively described elsewhere.[38]

The microstructure of the thin films was investigated through grazing angle X-ray diffraction to minimise the contribution of the silica substrate. The 800° C calcined samples of both the zirconium and hafnium based silica films display a featureless XRD pattern, characterised only by the presence of a broad band, peaked at 21.5° and ascribed to amorphous silica. The absence of diffraction peaks can be either ascribed to the presence of amorphous zirconia or hafnia or to the presence of undetectable crystallites. This latter hypothesis appears more reasonable in our case,

since the adopted approach, based on the grafting of the cluster to the forming silica matrix, should favour nucleation and avoid agglomeration of host particles. Selected samples were further thermal calcined twice at 1000° C for 5 h. After the calcination at 1000° C, diffraction peaks were observed for both zirconia (Fig. 9a) and hafnia samples (Figure 9b).

place figure 9a-b here

As far as the SiZr5 zirconia-based sample is concerned, as it can be seen in figure 9a, sharp peaks were detected which, on the basis of data reported in JCPDS (*Joint Commitee on Powder Diffraction Standards*), were ascribed to tetragonal zirconia. The most intense peak at 2θ=22° was ascribed to silica, while the peaks at 30.2° (011), 35.5° (110), 50.5° (112) to tetragonal ZrO_2. The second thermal treatment at 1000° C for 5 h does not remarkably change the diffraction pattern.

By applying the Scherrer formula[39] at the peak at 30.2°, the zirconia crystallite size was estimated to be 10 nm.

The SiHf24 thin film was calcined as already described for zirconium. In this case, the diffraction pattern, ascribed to the formation of tetragonal hafnia, show broader peaks than in the case of the zirconia-based sample.

The calcination conditions being equal, this fact can be ascribed to a lower content of the guest oxide in the host matrix. While in the case of SiZr5 the zirconium oxide is about the 16.7% molar with respect to silica, in this latter case the molar ratio is 4% at.

As already observed in the case of zirconia, also in the hafnia-based sample, a noticeable delay in crystallisation was observed.[19]

The crystallisation of these binary systems has been thoroughly investigated, since, as mentioned, the obtainment of microstructurally homogeneous materials is a key concern to be addressed, and since phase transitions can dramatically affect the properties of the final materials.[17, 40-48] Generally, the crystallisation of tetragonal zirconia has been reported to occur after calcination at 400° C,[18] while partial transformation from tetragonal to monoclinic was reported to occur at 800-900 °C and the single monoclinic phase is present at temperature higher

than 1000-1200 °C. In a previous study from Neumayer,[18] addition of silica to zirconium and hafnium oxide was found to increase the temperature of crystallisation of zirconium oxide, to stabilise the formation of tetragonal hafnia and to increase the temperature at which the transformation of ZrO_2 or HfO_2 from the tetragonal to the monoclinic phase occurs. The lower the content of hafnia or zirconia is, the higher is the crystallisation temperature. As extensively reported by Terry *et al*.,[49] the initial formation of the thermodynamically instable tetragonal (t) zirconia and the delayed formation of monoclinic (m) zirconia have been explained in terms of surface and strains energies of hafnia or zirconia nanoparticles and in the hindered nucleation of the martensitic t/m transition, which is also slightly displacive. Whenever zirconia or hafnia are homogeneously dispersed in a silica matrix, the crystallisation requires both diffusion as well as grain growth, and a correlation between this delayed crystallisation and the homogeneity of the materials has been established.[49] Well-mixed samples display higher crystallisation temperature,[50] which in turn make them suitable for high temperature applications thanks to their enhanced resistance to the "thermal shock" associated with the mentioned martensitic transformation.

As described, XPS and SIMS depth profiles show a homogeneous in-depth distribution of the host species. A homogeneous in-depth profile of the involved species (Si, O, Hf/Zr) could be ascribed either to a) a complete intermixing of the host oxide with the guest matrix (formation of a mixed oxide solid solution) or b) to the formation of well distributed host clusters in the guest matrix having a size smaller than the lateral resolution of the two methods. The TEM micrographs acquired to further investigate the distribution of the clusters into the matrix definitely rule out this former hypothesis and clearly show the presence of isolated clusters. The two calcined samples SiZr5 and SiHf24, characterised by different compositions, were analysed by TEM (Fig. 10 and 11, respectively).

place figure 10 and 11 here

In both samples isolated nanoparticles having a diameter ranging in the interval 5-10 nm were detected. The average diameter of particles seen in the TEM images well correlates with the crystallite size obtained by Scherrer equation from XRD data. The presence of crystalline

nanoparticles of hafnia in SiHf24 and zirconia in SiZr5, respectively, was proved by electron diffraction (data not shown). The SiZr5 sample, characterised by a quite high concentration of zirconia, shows also some agglomeration, which can be ascribed to the relatively high concentration of zirconia in the silica matrix, leading to some coalescence of the nanoparticles. On the contrary, these agglomeration phenomena are not pointed out in the more diluted sample containing hafnia clusters.

The morphology of the thin films was analysed through AFM. For each analysed sample, three micrographs of different surface areas were examined to test the topography uniformity of the films. The zirconia- and hafnia-based samples are characterised by a quite smooth, crack-free and homogeneous surface. The surface morphology of the sample SiZr17 before and after calcination is shown in figure 12.

place figure 12 here

The average roughness of the specimens was also evaluated and the obtained values for two samples before and after calcination are summarised in table 3.

The adhesion of the films on the substrate was evaluated by pull-off tests. Two different series of calcined samples, each consisting of 4 specimens and characterized by two different compositions, namely SiZr0 and SiZr5, were tested. Both the series provided an average adhesiveness value of about 650 N/cm^2, thus showing that the presence of the cluster does not significantly influence the adhesion. This value can be viewed as a lower bound of the adhesiveness since in most cases the bonding tape (SCOTCH-WELD^{TM} brand bonding film 588) used to contact the test-stud to the coating failed. A direct bonding of the test stud to a glass substrate yielded similar values, so the adhesion of the coating to the substrate can be considered as excellent.

4. Conclusion

ZrO_2-SiO_2 and HfO_2-SiO_2 films of different compositions were grown by a modified sol-gel procedure, involving the use of a bifunctional siloxane and of Hf- and Zr-oxocluster as molecular building blocks. The adopted approach has been proved to be effective to obtain an homogeneous distribution of the two guest oxides in the host silica matrix and to favour the formation of well-dispersed nanosized clusters. In particular, XPS and SIMS in-depth profiles point out a very smooth distribution of the two oxides within the whole thickness of the layers. From XRD data, the addition of silica to the two oxides was found to increase the crystallisation temperature of the crystalline phase. This has been ascribed to the preservation of the molecular-level homogeneity in the transition from the solution precursors to the final ceramic materials. TEM micrographs confirmed the presence of isolated crystalline clusters of zirconia and hafnia whose size, in agreement with XRD data, are about 5-10 nm.
The grafting of the cluster (molecular precursor for the guest oxides) to the bifunctional silane (precursor for the host matrix) has been demonstrated to represent an effective route to achieve highly dispersed transition metal oxides in silica. The prepared films are furthermore smooth, transparent and characterised by a very high adhesion to the silica substrate.

Acknowledgments

Antonio Ravazzolo, Daniele Camozzo and Fabrizia Poli are gratefully acknowledged for their precious technical assistance. Ministero degli Affari Esteri, Rome, Italy and the Österreichischer Austauschdienst (ÖAD), Vienna, Austria, are gratefully acknowledged for the financial support of an Italy-Austria Bilateral Scientific Cooperation (Project 17/2004). A. Z. thanks Whirlpool Europe s.r.l for a research scholarship.

References

(1) Brinker, C. J.; Scherer, G. W. *Sol-Gel Science - The Physis and Chemistry of Sol-Gel Processing*; Academic Press: New York, 1990.

(2) Mountjoy, G.; Holland, M.A.; Gunawidjaja, P.; Wallidge, G. W.; Pickup, D.M.; Newport, R.J.; Smith M.E. *J. Sol-Gel Sci. Techn.* **2003**, *26*, 161, and references therein.

(3) Saravanamuttu, K.; Xin Min D.; Najafi, S. I.; Andrews, M.P. Can. J. Chem. **1998**, 76, 1717.

(4) Park, O. K.; Jung, J. I.; Bae, B.S. *J. Mater. Res.* **2001**, *16*, 2143.

(5) Soppera, O.; Croutxé-Barghorn, C.; Carrè, C.; Blanc, D. *Appl. Surf. Scie.* **2002**, *186*, 91.

(6) Itoh, M.; Hattori, H.; Tanabe, K.J. *J. Catal*. **1974**, *35*, 225.

(7) Miller, J.B.; Ko, E.I.; *J. Catal.* **1996**, *159*, 58.

(8) Soled, S.; McVicker, G.B. *Catal. Today* **1992**, *14*, 189.

(9) Feng, Z. T.; Postula, W. S.; Erkey, C.; Philip C. V.; Akgerman, A.; Anthong, R. G. *J. Catal.* **1994**, *148*, 84.

(10) Lopez, T.; Tzompantzi, T.; Navarrete, J.; Gomez, R.; Boldù, J.L.; Munoz, E.; Novaro O. *J. Catal.* **1999**, *181*, 285.

(11) Bosman, H. J. M.; Kruissink, E. C.; Vanderspoel, J.; Vandenbrink F., *J. Catal.*, **1994**, *148*, 660.

(12) Simhan, R.G. *J. Non-Cryst. Solids* **1983**, *54*, 335.

(13) Paul, A. *J. Mater. Sci.* **1977**, *12*, 2246.

(14) Wilk, G.D.; Wallace, R.M.; Anthony, J.M. *J. Appl. Phys.* **2000**, *87*, 484.

(15) Wilk, G.D.; Wallace, R.M. *Appl. Phys. Lett.* **1999**, *74*, 2854.

(16) Wilk, G.D.; Wallace, R.M. *Appl. Phys. Lett.* **2000**, *76*, 112.

(17) Maria, J. P.; Wickaksana, D.; Parrette, J.; Kingon, A.I. *J. Mater. Res.* **2002**, *17*, 1571.

(18) Neumayer, D.A.; Cartier, E. *J. Appl. Phys.* **2001**, *90,* 1801.

(19) Del Monte, F.; Larsen, W.; Mackenzie, J.D. *J. Am. Ceram. Soc.* **2000**, *61*, 371.

(20) Zhan, Z.; Zeng H.C. *J. Non-Cryst. Solids* **1999**, *243*, 26, and references therein.

(21) Miller, J.B.; Ko, E. I. *Catal. Today* **1997**, *35*, 269.

(22) Trimmel, G.; Gross, S.; Kickelbick, G.; Schubert, U., *Appl. Organom. Chem.* **2001**, *15*, 410.

(23) Gross, S.; Kickelbick, G.; Puchberger, M.; Schubert, U. *Monatshefte für Chemie* **2003**, *134*, 1053.

(24) Schubert, U. *Chem. Mater.* **2001**, *13*, 3487, and references therein.

(25) Kickelbick, G. *Prog. Polym. Sci.* **2003**, *28*, 83.

(26) Schubert, U. *J. Sol-Gel Scien. Techn.* **2003**, *26*, 47.

(27) Schubert, U. *Polymers Reinforced by Covalently-Bonded Metal Oxide Clusters; in: Organic/Inorganic Hybrid Materials*; Electronic Publ. Services: Hattiesburg, 2003.

(28) Armelao, L.; Gross, S.; Lavrencic-Stangar, U.; Orel, B.; Sassi A.; Zattin, A. *in preparation.*

(29) Armelao, L.; Bertoncello, R.; Coronaro, S.; Glisenti, A. *Science and Technology for Cultural Heritage* **1998**, *7*, 4.

(30) Briggs, D.; Seah, M.P. *Practical Surface Analysis*; John Wiley & Sons: 1990.

(31) Moulder, F.; Stickle, W. F.; Sobol, P. E.; Bomben, K. D. *Handbook of X-Ray Photoelectron Spectroscopy*; Perkin Elemer Corporation: Eden Prairie MN, 1992.

(32) Del Monte, F.; Larsen, W.; Mackenzie, J. D. *J. Am. Ceram. Soc.* **2000**, *83*, 628.

(33) Nishide, T.; Honda, S.; Matsuura, M.; Ide, M. *Thin Solid Films* **2000**, *371*, 61.

(34) Innocenzi, P. *J. Non-Cryst. Solids* **2003**, *319*, 309.

(35) Pauthe, M.; Phalippou, J.; Corriu, R.; Declercq, D.; Vioux, A. *J. Non-Cryst. Solids* **1989**, *113*, 21.

(36) Innocenzi, P.; Brusatin, G.; Licoccia, S.; Di Vona, M. L.; Babonneau, F.; Alonso, B. *Chem. Mater.* **2003**, *15*, 4790.

(37) Moon, S.C.; Fujino, M.; Yamashita, V H.; Anpo, M. *J. Phys. Chem. B* **1997**, *101*, 369.

(38) Armelao, L.; Bleiner, D.; Di Noto, V.; Gross, S.; Sada, C.; Schubert, U.; Tondello, E.; Vonmont, H.; Zattin, A. submitted to *Appl. Surf. Sci.*

(39) Klug, H.P.; Alexander, L.E. *X-ray diffraction procedures for polycrystalline and amorphous materials*; John Wiley & Sons: New York, 1954.

(40) Osendi, M. I.; Moya, J. S.; Serna, C. J.; Soria, J. *J. Am. Ceram. Soc.* **1985**, *68*, 135.

(41) Garvie, R. C. *J. Phys. Chem.* **1965**, *69*, 1238.

(42) Garvie, R. C. *J. Phys. Chem.* **1978**, *82*, 218.

(43) Nagarajan, V. S.; Rao, K. J. *J. Mater. Sci.* **1989**, *24*, 2140.

(44) Lange, F. F. *J. Mater. Sci.* **1982**, *17*, 225.

(45) Lange, F. F. *J. Mater. Sci.* **1982**, *17*, 235.

(46) Cannon, W. R. *J. Am. Chem. Soc.* **1994**, *77*, 1706.

(47) Heuer, A. H.; Claussen, N.; Kriven, W. M.; Rühle, M. *J. Am. Ceram. Soc.* **1982**, *65*, 642.

(48) Skandan, G.; Hahn, H.; Roddy, M.; Cannon, W. R. *J. Am. Ceram. Soc.* **1994**, *77*, 1706.

(49) Terry, K. V.; Lugmair, C. G.; Tilley, T. D. *J. Am. Chem. Soc.* **1997**, *119*, 9745.

(50) Nogami, M.; Nagasaka, K.; Kadono, K.; Kishimoto, T. *J. Non-Cryst. Solids* **1988**, *100*, 298.

Captions to tables and figures

Table 1- Composition and labelling of the samples

Table 2- Thickness of some selected film (FWHM = Full Width at Half Maximum)

Table 3- Average roughness of the samples SiZr21 and SiHf24 before and after calcination

Fig. 1- Flow-chart describing the synthesis route

Fig. 2- C=C/C=O intensity ratio as a function of the polymerisation time

Fig. 3- IR spectra of the *as-prepared* (a) and of the calcined (b) SiHf11 sample

Fig. 4-Survey of the *as-prepared* samples SiHf11**,** SiZr17 and SiHf0

Fig. 5-Survey of the samples SiHf11 and SiZr17 after calcination

Fig. 6-Si/Zr atomic ratio in *as-prepared* and calcined SiZr17 sample as a function of the sputtering time

Fig. 7-Si/Hf atomic ratio in *as-prepared* and calcined SiHf11 sample as a function of the sputtering time

Fig. 8-SIMS depth profiles of the sample SiHf24 *as-prepared* (a) and calcined (b)

Fig. 9-GI-XRD pattern of the samples SiZr5 (a) and SiHf24 (b) calcined at 1000° C 5 h

Fig. 10-TEM micrograph of the sample SiZr5 calcined

Fig. 11-TEM micrograph of the sample SiHf24 calcined

Fig. 12-AFM micrographs of the samples SiZr17 *as-prepared* (a) and calcined (b)

Table 1

Sample	Si/M
SiHf5	5
SiHf11	11
SiHf24	24
SiHf39	39
SiHf0	without cluster
SiZr5	5
SiZr17	17
SiZr21	21

Table 2

Sample	Thickness FWHM (nm) as prepared	Thickness FWHM (nm) after calcination
SiHf39		247±27
SiHf5		198±21
SiZr17		209±18
SiZr5	431±37	258±18

Table 3

sample	thermal treatment	mean roughness (nm)
SiZr21	no	0.5
SiZr17	800° C for 3h	0.4
SiHf24	no	0.6
SiHf24	800° C for 3h	0.4

Figure 1

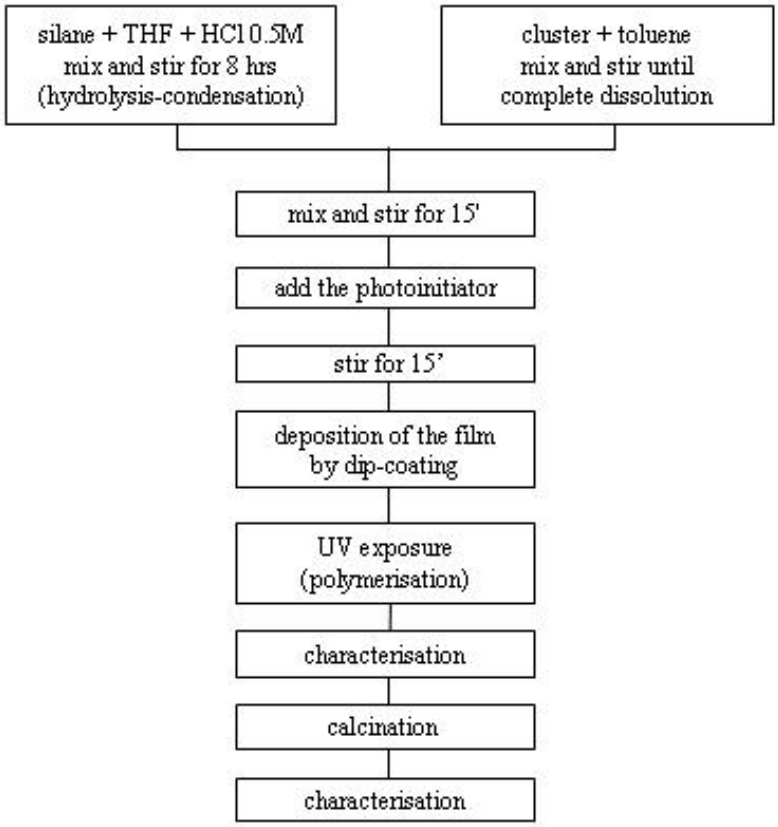
silane + THF + HCl 0.5M
mix and stir for 8 hrs
(hydrolysis-condensation)
cluster + toluene
mix and stir until
complete dissolution
mix and stir for 15'
add the photoinitiator
stir for 15'
deposition of the film
by dip-coating
UV exposure
(polymerisation)
characterisation
calcination
characterisation

Figure 2

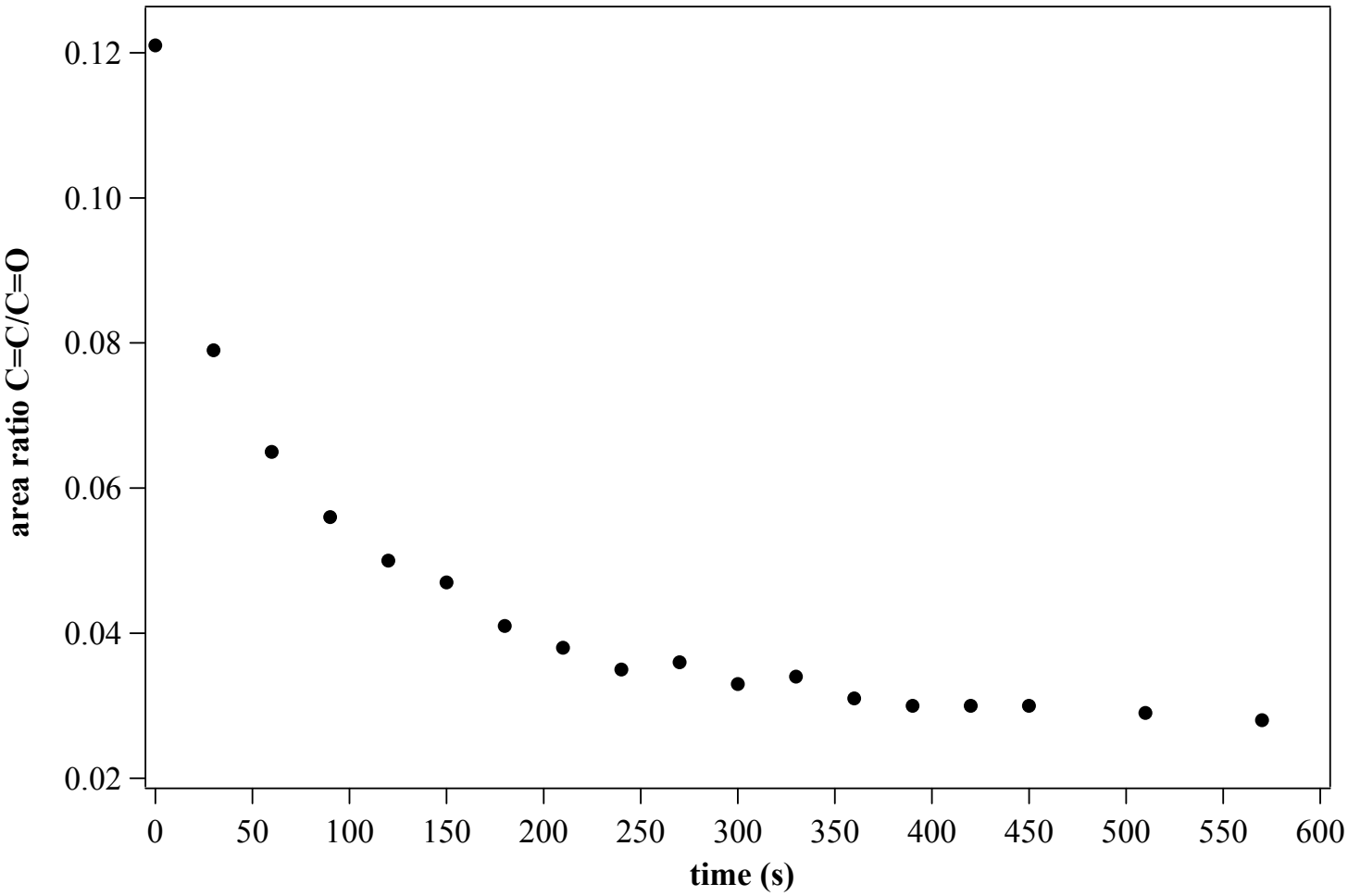
0.12
0.10
0.08
0.06
0.04
0.02
area ratio C=C/C=O
0
50
100
150
200
250
300
350
400
450
500
550
600
time (s)

Figure 3

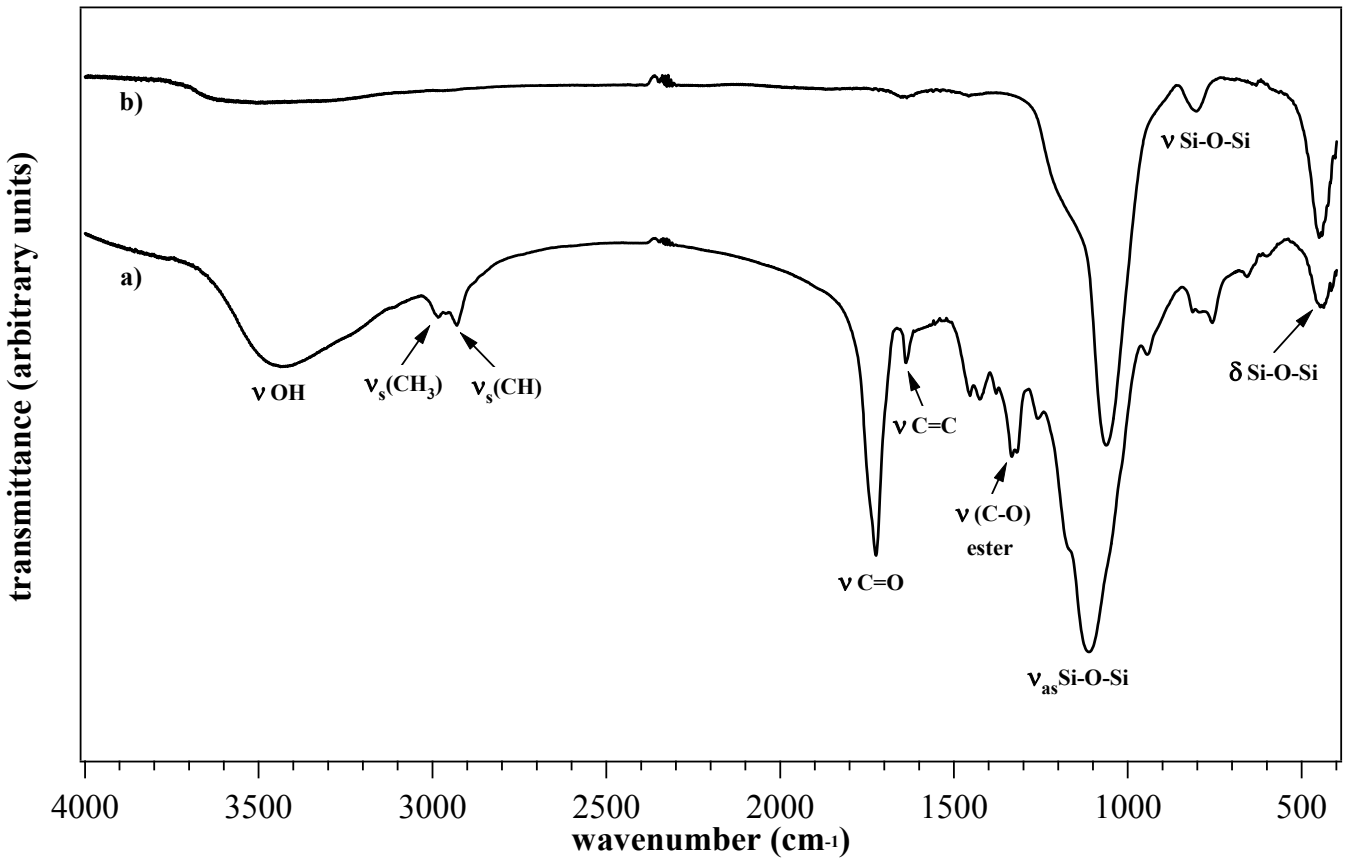
b)
a)
ν Si-O-Si
ν OH
$\nu_s(CH_3)$
$\nu_s(CH)$
ν C=C
ν (C-O)
ester
ν C=O
ν_{as}Si-O-Si
δ Si-O-Si
transmittance (arbitrary units)
4000
3500
3000
2500
2000
1500
1000
500
wavenumber (cm^{-1})

Figure 4

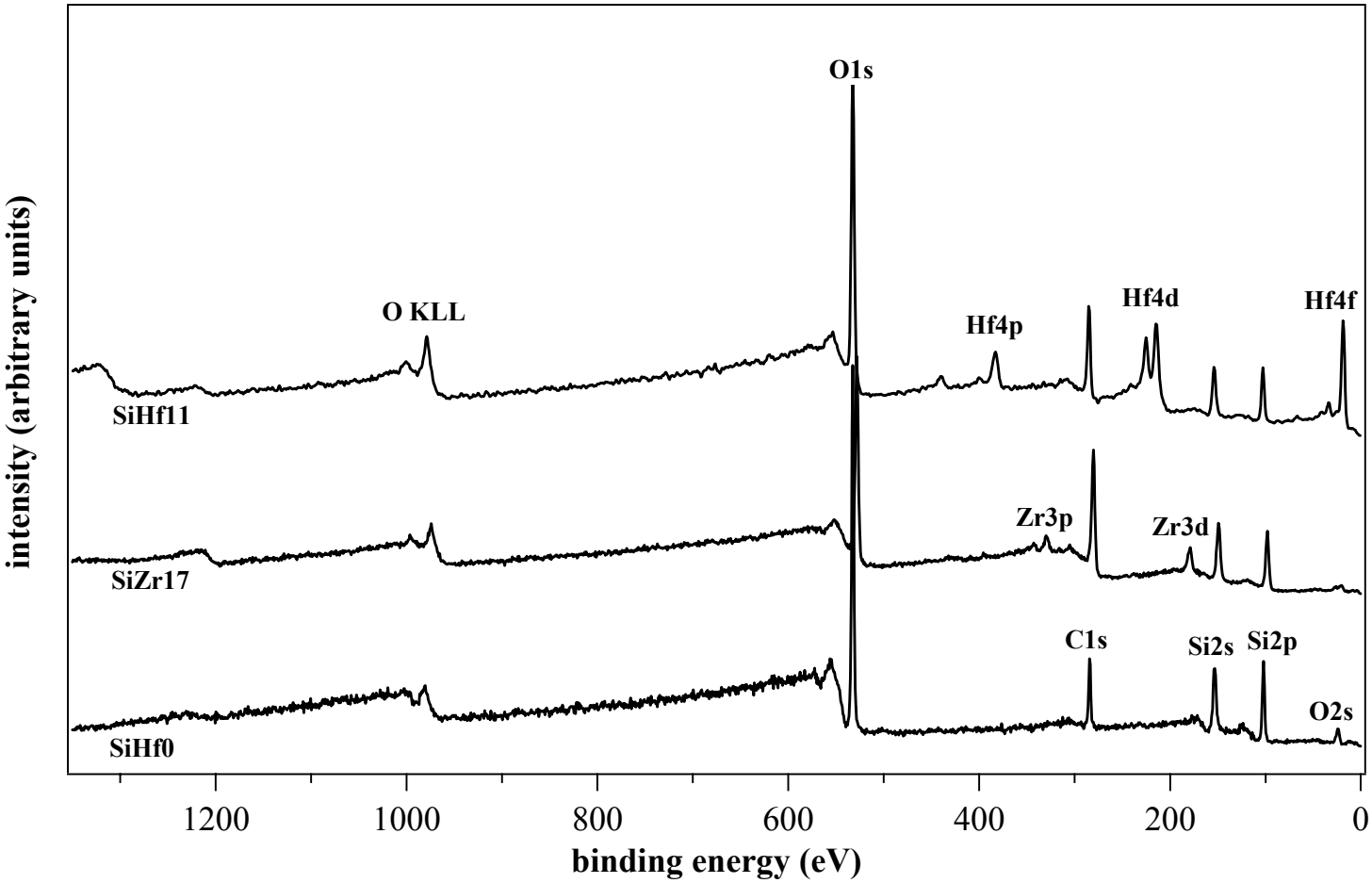
O1s
O KLL
Hf4p
Hf4d
Hf4f
SiHf11
Zr3p
Zr3d
SiZr17
C1s
Si2s
Si2p
O2s
SiHf0
intensity (arbitrary units)
1200
1000
800
600
400
200
0
binding energy (eV)

Figure 5

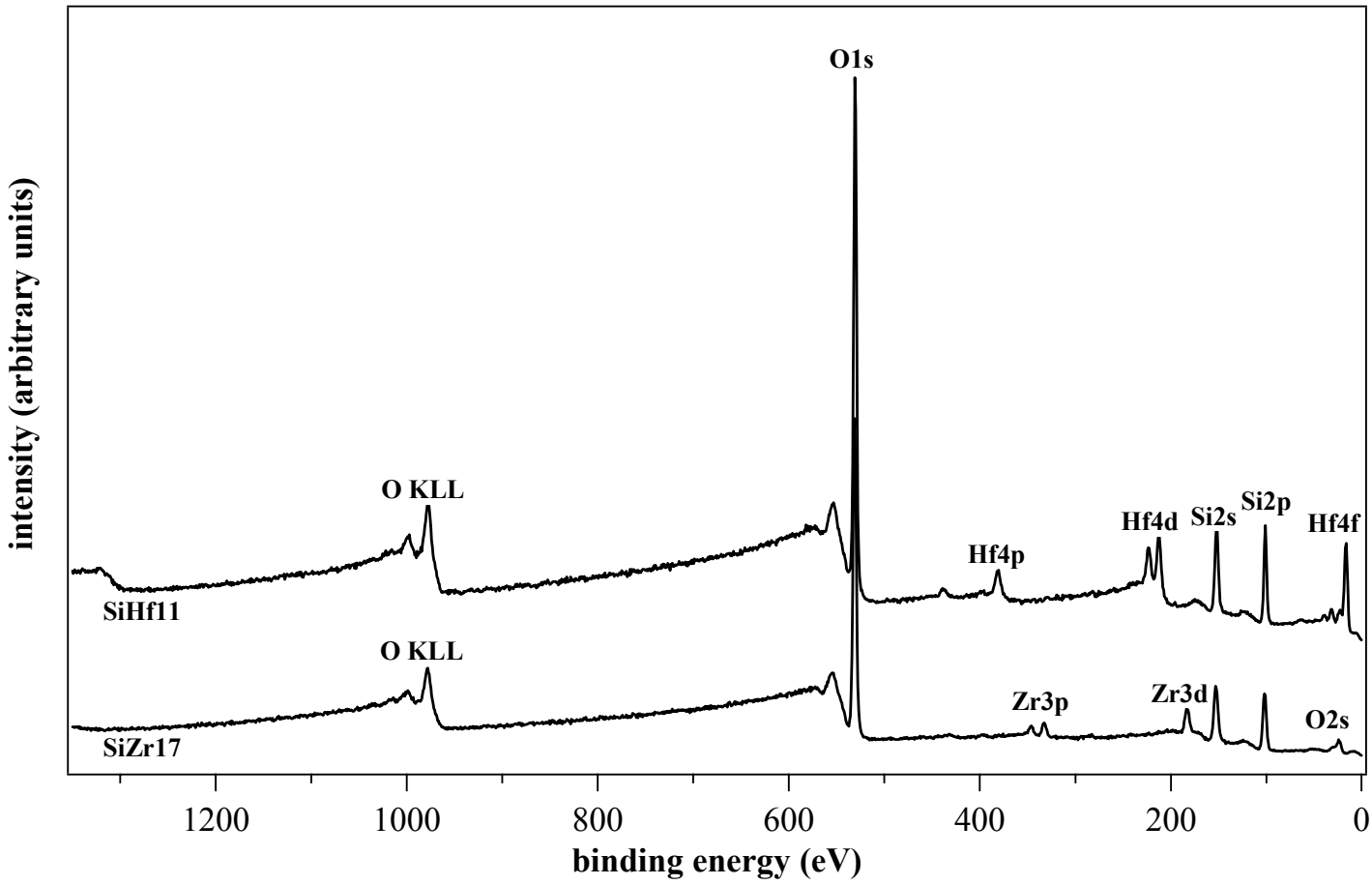
O1s
O KLL
Hf4p
Hf4d
Si2s
Si2p
Hf4f
SiHf11
O KLL
Zr3p
Zr3d
O2s
SiZr17
intensity (arbitrary units)
1200
1000
800
600
400
200
0
binding energy (eV)

Figure 6

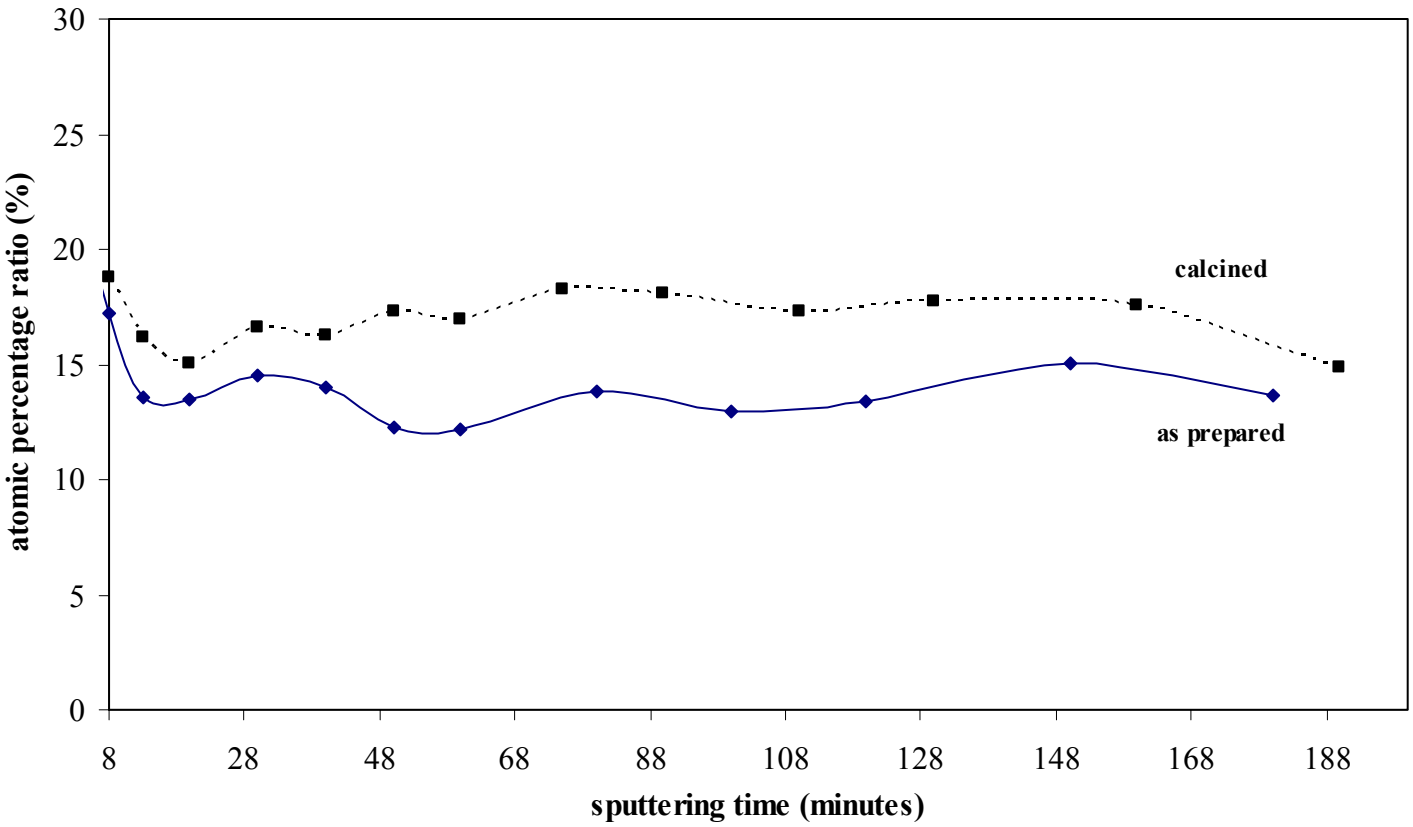
30
25
20
15
10
5
0
atomic percentage ratio (%)
calcined
as prepared
8
28
48
68
88
108
128
148
168
188
sputtering time (minutes)

Figure 7

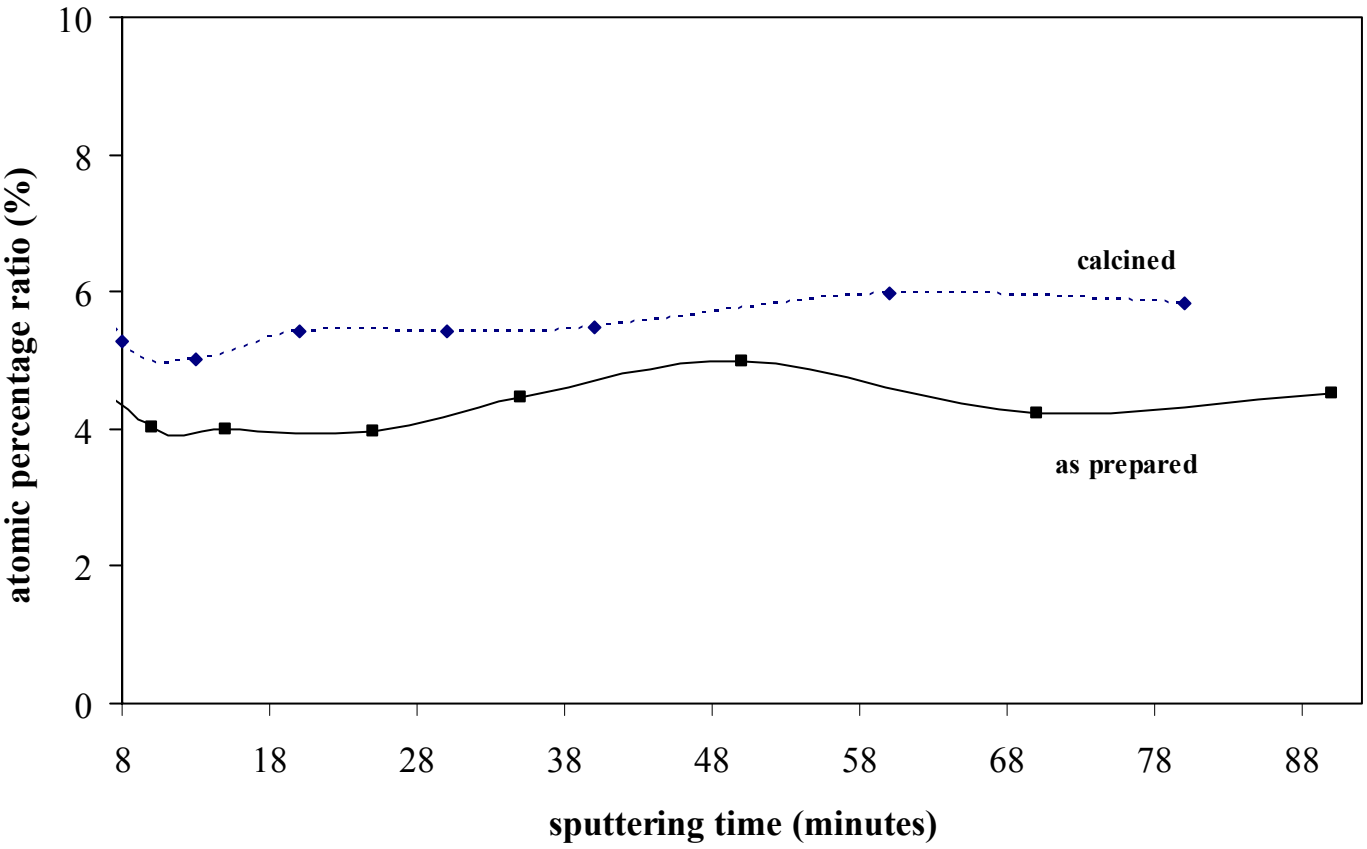
10
8
6
4
2
0
atomic percentage ratio (%)
calcined
as prepared
8
18
28
38
48
58
68
78
88
sputtering time (minutes)

Figure 8

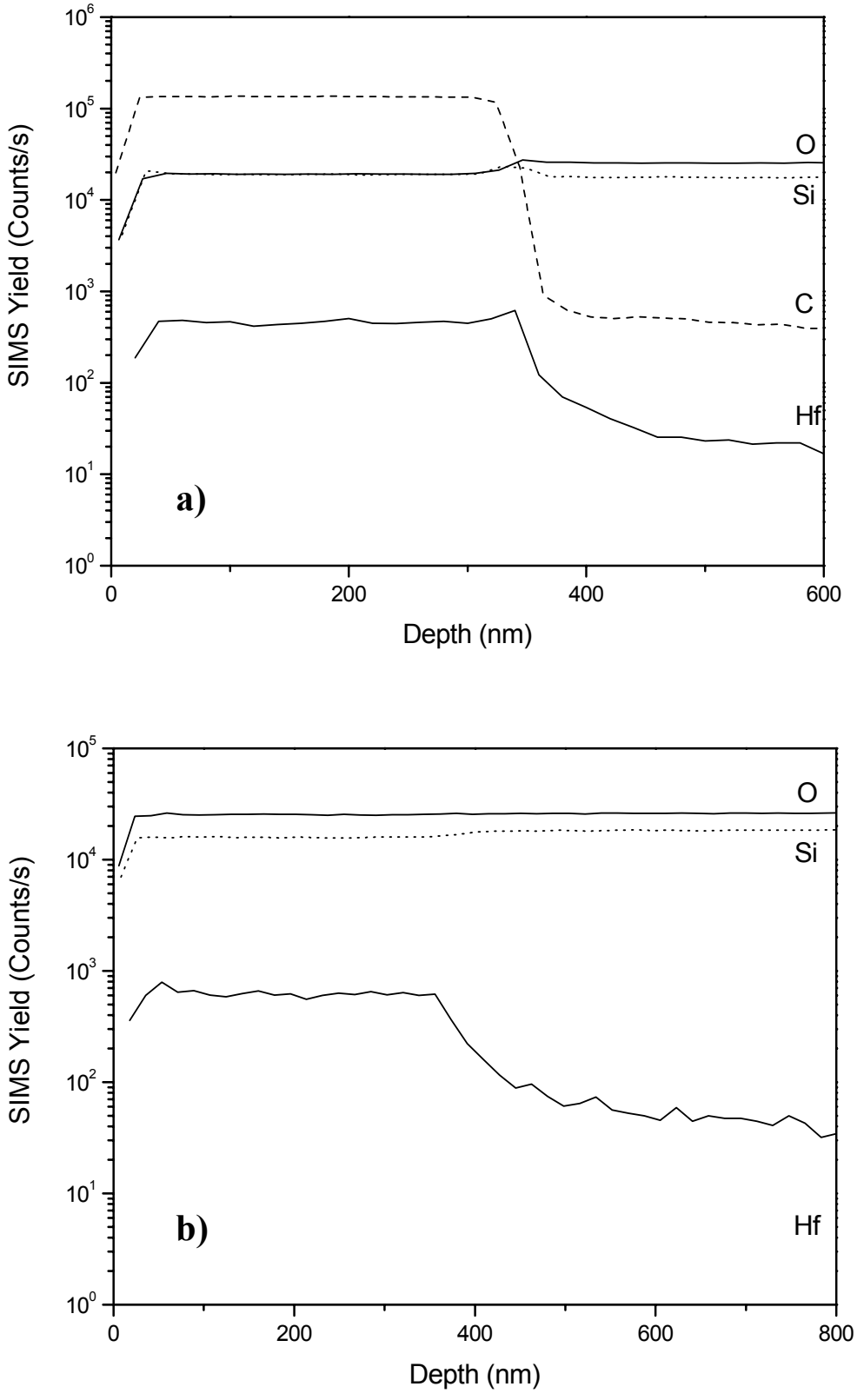

Figure 9

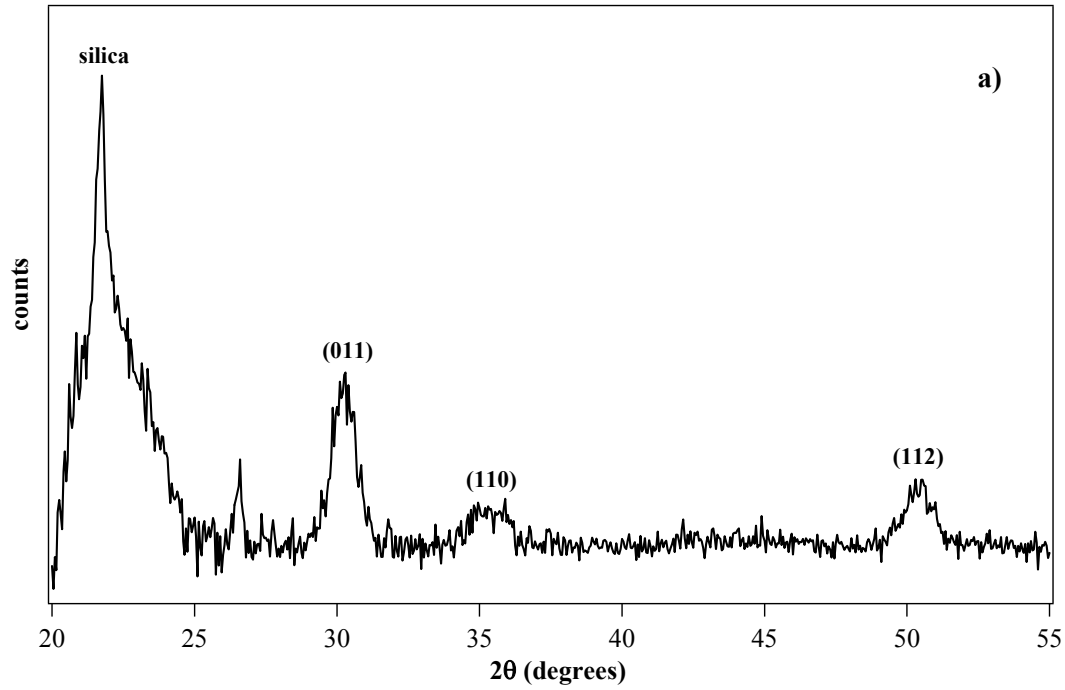
silica
a)
counts
(011)
(110)
(112)
20
25
30
35
40
45
50
55
2θ (degrees)

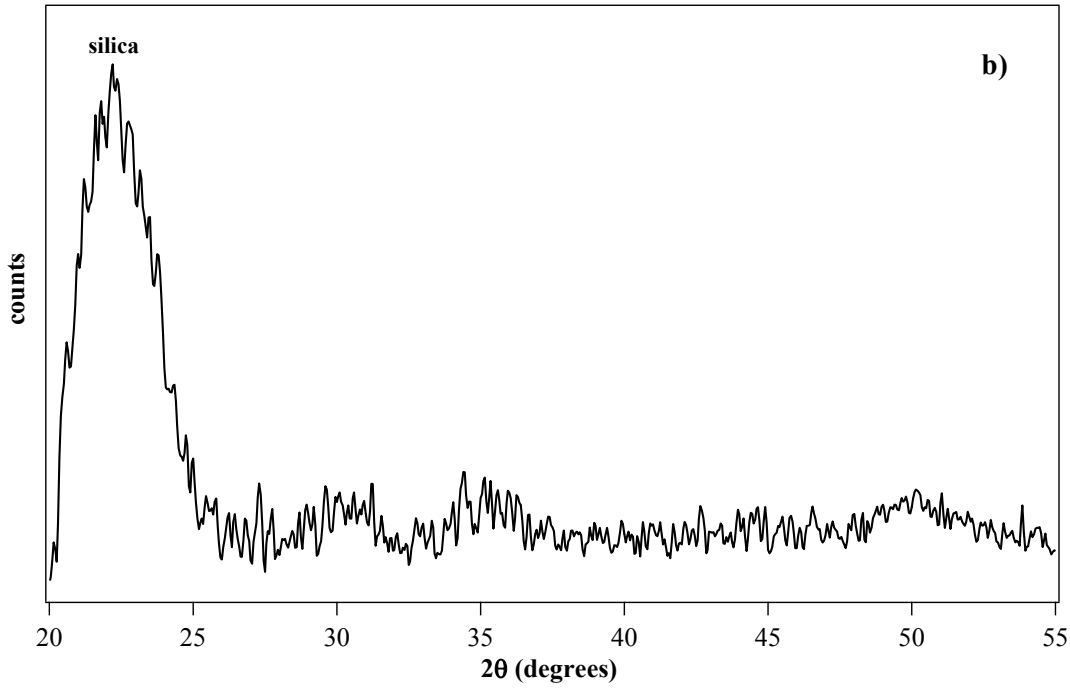
silica
b)
counts
20
25
30
35
40
45
50
55
2θ (degrees)

Figure 10

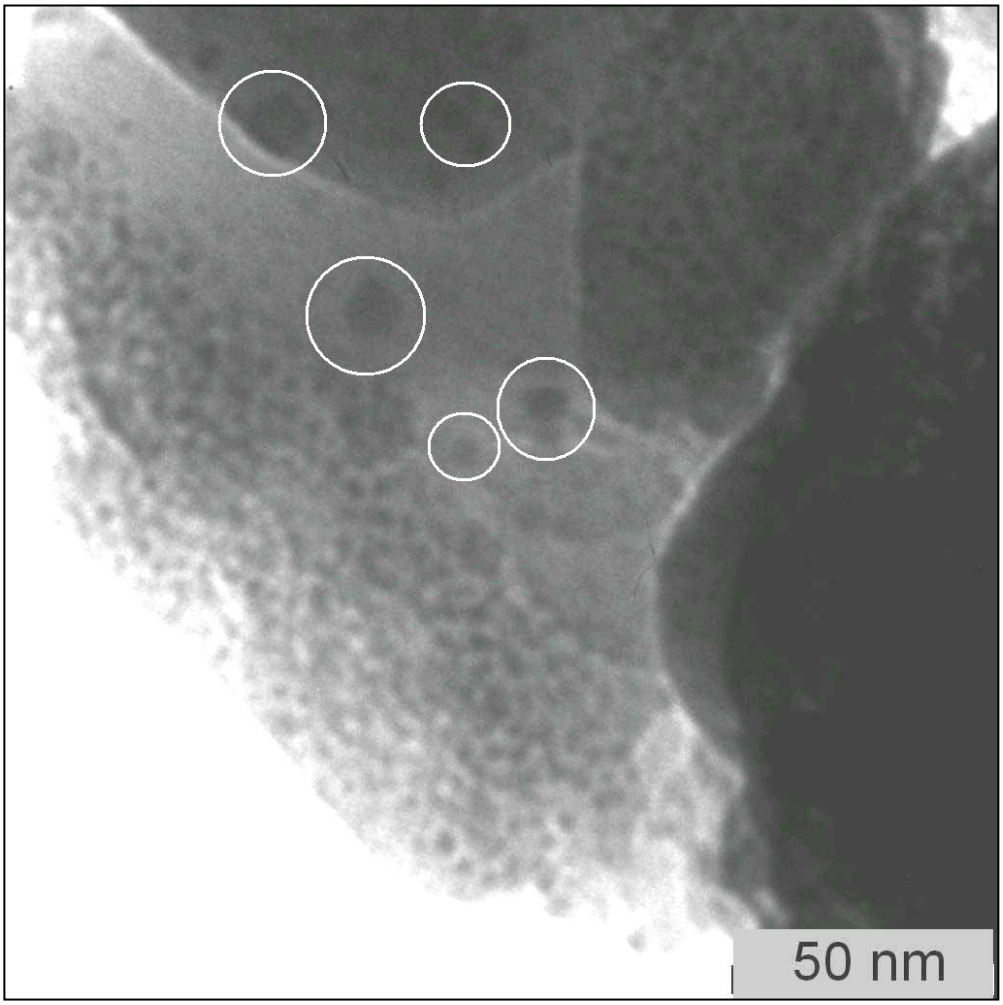

Figure 11

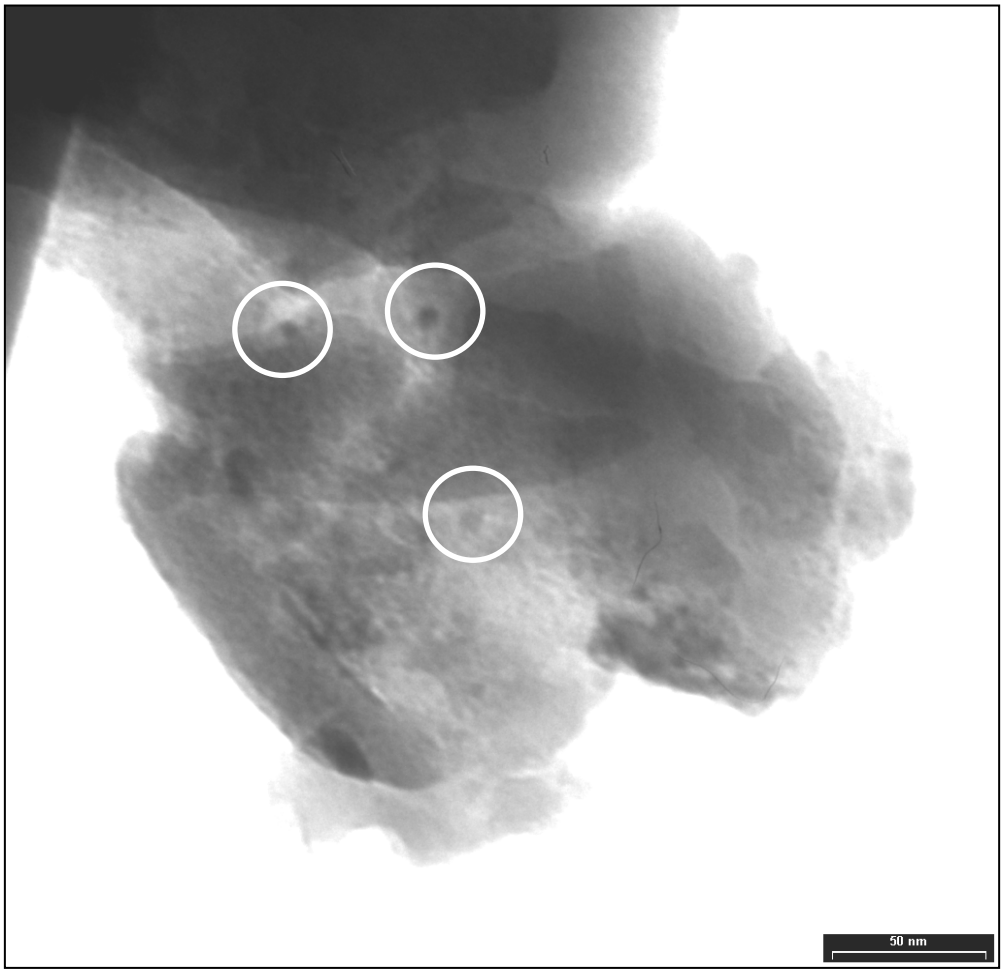

Figure 12